INVESTIGATION OF THE CO_2 STORAGE CAPACITY OF AQUIFER STRUCTURES: CO_2 STORAGE IN A BUNTSANDSTEIN PROTOTYPE AQUIFER

Doctoral Thesis
to be awarded the degree of
Doctor of Engineering (Dr.-Ing.)

submitted by
Emine Buket Ülker
from Niksar, Turkey

approved by the Faculty of Energy and Economical Sciences,
Clausthal University of Technology,
Date of Oral Examination
29 January 2009

Chairperson of the Board Examiners
Prof. Dr.-Ing. Oliver Langefeld

Chief Reviewer
Prof. Dr. mont. Günter Pusch

Reviewer
Prof. Dr. Martin Bremeier

Dissertation Clausthal University of Technology
D104

Contents

List of Tables

List of Figures

Abstract

Carbon dioxide can remain trapped underground through a combination of physical and chemical mechanisms, such as: trapping under an impermeable, confining layer (cap rock); retention as an immobile phase trapped in the pore spaces of the storage formation; dissolution in the formation fluids. In the long term CO_2 may be trapped as carbonate minerals by reacting with the minerals in the storage formation and cap rock.

A critical aspect of CO_2 sequestration projects is the risk of leakage. CO_2 may escape from the storage formation through the cap rock, if the capillary entry pressure at which CO_2 may enter the cap rock is exceeded, through faults, fractures and damaged or abandoned wells. The prerequisite for the occurrence of volume flow is that the pressure difference across the cap rock exceeds the entry pressure of the cap rock. In order to avoid volume flow through the cap rock, the cap rock sealing pressure should be determined before the CO_2 storage project and should be monitored. On the other hand, the simulation study identified that vertical permeability, and thin shale layers within the storage formation strongly influences the vertical migration of gaseous CO_2 plume. Low permeability layers within the storage formation therefore have the effect of impeding the vertical migration of CO_2 and thus decreases the leakage risk.

This project focuses only on the solubility and capillary trapping to estimate the CO_2 storage capacity of a saline aquifer. Solubility and capillary trapping are the essential mechanisms controlling the upward and lateral migration of CO_2 during the injection and post-injection period. The phase-solubility calculations are most critical for the prediction of solubility trapping capacity of the aquifers. The migration capacity of the higher density plumes is dependent on the solubility modeling of CO_2 in brine. The results indicate an obvious sensitivity to the varying solubility of CO_2 in various types of brines (NaCl, $CaCl_2$)

with changing salinities. In the immediate post-injection phase, the governing forces on the injected gas are gravity and diffusion. CO_2 is more buoyant than brine, therefore as CO_2 migrates vertically to the top of the geologic structure, leaving trapped residual gas around the injector. Therefore, assessment of CO_2 immobilization requires accurate modeling of multi phase flow performance. The results show that the hysteresis phenomena play a significant role in the post-injection period. When hysteresis effects are taken into account, more gas is trapped in the vicinity of the well. Due to the entrapment, the areal extension of the gas plume is reduced and gives less contact with cap rock and thus decreases the risk of leakage through the cap rock. On the other hand when hysteresis effects are neglected, the capillary entrapment prediction can not be modeled precisely and the solubilization of gas into brine may be overestimated.

A geologic model of a Buntsandstein aquifer was created with PETREL based on existing gas storage model. Much of the available data is necessarily site specific; however some data is integrated into geological model to simulate the CO_2 storage performance and assess how much CO_2 can be stored at the selected site. Therefore, the simulations were performed with different sensitivity cases. From the results it can be concluded that the critical saturation for the flow of gas and water, salinity and brine composition as well as the permeability anisotropy were defined as main parameters influencing the solubility trapping of CO_2. The capillary trapping is mainly affected by varying the CO_2 injection rate, hysteresis between drainage and imbibition processes and residual phase saturations. The vertical and horizontal wells were also compared to identify the effective injection geometry. Vertical injection across the entire storage formation interval leads to extensive contact with cap rock and leakage through it. Horizontal wells located in the lower part of the formation both increase the aquifer utilization and eliminate contact with cap rock. Thus horizontal wells can be an alternative to inject more CO_2 and minimize leakage. A basic investigation of the phase behavior and pVT characteristics of the CO_2-brine mixtures and the effect of relative permeabilities and capillary forces on the CO_2 storage performance by using the CO2SEQ option of ECLIPSE simulator is presented in this study. The study also includes some other sensitivity cases such as; the effect of permeability anisotropy within the storage formation and the injection geometry to minimize the risk of CO_2 leakage and subsequently increase CO_2 storage.

Acknowledgements

I would like to thank my supervisor, Prof. Dr. mont. G. Pusch, for his excellent guidance, support and encouragement throughout this work.

I would also like to thank Dr. H. Alkan,for his several enlightening ideas and constructive comments which have helped me to improve my views of simulation and reservoir engineering theory.

Prof. Dr. L. Ostrowski got involved in my work and encouraged me to take a different view on my approach.

I should also mention that my graduate study in Germany was supported by BGR. I would like to thank Dr. F. May and Dr. P. Gehrling from BGR for their support and encouragement during my study.

Schlumberger is acknowledged for making available ECLIPSE simulator and supporting software.

I would like to thank all the staff of Petroleum Engineering Department at TU Clausthal.

Finally, I thank my parents and my sister.

E.Buket Ülker

Clausthal, 2009

Chapter 1

Introduction

The Federal Institute for Geosciences and Natural Resources (Bundesanstalt für Geowissenschaften und Rohstoffe, BGR) in Hannover has introduced a research programme on contract research with qualified Universities in order to utilize their special know-how for the prime task of the BGR, to contribute for the advice of the German Federal Government in all geo-relevant questions. The actual project belongs to the contract research in the area of reservoir and natural resources research.The working programme of the study performed on the following frame work:

- Acquisition and evaluation of geophysical and geological data of a prototype Buntsandstein aquifer structure, provided by company ESK, Buntsandstein prototype reservoir
- Identification of anisotropy elements in the storage
- Build-up of a 3-D geological model of the aquifer structure
- Up-scaling and conversion of the geological model into a structured/unstructured numerical grid model of the simulator ECLIPSE
- Compilation and interpretation of relevant phase behavior and phase property data CO_2/ brine
- Adaptation of flow parameters CO_2/ brine in 2-phase mode and for dissolved gas in brine

- Simulation of different strategies of CO_2 injection, using efficient reservoir access methods via vertical and horizontal wells as well as determination of gas losses into the cap rock via geologic anomalies
- Determination of the CO_2 storage capacity in free gas phase mode and in dissolved mode
- Definition of a generic model of the Aquifer structure and performance of parameter evaluation to study the sensitivity of main parameters on the storage capacity

The study was initiated in March 2004 and completed on 31 May 2007.

1.1 Geological Storage of CO_2

Climate change is a major environmental problem despite the remaining uncertainties about the scale of the phenomenon. The atmospheric concentration of CO_2 has increased from the pre-industrial age level of 280 ppm to 380 ppm at the present time [27]. It is believed that there is a cause and effect relationship between the CO_2 concentration and global temperature.

It seems certain that the change in CO_2 concentration in the atmosphere is primarily due to the large-scale burning of fossil fuels such as coal, natural gas and crude oil. It has been anticipated that world's yearly energy-related CO_2 emission, which is currently about 25 Gt *(billion tons CO_2)*, will rise to 38 Gt by the year 2030 which is 50 % higher than the current level and yet by 2020 90 % of world primary energy will be supplied through burning fossil fuels [8]. This indicates there is an urgent need for short- and long-term solutions to reduce CO_2 emission.

There are two major approaches to reduce the CO_2 emissions, either by mitigating the release of CO_2 into the atmosphere through the storage of the gas or its carbon component, called carbon sequestration or reducing the production of CO_2. Greater reductions could also be attained by switching to non-carbon fuels. However the world is presently heavily dependent on energy supply by the use of fossil fuels. Therefore, storage of carbon has become an important research topic. The injection of carbon dioxide (CO_2) into deep oceans, coal-beds, depleted oil reservoirs and saline aquifers have been proposed to reduce

atmospheric emissions. Among these options, storage in saline aquifers seems to be a wide spread option due to its large scale availability and closeness to the emission sites. The world wide CO_2 storage capacity of deep saline aquifers has been estimated to range from $10,000$ $GtCO_2$ to $200,000$ $GtCO_2$. When economical and technological constraints are included in the storage analysis, capacity is estimated between 200 and 500 $GtCO_2$. Current global emissions are in comparison in the order of 30 $GtCO_2$ per year. The available capacity is therefore sufficient for 8-16 years [3].

Geological storage can be achieved through a combination of physical and chemical mechanisms[7] which can be summarized into the following forms of trapping.

- The injected CO_2 tends to migrate vertically to the top of the storage formation due to the gravity forces. A cap rock layer that overlies the storage formation prevents the vertical migration. This referred to as *stratigraphic trapping*.

- When CO_2 is dissolved into the aquifer water, the formation water density increases. The denser saturated water relative to the under-saturated water will sink, and limit the upward migration of CO_2 and thus the leakage risk through the cap rock. This is called *solubility trapping*.

- Injection of CO_2 into saline aquifers is in a two-phase flow condition. CO_2 can form a CO_2-rich gas phase that is immobile due to trapping by capillary forces for saturations below the critical gas saturation. This referred as *capillary trapping*.

- In the long term perspective CO_2 and its aqueous-phase derivatives may react with aquifer solids and can be consequently stored as precipitates. Another reaction is the chemical conversion of rock matrix minerals upon contact with CO_2. This storage mechanism is known as *mineral trapping*.

Several research topics arise from the above. It is of general interest to determine the storage capacity and confining ability more precisely, in order to inject more CO_2 and to retain this gas for a long period. The risks that the injected CO_2 may leak into the atmosphere through faults, cap rock formation or wellbores must be carefully evaluated. In this study, focus is on determining the extent of CO_2 migration during injection and post-injection period, and leakage through the cap rock and faults.

1.2 Objectives of the Thesis

The study comprises, through numerical modeling, the influence of structural heterogeneities in Buntsandstein aquifers on the behavior of injected CO_2. Specific targets are;

- Characterization of the Buntsandstein prototype aquifer, and construction of a geologic model to define the spatial distributions of reservoir rock properties
- Determine the sensitivity of flow performance of the injected CO_2 on the reaction with the rock and on the sediment heterogeneity
- Model the time dependent changes in the distribution and dissolution of injected CO_2 in the heterogeneous aquifer
- Assess the validity of hysteretic relative permeability models and examine the impact of relative permeability and capillary forces on capillary trapping
- Determine the extent of CO_2 migration
- Assess the optimal CO_2 injection rate and injection pattern
- Evaluate the leakage risk of CO_2 to the surface through the existing wells and cap rock formation

1.3 Structure of the Thesis

An introduction addressing the general reasons for the CO_2 storage is provided in Chapter 1. Chapter 2 gives information about the characterization of the Buntsandstein prototype, and the construction of the geological and property model. Chapter 3 provides a comprehensive evaluation of phase and petrophysical behavior of CO_2 containing aqueous solutions in porous rocks. It is well understood that these parameters effect the result of solubility and capillary trapping mechanisms. Chapter 4 summarizes the common "two-phase" hysteretic models responsible for the trapping of the non-wetting phase. Chapter 5 gives a brief overview of the development of the numerical simulator, ECLIPSE which uses EOS to correlate the phase behavior of multi component systems. Chapter 6 provides the result of sensitivity analysis of generic model corresponding to the constructed geologic model and

its average reservoir properties including cap rock. It was intended to extend the numerical investigation and to perform simulations on a realistic three dimensional heterogeneous reservoir, modified from the well known gas storage field in Germany. The extract of the simulation results as well as statements regarding the main results which were already accepted for the presentation and publication are given in Chapter 6. General conclusions drawn from all the work in this report, along with some ideas and recommendations for future research are presented in the final chapter.

Chapter 2

Geological Modeling of a Buntsandstein Prototype Aquifer

According to the commitments of the Kyoto protocol the EU countries are challenged to reduce the emission of carbon dioxide (CO_2) by 8 % from 1990 levels till the period 2008-2012. For Germany this means a reduction of greenhouse gases by 21 % till this period. But the government went still beyond this goal. In October 2000 they released a national climate protection programme with a national target to reduce the anthropogenic CO_2 emissions by 25 % until 2005. A further aim is to achieve a reduction of 40 % for the year 2020 under the precondition that the EU reduces greenhouse gas emissions by 30 %. and by 40 % till 2020. In the early 90's Germany was quite successful in reducing the CO_2 emissions. In the first five years the emissions dropped by 13 % or 150 million tons of CO_2. However, a considerable part of this initial progress was directly connected with the break-down of the smokestack industries (heavy industry) in former Eastern Germany and the consequences of economic restructuring. For the last 8 years the CO_2 emissions remained nearly static with a small decline of only 4 %. The overwhelming part of this greenhouse gas is emitted by power plants (44 %) traffic follows with 20 %, industry with 19 % and the private sector emitted 14 % CO_2 in 2003.

Therefore, the geological storage of CO_2 has been proposed in order to reduce the atmospheric emission. Regarding the preliminary results, CO_2 storage in Germany is promising in different regions and geological formations. The primary storage aim for CO_2 in Germany are depleted and active gas fields in Permian and Triassic sandstones of the North and Middle German Sedimentary Basin. They are proven gas tight and from the economical point of view they are interesting due to the combination of CO_2-storage and the enhancement of the recovery of residual methane gas. The storage capacity of German gas fields, including existing gas reserves has been estimated by BGR as approximately 2.5 Gt of CO_2. But the recent annual emission rate of all coal power plants in Germany is around 370 million tonnes of CO_2. In order to reduce the emission of power plants an enormous storage capacity is required therefore, the deep saline aquifers are proposed with an estimated capacity of 16 Gt in Germany (BGR).

Therefore this study first comprises the construction of geological model, then definition of the spatial distributions of reservoir rock properties in order to incorporate them into the numerical model, and determine the influence of structural heterogeneities in a Buntsandstein prototype aquifer on the impact of injected CO_2.

2.1 Geo-Model Setup

The definition of the geologic model of the reservoir represents one of the most important phases in the work-flow of a typical reservoir study, both concerning the volume of work involved and the impact on the final results. The geological model is often generated making use of static information such as core, log, and seismic data while the dynamic information is used mostly for the calibration and the validation of the model. A geological model is composed of a multitude of single building blocks, which are marked all by spatial coordinates, x, y and z and assigned specific corresponding characteristic of porous media. These characteristics include facies and petrophysical parameter such as porosity, permeability

and gas saturation. The aim of this section was to model the geological structure of an existing aquifer gas storage with the aid of the model maker PETREL. Reservoir is located in north-west Germany, the geologic structure is a smooth anticline striking WNW-ESE with NW-SE striking normal faults. At first glance, the lithostratigraphic framework of Permian Triassic deposits in NW Europe well defined. Terms such as *Rotliegend*, *Zechstein*, *Buntsandstein*, *Muschelkalk* and *Keuper* are established in the stratigraphy of the surrounding countries as well as in Germany. For this study *Buntsandstein* especially the *Middle Buntsandstein* is important for containing large aquifer structures. The typical geological model is generated with the following aspects:

- Structural Model: The different available information such as geologic evidence and well data are used to define the structural top map of the reservoir and associate fault pattern.

- Stratigraphic Model: Well correlation is performed in this stage to identify the continuity of layers.

- Lithological Model: The reservoir is subdivided into a number of elementary facies and the facies are characterized in this section. A detailed 3D facies distribution is obtained with available stochastic techniques.

- Reservoir Heterogeneity: To the geologist the first three provides a sufficiently detailed characterization of the overall geological complexity of the reservoir. However, such characterization may be still unsatisfactory when the dynamic performance of the field is being considered. In the framework of a reservoir study, where the final objective is a dynamic reservoir characterization, the study of the types of reservoir heterogeneity and their impact on fluid flow is a mandatory work.

2.1.1 The Buntsandstein

The Buntsandstein was deposited under calm tectonic conditions and represents the main subsidence period of the North German Basin. Therefore, deposits exhibit uniform lithologies and thickness over large distances. The Buntsandstein represents the lower group of the tripartite classic Germanic Triassic. It is traditionally subdivided by lithological criteria into three subgroups: (a) the fine-grained Lower Buntsandstein, comprising characteristic oolites, (b) the Middle Buntsandstein composed of coarse-grained sandstones and shales, and (c) the shaly Upper Buntsandstein containing evaporites. The Lower Buntsandstein is subdivided into the Calvorde Formation and Bernburg Formation. Its lower boundary is placed at the base of the first distinct sandstone interval above the Zechstein. The boundary between the Lower and Middle Buntsandstein, the base of the Volpriehausen Formation, is marked by a hiatus. Here, an additional sandstone unit occurs between the Lower Buntsandstein and the Volpriehausen Formation. The unconformity at the base of the so-called Quick-born Sandstone forms the boundary between the Lower and Middle Buntsandstein. The Middle Buntsandstein is composed of the Volpriehausen, Detfurth, Hardgessen and Sölling Formations. Each formation represents a large-scale fining upward sequence, with sandstones in the basal part, grading into claystone and siltstone towards the top. Important characteristics of the deposits of this subgroup are the tectonically induced unconformities at the bases of Volpriehausen, Detfurth and Sölling Formations ("V", "D" and "H" unconformities, Trusheim 1961). The Upper Buntsandstein consists of Röt-Formation. In this Röt-Formation, an additional two tectono-stratigraphic sequences the Lower Röt and Upper Röt have been identified. Geluk-Röhling, 1997 represents the stratigraphic sequence of Permian-Triassic deposits (Figure 2.1). The deepest aquifer complex deposit formed by the Middle Buntsandstein comprises four clastic units, each representing a cycle of fining upward sediments composed of coarse sandstone at the base overlain by alternating sandy-silty strata. For a CO_2 storage project; the Volpriehausen-Formation which

consists of Volpriehausen Sandstone, Volpriehausen Wechselfolge and Volpriehausen Avicula Schichten was selected as storage formation sealed by the overlaying cap rock formation[2].

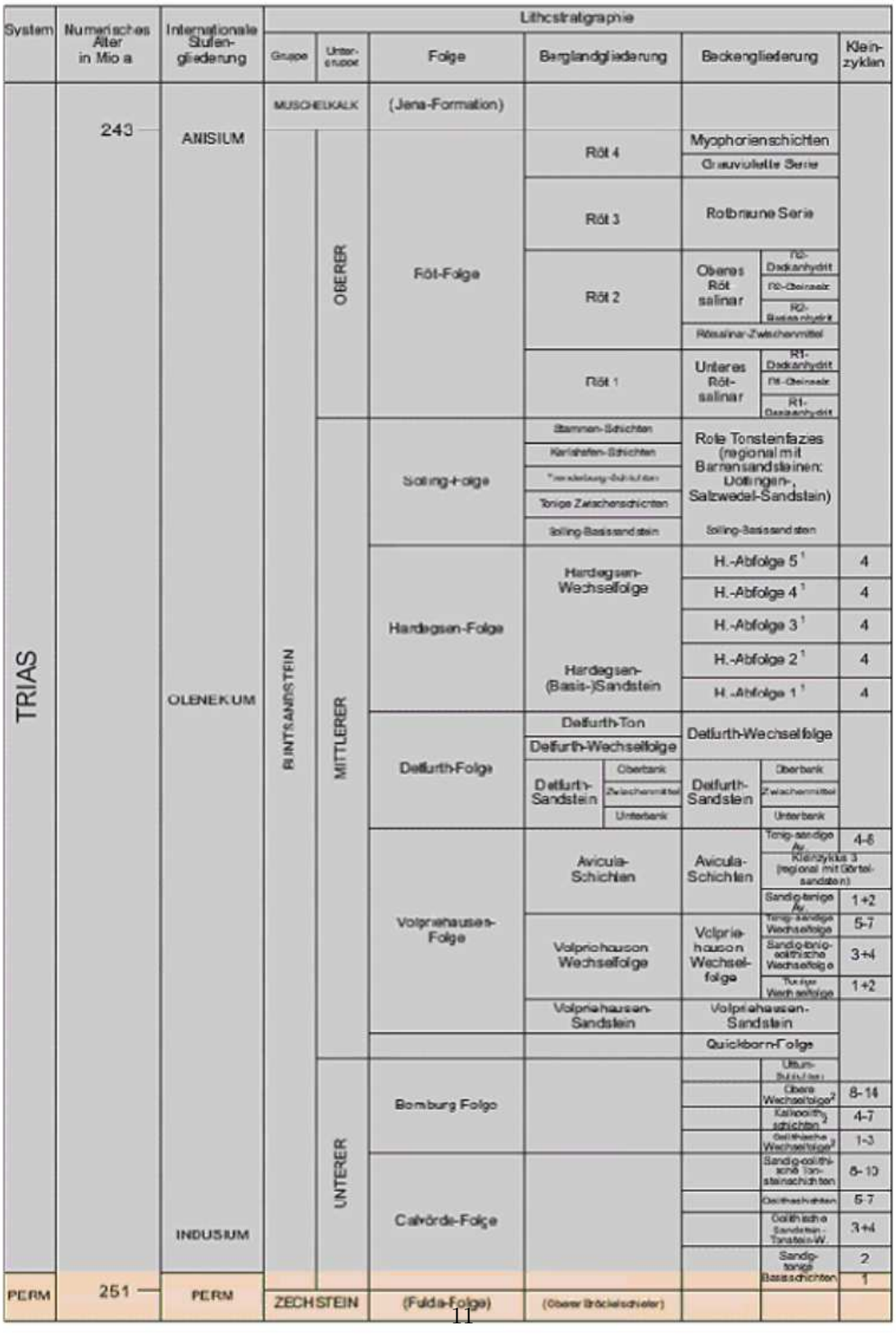

Figure 2.1: Stratigraphic sequence of Permian-Triassic

2.1.2 Volpriehausen Formation

The Volpriehausen Formation comprises basal sandstone, followed by an alternation of clay-siltstone and thin sandstones which can be seen in Figure 2.2.

Figure 2.2: Stratigraphic sequence of Volpriehausen formation

The thickness of the Volpriehausen Formation is at maximum 130 m - 140 m and minimum 80 m - 90 m. The storage zone in the Volpriehausen Sandstone is only 15 m - 17 m of this formation. Volpriehausen Wechselfolge acts as cap rock of storage formation due to its consistent shale content. Quick-born Sandstone is the boundary between the Lower and Middle Buntsandstein. The base of the Volpriehausen sandstone is well identified from medium-to coarse-grained sandstone facies and also from Gamma-Ray Logs. The Volpriehausen-Wechselfolge is in its lower part predominantly fine grained ("lower shale part") however the corresponding Gamma-Ray Log value for fine-grained sand is relatively high. Above the Wechselfolge, Avicula strata appear and in this zone thin sandstone layers are intercalated. The uppermost part of the formation is discontinuously represented due to erosion of the sediments and this erosion caused the Detfurth Unconformity. The concurrence of Gamma-Ray Log values and formation descriptions can be seen in Figure 2.3. The

figure shows correlation for two wells, S101 and S102. From bottom to the top the stratigraphy is sequenced as quick-born sandstone which was used in this geological modeling as the base of Volpriehausen sandstone. The thickness ranges between 1.5 m - 2.5 m in every wells. Above this formation the clay siltstone strata follows with thickness between 1 m - 1.5 m. Following the clay-siltstones is the sandstone formation with thickness in the range of 12 m and 14 m. Totally the Volpriehausen sandstone in reservoir has a thickness about 15 m - 17 m. Above this storage formation, the cap rock clay-siltstone formation appears and then the Avicula strata follows with thin sandstone layers.

The geologic structure is a smooth anticline striking WNW-ESE with NW-SE striking normal faults. There are nine wells in the area which are located very close to each other. Two of these wells S108 and S109 are horizontal wells and the others are fully perforated vertical wells. The geological modeling is performed in four stages; structural modeling, stratigraphic modeling, lithological modeling (facies modeling) and reservoir heterogeneity which is the mandatory work to perform the reservoir simulation.

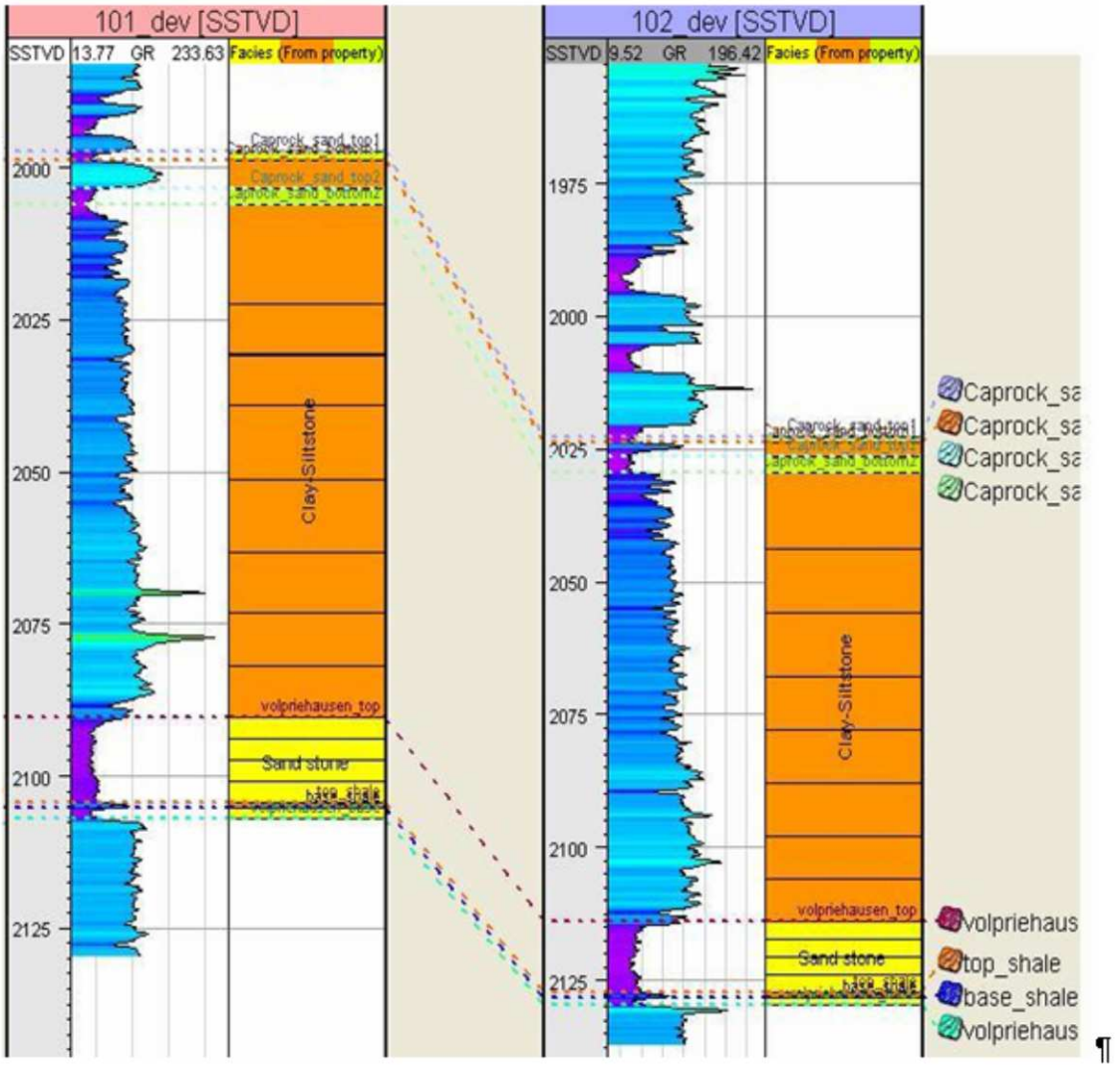

Figure 2.3: Well-to-well correlation based on gamma ray log and formation boundary in S101 and S102

2.1.3 Reservoir Heterogeneity

In the previous headings, brief information was given about building a geological model of a reservoir, focusing on the integration of available static information. Such a comprehensive description based on the definition of a structural, a stratigraphic and a lithological model provides a sufficiently detailed characterization of the overall geological complexity of the reservoir. When the reservoir simulation meaning consideration of the dynamic performance of the field, the study of reservoir heterogeneity and their impact on the fluid flow is a mandatory work. The impact of reservoir heterogeneity is related to the non-geologic parameters, like phase mobility, relative permeability, pVT properties, and also aquifer strength. It is known that fluid flow takes place in an interconnected network of pore spaces. There is a close relationship between porous network, rock properties and fluid flow which form the cornerstone of the reservoir study.

2.2 Petrophysical Property Modeling

A correct description of the petrological and petrophysical properties of the reservoir rock is a fundamental requisite in order to correctly represent the dynamic behavior of the field in the numerical simulation study. The identification and the quantification of porosity is a very important stage in the reservoir characterization process.

2.2.1 Porosity

The most common procedure to evaluate the porosity of a reservoir is a thorough log interpretation (neutron, density, sonic) since the data required are normally available in the majority of the wells. In this study the porosity was calculated from the density log. The density tool provides an estimate of the bulk density of the rock by measuring decrease of gamma rays between a source and receiver. Density is related to the porosity by the simple equation:

$$\phi = \frac{(\rho_{ma} - \rho_b)}{(\rho_{ma} - \rho_f)} \tag{2.1}$$

where, ρ_{ma} is matrix density, ρ_b is bulk density and ρ_f is fluid density. Bulk density is the density which is read from density log, matrix density and fluid densities are required prior knowledge of lithology and fluid type. The fluid is water, thus the fluid density was taken as 1.013 g/cm^3 and the sandstone matrix density was taken as 2.65 g/cm^3 whereas the siltstone matrix density is 2.71 g/cm^3.

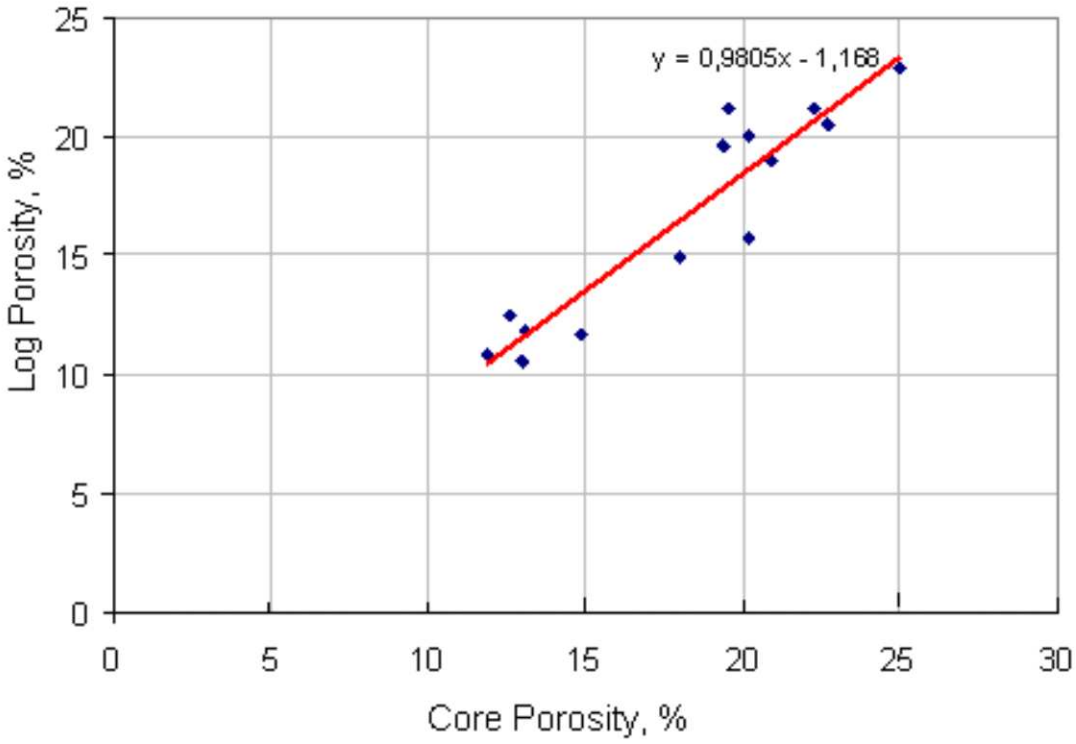

Figure 2.4: Core porosity versus log porosity of Volpriehausen sandstone formation

Figure 2.4 represents the comparison of core porosity and log porosity. For the Volpriehausen sandstone characterization, the core porosity values have been used, but the net pay thickness is only between 15 and 17 m. For the other parts of the reservoir, the only

available data are log data. Porosity values in cap rock and also in the respective sandstone formations have been derived from the available density log. In Figure 2.4, it is obviously seen that the porosity values calculated from well logs and porosity values from core data more or less correspond to each other. This comparison has been performed from the log data of five vertical wells. S101 and S105 do not have either density log data or neutron porosity data. Therefore these two wells were not taken into account in the calculations. Between the wells the porosity values have been calculated using the Kriging method. In Figure 2.5 the total data set is represented in a probabilistic distribution diagram.

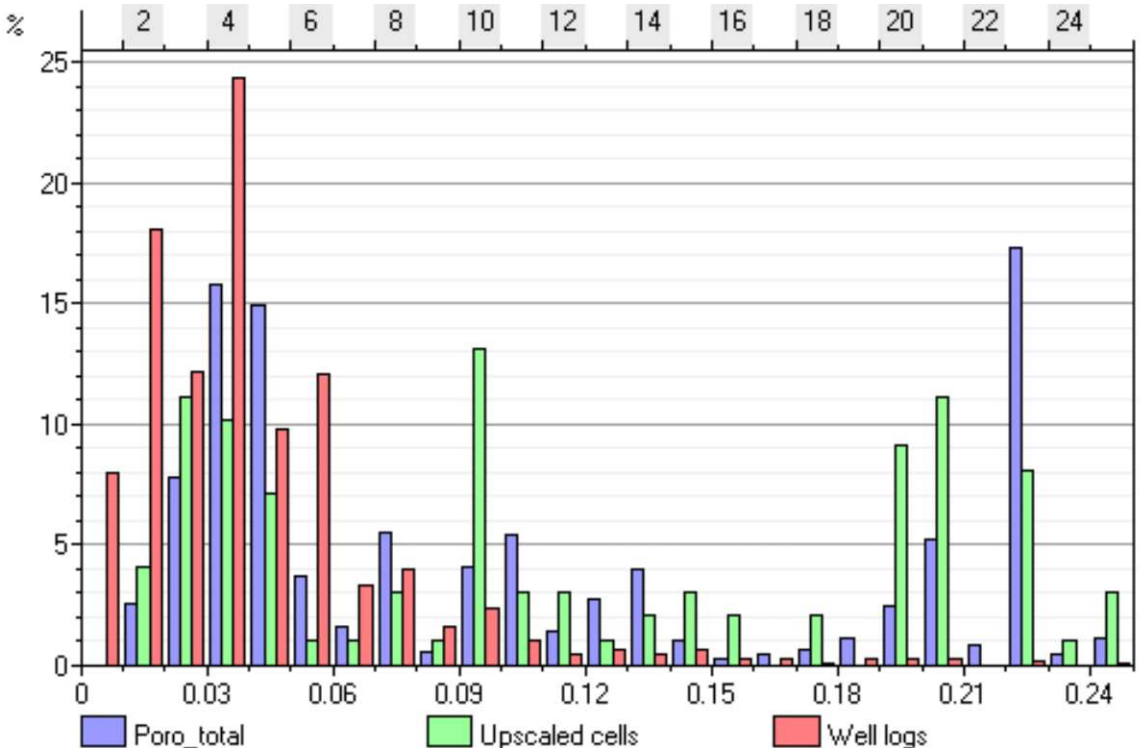

Figure 2.5: Histogram of porosity in reservoir

The purpose of a histogram is to graphically summarize the distribution of an univariate data set. The porosity values range between 1.34 % and 25 % and include data from sandstones in the aquifer as well as in the cap rock.

Figure 2.6 represents the up-scaled porosity distribution in vertical wells. Well log data must be scaled up before they can be used in the usual grid size. When modeling petrophysical properties, the modeled area is subdivided up by generating a 3D grid. Each grid cell needs a single value for each property. As the number of grid cells in the vertical directions are often much larger than the sample density for well logs, well log data must be scaled up before they can be entered into the grid. In wells S101 and S105, no density log was available. Therefore the core porosity values were provided by ESK.

Figure 2.7 represents the density log and up- scaled porosity in five vertical well profiles, S102, S103, S104, S106 and S107.

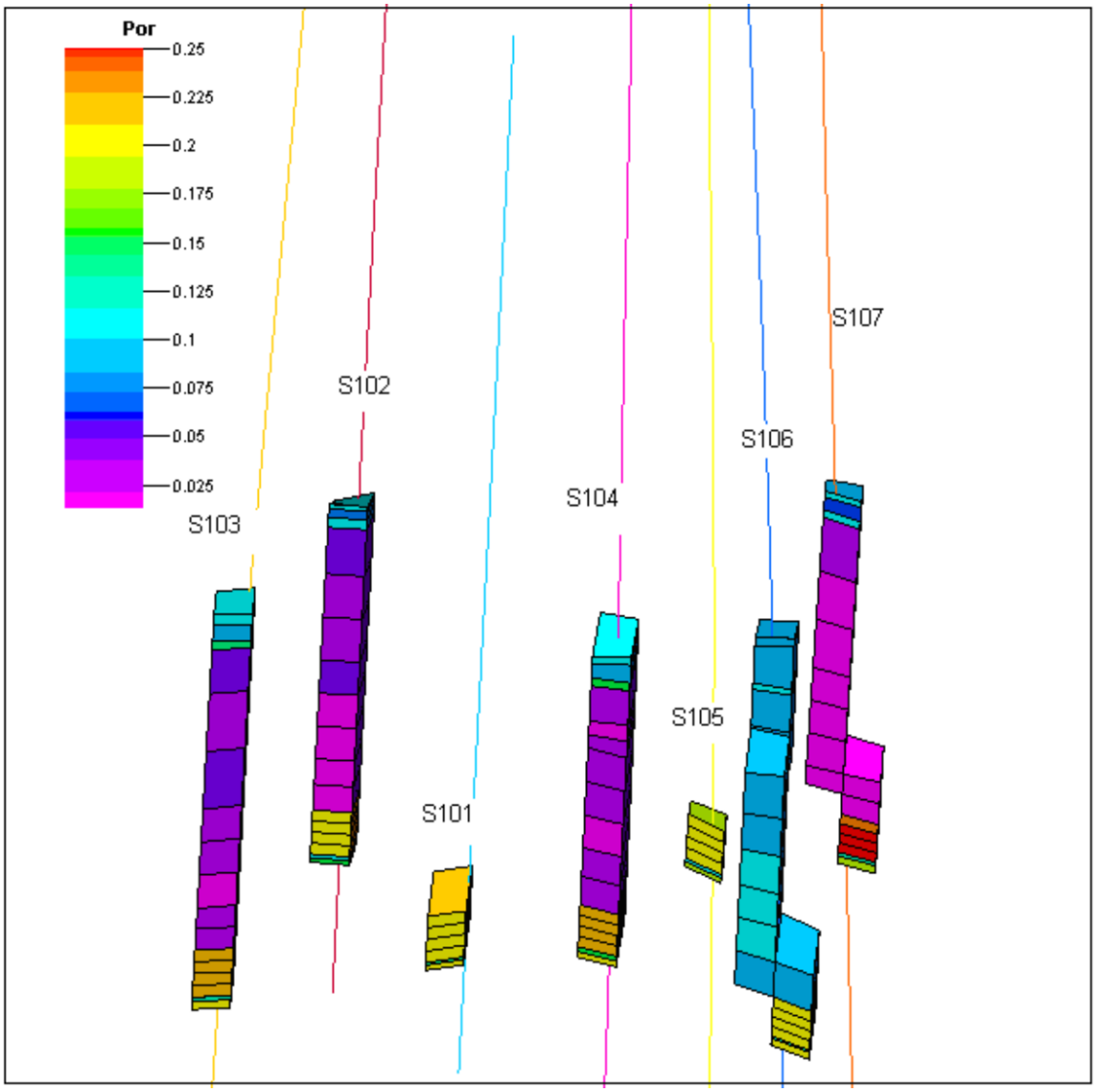

Figure 2.6: Up-scaled porosity distribution in vertical wells

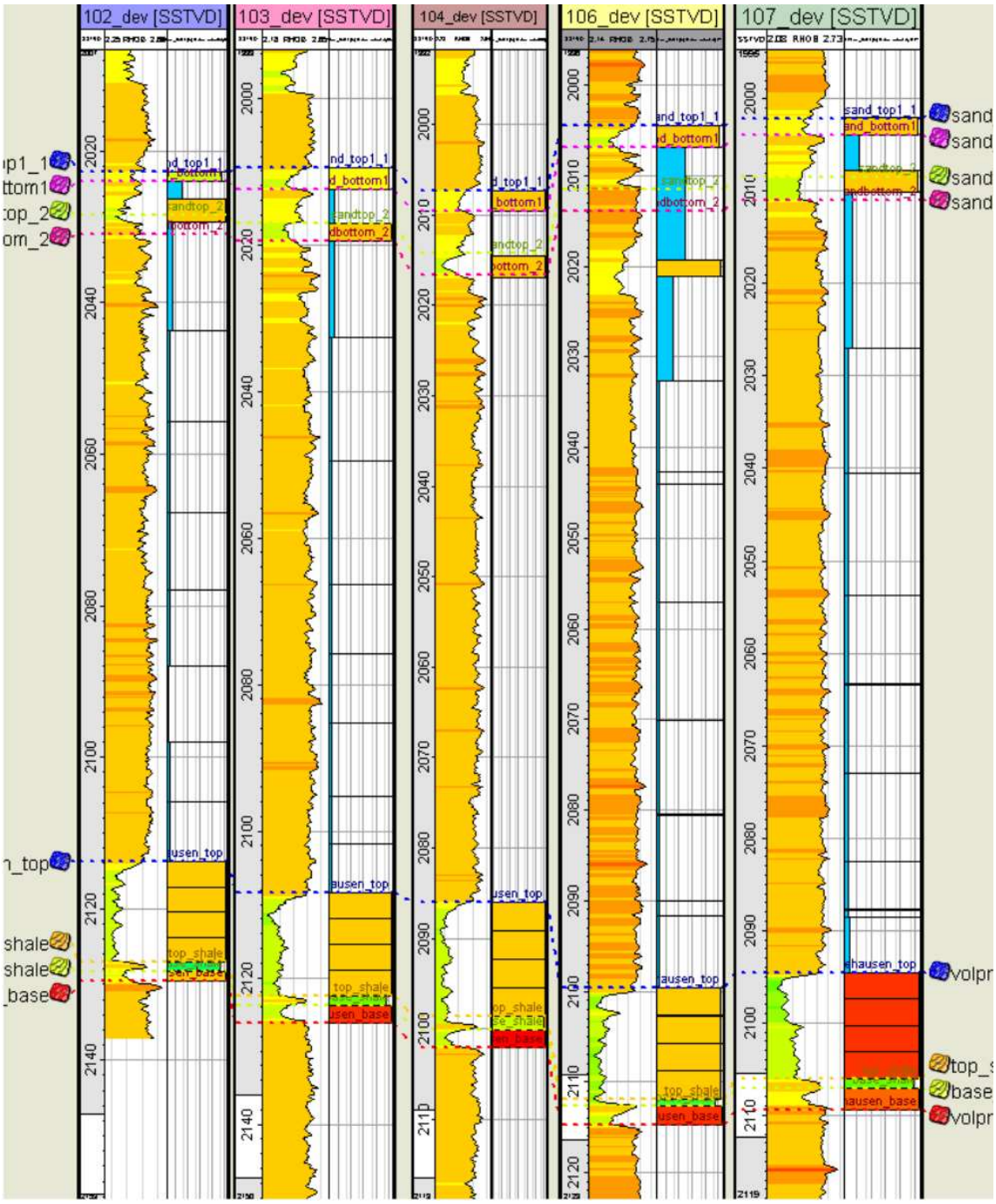

Figure 2.7: Density log and up-scaled porosity in vertical wells profile

2.2.2 Permeability

Permeability is as the ability of a rock to conduct fluids. Beyond any doubt, it is the most important petrophysical property of a reservoir. The most common way to estimate permeability profiles in un-cored wells is by using some permeability predictor, typically in the form of empirical equation from analog rock examples (other reservoirs or outcrops). Most reservoir rocks show a reasonably linear relationship between these parameters in a semi-log scale, which allows the estimation of permeability when a porosity profile and some reliable core measurements are available.

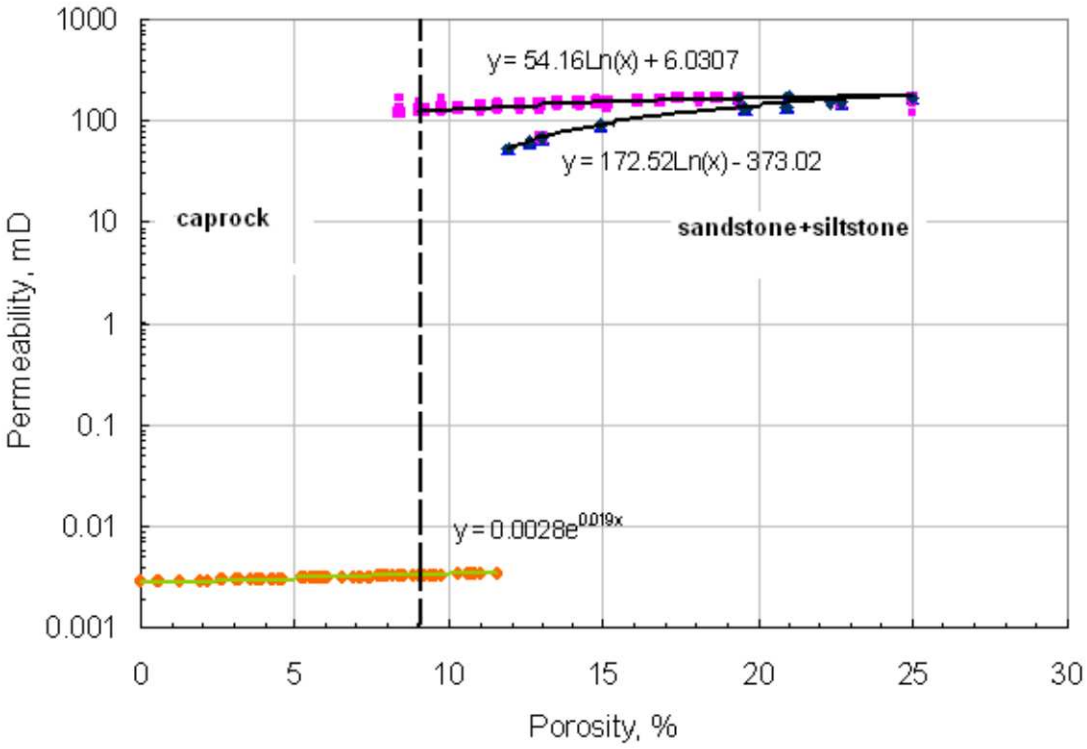

Figure 2.8: Porosity-permeability relationship between wells in Volpriehausen formation

Figure 2.8 shows the porosity-permeability correlations for the storage and barrier rock data provided by ESK. The core data of porosity and permeability have been measured

from well S109. It can be seen from the diagram; that the correlations are characterizing two zones respectively clay-siltstone formation and sandstone formation. The data used in the correlation were representative only for the wells. However Figure 2.9 represents the correlation in all cells and also in up-scaled cells. For the lower part of the graph where the porosity values are less than 10 %, the unpublished correlation for the Buntsandstein reservoir Barrien (Wintershall) has been used. To obtain more representative and reliable results for the layers different k/ϕ plots plots of individual facies have been correlated for the field. This data set show a more homogeneous behavior. Before petrophysical modeling, the facies analysis has been already performed since the facies classification criteria are closely related to petrophysical properties.

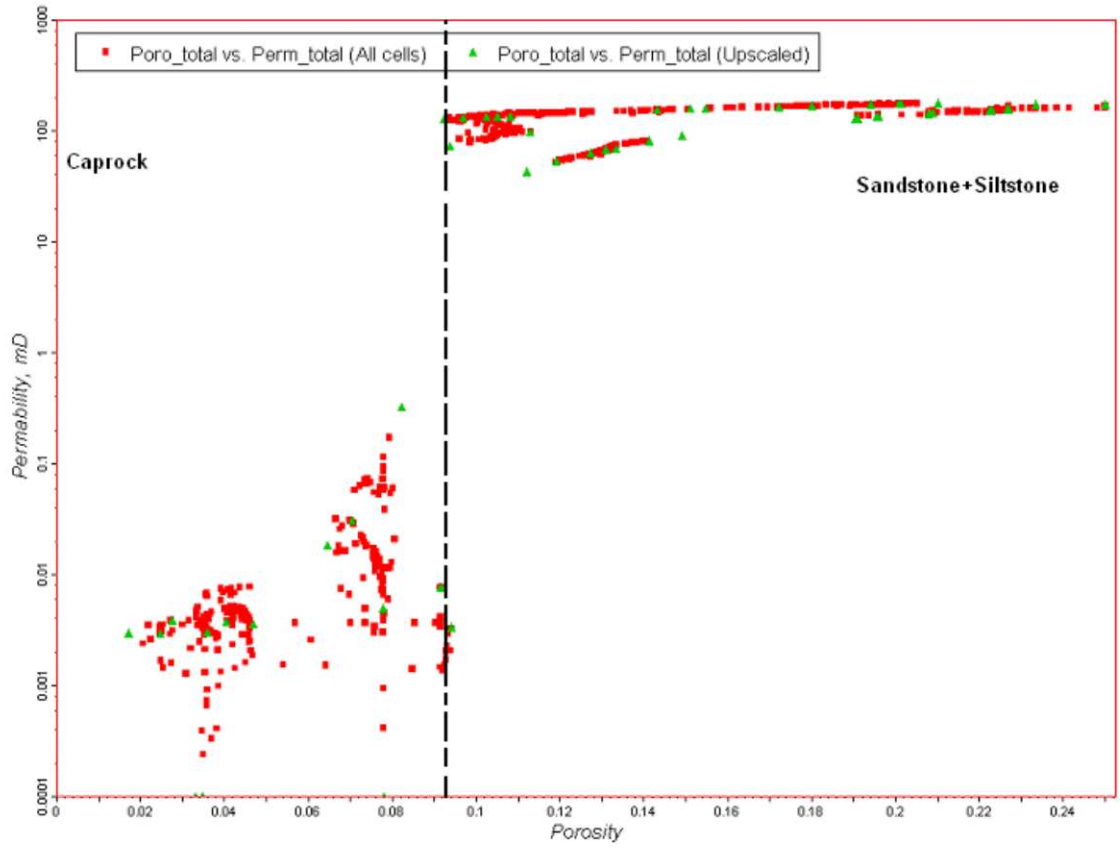

Figure 2.9: Porosity-permeability correlation in Volpriehausen formation

Figure 2.9 represents the k/ϕ correlation in all Volpriehausen formation; for sandstones and also for clay-siltstone. The lower part of this graph, where the porosity is less than 10 %, shows the correlation in cap-rock, i.e. clay-siltstone zone.

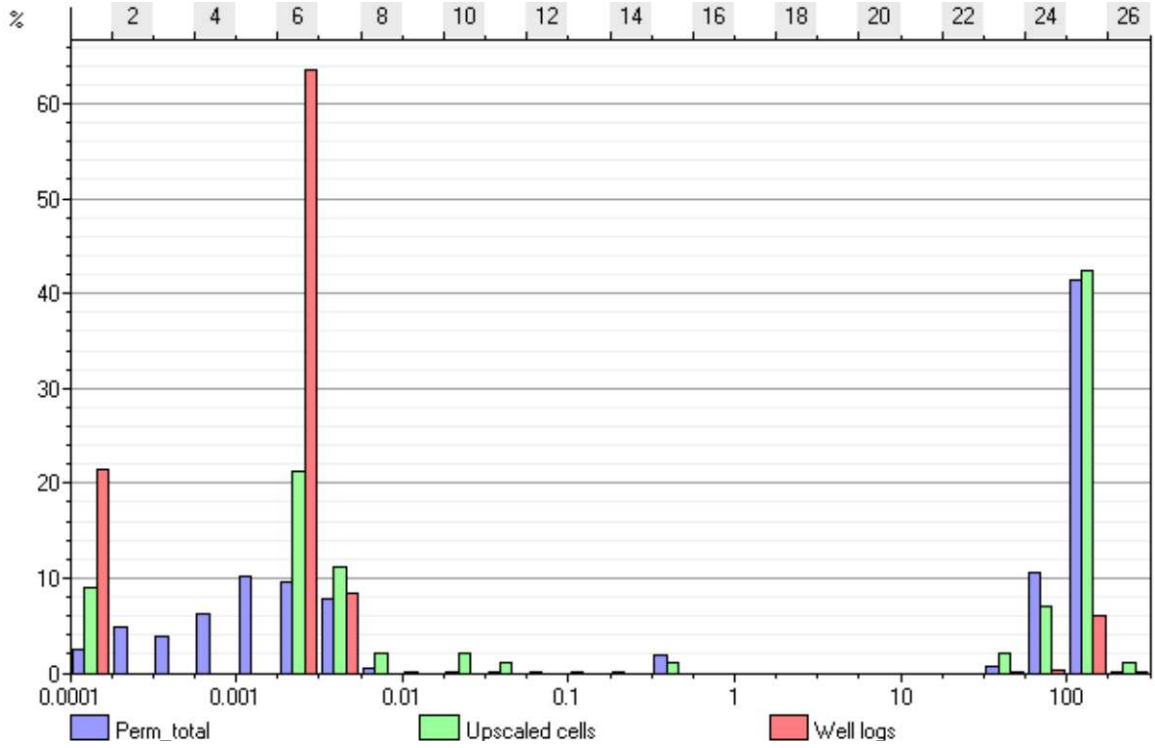

Figure 2.10: Histogram of permeability in reservoir

The permeability values range between 0.0001 mD and 178 mD. Figure 2.10 represents the permeability distribution in the reservoir. According to this histogram the permeability is classified in three regions. The left side of this histogram below the target formation limit of 0.1 mD shows the permeability in clay-siltstone formation, the right side where the permeability is in the range from 40 to some hundred mD shows the range of the sandstone and the silt intercalations in the storage formation.

Figure 2.11 represents the up-scaled permeability distribution in vertical wells. Regarding the lack of density log data in wells S101 and S105, the porosity and the permeability could not be evaluated. However the core porosity values were provided by ESK. In these

wells the storage formation permeability was obtained from the porosity-permeability correlation given in Figure 2.9. The cap rock permeability distribution was obtained using Kriging (interpolation). Permeability shows a logarithmic distribution different from normal distributed porosity. This is considered in Kriging process and also porosity was used as a trend property in order to obtain permeability.

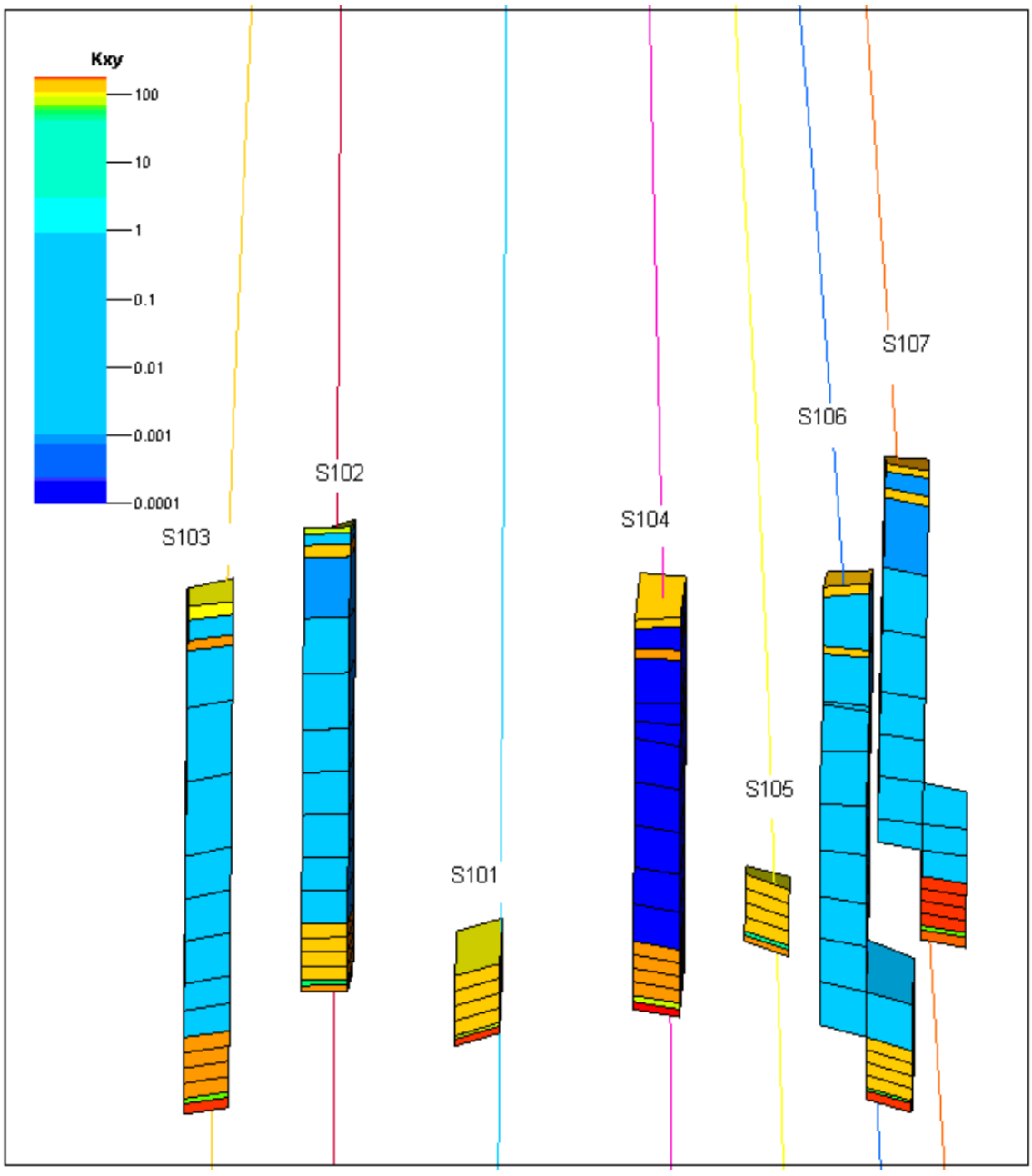

Figure 2.11: Up-scaled permeability distribution in vertical wells

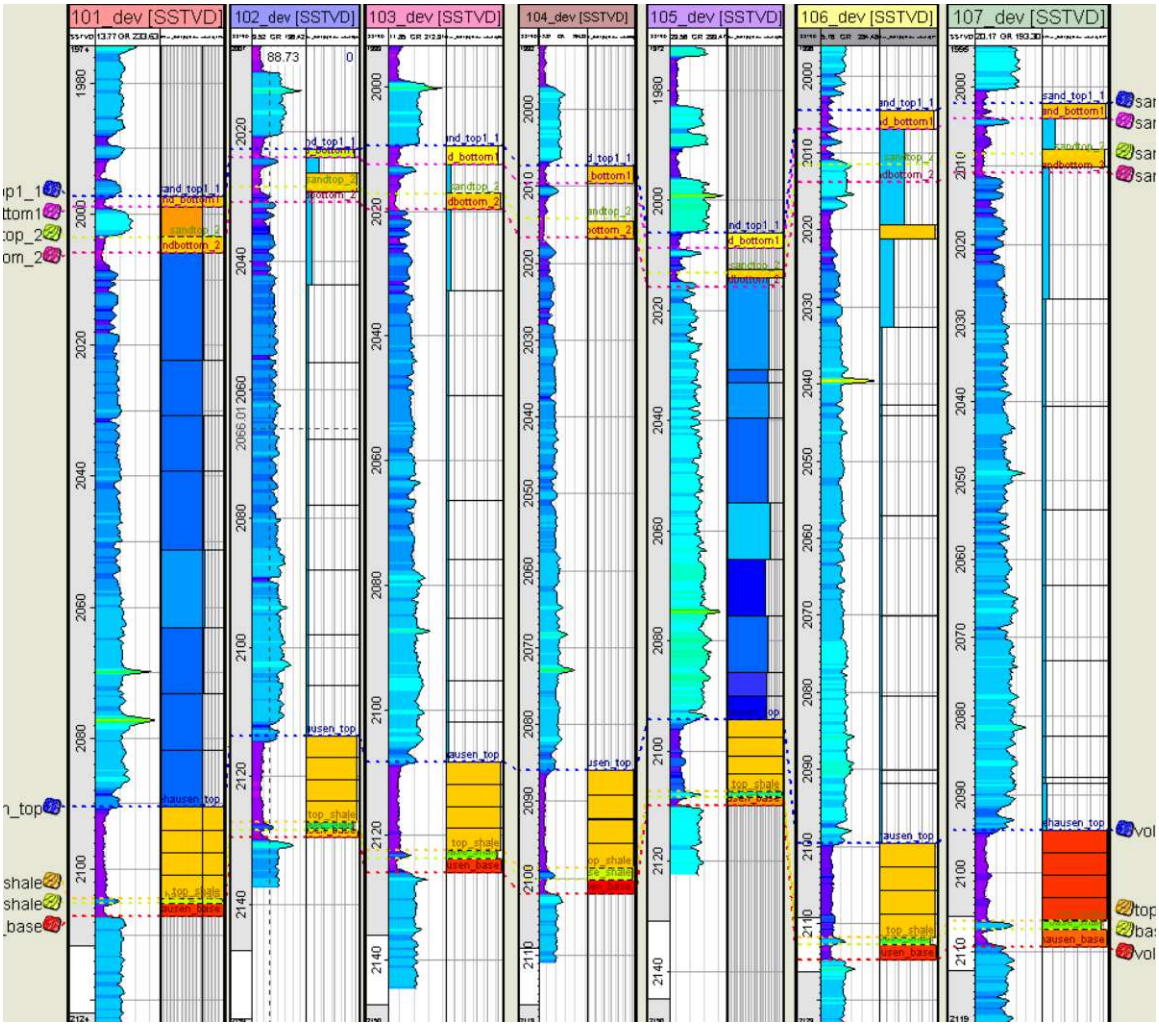

Figure 2.12: Gamma ray log and up-scaled permeability

Figure 2.12 represents the gamma-ray log and up- scaled permeability in 7 vertical well profiles. Interpolated permeability values can be easily noticed in wells S101 and S105, where the storage formation core samples are available.

The objective of petrophysical interpretation is to estimate the various petrophysical properties of the reservoir rock and their interrelations, at the well locations. Up to here, the properties were defined for every vertical well. Therefore the following step should be the analysis of the lateral variation of these properties, in order to generate 2-D or

3-D distributions at the scale of the reservoir. In the previous pages two petrophysical properties porosity and permeability have been discussed. We will be dealing with these important properties in order to generate 3-D distribution in the reservoir. Starting from the petrophysical interpretation available at the well locations, possibly averaged for given vertical sections (the reservoir layers), a spatial distribution of porosity can be obtained in different ways, depending on the amount and quality of the available data. The simplest way of obtaining a porosity map, for a given reservoir layer, is by simple linear interpolation of posted well values. In this study the wide spread application of geostatistics, i.e. kriging was used. For this purpose, the spatial correlation function of the variable being described, porosity in this case, is determined from the available data by the use of variogram technique, rather than assumed a priori by the griding algorithm. This correlation function provides the spatial continuity of the variable. Normal kriging is the simplest estimation according to the input model.

Porosity can be modeled by means of geostatistics thorough one of the two following approaches;

1. **Direct Estimation:** Porosity is modeled directly in the entire volume of the reservoir starting from a number of vertical porosity profiles at well locations and a spatial correlation function.

2. **Two-stage Model:** A 3-D lithological model for the reservoir is generated first, using a selected number of facies types. Porosity is modeled afterwards, within each lithological facies unit.

The direct estimation porosity gives satisfactory results in simple lithological environments and in general in all those cases where lithology is not the controlling parameter in terms of petrophysical properties. The two-stage method, although more demanding, gives much better results especially in lithological complex reservoirs. Even though, the lithology

is not complex in the interest reservoir, the second approach has been chosen in order to generate 3-D model. In fact, when sufficient information is available a different correlation function can be used for porosity within each facies, or group of facies. 3-D model of porosity distribution can be seen in Figure 2.13. From a total of 17 layers, the last 6 layers of this model are storage formations; sandstone and siltstone intercalations. The legend tells that porosity in the reservoir varies between 1.34 % and 25 %.

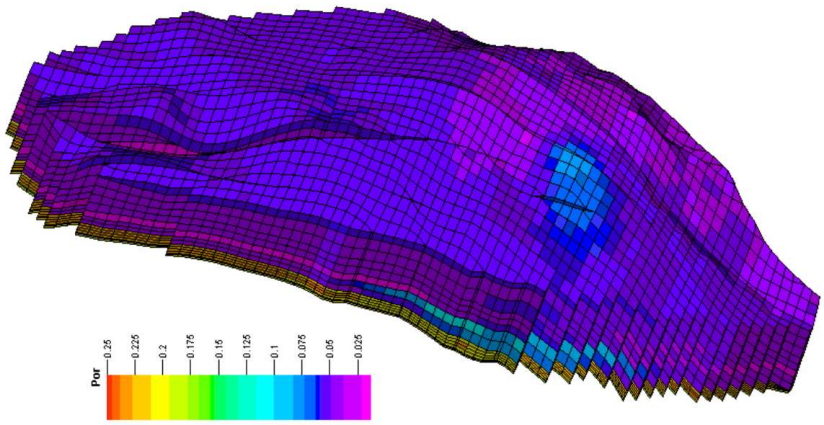

Figure 2.13: 3-D Model of porosity distribution in reservoir

As in the case of geometry, the assignment of petrophysical properties to the grid blocks is, in itself, a simple operation in the case of 3-D input data derived from geocellular modeling. Geocellular modeling is a general term that describes the possibility of generating detailed 3-D geological models starting from sparse well data. The following figures (Figure 2.14, 2.16, 2.18) represent the map-view of porosity values obtained from a two-stage model.

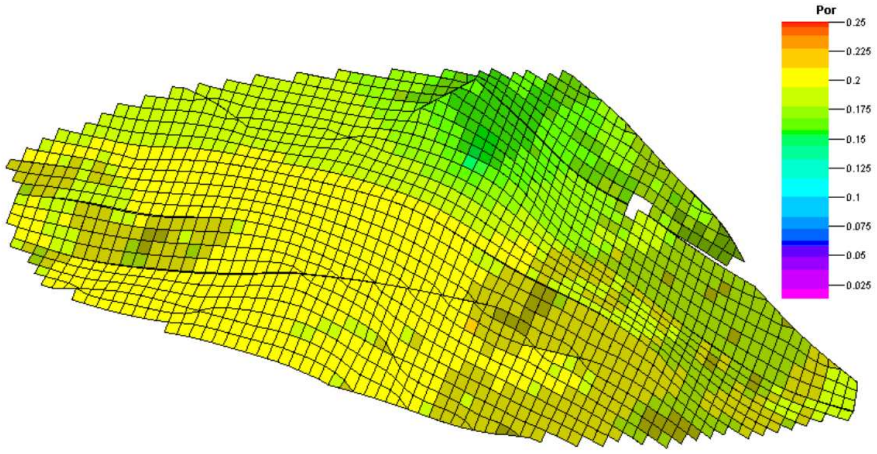

Figure 2.14: Porosity distribution in zone 7, layer 17

Zone 7 is the boundary between the Middle Buntsandstein and Lower Buntsandstein. Zone 7 is a sandstone zone thus the porosity value varies between 15 % and 21 %. Figure 2.15 shows that the porosity distribution is concentrated between 19.5 % and 21 % in Zone 7.

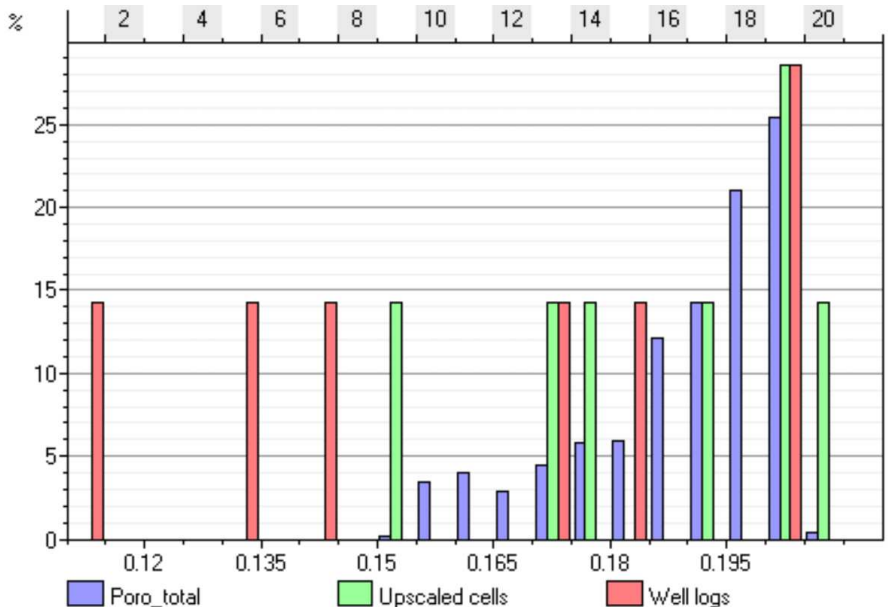

Figure 2.15: Histogram of porosity in zone 7, layer 17

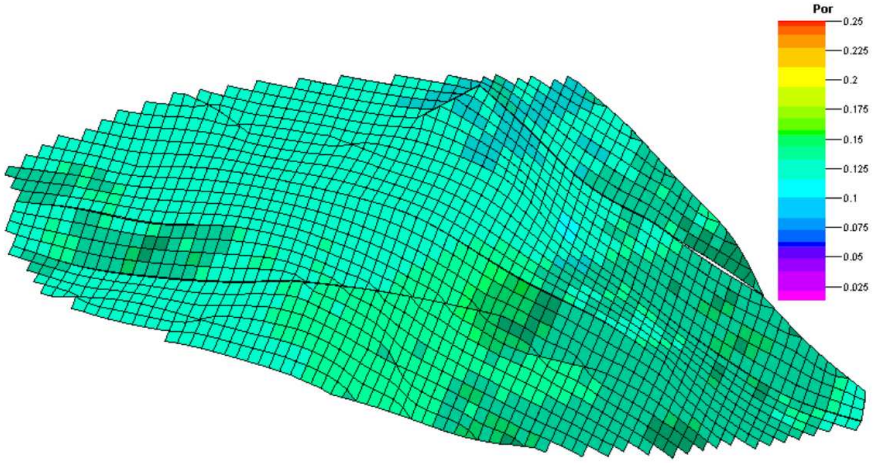

Figure 2.16: Porosity distribution in zone 6, layer 16

Zone 6 is the zone where the sandstone and intercalated-siltstone formation appears; consequently the porosity value in this zone is less than in other sandstones. It is between 11.20 % and 15 %. The histogram for Zone 6 is given in the following figure, 2.17.

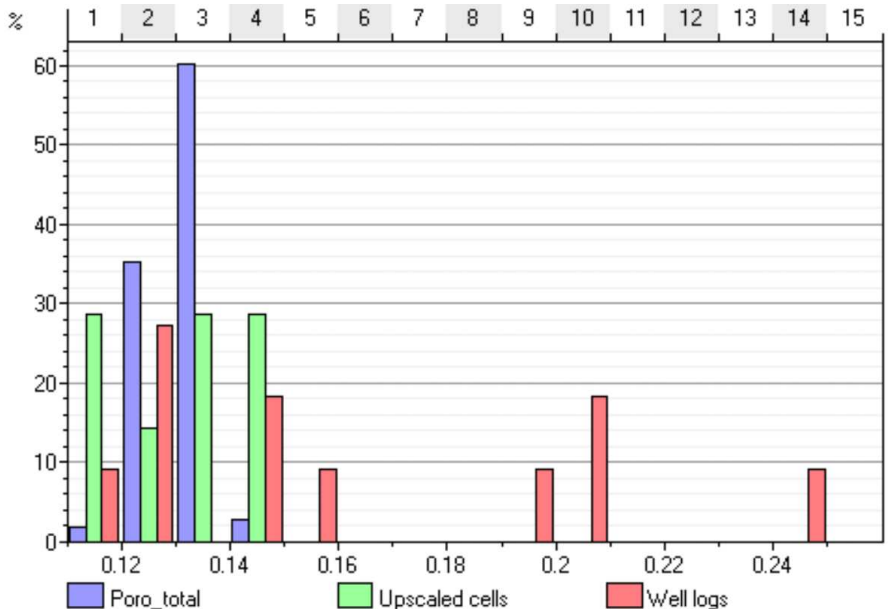

Figure 2.17: Histogram of porosity in zone 6, layer 16

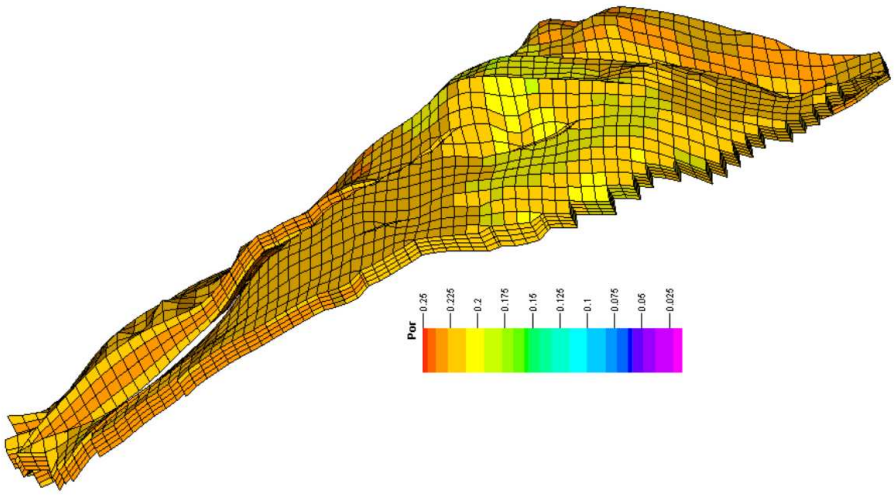

Figure 2.18: Porosity distribution in zone 5, layer 12-15

In zone 5 there are 4 layers. It is the sandstone zone thus the porosity values are relatively high in comparison with other zones described previously. Porosity values vary between 19 % and 25 % as it can be seen in Figure 2.19,the histogram of porosity of zone 5.

The geological model presented in Figure 2.18 shows no great difference between the four layers (layers 12,13,14,15) in porosity distribution in zone 5. However, it is known that the success of a simulation depends absolutely on the degree of the input data reflecting the real situation. The derivation of reliable distribution of permeability is one of the essential issues of an integrated reservoir study, since the characteristics of the fluid flow in the reservoir simulator depends on the spatial architecture attributed to permeability. In this study the permeability distribution is represented by a porosity/permeability transform. In this case, the resulting permeability distribution will strongly resemble the primary porosity distribution. In practice, interpolating well test permeability (hard data) produces reliable results and actually it is mostly considered that these maps are the best representation of the real permeability distribution in the reservoir. Well test analysis was also conducted and

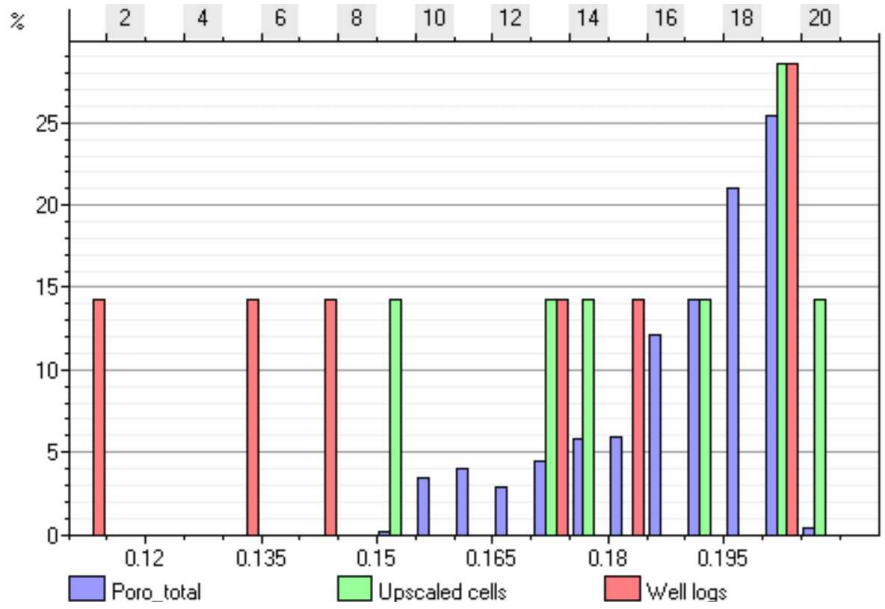

Figure 2.19: Histogram of porosity in zone 5, layer 12-15 (sandstone)

from this analysis the permeability values are observed between 40 mD and 202 mD derived from water injection testing. Interference test was also performed to investigate larger area and also to obtain the inter-well connectivity, reservoir heterogeneities and anisotropy. The permeability values from interference testing are found between 30 mD and 335 mD. In interference testing the value of k determined in the analysis is the average water permeability of the region between the wells that means the permeability was assumed to be a constant in the area of the investigation of the test. After this brief information, a 3-D distribution can be generated by deterministic interpolation. 3-D model of permeability distribution can be generated by deterministic interpolation of a number of vertical permeability properties at well locations. Such 3-D models of permeability distribution can be seen in Figures 2.20 and 2.21. The permeability scale in this Figures is logarithmic and represents values between 0.0001 mD and 178 mD in the reservoir.

The zone seen in Figures 2.20 and 2.21 with blue color is the cap rock, incorporating the siltstone formation. The permeability in the cap rock formation is below 0.01 mD. The

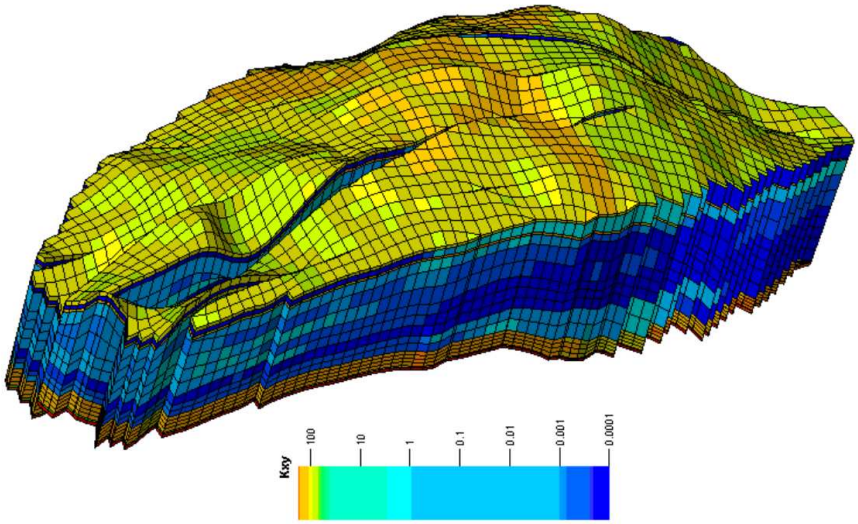

Figure 2.20: 3-D Model of permeability distribution in reservoir

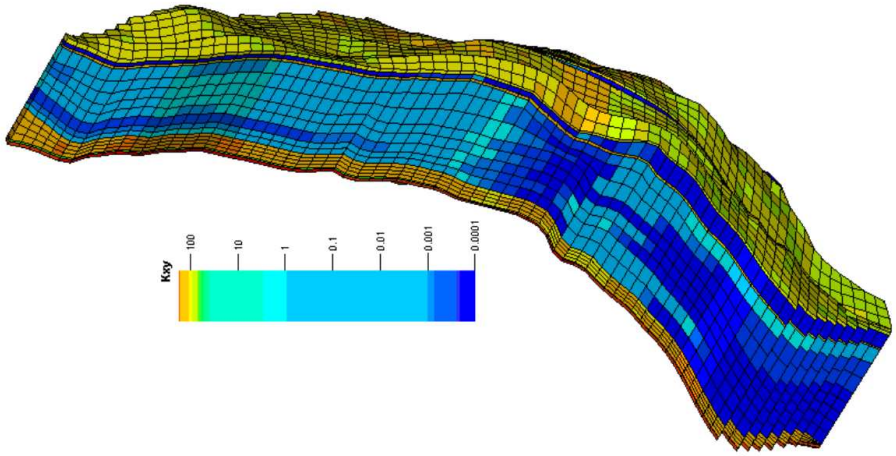

Figure 2.21: Cross section of permeability distribution in reservoir

map view of permeability distribution in the sandstone formation in zone 7 is given in the following Figure 2.22.

Zone 7 as already stated is the boundary between the Middle Buntsandstein and Lower

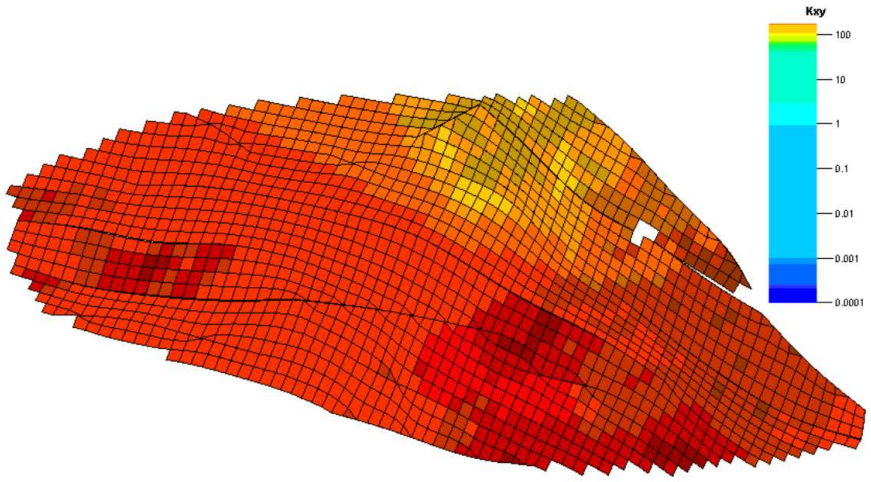

Figure 2.22: Permeability distribution in zone 7, layer 17

Buntsandstein. Representing a sandstone facies the permeabilities range 40 and 180 mD. Figure 2.23 shows that the permeability frequency distribution concentrated between 150 mD and 178 mD in Zone 7.

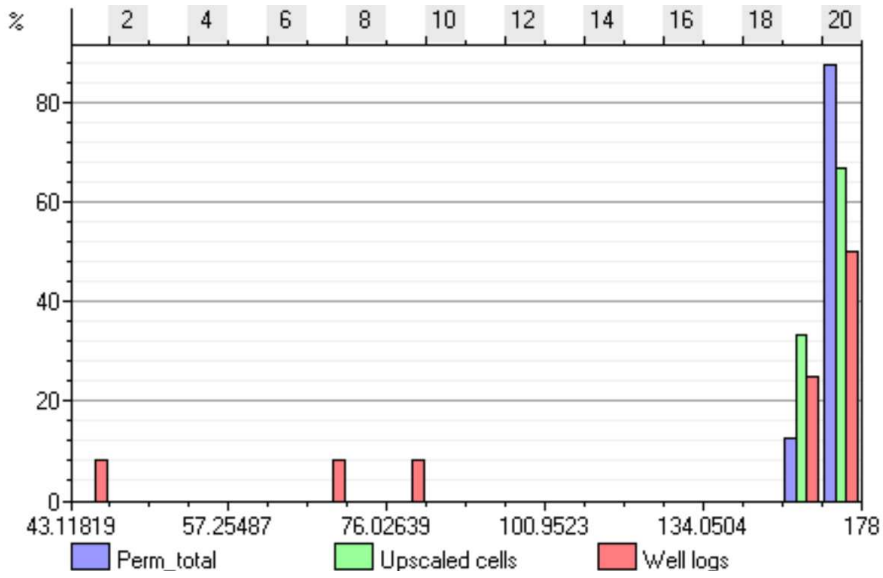

Figure 2.23: Histogram of permeability in zone 7, layer 17

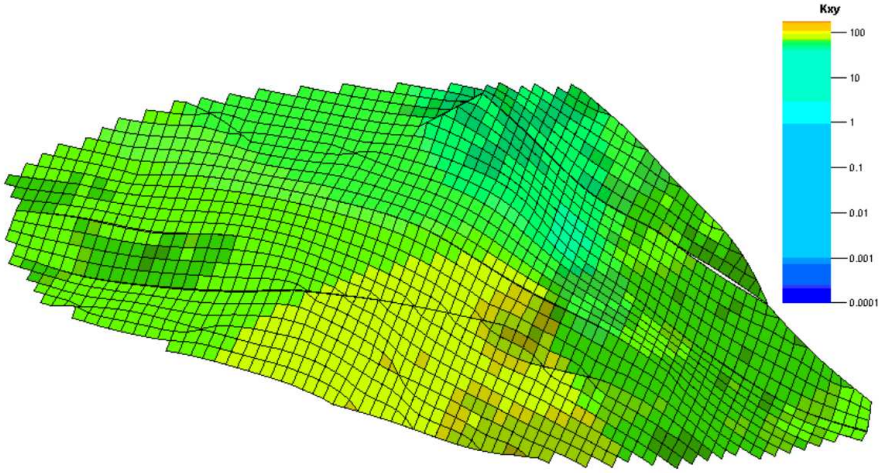

Figure 2.24: Permeability distribution in zone 6, layer 16

Figure 2.24 represents the permeability distribution in Zone 6 in which the sandstone intercalating siltstone formation appears. Due to the clay content the permeability values in this zone is less comparatively to the other sandstone zones. It varies between 43 mD and 90 mD. The histogram of Zone 6 is given in Figure 2.25.

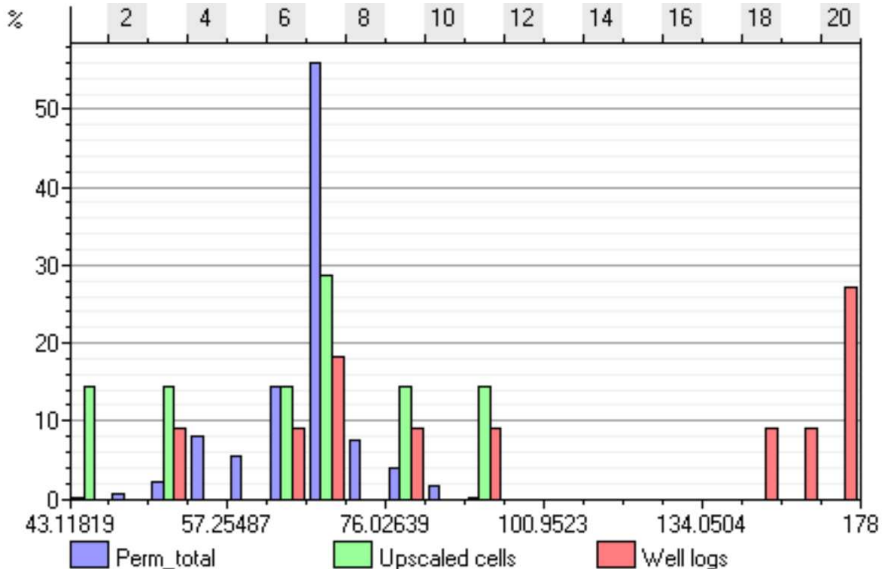

Figure 2.25: Histogram of permeability in zone 6, layer 16 (intercalated-sandstone)

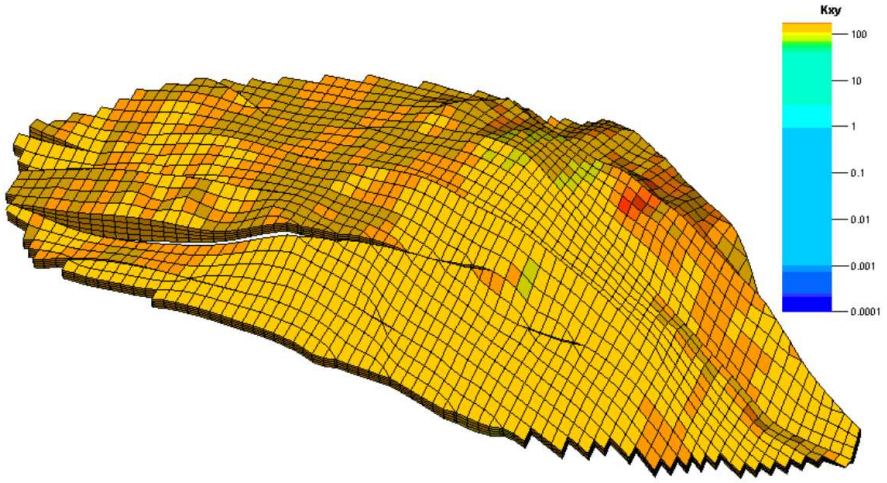

Figure 2.26: Permeability distribution in zone 5, layer 12-15

Figure 2.26 represents the permeability distribution in Zone 5 which has 4 layers. The permeability values are between 129 mD and 178 mD. . The histogram representing the distribution is shown in Figure 2.26.

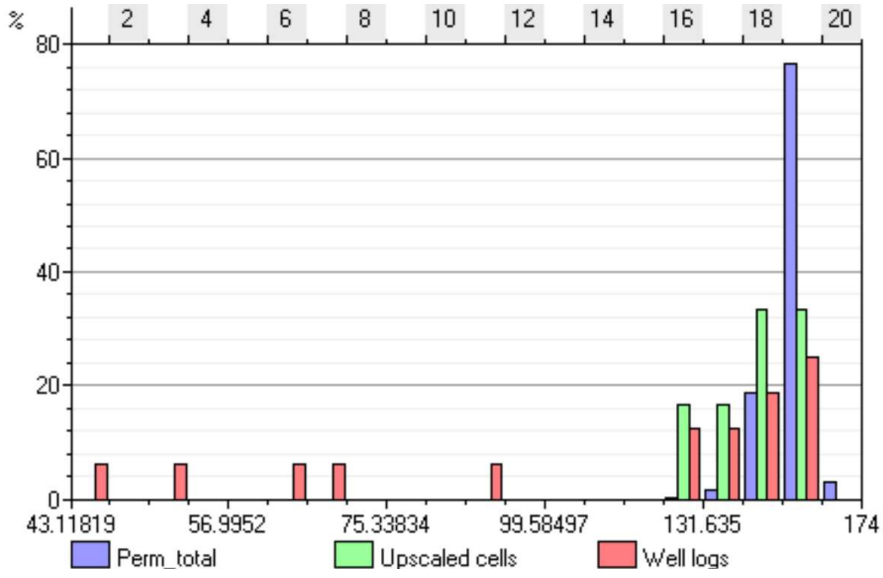

Figure 2.27: Histogram of permeability in zone 5, layers 12-15 (sandstone)

In the aspect of flow modeling, the important part of this study is the conversion of the static model into a dynamic model. Up to here, the geological model of this study was constructed. Structural modeling, stratigraphic modeling, lithological modeling has been carried out. In large reservoir areas the number of grids in the geological model and simulation model is different from each other. For geological grid small features from well logs and seismic data is significant. These grids are designed to preserve the heterogeneity of the reservoir by typically subdividing it on a fine scale vertically as well as keeping the XY-representation of the grid cells as small as possible. However in this study the geological model model gridding was used in the simulation. The reservoir area is not very large the increment in X and Y direction is 50m. In simulation model there are 75 cells in X-direction, 34 cells in Y-direction and 17-cells in Z-direction that means total number of cells in the reservoir area is 43350. The reservoir model can be summarized as in the following topics:

1. There are 75x34x17 cells in the reservoir area.

2. 8 horizons, 7 zones and 17 layers were defined to have a fine scale grid model.

3. There are nine wells, two of them are horizontal wells, and the others are fully perforated vertical wells. The perforations placed relative near to the top owing to be an aquifer reservoir. The perforated zone can be seen in Figure 2.28.

4. In these 17 layers, 5 of them are sandstone facies type (layer 17,12-15), one of them is sandstone-clay intercalations (layer 16), 9 of them (layer 4-11 and 2) are clay-siltstone and 2 of them (layer 1-3) are avicula-sandstone.

5. Porosity values are between 1.34 % and 25 % in the reservoir. In the storage formation thus cut-off values have been considered and values are in the range of 15 %-25 %.

6. The permeability is derived from porosity/permeability correlation. Therefore the

resulting permeability distribution will strongly resemble the primary porosity distribution. The permeability values are between 129 mD and 178 mD in sandstone zones. In the intercalated-sandstone zone of the cap rock permeability values are in the range of 43 mD - 90 mD.

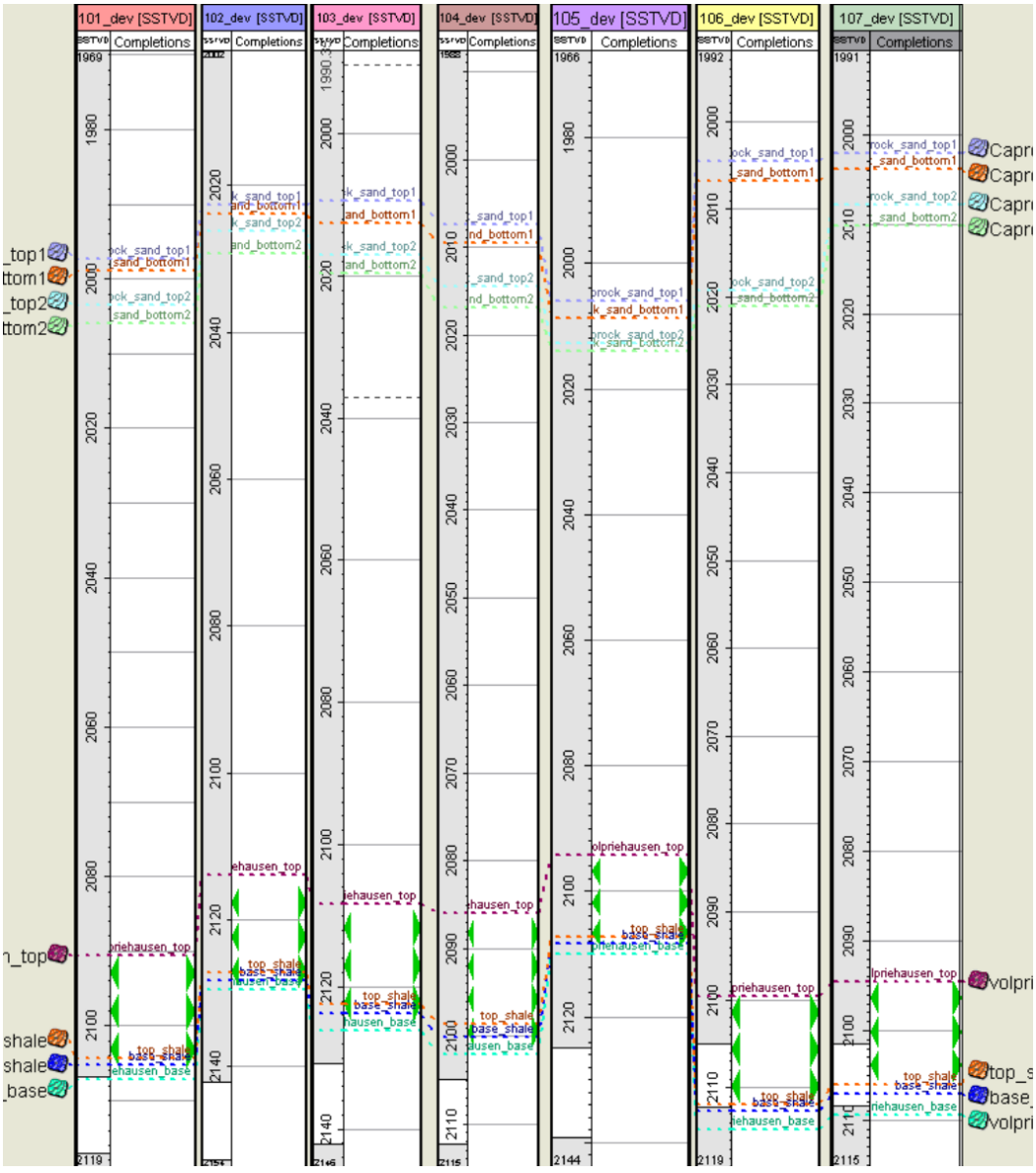

Figure 2.28: Perforated zone in the vertical wells

Chapter 3

Phase Behavior of CO_2 Containing Aqueous Solutions

Injection of CO_2 into saline aquifers requires reliable models for predicting the overall thermophysical behavior of the system CO_2-H_2O-NaCl in a geologic carbon sequestration context.

This chapter describes the thermophysical properties of pure fluids as well as fluid mixtures, evaluating the impact of the various corrections for aqueous and gaseous phases (activity, fugacity, influence of pressure on thermodynamic constants) to be considered in geochemical models when attempting to calculate CO_2 solubility accurately. The conditions in which CO_2 is likely to be injected, make numerical investigations complex as, in particular, it is necessary to take into account the non-ideal behavior of both the mixed electrolytes dissolved in brine and the CO_2 gaseous phase.

3.1 Thermophysical Properties of CO_2

The discussions on the greenhouse effect and global warming have focused technical interest on carbon dioxide thermophysical properties from low temperature (hydrate formation, ocean carbon sequestration) and low pressure (atmospheric) to intermediate pressures and temperatures (geological carbon sequestration).

The numerical modeling of CO_2 in geologic structures requires the main fluid properties such as the density, and viscosity of individual phases in the governing mass balance equations. This requirement explains the relevance of accurate Pressure-Volume- Temperature (pVT) has been used throughout and should be maintained as such relationships. The thermodynamic properties of gases are influenced by the location of the critical region, in contrast CO_2 properties are dominated by its molecular structure and its strong quadrupole moment. Therefore, sufficiently accurate calculation of thermodynamic properties is more difficult for CO_2 than other substances such as CH_4, N_2. Critical and triple point data for CO_2 reported by Vargaftik et al. (1996) is tabulated in Table 3.1.

Table 3.1: Triple and critical point parameters of CO_2 [48]

	$TriplePoint$	$CriticalPoint$
P (bar)	5.18	73.82
T (K)	216.55	304.19
ρ_v (kg/m^3)	13.80	468.16
ρ_l (kg/m^3)	1179.25	468.16

3.1.1 Density Correlations for CO_2

Recent efforts have been focused on reviewing and acquiring reliable thermophysical data for pure carbon dioxide. The result of this effort is the availability of accurate correlations of CO_2 pVT data covering a wide range of temperatures and pressures. Therefore, there exist a lot of experimental data from phase studies of CO_2. Many studies have been performed near the critical point not only because its practical interest but also because it is less intensive to create critical conditions of CO_2 under laboratory conditions. Many of the experimental data are measured at pressures and temperatures that are smaller than the intervals of interest for the purpose of CO_2 disposal in aquifers. But there exists also some data in the regime (1 to 600 bar and 0 to 150°C) of interest for this study. The most

relevant experimental data sets are listed in Table 3.2.

Table 3.2: Selected experimental density data of CO_2

Authors	*Year*	$Temperature, °C$	$Pressure, bar$
Michels. et al	1935	0-150	16-250
Reamer	1944	38-238	14-700
Kennedy	1954	0-1000	25-1400
Vukalovich et al.	1968	0-750	1-600

Also, accurate correlations for carbon dioxide pVT data are available from several published scientific papers and monographs. Among them, those proposed by Altunin (1975), Angus et al. (1976), Mäder and Berman (1991) and Span and Wagner (1996) are the most broadly accepted and used. The most recent and widely used equation of state is that of Span and Wagner. They presented an empirical equation of state explicit in Helmholtz energy as a function of density and temperature [44].

In numerical modeling, equation of states are used to provide the phase data of the mixtures. In ECLIPSE, four equations of state are available namely *Redlich-Kwong, Soave-Redlich-Kwong, Peng-Robinson* and *Zudkevitch- Joffe* and it is possible to use a volume shift parameter with any of these equations. CO2SEQ option uses the *Redlich-Kwong* equation with Spycher et al.(2003) modification. Spycher et al. correlation were optimized to obtain the best fugacity coefficients that fit actual mutual solubility data in the system CO_2-H_2O. Figure 3.1 and 3.2 indicate the CO_2 density comparison at different temperatures and pressures. The CO_2 density obtained from *Peng-Robinson* 3-parameter, *Zudkevitch-Joffe* and *Redlich-Kwong* modified with Spycher et al. parameters were compared with experimental density value of Michels and Vukalovich given in Table 3.2.

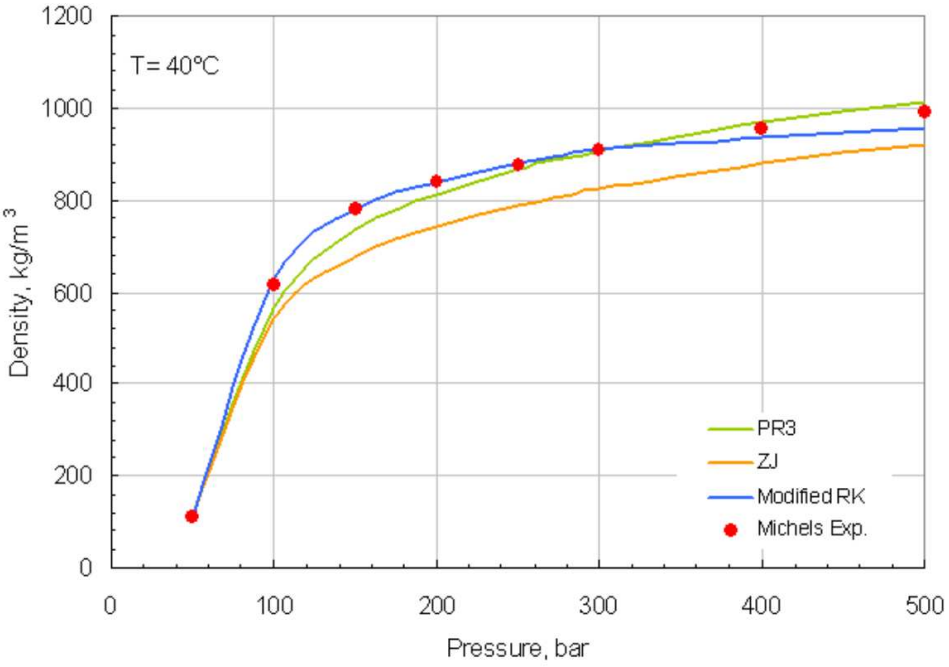

Figure 3.1: CO_2 density comparison at 40°C

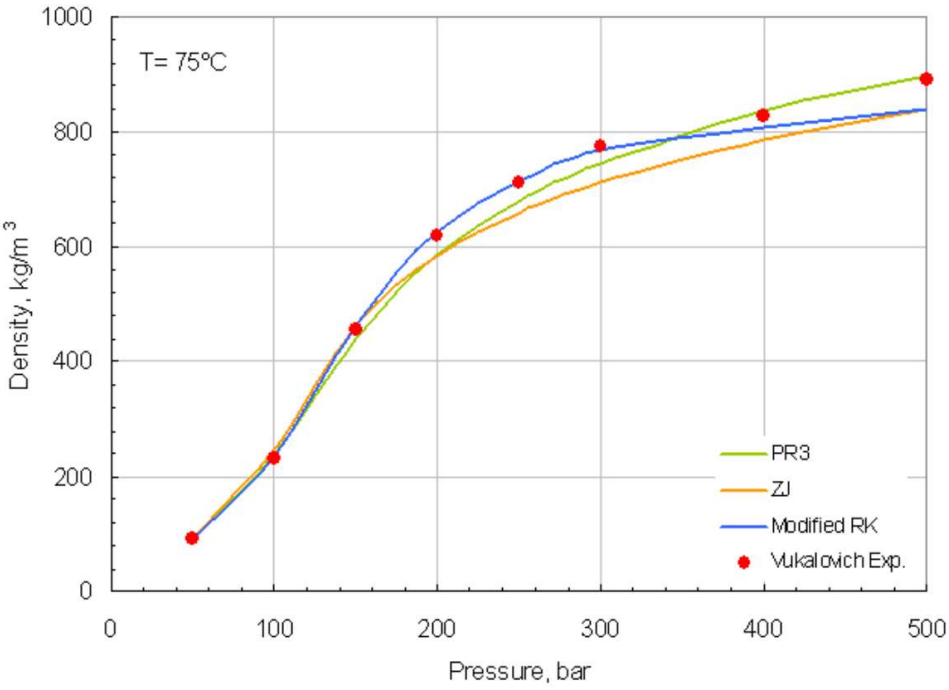

Figure 3.2: CO_2 density comparison at 75°C

3.1.2 Viscosity Correlations of CO_2

The inconsistencies among the various literature sources for viscosity of CO_2 caused the adoption and use of different equations. Therefore, several correlations have been published including more recent and accurate data after Altunin (1975) which presented the critical review of the viscosity of CO_2. According to a recent review by Vesovic et al. (1990), large discrepancies appear for the liquid-phase viscosity when comparing new and old sources of information. In an effort to reconcile the differences, they proposed a new correlation for the dynamic viscosity of CO_2 which was later reviewed and updated by Fenghour et al. (1998). Fenghour et. al representation express the viscosity in the customary way as a function of density and temperature. The accurate representation of viscosity of gases can be achieved if it is decomposed into three separate contributions:

$$\eta(\rho, T) = \eta_0(T) + \Delta\eta(\rho, T) + \Delta\eta_c(\rho, T) \tag{3.1}$$

$$\eta(\rho, T) = \bar{\eta}(\rho, T) + \Delta\eta_c(\rho, T) \tag{3.2}$$

where $\eta_0(T)$ is the viscosity in the zero-density limit, $\Delta\eta(\rho, T)$ an excess viscosity which represents the increase in the viscosity at elevated density over the dilute gas value at the same temperature, $\Delta\eta_c(\rho, T)$ and a critical enhancement accounting for the increase in the viscosity in the immediate vicinity of the critical point. The first two terms on the right hand side of Equation 3.1 are often regrouped and the resulting quantity is termed the background contribution, $\bar{\eta}(\rho, T)$. This brief information is given because the CO_2 gas viscosity was calculated from Vesovic et al. and Fenghour et al. correlations in CO2SEQ option of ECLIPSE.

3.2 Phase Behavior of Carbon Dioxide-Water System

Evaluating the feasibility of CO_2 geologic storage requires the use of pressure-temperature-composition *(pT-x)* data for mixtures of CO_2 and H_2O at moderate pressures and temperatures. For this purpose, published experimental pT-x data in the sequestration temperature and pressure range are reviewed. These data cover the two-phase region where a CO_2-rich phase (generally gas) and an H_2O-rich liquid phase coexist and are reported as the mutual solubilities of CO_2 and H_2O in the two coexisting phases. The main objective is to acquire a better understanding of the phase behavior and to provide simple but realistic models for predicting mutual solubilities of CO_2-H_2O mixtures.

3.2.1 Solubility Modeling

Accurate prediction of CO_2 solubility over a wide range of temperature, pressure and ionic strength is important to studies of geological CO_2 storage. A large number of experimental and modeling studies have been conducted to determine the thermodynamics and phase relations of system CO_2- H_2O. CO_2 solubility data in pure water has been measured for a wide range of temperatures and pressures (Wiebe and Gaddy (1940, 1941); Wiebe et al. (1933), Tödheide and Franck (1963), and Takenouchi and Kennedy (1964)). Spycher et al. (2003) and Duan and Sun (2003) provided extensive reviews of experimental solubility data for the system CO_2-H_2O.

The simplest models for vapor and liquid equilibrium are given by Raoult's and Henry's Law. Raoult's law assumes that the vapor is an ideal gas and the liquid phase is an ideal solution.

$$y_i P = x_i p_i^{sat} \tag{3.3}$$

where y_i and x_i are the mole fractions of component i in the vapor and liquid phase

respectively. Raoult's law requires p_i^{sat} at the temperature of application and is not appropriate for species whose critical temperature is less than the temperature of application. On the other hand, for volatile species present as a very dilute solute in the liquid phase, Henry's law states that the partial pressure of the species in the vapor phase is directly proportional to its liquid-phase mole fraction.

$$y_i p = x_i K_{Hi} \tag{3.4}$$

where K_{Hi} is the Henry's constant. This approach was used successfully to model the solubility of CO_2 in water for pressure up to about 1MPa [10]. However, Garcia (2001) and Spycher et al. (2003) showed that the two previous models Raoult's and Henry´s law fail to accurately represent the equilibrium between phases. While Henry's law (Equation 3.4) assumes that the gas fugacity is equal to the partial pressure, Garcia [24] and Spycher et al. [45] considered that this assumption is not necessary and is removed by including the gas phase fugacity coefficient Φ.

$$f_2 = \Phi_{2y_2} p = K_{H\,2,1} x_2 \tag{3.5}$$

where 1 stands for H_2O and 2 stands for CO_2. In general, they define the fugacity coefficient of component i, Φ_i as;

$$\Phi_i = \frac{f_i}{y_i p} \tag{3.6}$$

The solubility model of Spycher et al. based on fugacity is given in details in Chapter 5.

CO_2 solubility correlation of Duan et al. (2003) is based on the balance between its chemical potential in the liquid phase μ^l_{CO2} and that in the gas phase, μ^v_{CO2} . The potential was written in terms of fugacity in the vapor phase and activity in the liquid phase as

$$\begin{aligned}\mu^{v}_{CO2}(T,p,y) &= \mu^{v(0)}_{CO_2}(T) + RT\ln f_{CO_2}(T,p,y) \\ &= \mu^{v(0)}_{CO_2}(T) + RT\ln y_{CO_2}p + RT\ln\Phi_{CO_2}(T,p,y)\end{aligned} \tag{3.7}$$

$$\begin{aligned}\mu^{l}_{CO_2}(T,p,m) &= \mu^{l(0)}_{CO_2}(T,P) + RT\ln a_{CO_2}(T,p,m) \\ &= \mu^{v(0)}_{CO_2}(T,p) + RT\ln m_{CO_2}p + RT\ln\gamma_{CO_2}(T,p,y)\end{aligned} \tag{3.8}$$

At equilibrium $\mu^{l}_{CO2} = \mu^{v}_{CO2}$, the following equation is obtained;

$$\ln\frac{y_{CO_2}p}{m_{CO_2}} = \frac{\mu^{l(0)}_{CO_2}(T,p) - \mu^{v(0)}_{CO_2}(T)}{RT} - \ln\Phi_{CO2}(T,p,y) + \ln\gamma_{CO2}(T,p,m) \tag{3.9}$$

According to the equation of state of Duan et al. (1992b), the fugacity coefficient of CO_2 in the vapor phase of CO_2-H_2O mixtures differs very little from that in pure CO_2 for temperatures between 273 and 533 K. Therefore, the parameter $\Phi_{\mathrm{CO_2}}$ in the equations can be obtained from the EOS for pure CO_2 and water vapor pressure of the mixtures can be assumed as the same as pure water saturation pressure. Figure 3.3 shows the calculated fugacity values of pure CO_2 at different temperatures and pressures.

Therefore, y_{CO_2} in Equation 3.9 can be approximately calculated as;

$$y_{CO_2} = \frac{p - p_{H_2O}}{p} \tag{3.10}$$

where P_{H_2O} is the pure water pressure, which can be taken from the steam tables (Haar, 1984).

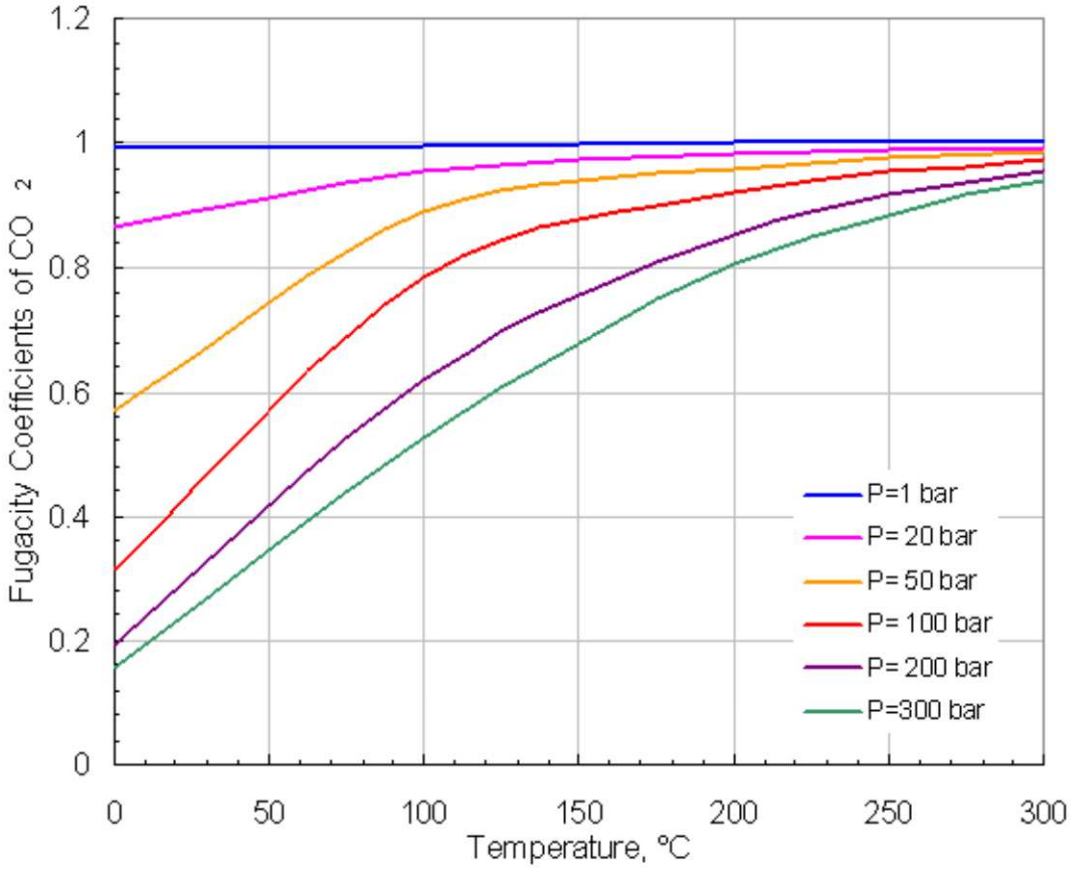

Figure 3.3: Fugacity coefficients of CO_2 for a range of temperature and pressure conditions, calculated from the correlation given by Duan et al. [16]

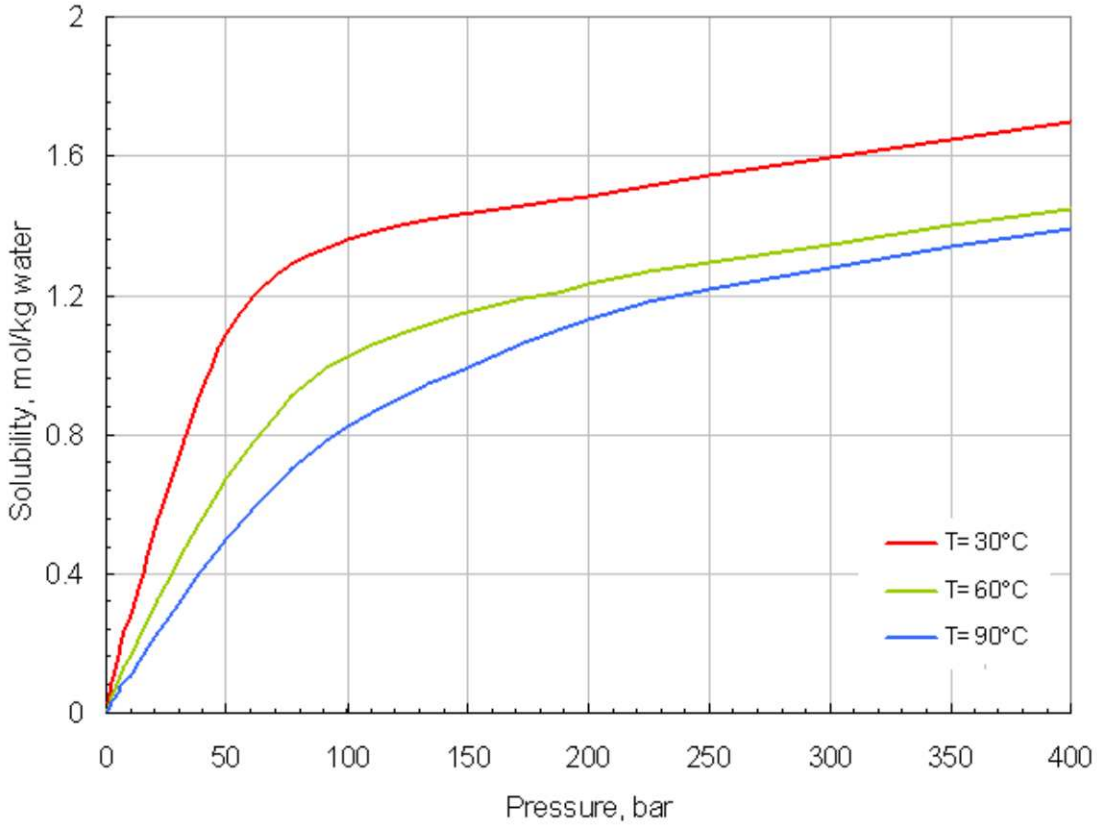

Figure 3.4: Solubility of CO_2 in fresh water at 30, 60, 90 °C, lines represent experimental data compiled by Duan et. al (2003) [18]

Figure 3.4 shows that the calculated values of CO_2 solubility in the aqueous phase at different temperatures and pressures by Duan et. al correlation.

In ECLIPSE 300, the amount of CO_2 dissolved in water, or in other aqueous phases are defaulted by Chang et. al correlation [11]. According to this correlation CO_2 solubility, R_w in fresh water can be estimated as;

$$R_w = 1.152^{-3} ap \left[1 - b \sin\left(\frac{\pi}{2} \frac{145cp}{145cp+1}\right)\right] \quad \text{for} p < p^0 \tag{3.11}$$

$$R_w = 1.152^{-3} \left[R_w^0 + m\left(145P - p^0\right)\right] \quad \text{for} p \geq p^0/145 \tag{3.12}$$

where the solubility R_w is in mol.cm^{-3}, and P is the total pressure of CO_2 and water, a, b, c, P^0, R_w^0 and m are the functions of temperature defined as follows;

$$a = \sum_{i=0}^{4} a_i 10^{-3i} (\frac{9}{5}T + 32)^i \tag{3.13}$$

$$b = \sum_{i=0}^{4} b_i 10^{-3i} (\frac{9}{5}T + 32)^i \tag{3.14}$$

$$c = 10^{-3} \sum_{i=0}^{4} c_i 10^{-3i} (\frac{9}{5}T + 32)^i \tag{3.15}$$

$$p^o = \frac{2}{\pi} \frac{\sin^{-1} b^2}{c\left(1 - \frac{2}{\pi}\sin^{-1} b^2\right)} \tag{3.16}$$

$$R_w^0 = a p^0 \left(1 - b^3\right) \tag{3.17}$$

$$m = a\left\{1 - b\left(\sin\left(\frac{\pi}{2}\frac{cp^0}{cp^0+1}\right) + \frac{\pi}{2}\frac{cp^0}{(cp^0+1)}\cos\left(\frac{\pi}{2}\frac{cp^0}{cp^0+1}\right)\right)\right\} \tag{3.18}$$

The temperature T is in $°C$. The forms of equations from Equation 3.13 to 3.18 are different from the original Chang and Coats equations due to the unit conversion. Values of coefficients a_i, b_i and c_i are given in Table 3.3

Table 3.3: Values of coefficients in Equations from 3.13 to 3.18

	i=0	i=1	i=2	i=3	i=4
a_i	1.163	-16.63	111.073	-376.859	524.889
b_i	0.965	-0.272	0.0923	-0.01008	0.0998
c_i	1.28	-10.757	52.696	-222.395	462.672

Figure 3.5 shows the comparison between the calculated values of CO_2 solubility in fresh water at different temperatures after Chang et al. and Spycher et al. correlation and experimental values of Wiebe and Gaddy [11, 45, 50, 51].

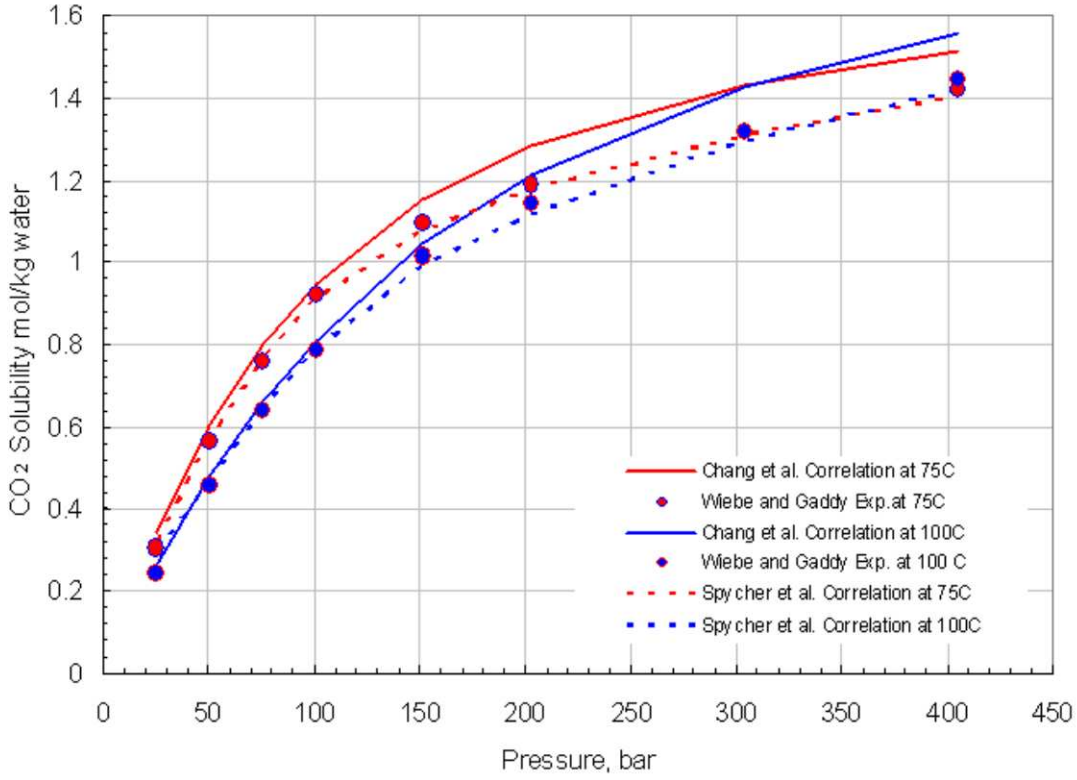

Figure 3.5: Solubility of CO_2 in fresh water at 75 and 100°C obtained from Chang et al.(1998) and Spycher et al.(2003) correlation compared with experimental data of Wiebe and Gaddy (1941) [11, 45, 50, 51]

3.3 System of Carbon Dioxide and Saline Solution

Attempts to predict the overall behavior of the CO_2-H_2O-NaCl system by a single EOS have been very limited. In spite of significance of thermophysical properties, there is limited experimental data on densities, or viscosities of aqueous CO_2-H_2O-NaCl systems. Generally, there are two sets of data, one for the H_2O-NaCl system and another for the CO_2-H_2O system.

Numerical modeling of the flow of brine and CO_2 requires a coupling of the phase behavior of water-salt-CO_2 mixtures with multiphase flow simulation techniques.

3.3.1 Solubility Modeling

Duan and Sun (2003) based on a review of large number of experimental data, proposed a model calculating CO_2 solubility in fresh water and aqueous NaCl solutions from 273 to 533 K and from 0 to 2000 bar. However, the model proposed by Duan et al. is based on computationally demanding EOS that makes application to large numerical simulations impractical. CO2SEQ option of ECLIPSE uses the model of Spycher et al. which accounts for the effect of salinity on CO_2 solubility in aqueous solution of NaCl using the model with Henry's coefficient that depends on the temperature and NaCl content [45]. Figure 3.6 represents the calculated solubility of CO_2 in 1 m and 2 m aqueous NaCl solution at 60°C with Duan et al. and Spycher et al. correlation.

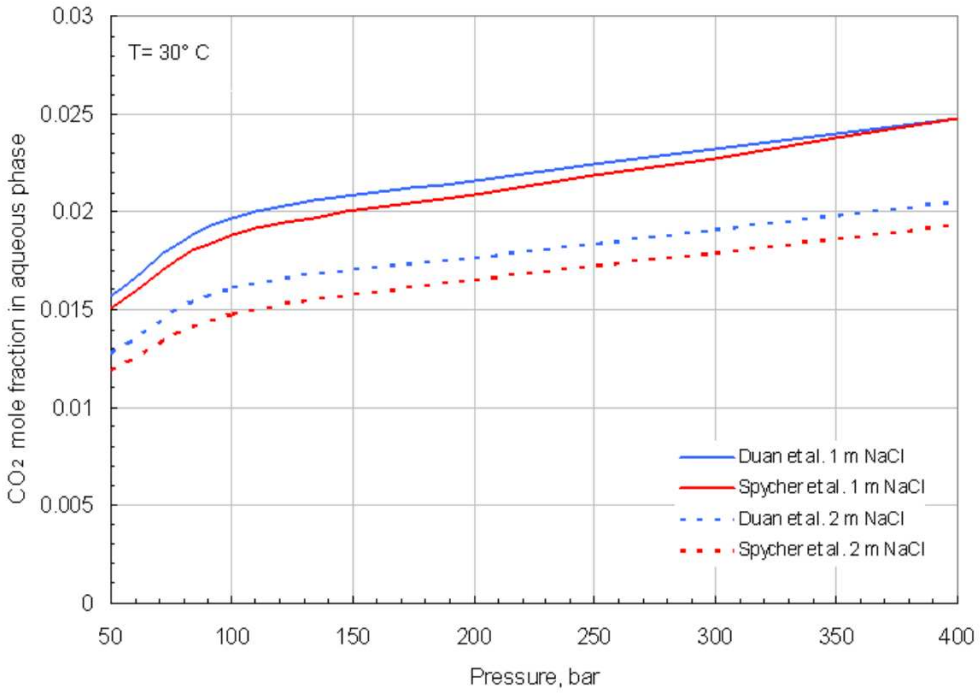

Figure 3.6: Solubility of CO_2 in 1 m and 2 m aqueous NaCl solution at 60°C obtained using Duan et al. and Spycher et al. correlation [18, 45]

Chang et al. adjusted the calculated solubility of CO_2 in fresh water for the effects of salinity to obtain the solubility of CO_2 in brine;

$$R_b = 10^{-\{0.028S\}/\left\{[(9/5)T+32]^{0.12}\right\}} R_w \tag{3.19}$$

where R_b is in mol.cm^{-3}, S is the salinity of brine, which is defined as the total dissolved salts in the solution in mass percent. Figure 3.7 depicts the change of CO_2 solubility with varying amount of total dissolved NaCl.

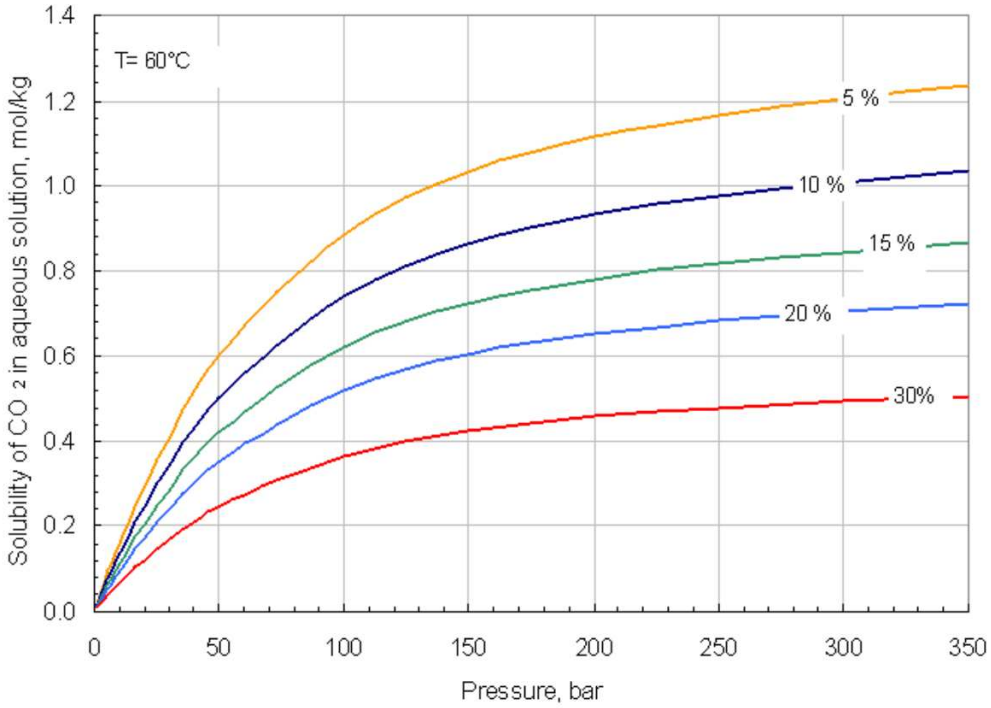

Figure 3.7: Solubility of CO_2 in aqueous solutions of NaCl with varying total salinity at 60°C obtained using Chang et al. correlation [11]

Injecting CO_2 into deep saline aquifer is one of the promising CO_2 sequestration option for the long term. Injected gas is stored in an aquifer, dissolving in brine or as gas phase. The solubility of CO_2 in brine is much higher than that of hydrocarbon components. Figure

3.8 shows the comparison of CO_2 and CH_4 solubilities in 4 m NaCl at 60°C and it is obvious that the solubility factor can not be neglected in the simulation process of geologic storage of CO_2.

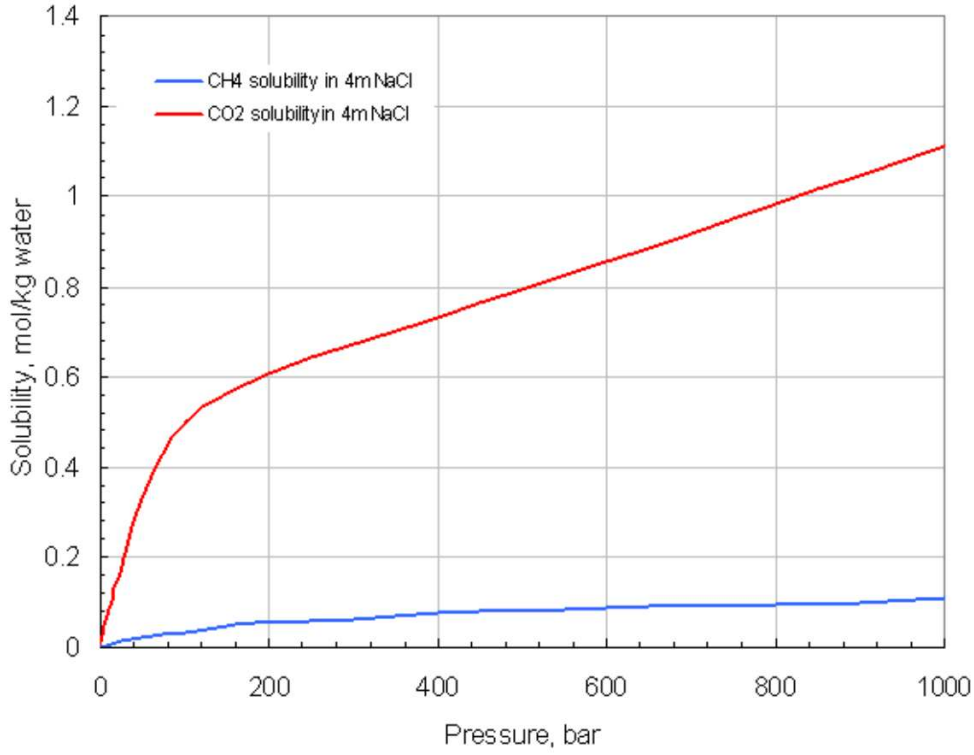

Figure 3.8: CO_2 and CH_4 solubilities in 4 m aqueous NaCl solution at 60°C [18]

3.3.2 Density of Aqueous Solution of CO_2

Most of brine density correlations consider only salinity effects with no CO_2 dependency, because the salinity effect which can be seen in Figure 3.9 is considerable stronger. However, the experimental data shows that the CO_2 content produces an increase in aqueous phase density in the order of 2 to 3 %. This assumption is acceptable in geothermal applications or CO_2 flooding processes. Nevertheless, CO_2 content is key processes in fluid flow dynamics of CO_2 sequestration.

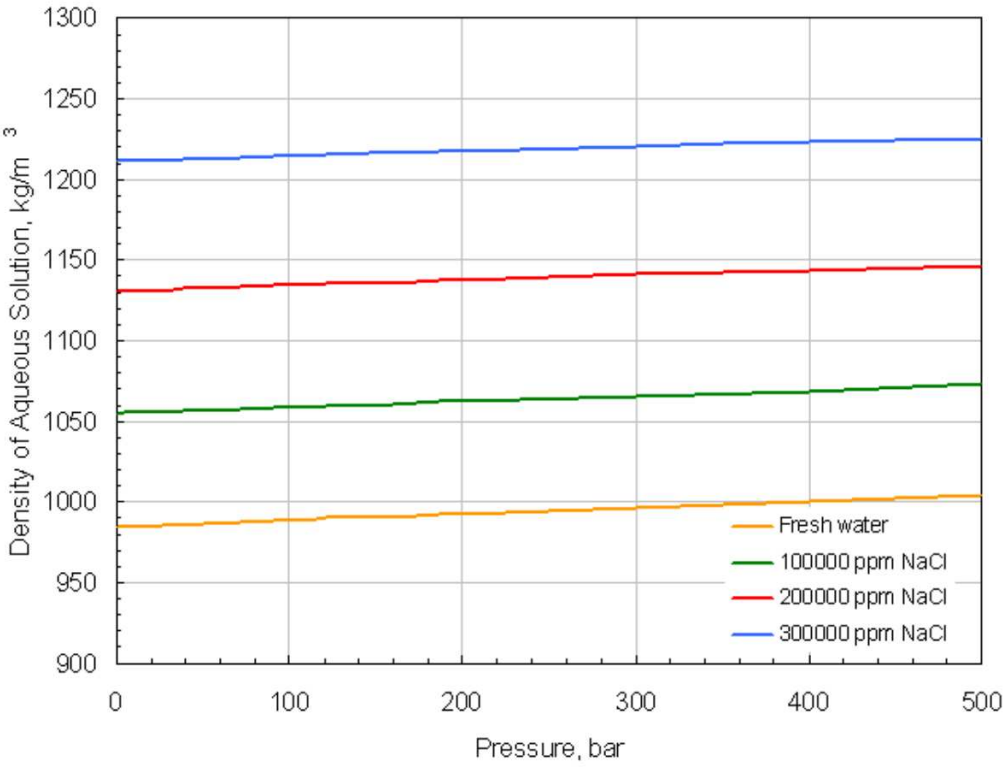

Figure 3.9: Density of aqueous solution at 60 °C containing different amounts of NaCl obtained from Batzle and Wang correlation [5]

Kumar et al. (2005) has introduced a volume shift parameter correlation for H_2O to match the density values. The correlation was developed only for NaCl salinity [31]. However, for the realistic characterization of pVT properties not only the amount of salinity

but also the brine composition is an important parameter [46]. The main fluid parameters, density and viscosity of phases, are functions of the pressure, temperature, salinity and solubility of CO_2 in the aqueous phase. The latter being also a function of the pressure, temperature and salinity. Figure 3.10 indicates the change of CO_2 solubility with different brine composition.

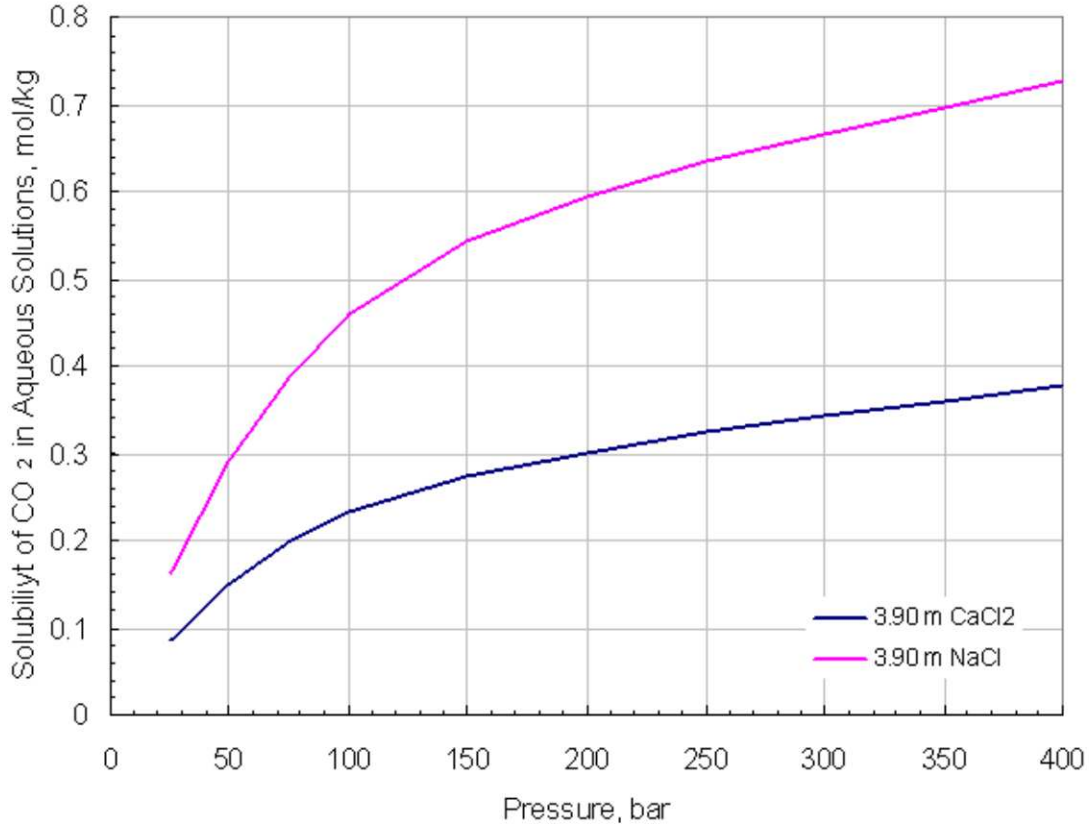

Figure 3.10: Solubility of CO_2 in aqueous solutions of NaCl and $CaCl_2$ at 60 °C [18, 41]

The CO2SEQ option of ECLIPSE simulator considers the effect of CO_2 content on the brine density in the following way. First the brine density is approximated by the pure water density and then corrected for salt and CO_2 dissolution effects by Ezrokhi´s method [52]. Figure 3.11 shows the density increase with the dissolution of CO_2 in water. Even

this small density increment creates instability and induces convective-diffusive mixing in the aquifer enhancing the dissolution rate of CO_2.

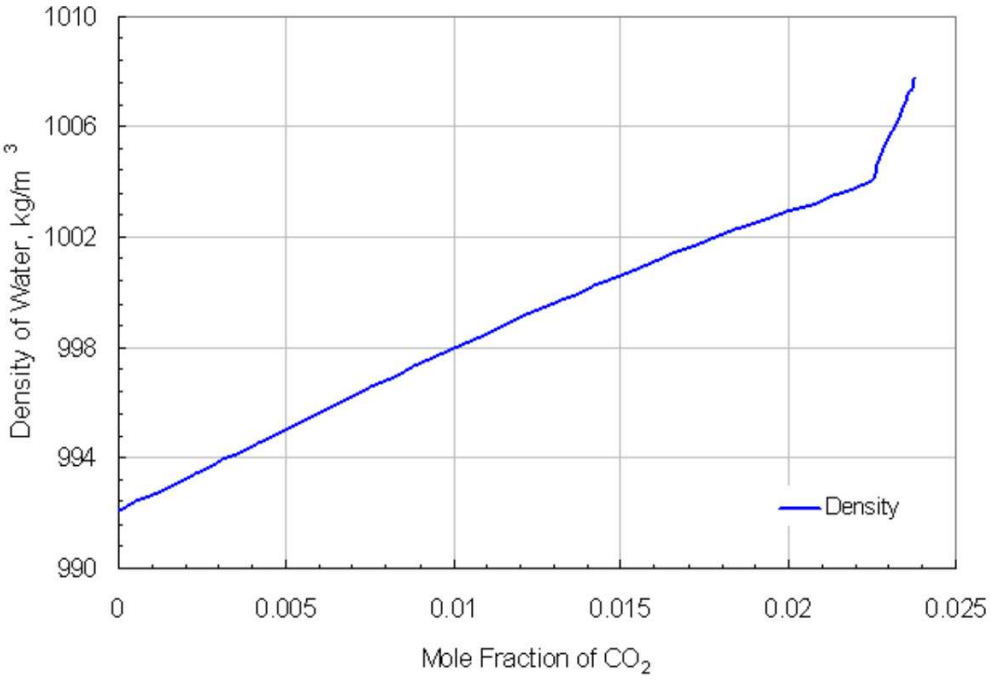

Figure 3.11: Density of fresh water with dissolved CO_2 at 60°C and 200 bar

3.3.3 Concluding Remarks

Experimental data for the ternary system of CO_2-H_2O-salt at the temperatures and pressures of interest for geologic carbon sequestration is relatively sparse. Therefore, the application of a single EOS is limited. The black oil and compositional simulators which were not designed for geologic CO_2 sequestration process fails to calculate accurately the pVT-x properties of gas-water mixtures, since the phase behavior modeling of gaseous/super critical CO_2 mixtures with reservoir brine exhibits constraints regarding thermodynamical complexity of the system as well as insufficiencies in computing approaches.

As discussed in this chapter, the necessary accuracy for the overall thermophysical behavior of the system CO_2-H_2O-$NaCl/CaCl_2$ can be obtained by properly linking a set of individual models.

The following are recommended for estimating thermophysical properties

for pure fluids

- Use Altunin (1975) correlations for density, enthalpy and viscosity of CO_2
- Use the correlations of IFC (1967) for thermophysical properties of pure water

for fluid mixtures

- Assume ideal mixtures for the vapor phase for the calculation of densities, viscosities and enthalpies
- Calculate liquid phase density according to either Bachu and Adams or Garcia
- Ignore the changes in water viscosity due to CO_2 dissolution in water

CO2SEQ calculates the overall thermophysical behavior of the system as follows;

- CO_2 density is obtained by an accurately tuned cubic equation of state.

- CO_2 viscosity is calculated from Vesovic and Fenghour correlations.
- First the brine density is approximated by the pure water density, and then corrected for salt and CO_2 effects.
- The mutual solubilities of CO_2 and H_2O calculations are based on fugacity equilibration between water and CO_2-phase.
- NaCl and $CaCl_2$ are the available brine types.

The phase/solubility calculations are most critical for the prediction of solubility trapping capacity thus the storage capacity of aquifer. The migration capacity of the higher density plumes is dependent on the solubility modeling of CO_2 in brine.

Chapter 4

Two-Phase Flow Properties

In multi phase flow, the process described by an increase in the non-wetting phase saturation (displacement of wetting phase) followed by an increase in wetting phase saturation causes a relative permeability hysteresis effect. Saline aquifers are predominantly water-wet. Whenever a change in saturation history from initial drainage to an imbibition process occurs, the non-wetting phase is subject to entrapment by wetting phase. Trapping of the non-wetting gas phase occurs during imbibition when the gas saturation is decreasing and the water saturation increases as it invades the pore spaces. During the injection phase of CO_2, the movement of CO_2 is dominated by a drainage relative permeability state, as CO_2 displaces the wetting phase, brine. Once the injection stops, gas still migrates towards the top of the storage formation and the gas saturation near the well decreases. As the water invades, the imbibition relative permeability dominates [33, 34, 30]. In order to predict the hysteretic behavior of gas relative permeability and thus the storage capacity, the accurate characterization of trapping which occurs during imbibition process is required.

Theoretical and empirical models which have been developed that attempt to describe the hysteresis phenomena and trapped saturation of the non-wetting phase after flow reversal will be discussed in the following sections.

4.1 Trapping Models

4.1.1 Land Trapping Model

Most relative permeability hysteresis calculations are based on the trapping model of Land. His model was developed for trapped gas saturation as a function of the initial saturation based on published experimental data from water-wet sandstone cores. In his model, it was assumed that during imbibition the non-wetting phase saturation can be split up into two different saturations; the saturation of trapped gas which does not contribute to the flow and the saturation of mobile gas [33]. In this model the trapped non-wetting phase saturation is calculated as;

$$S_{gt}(S_{gi}) = \frac{S_{gi}}{1 + CS_{gi}} \tag{4.1}$$

where S_{gi} is the initial gas saturation, or the saturation at the flow reversal, and C is the Land trapping coefficient which can be computed as;

$$C = \frac{1}{S_{gt,\max}} - \frac{1}{S_{g,\max}} \tag{4.2}$$

Where $S_{gt,max}$ is the maximum trapped gas saturation and $S_{g,max}$ is the maximum gas saturation which can be seen in Figure 4.1. The C-factor depends on the pair of fluids (water-gas, water-oil or oil-gas), the permeability of the medium, micro-porosity, clay content and maximum gas saturation. $S_{gt,max}$ can be calculated as a function of porosity, ϕ, which was obtained by fitting a range of sandstone data from the literature [14].

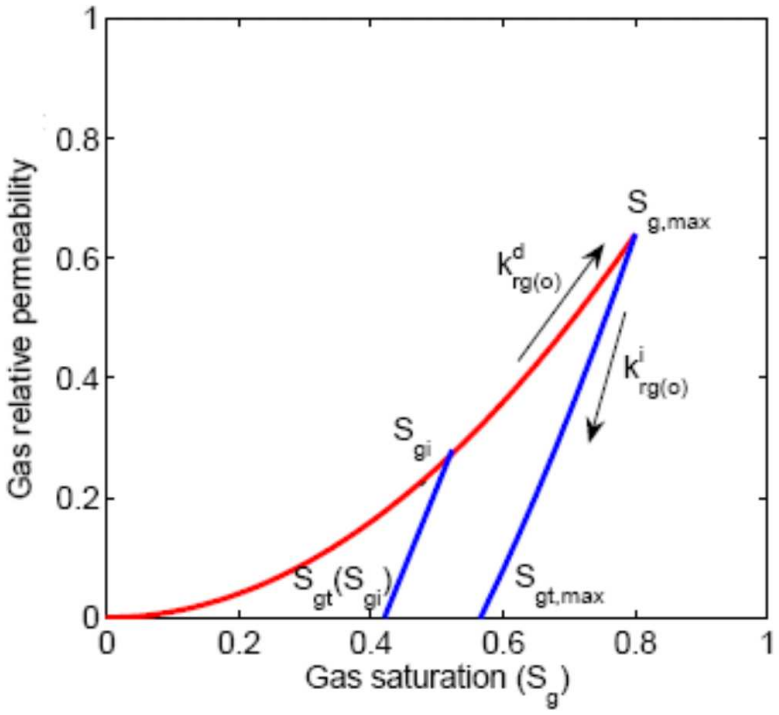

Figure 4.1: Land's model parameters required in the evaluation of trapping and relative permeability hysteresis models

4.1.2 Carlson Trapping Model

Carlson's method produces a scanning curve that is parallel to the imbibition curve.The trapped gas saturation is determined by shifting the bounding imbibition curve to intersect the intermediate initial gas saturation during flow reversal. This geometric extrapolation procedure can be seen in Figure 4.2.

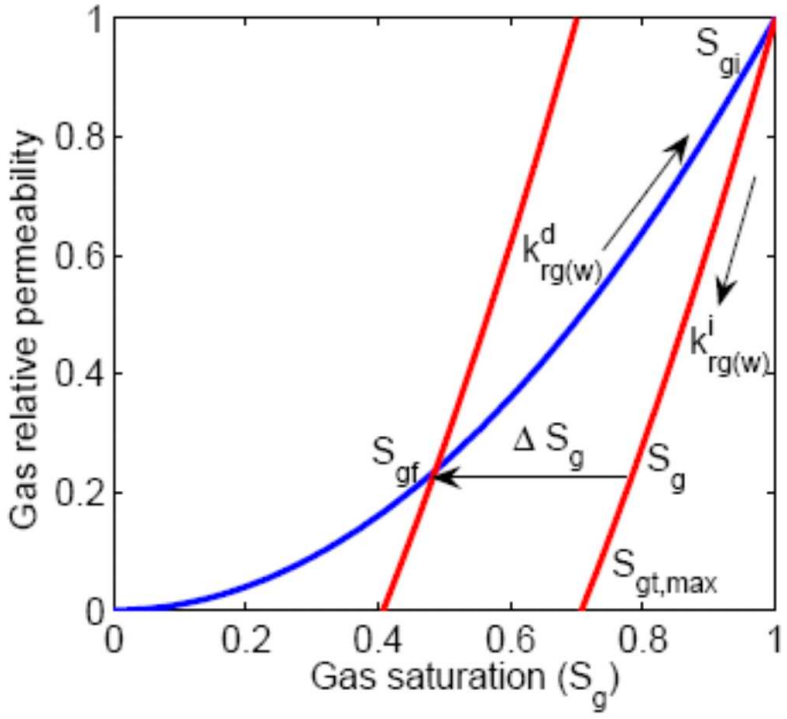

Figure 4.2: Geometric extrapolation of the gas relative permeability and trapped saturation during an imbibition process, as proposed by Carson [9]

The trapped wetting-phase saturation is computed as

$$S_{gt} = S_{gr} - \Delta S_g \tag{4.3}$$

where ΔS_g is the shift in the imbibition scanning with respect to imbibition scanning curve.

4.1.3 Jerauld Trapping Model

Jerauld's trapping model is an extension of Land trapping model. He introduced a second tuning parameter b in addition to Land coefficient, C. The trapped non-wetting phase saturation is given by;

$$S_{gt} = \frac{S_{gi}}{1 + C(S_{gi})^{1+\frac{bS_{gr}}{1-S_{gr}}}} \tag{4.4}$$

If this parameter, b taken as zero, Jerauld's model reduces to the Land trapping model.

4.2 Empirical Hysteresis Models

Both wetting (brine) and non-wetting (gas) phases relative permeabilities may exhibit hysteresis. However, the hysteresis in wetting phase is believed to be very small and thus difficult to distinguish. Therefore, in two phase systems, hysteresis is more prominent in the relative permeability of the non-wetting phase.

Relative permeability hysteresis models typically used in ECLIPSE reservoir simulator, and discussed in this section, are those by Killough [30], Carlson [9], Jargon [1].

4.2.1 Killough Hysteresis Model

Killough [30] used Land's trapping model to derive a relative permeability hysteresis function. It results in an interpolative scheme for defining the intermediate scanning curves, the intermediate imbibition relative permeability curves between the bounding drainage and imbibition relative permeability curves (Figure 4.1). This allowed for the use of empirical or analytical curves if experimental data were not available. In Killough's method, the non-wetting phase relative permeability along a scanning curve is computed as:

$$k^i_{rg}(S_g) = \frac{k^i_{rg(w)}(S_{g,norm}).k^d_{rg(w)}(S_{gi})}{k^d_{rg(w)}(S_{g,\max})} \tag{4.5}$$

where S_{gi} is the initial gas saturation, $S_{g,max}$ is the maximum gas saturation from the bounding imbibition curve and $S_{g,norm}$ is the normalized gas saturation calculated as;

$$S_{g,norm} = S_g + \frac{(S_g - S_{gt,\max})(S_{gt,\max} - S_g)}{S_{gi} - S_{gt,\max}} \tag{4.6}$$

In Equation 4.5, $k^i_{rg(w)}$ and $k^d_{rg(w)}$ represent the relative permeability values on the bounding imbibition and drainage curves, respectively. Each of these variables are illustrated in Figure 4.1 [1].

4.2.2 Carlson Hysteresis Model

In Carlson's model [9], as already explained, the scanning curve is assumed to be parallel to the imbibition curve. It can be obtained by simply shifting the imbibition curve horizontally until it cuts the drainage curve at the saturation S_{gi}, Figure 4.2 . The imbibition curve must be steeper than the drainage curve at all values of k_r. Therefore, a failure in shifting can result in a scanning curve that will cross to the right side of the drainage curve and may produce a negative value of $S_{gt,\max}$.

4.2.3 Jargon Hysteresis Model

Jargon method [1] has introduced a modification to Killough's method that overcomes the inconsistent scanning curves. In this model the trapped saturation is constructed by moving the drainage critical saturation towards the imbibition critical saturation by the same fraction that the hysteresis saturation has moved towards the maximum non-wetting saturation:

$$S_{gt,\max} = S^d_g + \frac{(S^i_g - S^d_g)(S_{gi} - S^d_g)}{S_{g,\max} - S^d_g} \tag{4.7}$$

Chapter 5

Approach and Tools: CO_2 related features of ECLIPSE

In this chapter some of the important features of ECLIPSE simulator are reviewed. ECLIPSE is licensed and supported by GeoQuest, the software division of Schlumberger Information Solutions (SIS). ECLIPSE consists of two separate simulators; ECLIPSE 100 specializing in black oil modeling and ECLIPSE 300 specializing in compositional modeling.

ECLIPSE 300 was chosen to model the CO_2 injection into the Buntsandstein aquifer although it does not have any geochemical reaction terms implemented. In its current version, ECLIPSE 300 modules are capable of;

- Modeling multi-phase, multi-component fluid flow with finite difference method.
- Using different grid systems; radial and cartesian block-center in 1, 2 or 3 dimensions. Both corner-point and conventional block-center geometry options are available. It also has an option for general unstructured, non-matching grids with local grid refinement.
- Implicit treatment of pressure and transport equations due to adaptive implicit, fully implicit or IMPES solutions in compositional models.
- Parallel processing in space and time.

- Defining different rock and pVT properties on a regional basis.
- Using a cubic equation of state or pressure dependent K−values. Four equations of state are available *Redlich-Kwong, Soave-Redlich-Kwong, Peng-Robinson* and *Zudkevitch-Joffe* and it is possible to use a volume shift parameter with any of these equations.
- Modeling both relative permeability and capillary pressure hysteresis effects.

5.1 Modeling of CO_2 Injection into an Aquifer Structure

Injection of CO_2 into saline aquifers will give rise to a variety of coupled physical and chemical processes, including pressurization of reservoir fluids, immiscible displacement of an aqueous phase by the CO_2 phase, partial dissolution of CO_2 into the aqueous phase, chemical interactions between aqueous CO_2 and primary aquifer minerals. Therefore the numerical simulation capabilities are developed and applied to gain an understanding of the physical and chemical processes involved to evaluate the technical feasibility of CO_2 storage into aquifers. The ECLIPSE version discussed in this chapter includes additional enhancements in the phase equilibria model and thermophysical properties of fluid mixtures. operational conditions.

For the aquifer storage modeling, ECLIPSE has two options;

- CO2SEQ; in this option two phases are considered CO_2-rich phase i.e. gas phase and H_2O-rich phase as liquid phase. This option gives accurate mutual solubilities of CO_2 in water, xCO_2 and water in the CO_2-rich phase, yH_2O. Salts are described as components of the liquid phase.
- GASWAT; this option provides a gas/aqueous phase equilibrium method. The liquid mole fraction xCO_2 is accurately predicted; however, the gas phase mole fraction

$y\mathrm{H_2O}$ is less accurate. The gas composition is not restricted to $\mathrm{CO_2/H_2O}$, as other gases and their solubility in water can be included.

The report through the numerical modeling with ECLIPSE simulator, is based on the following assumptions;

1. Multi phase flow extension of Darcy´s Law.
2. Storage conditions are 12-100°C and up to 600 bar.
3. The phases are in chemical and thermal equilibrium.
4. No chemical reactions take place other than partitioning of mass components among phases.
5. At the moderate temperatures of interest water mole fraction in the $\mathrm{CO_2}$-rich phase is small thus, water partitioning is modeled as an evaporation process.
6. Salts stay in liquid phase.
7. Changes in water viscosity from $\mathrm{CO_2}$ dissolution are ignored.
8. Mechanical stress is neglected.

5.2 Governing Equations

5.2.1 Solubility Model

Here we present the governing equations of CO2SEQ module in ECLIPSE. In CO2SEQ option, the mutual solubilities of $\mathrm{CO_2}$ and $\mathrm{H_2O}$ including the effect of chloride salts are calculated to match the experimental data at conditions 12-100°C and up to 600 bar. The formulation of mutual solubilities of $\mathrm{CO_2}$ and $\mathrm{H_2O}$ was developed by Spycher et al. (2003)

and then the basic model was extended with an activity coefficient for aqueous CO_2 and a correction to the activity of H_2O to account for the effects of dissolved salts.

The basic model based on the standard approach of equating the fugacities of phases at equilibrium for calculating the mutual solubilities of liquids and compressed gases is exhaustively described by Prausnitz et al. (1986). At equilibrium, the following reactions and corresponding equilibrium constant can be written:

$$H_2O_{(l)} \Leftrightarrow H_2O_{(g)} \ldots\ldots\ldots\ldots K_{H_2O} = \frac{f_{H_2O(g)}}{a_{H_2O(l)}} \tag{5.1}$$

$$CO2_{(aq)} \Leftrightarrow CO_{2(g)} \ldots\ldots\ldots\ldots K_{CO_2} = \frac{f_{CO_2(g)}}{a_{CO_2(aq)}} \tag{5.2}$$

where K are true equilibrium constants which are directly related to the standard Gibbs free energy reaction as

$$\Delta G^{\circ} = -RT \ln K$$

f are the fugacities of the gas components, and a are activities of components in aqueous phase. K_{H_2O} and K_{CO_2} values are dependent on temperature and pressure. The temperature dependence is taken into account by expressing these equilibrium constants as a polynomial function of temperature. The pressure correction at a given temperature is approximated by;

$$K_{(T,p)} = K^0_{(T,p)} \exp\left(\frac{\left(p - p^0\right)\bar{V}_i}{RT}\right) \tag{5.3}$$

where $\bar{V}_i$ is the average partial molar volume of the pure condensed component i over the pressure interval p^0 to p, and p^0 is the reference pressure taken as 1 bar.

From the definition of fugacity and partial pressures, fugacity can be written as

$$f_i = \Phi_i y_i p_{tot} \tag{5.4}$$

where f_i is the fugacity, Φ_i is the fugacity coefficient, y_i is the mole fraction of component i in the gas phase, and p_{tot} is the total pressure. In ECLIPSE CO2SEQ option, mole fraction in CO_2-rich phase is denoted as y and x is used for mole fraction in aqueous phase. Substituting Equation 5.4 into Equation 5.1 and 5.2 results in the following:

$$f_{H_2O} = \Phi_{_{H_2O}} y_{_{H_2O}} P_{tot} = K_{H_2O} a_{H_2O(l)} \tag{5.5}$$

$$f_{CO_2} = \Phi_{_{CO_2}} y_{_{CO_2}} p_{tot} = K_{CO_2} a_{CO_2(aq)} \tag{5.6}$$

Equation 5.5 is rewritten to express the water mole fraction in the gas phase and the pressure correction is applied to K_{H_2O} from Equation 5.3 yields

$$y_{_{H_2O}} = \frac{K^0_{_{H_2O}} a_{H_2O(l)}}{\Phi_{_{H_2O}} p_{tot}} \exp\left(\frac{\left(p - p^0\right)\bar{V}_{H_2O}}{RT}\right) \tag{5.7}$$

Raoult´s Law is used to set the water activity (a_{H_2O}) equal to its mole fraction in the water phase ($x_{_{CO_2}}$). For a binary system where CO_2 and H_2O are the only components, $x_{_{H_2O}}$ directly calculated as 1- $x_{_{H_2O}}$. The H_2O mole fraction in the CO_2-rich phase ($y_{_{H_2O}}$) and the mole fraction in the aqueous phase ($x_{_{CO_2}}$) are respectively expressed as :

$$y_{_{H_2O}} = \frac{K^0_{_{H_2O}} \left(1 - x_{CO_2}\right)}{\Phi_{_{H_2O}} P_{tot}} \exp\left(\frac{\left(p - p^0\right)\bar{V}_{H_2O}}{RT}\right) \tag{5.8}$$

The mole fraction of aqueous CO_2 ($x_{_{CO_2}}$) is calculated from its molality, m, with the convention that $a_{_{CO_2}} = \gamma m_{_{CO_2}}$ where γ is the activity coefficient of dissolved CO_2. For binary system, if no salts are present, γ is set to

$$\gamma = \frac{1}{1 + \frac{m_{CO_2}}{55.508}}$$

which is a molality to mole fraction correction (Helgeson et al. 1981). This relationship between the activity coefficient and mole fraction of dissolved CO_2 yields

$$a_{CO_2} = 55.508 x_{CO_2} \tag{5.9}$$

Substituting Equation 5.3 and 5.9 into Equation 5.6 results in

$$x_{CO_2} = \frac{\Phi_{CO_2}\left(1 - y_{H_2O}\right) P_{tot}}{55.508 K^0_{CO_2(g)}} \exp\left(-\frac{\left(p - p^0\right)\bar{V}_{CO_2}}{RT}\right) \tag{5.10}$$

In Equation 5.8 and 5.10, K^0 is the thermodynamic equilibrium constant for each component at temperature T and reference pressure $p^0 = 1$ bar. The effect of dissolved salts is expressed through a_{H_2O} the activity of liquid water, and γ the activity coefficient of dissolved CO_2. However, the salinity ranges up to ionic strength around 6 molal.

Equations 5.8 and 5.10 are solved by setting

$$A = \frac{K^0_{H_2O}}{\Phi_{H_2O} p_{tot}} \exp\left(\frac{\left(p - p^0\right)\bar{V}_{H_2O}}{RT}\right) \tag{5.11}$$

$$B = \frac{\Phi_{CO_2} P_{tot}}{55.508 \gamma K^0_{CO_2(g)}} \exp\left(-\frac{\left(P - P^0\right)\bar{V}_{CO_2}}{RT}\right) \tag{5.12}$$

Equation 5.8 can be rewritten as in Equation 5.13 by taking the water mole fraction as a reasonable approximation of water activity defined as

$$y_{H_2O} = A(1 - x_{CO_2} - x_{salt}) \tag{5.13}$$

and the mutual solubilities are then calculated as;

$$y_{H_2O} = \frac{(1 - B - x_{salt})}{(1/A - B)} \tag{5.14}$$

$$x_{CO_2} = B\left(1 - y_{H_2O}\right) \tag{5.15}$$

where x_{salt} is the mole fraction of dissolved salt on a fully ionized basis and including dissolved CO_2. It is given as:

$$x_{salt} = \frac{\upsilon m_{salt}}{55.508 + \upsilon m_{salt} + m_{CO_2(aq)}} \tag{5.16}$$

where m stands for molality and υ is the stoichiometric number of ions contained in the dissolved salt. The molality of CO_2 is expressed from the mole fraction as

$$m_{CO_2} = \frac{x_{CO_2}\left(\upsilon m_{salt} + 55.508\right)}{\left(1 - x_{CO_2}\right)} \tag{5.17}$$

It is more advantageous using the salt molality (Equation 5.16) instead of mole fraction (Equation 5.17) as an input parameter because it is independent of the CO_2 solubility, $m_{CO_{2(aq)}}$. Therefore, Equation 5.14 can be rewritten as:

$$y_{H_2O} = \frac{(1 - B)55.508}{(1/A - B)\left(55.508 + \upsilon m_{salt}\right) + \upsilon m_{salt} B} \tag{5.18}$$

At subcritical temperatures and pressure above saturation values, $K^0_{CO_2(g)}$ in Equation 5.12 should be replaced with $K^0_{CO_2(l)}$, referring to liquid instead of gaseous CO_2. The method implemented in CO2SEQ uses $K^0_{CO_2(l)}$ rather than $K^0_{CO_2(g)}$ when both the following conditions are met;

- temperature is below 31°C (rounded-off value of the critical temperature of pure CO_2)
- the calculated volume of compressed gas phase is less than 94 cm^3/mole (rounded-off value of the critical volume of pure CO_2)

The calculated phase-change boundary for the CO_2-rich phase is assumed the same as for pure CO_2 and the P-T space in which three phases coexist (CO_2 gas, CO_2 liquid and H_2O liquid) is ignored. This simplification does not cause significant problems, while the three-phase p-T space is relatively small.

5.2.2 Equation of State

Equation of state is used in order to derive the fugacity coefficients in Equations 5.11 and 5.12 from the pVT-x properties of H_2O and CO_2. In the literature mentioned in Chapter 3, many equation of state and mixing rules with various degrees of complexity and accuracy have been presented. The Redlich-Kwong (1949) and Peng-Robinson (1976) equations and their various modifications have been used to successfully represent the properties of CO_2-H_2O mixtures over various p-T ranges. However, they behave less accurately in the vicinity of the critical point.

CO2SEQ option uses the modified Redlich-Kwong equation with the intermolecular attraction and repulsion parameters (a, b).

Redlich-Kwong Equation of State and Mixing Rules

Attempts at predicting the mutual solubilities with a conventional equation of state including the effect of salts in the aqueous phase requires some modifications in conventional Redlich-Kwong EOS.

$$p = \left(\frac{RT}{V-b}\right) - \left(\frac{a}{T^{0.5}V(V+b)}\right) \tag{5.19}$$

where parameter a and b represent the measures of intermolecular attraction and repulsion, respectively. V is the volume of the compressed gas phase at pressure p and temperature T, and R is the gas constant. In the standard equation (Equation 5.20, 5.21) the coefficients a and b varies with the critical temperature *(T_c)* and pressure *(p_c)*.

$$a = \frac{0.4278 T_c^{2.5} T^2 R^2}{p_c T^{2.5}} \tag{5.20}$$

$$b = \frac{0.0867 T_c T R}{p_c T} \tag{5.21}$$

Spycher and Pruess modified these parameter by setting;

$$a = k_0 + k_1 T \tag{5.22}$$

and fitting k_0, k_1 and b to reference pVT data. The only Redlich-Kwong parameters requiring this proposed modification are the attraction and repulsion parameters for pure CO_2 (a_{CO_2} and b_{CO_2}) , the repulsion parameter for pure water b_{H_2O} , and the $H_2O - CO_2$ binary interaction parameter $a_{H_2O-CO_2}$. Standard mixing rules described by Prausnitz et. al (1986) is applied for calculating the intermolecular attraction and repulsion parameters.

$$a_{mix} = \sum_{i=1}^{n} \sum_{j=1}^{n} y_i y_j a_{ij} \tag{5.23}$$

$$b_{mix} = \sum_{i=1}^{n} y_i b_i \tag{5.24}$$

Substituting a_{mix} and b_{mix} in place of a and b in Equation 5.19. For the binary H_2O-CO_2 mixture, the following equations can be written;

$$a_{mix} = y_{H_2O}^2 a_{H_2O} + 2 y_{H_2O} y_{CO_2} a_{H_2O-CO_2} + y_{CO_2}^2 a_{CO_2} \tag{5.25}$$

$$b_{mix} = y_{H_2O} b_{H_2O} + y_{CO_2} b_{CO_2} \tag{5.26}$$

From these mixing rules and Equation 5.19, the fugacity coefficient, Φ_k of component k in mixtures with other components i is calculated by Prausnitz et al. definition.

$$\begin{aligned} ln\left(\Phi_k\right) &= \ln\left(\frac{V}{V - b_{mix}}\right) + \left(\frac{b_k}{V - b_{mix}}\right) - \left(\frac{2\sum_{i=1}^{n} y_i a_{ik}}{RT^{1.5} b_{mix}}\right) \ln\left(\frac{V + b_{mix}}{V}\right) \\ &+ \left(\frac{a_{mix} b_k}{RT^{1.5} b_{mix}^2}\right) \left[\ln\left(\frac{V + b}{V}\right) - \left(\frac{b_{mix}}{V + b_{mix}}\right)\right] - \ln\left(\frac{PV}{RT}\right) \end{aligned} \tag{5.27}$$

It is evident from Equation 5.27 that the fugacity coefficient depends on the temperature, pressure and each components in the gas mixture. Equation 5.19 is used to calculate p, V, or T. The volume of the compressed gas phase is computed numerically by rewriting the Equation 5.19 as a general cubic equation in terms of volume;

$$V^3 - V^2\left(\frac{RT}{P}\right) - V\left(\frac{bRT}{P} - \frac{a}{PT^{0.5}} + b^2\right) - \left(\frac{ab}{PT^{0.5}}\right) = 0 \tag{5.28}$$

This equation is solved directly using the method of Nickalls (1993). The volume of the gas phase, V_{gas}, is always given by the maximum root of Equation 5.28. The minimum root always provides the volume of the liquid phase, V_{liquid}.

The phase transition occurs at the point where the work w_1 done from V_{gas} to V_{liquid} along a straight path is the same as the work w_2 done along the curved path indicated by Equation 5.19. From the definition of work it can be written as;

$$w_1 = P(V_{gas} - V_{liquid}) \tag{5.29}$$

$$w_2 = RT\ln\left(\frac{V_{gas} - b}{V_{liquid} - b}\right) + \frac{a}{T^{0.5}b}\ln\left(\frac{(V_{gas} + b)\,V_{liquid}}{(V_{liquid} + b)\,V_{gas}}\right) \tag{5.30}$$

Once the volume of compressed gas phase is calculated and it is substituted into Equation 5.27 to compute the fugacity coefficients and then this equation need to be solved simultaneously with Equation 5.11 and 5.15 to compute the mutual solubilities of CO_2 and water.

The modification done by Spycher et al.(2003) aimed at representing the solubility data at low temperatures and elevated pressures, in the p-T range of CO_2 storage projects. However, the accurate volumetric properties in the vicinity of the CO_2 saturation curve is not estimated accurately. The solubility model was extended to include the effect of chloride salts in the aqueous phase (2004). The approach implemented in ECLIPSE is

intended for an efficient calculation of mutual solubilities in numerical modeling of the geologic CO_2 storage projects at temperatures between 12 and 100°C, pressures up to 600 bar and salinity up to 6 m NaCl, or 4 m $CaCl_2$.

Mixing Mechanisms and Analysis of Convective Mixing

Natural convection in porous media has been extensively studied [39]. However, the convective mixing in the framework of CO_2 storage has been investigated only in the recent years. In aquifer storage, the injected CO_2 is less dense than the resident formation brine, and driven by buoyancy CO_2 flows upward to the storage formation. During the injection, a portion of CO_2 is trapped as residual gas, and the free-phase CO_2 dissolves in the formation water. The CO_2-saturated formation water is denser than the surrounding formation water potentially leading to natural convection. The convective mixing promotes the dissolution of more CO_2 by replacing CO_2-saturated formation water with under-saturated brine.

CO_2 storage in saline aquifers can be investigated in short-and long term processes. Short-term processes include gravity override or viscous displacement, and long-term processes can be defined as diffusion and convection which might be caused by diffusion of CO_2 into underlying formation water.

In CO2SEQ of ECLIPSE simulator, CO_2 solubility in water is introduced and it assumes that the component existing in gaseous and aqueous phase will be distributed across two phases in such a way that the chemical potentials of two components are in equilibrium [35]. For the equilibrium concentrations of CO_2 dissolved in formation water, the modified Redlich-Kwong equation given in Subsection 5.2.2 is applied. The simulations runs performed in order to investigate the effect of the diffusion coefficient however shows that with the different diffusion coefficients used, no discernable differences can be observed. Therefore, it could be inferred that CO2SEQ option of ECLIPSE does not adequately take the diffusion of CO_2 across the grid blocks into account.

If it is ignored, it can be explained by the fact that the implicit calculation assumes that Darcy flow is the dominant mechanism of convective transport across grid cell blocks and the diffusion of CO_2 is ignored. This approach can be correct provided at the reservoir/aquifer scale, the diffusion time scale T_{diff} is much larger than the convection time scale T_{conv}. This can be approximated by Peclet number which is a dimensionless number relating the rate of advection of a flow to its rate of diffusion.

$$P_e = \frac{T_{diff}}{T_{conv}} \tag{5.31}$$

Figure 5.1 indicates the typical CO_2 injection scenario into saline aquifer, in which L is the horizontal distance from the injector, and the depth of plume is a function of distance from the injector, L and the time, t.

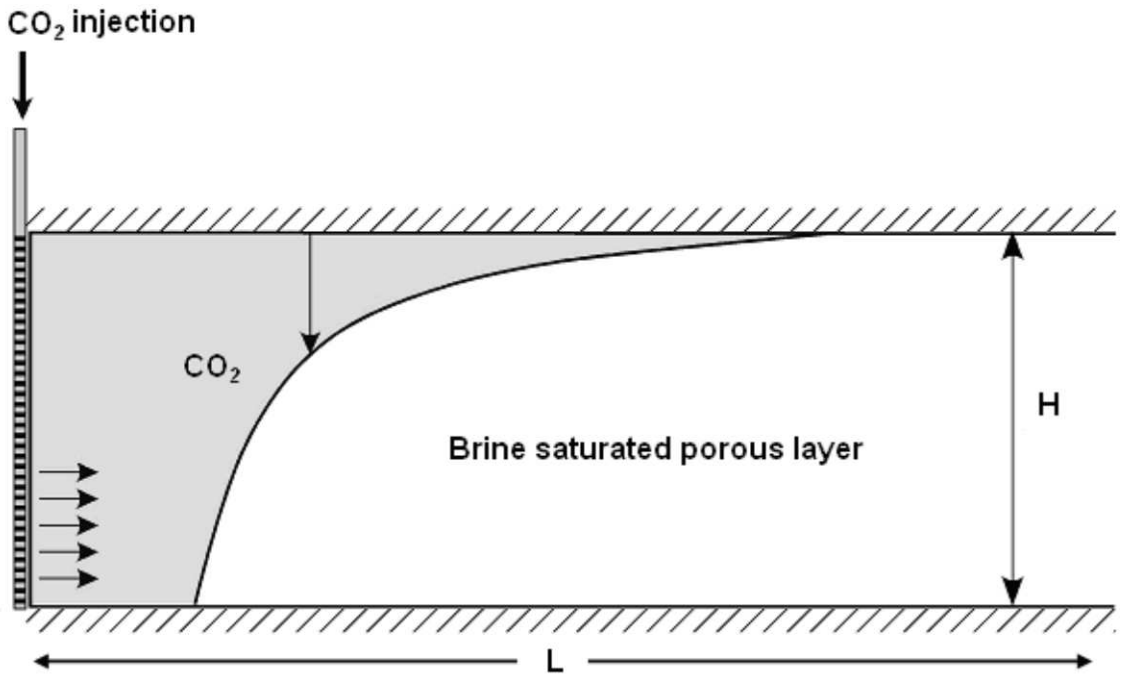

Figure 5.1: CO_2 injection scenario into saline aquifer

For mass diffusion Peclet number can be written as;

$$P_e = \frac{Lv}{D} \tag{5.32}$$

Where v is the gas phase Darcy flow velocity which can be written as in Equation 5.33;

$$q = -\frac{kA}{\mu}\frac{\Delta P}{L} \tag{5.33}$$

Substituting Darcy velocity Equation 5.33 into the Equation 5.32 results in;

$$P_e = \frac{L}{D}\frac{k}{\mu}\frac{\Delta P}{L} = \frac{k}{\mu}\frac{\Delta P}{D} \tag{5.34}$$

where ΔP is the pressure difference due to injection of CO_2, k is the horizontal permeability, μ is the viscosity and D is the molar diffusion of CO_2.

After injection due to gravity effects, lateral migration or upward migration of the gaseous phase and convective transport dominates. The CO_2 is trapped as residual gas, as it dissolves in formation water and the CO_2 saturated brine migrates downward to the storage aquifer. Convection is important as it mixes the dissolved gas faster into the liquid phase than the diffusion alone, and thus promotes the overall dissolution of CO_2 in the formation brine. Again, the Peclet number can be used to estimate the importance of convective mixing relative to the diffusion.

$$P_{e\_con} = \frac{H^2}{D}\frac{k_v \Delta\rho g}{\mu H} \tag{5.35}$$

in which H is the thickness of the aquifer, $\Delta\rho$ is the density difference in brine with dissolved CO_2 and without dissolved CO_2 (10-15 kg/m^3), g is the gravity acceleration and k_v is the vertical permeability. As a result of Equation 5.35, the diffusion coefficient in the simulation can be neglected compared to convection especially in aquifer scales.

In grid blocks although equilibrium occurs only on the interface of the CO_2-gas phase and aqueous phase, the equilibrium conditions applied for the entire volume of the grid cell.

Therefore, in ECLIPSE, numerical diffusion dominates and the result of the simulation represents the maximum estimate of the dissolved CO_2 in the block, depending on the grid size.

From the Peclet number in equations 5.34 and 5.35, the size of the grid block can be determined in which the numerical diffusion matches the real diffusion. For one grid block, the Peclet number can be written as in Equation 5.36.

$$P_e = \frac{k_h}{\mu}\frac{\Delta p}{D} \tag{5.36}$$

In order to estimate the grid block size, the pressure difference is written in terms of pressure gradient in Equation 5.37.

$$P_e = \frac{k_h}{\mu}\frac{(\Delta p/\Delta x)\,\Delta x}{D} \tag{5.37}$$

Substituting the average reservoir parameters in Equation 5.37, it can be estimated what Δx should be in order to see the numerical diffusion. Assuming the pressure gradient 1 bar/100 m, μ= 5.10^{-4} Pas, k_h=2.10^{-13} m^2 and D=5.10^{-9} m^2/s and substituting into the equation;

$$\Delta x = 1.25m$$

This result shows that for the grid block size used typically in simulation with dimensions of approximately 50 m, the numerical diffusion is several order magnitude of faster than the real diffusion. This numerical diffusion can also be interpreted to account for interference zone where the gaseous CO_2 phase migrates laterally into the brine-saturated formation, and thus increase the contact area of CO_2 and undersaturated formation brine.

Chapter 6

Simulation of CO_2 Storage in Buntsandstein Aquifer

Carbon dioxide can be sequestered in aquifers through a combination of physical and chemical mechanisms. CO_2 can be trapped under a low-permeability caprock, similar to the way that natural gas is trapped in reservoirs or stored in aquifers. This mechanism, called stratigraphic trapping, relies on the physical displacement of pore fluids. Secondly, pore fluids can accumulate dissolved CO_2 through aqueous solubility trapping. The injection of CO_2 into a saline aquifer is a two-phase flow condition and CO_2 can form a CO_2-rich residual gas phase after displacement by water. This residual gas phase becomes immobile due to trapping by capillary forces, which is known as capillary trapping.

It is of interest to determine the storage capacity and confining ability more precisely, in order to inject and retain more CO_2 for a long period, since the injected CO_2 may potentially leak through faults, cap rock formation or wellbore in the atmosphere. In this study, we focus on determining the extent of CO_2 migration during injection and post-injection period as well as leakage through cap rock and faults. The results of the analysis stratigraphic, solubility and capillary trapping are presented in this chapter.

An outline of this chapter is as follows. In Section 6.1, the basic problem of CO_2 injection into a generic aquifer model is presented. Because simplified radial flow model allows the

observation of processes without any geologic complications, a simplified radial model case will be used to check the validity of governing equations of the numerical model. The phase behavior modeling of gas/super critical CO_2 mixtures with reservoir brine is given in Section 6.2. The multi-phase flow performance and its impacts on CO_2 storage predictions are given in Section 6.3. Finally, a more complex flow problem is considered in Section 6.7, representing the proposed CO_2 injection project at the Buntsandstein prototype reservoir in Germany.

6.1 Generic Model for CO_2

The idea of generic model simulation was to simulate a prototype deep aquifer for systematic investigation of sensitivity parameters such as aquifer properties, injected gas and injection well, and their effects on the prediction of a CO_2 storage process. The CO_2 injection process is modeled as a two-phase flow of CO_2 and formation water for simplified flow geometry and medium properties. The aquifer is assumed to be infinite-acting, homogeneous, and at isothermal conditions of 60°C. Gravity, inertial effects and chemical interactions between the system components are neglected. Processes being studied comprises;

1. Two phase flow of CO_2-formation water subject to relative permeability and capillary pressure effects
2. Diffusive transport of CO_2 in the aqueous phase
3. Change of CO_2 solubility with pressure, temperature, salinity and brine composition
4. Change of fluid density with dissolution of CO_2, pressure and salinity
5. Gravity-driven advection in response to density gradients induced by dissolution of CO_2 into saline aquifers and convective mixing

An important advantage of the generic model simulation is that the sensitivity of parameters such as relative permeability hysteresis, permeability anisotropy, residual phase saturations, injection rate can be investigated without influence of the heterogeneity of the aquifer. This makes interpretations easier and more unambiguous. The smaller generic model compared to the reservoir model reduces the simulation run time, thus more sensitivity analysis can be performed in less time.

6.1.1 Dynamic Geologic Model Description

The dimensions of the generic model are 3000 m in X-direction and 3000 m in Y-direction with a net thickness of 40 m. The reservoirs parameters were defined corresponding to the average reservoir properties of the Buntsandstein aquifer including the cap rock. Table 6.1 summarizes the base case input parameters including aquifer parameters and injection conditions. The reservoir parameters marked with * means measured data were not available, therefore the most appropriate literature data are used in the simulation. Pure CO_2 was injected at a maximum rate of 100,000 sm^3/day for 20 years. However, the injection was controlled by a maximum bottom hole pressure (BHP) of 300 bar, in order to avoid formation fracturing. Consequently, when the pressure exceeds the BHP limit during the injection, the injection rate was reduced automatically, Figure 6.1.

Among different proposed relative permeability curves for CO_2-water-rock systems. Corey correlations and literature data [6] were used. Drainage and imbibition curves were considered as reversible, which is not realistic but was used for the sake of simplicity. In the further sections, the relative permeability hysteresis effect will be taken into account in order to determine its importance for mechanical trapping and as well as for solution trapping.

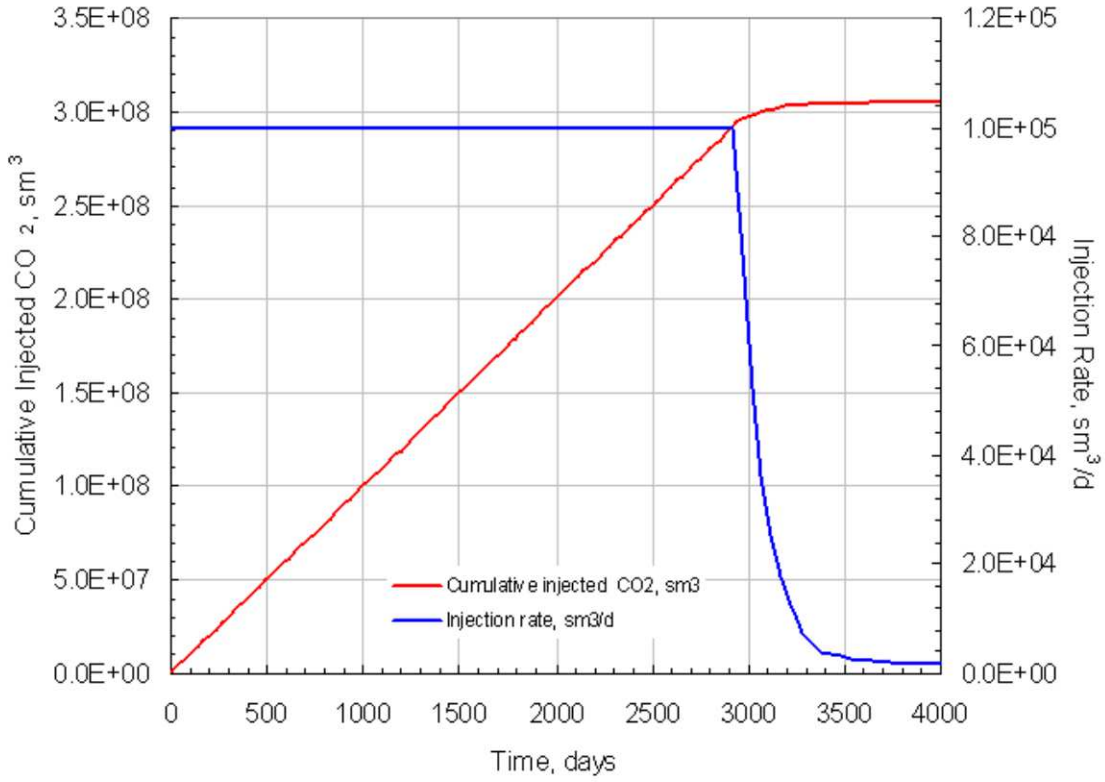

Figure 6.1: Gas injection history

Table 6.1: Reservoir and process properties of CO_2 injection model

Property	*Reservoir Model*	*Generic Model*
Aquifer size	App. $3500m \times 1400m$	$3000m \times 3000m$
Storage formation thickness	$15m$ to $20m$	$40m$
Porosity in storage formation	19.5% to 25%	20%
Porosity in cap rock	1.3%to 9%	5%
Permeability in storage formation	$158mD$ to $178mD$	$200mD$
Permeability in cap rock	$0.01mD$ to $0.001mD$	$0.001mD$
Vertical to horizontal permeability	0.1	0.1
Reservoir temperature	$87°C$	$60°C$
Initial reservoir pressure	$200bar$	$200bar$
Salinity	$315g/l$(287.5g/l NaCl+4.6$g/l$$MgCl_2$+ 24.5$g/l$ $CaCl_2 + 1.4g/l$ $CaBr_2 + 1.1g/l CaSO_4$)	$200,000ppm$
Diffusion Coefficient	$210^{-}9$	$210^{-}9$
Relative permeability and capillary pressure	Corey (1954), Van Genuchten (1980)*	Corey (1954), Van Genuchten (1980)
Initial water saturation	100%	100%
Irreducible water saturation	25%∗	25%
Critical gas saturation	10%∗	10 %
Maximum injection rate	$100,000sm^3$/day per well	$100,000sm^3$/day
Maximum injection pressure	$300bar$	$300bar$
Number of well	7 vertical, 2 horizontal wells	1

6.2 Solubility Trapping

Phase/solubility calculations are most critical for the prediction of the solution trapping capacity of the aquifer. The migration of the gas plume is dependent on the solubility modeling of CO_2 in brine.

In the base case model as described in Section 6.1.1, Corey (1954) and van Genuchten (1980) correlations were used to determine the relative permeability and capillary pressure functions [12, 47]. Figure 6.2 represents the relative permeability curves of gas-water system for the formation and cap rock.

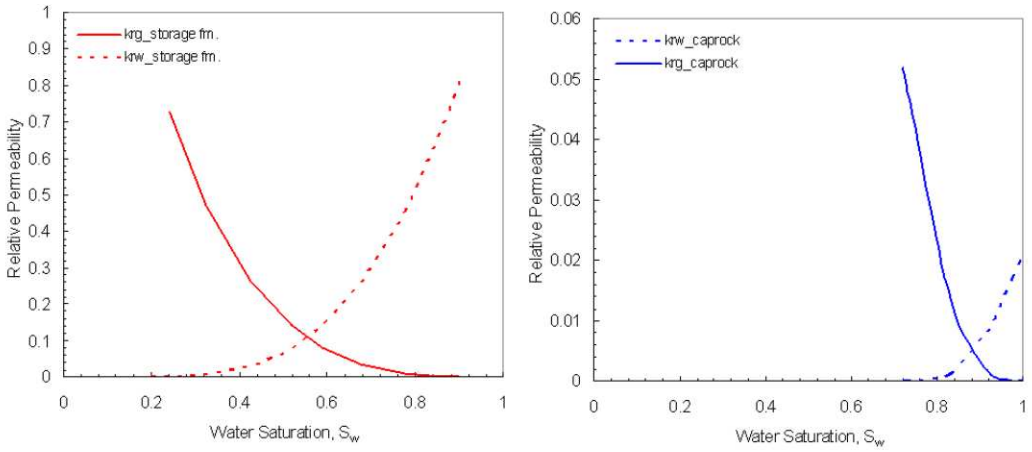

Figure 6.2: Relative permeability curve for CO_2-water-rock system, left=sandstone formation, right=caprock formation

The sensitivity of the aquifer solubility storage capacity to parameters such as permeability, brine composition and salinity, permeability anisotropy k_v/k_h, and residual phase saturations were studied by use of variations of the base case. A systematic compilation of the used sensitivity parameters together with the section numbers are given in Table 6.2. The capital A denotes the aquifer, whereas the G denotes the generic model and the K refers to Buntsandstein prototype reservoir model. The base case is labeled with number

0. It is assumed that each of these parameters is varied independently.

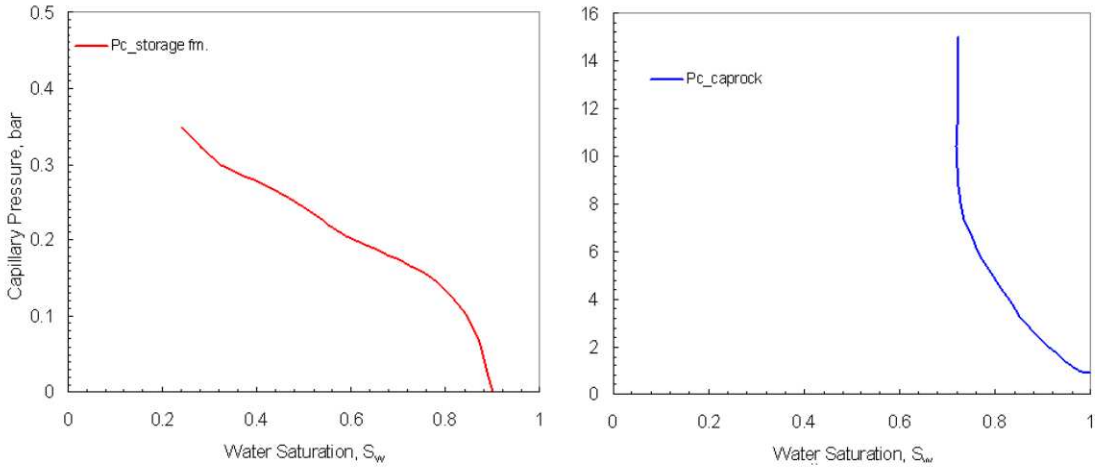

Figure 6.3: Capillary pressure curve for CO_2-water-rock system, left=sandstone formation, right=caprock formation

Table 6.2: Updated sensitivity parameters

Brine salinity and composition (BS)	6.2.1	Time
AG_BS 0	200,000 ppm NaCl containing saline aquifer	250 years
AG_BS 1	No salinity (fresh water)	250 years
AG_BS 2	200,000 ppm $CaCl_2$ containing saline aquifer	250 years
k_v/k_h (VtHP)	6.2.2	Time
AG_VtHP 0	0.1	100 years
AG_VtHP 1	0.01	100 years
AG_VtHP 2	1	100 years
Residual phase saturations (PS)	6.2.3	Time
AG_PS 0	$S_{wi} = 0.25$, $S_{gc} = 0.10$	100 years
AG_PS 1	$S_{wi} = 0.25$, $S_{gc} = 0.30$	100 years
AG_PS 2	$S_{wi} = 0.15$, $S_{gc} = 0.30$	100 years
Capillary trapping (CT)	6.3.1	Time
AG_CT 0	Capillary pressure and hysteresis	500 years
AG_CT 1	No capillary pressure and hysteresis	500 years
AG_CT 2	Capillary pressure but no hysteresis	500 years
Aquifer volume (AV)	6.4.1	Time
AG_AV 0	$40m$	100 years
AK_AV 0	$20m$	100 years
AG_AV 1	$120m$	100 years
Absolute permeability of aquifer (AP)	6.4.2	Time
AG_AP 0	$200mD$	100 years
AK_AP 0	$90 - 178mD$	100 years
AG_AP 1	$1000mD$	100 years
Shale layers in storage fm.(LS)	6.4.3	Time
AG_LS 0	5 Shale layers	500 years
Gas threshold pressure (TP)	6.5.1	Time
AG_TP 1	$15bar$	500 years
AG_TP 2	$34.4bar$	500 years
Injection interval (II)	6.6	Time
AG_II 0	vertical well	500 years
AG_II 1	vertical well across the entire storage fm.	500 years
AG_II 2	horizontal well	500 years
Injection rate (IR)	6.6.2	Time
AG_IR 1	Total injection amount/1 year	100 years
AG_IR 2	Total injection amount/10 years	100 years
AG_IR 3	Total injection amount/50 years	100 years

6.2.1 Effect of Brine Salinity and Composition

An important aspect of the multi-component system of Water-CO_2-Salt is the partioning of components among phases and the impact of constituents on thermophysical properties. For the realistic characterization of pVT properties, salinity and brine composition are important parameters. The main fluid parameters, density and viscosity, are functions of the pressure, temperature, salinity and solubility of CO_2 in the aqueous phase. Solubility is also a function of the pressure, temperature and salinity. CO2SEQ option of ECLIPSE, which is characterized by an improved equation of state for CO_2-brine mixtures as indicated in the previous chapter was used to estimate the CO_2/brine system properties. Four components are currently allowed in CO2SEQ option; CO_2, H_2O, NaCl and $CaCl_2$.

Figure 6.4 and 6.5 show the gas distribution for the base case in a X-Z cross section through the injector after 10 years and 250 years respectively for an observation grid block (1, 15). The injection interval (perforations) between the layers 6 and 10 is shown by black dots. The boundary between the caprock and storage formation is indicated by the solid white line.

From the gas saturation profiles, it can be seen that during the injection phase CO_2 is mostly present in the reservoir as a gas phase and less volume is dissolved. Due to the density difference between the injected CO_2 and formation brine, the gas tends to migrate to the top of the storage formation accumulating below the cap rock. After termination of injection, CO_2 continues to spread out underneath the cap rock laterally. The maximum lateral distance in 250 years is approximately 1200 m from the injector. Dissolved gas migrates into the caprock by diffusion whereas the free gas below critical saturation and is not displaced. Figures 6.6 and 6.7 indicates the gas saturation performance and the mole fraction of CO_2 (x_{CO2}) in the aqueous solution of NaCl at different distances from the injector in the layer just below the cap rock. In the vicinity of the injection well, the gas saturation increases rapidly. Once the injection stops, the gas saturation decreases

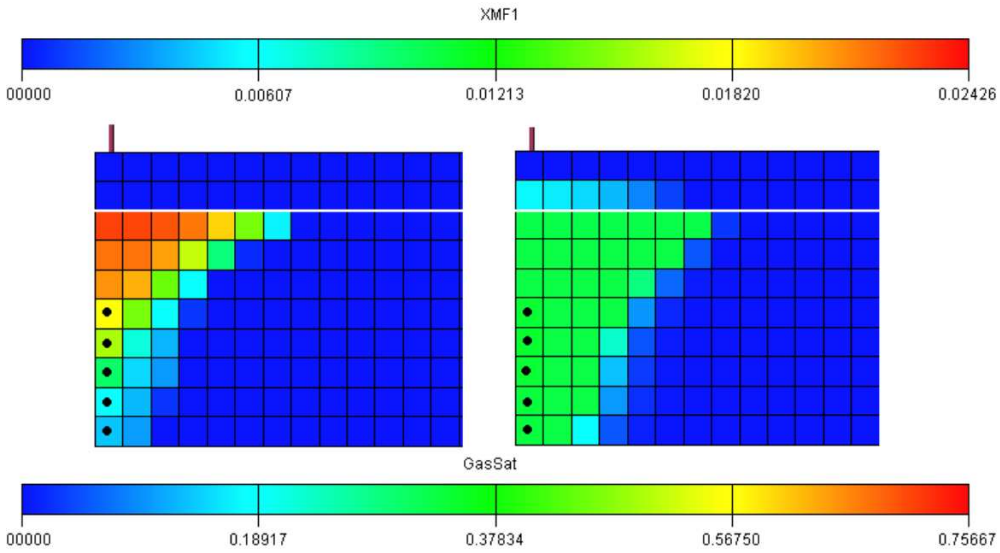

Figure 6.4: Gas saturation profile and mole fraction of CO_2 in aqueous phase after 10 years injection into the aquifer containing 200,000 ppm NaCl left=saturation profile, right= mole fraction (gas saturation scale is in the bottom, and mole fraction scale is in the top)

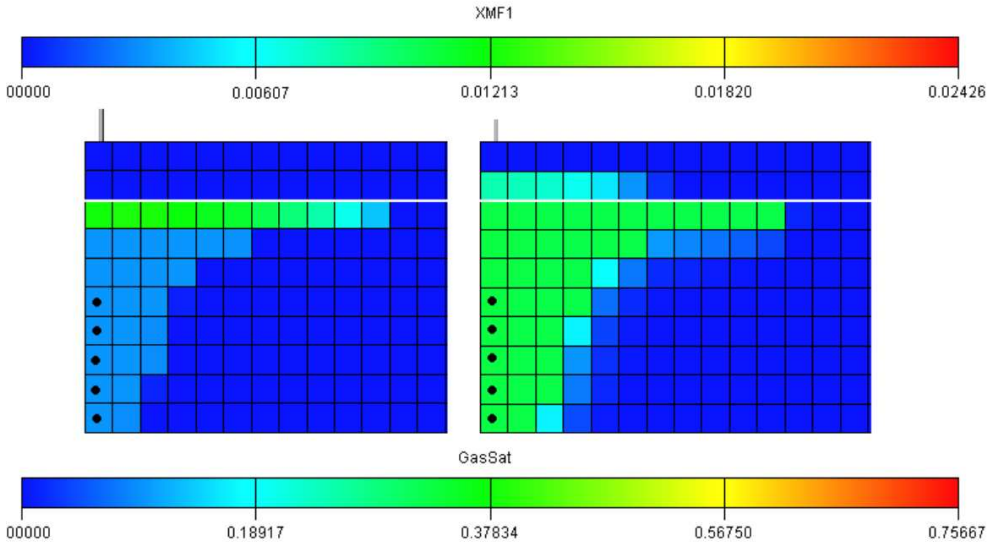

Figure 6.5: Gas saturation profile and mole fraction of CO_2 in aqueous phase 240 years after termination of injection into the aquifer containing 200,000 ppm NaCl left=saturation profile, right= mole fraction (gas saturation scale is in the bottom, and mole fraction scale is in the top)

due to the dissolution of gas and lateral movement along the cap rock. The increasing gas saturation at 1050 m distant from the injector is an indication of lateral movement. k_v/k_h ratio has a significant effect on the flow path. The k_v/k_h ratio promotes the vertical migration which brings the gas into contact with larger volume of formation brine, and thus increases the dissolution of CO_2 as well as the risk of gas losses through conductive zones in the cap rock.

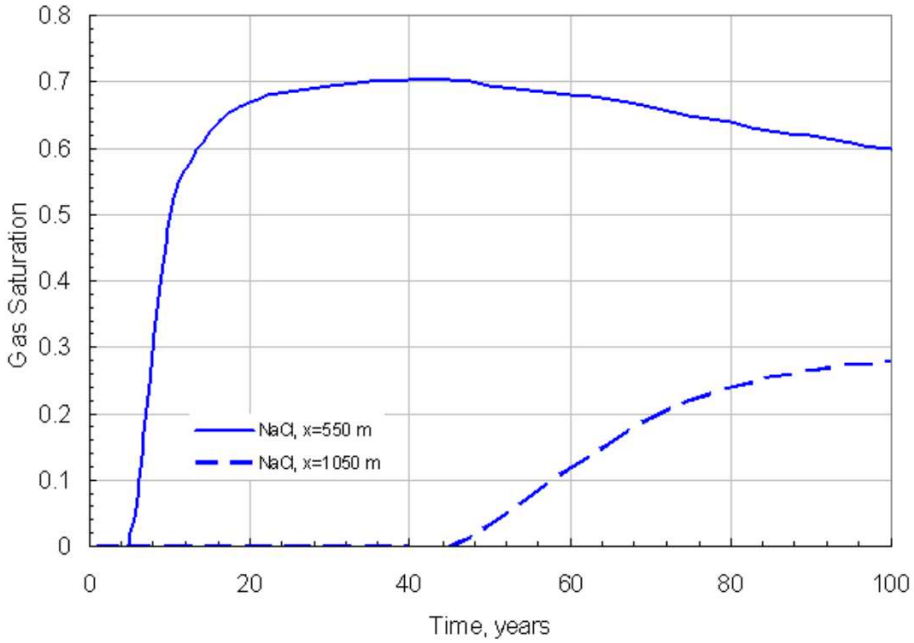

Figure 6.6: Gas saturation performance in the 3^{rd} layer (just below the cap rock) at different distances from the injector

As salinity increases, the solubility of CO_2 decreases and solubility trapping becomes more effective. Figure 6.4 depicts the plume migration after 10 years of CO_2 injection into a 200,000 ppm NaCl containing formation brine. In comparison, the gas saturation profile in a fresh water aquifer is indicated in Figure 6.8.

Free gas and correspondingly saturation is lower than in the case of 200,000 ppm NaCl containing aquifer due to smaller buoyancy force and the dissolution rate is higher in fresh

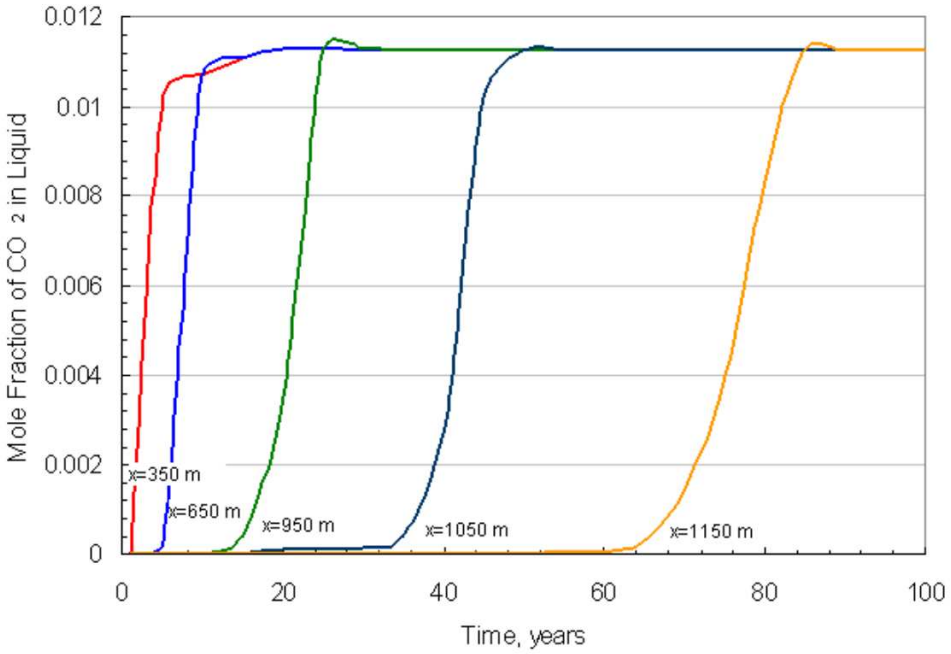

Figure 6.7: Gas solubility performance in the 3^{rd} layer (just below the cap rock) at different distances from the injector

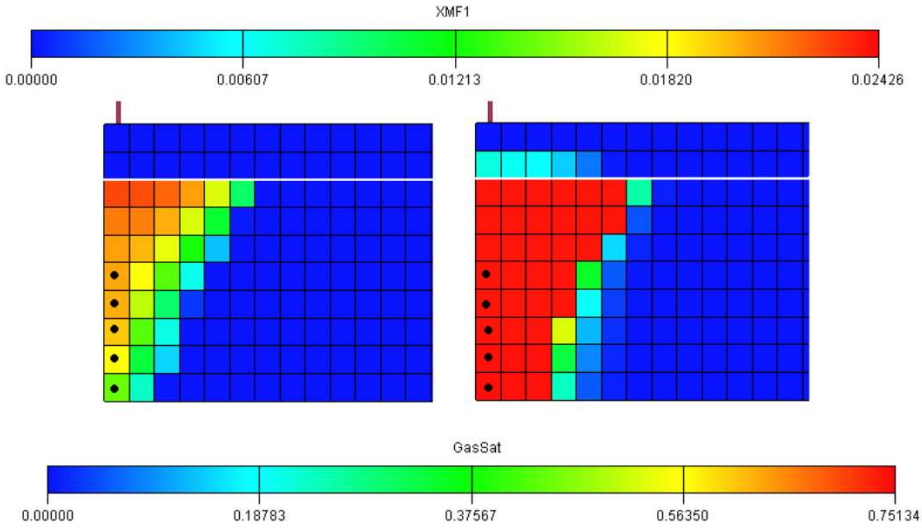

Figure 6.8: Gas saturation profile and mole fraction of CO_2 in an aqueous phase after 10 years injection into a fresh water aquifer left=saturation profile, right= mole fraction (gas saturation scale is in the bottom, and mole fraction scale is in the top)

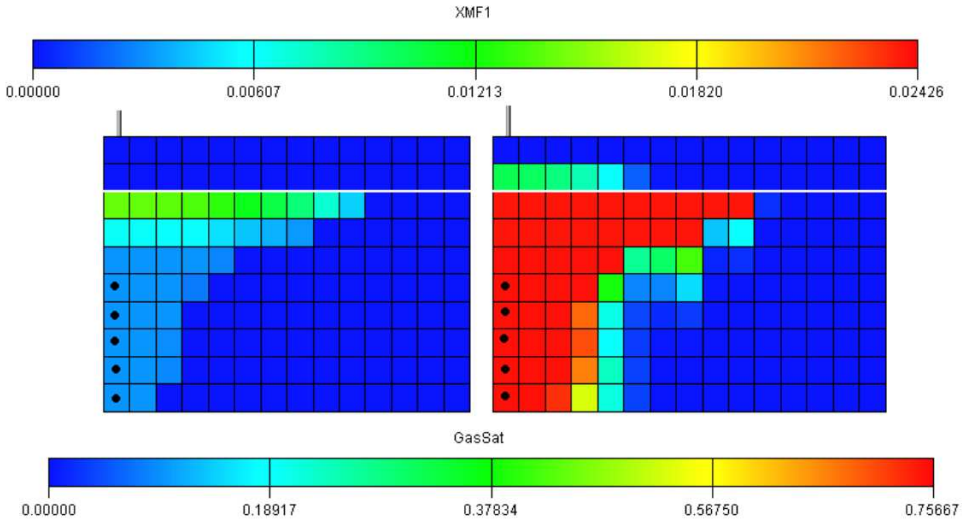

Figure 6.9: Gas saturation profile and mole fraction of CO_2 in an aqueous phase 240 years after termination of injection into a fresh water aquifer left=saturation profile, right= mole fraction (gas saturation scale is in the bottom, and mole fraction scale is in the top)

water aquifer. Figure 6.10 shows the gas saturation build up in layer 3, which is just below the cap rock for saline and fresh water aquifer after 10 and 20 years injection with lateral distance from the injector.

The gas saturation profile in the case of the saline system is influenced by the lower dissolution of CO_2 into the saline aqueous phase, whereas fresh water on the other hand, promotes the dissolution of CO_2. Figure 6.11 indicates the mole fraction of CO_2 (x_{CO2}) in the fresh water and aqueous solution of NaCl in layer 3 (top of reservoir) over time. It can be seen that up to a lateral distance of 650 m the gas dissolves approximately with comparable rate but due to the different contact times different individual level of dissolution occurs. At distances greater than 650 m, the time required for the dissolution of CO_2 into fresh water becomes longer than that required in aqueous solution of NaCl, due to smaller contact areas. The buoyancy effects of gas depend on the density differences between gas and brine. The higher the salinity the more pronounced is the lateral extension.

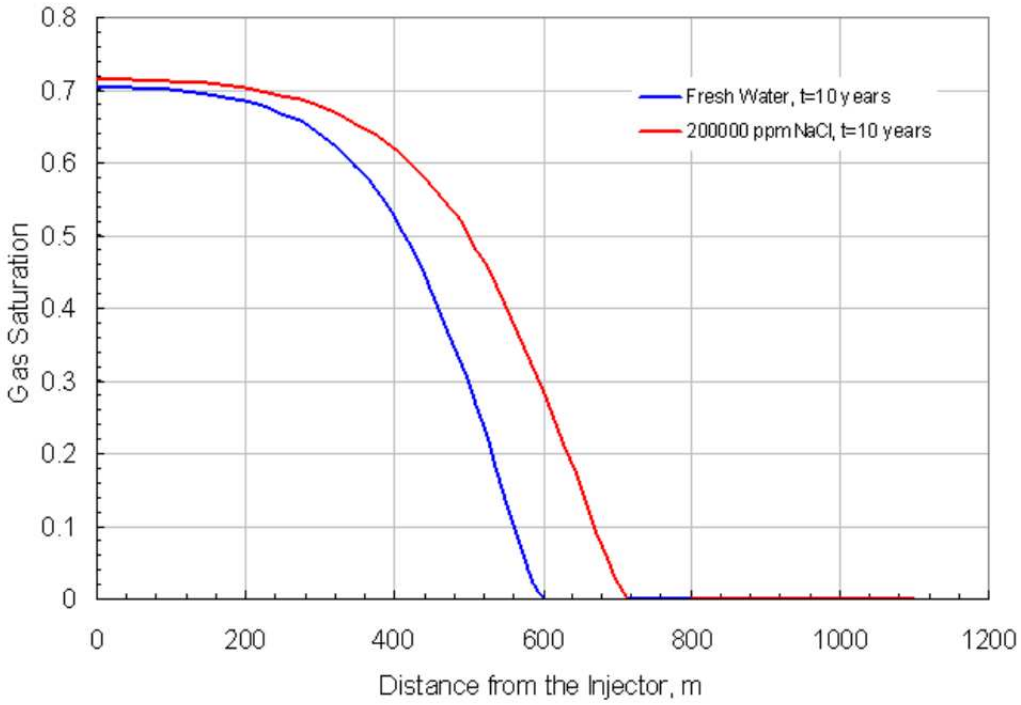

Figure 6.10: Gas saturation performance after 10 years of injection into the fresh water aquifer compared with 200,000 ppm NaCl brine

The solubility of CO_2 changes with varying brine composition. Figures 6.12 and 6.14 shows the gas saturation and solubility profiles of CO_2 in 200,000 ppm $CaCl_2$ brine aquifer after 10 years (end of injection) and after 250 years. An indication of the lateral migration of the plume can be seen.

Figure 6.13 shows the mole fraction of CO_2 in fresh water and aqueous solutions containing the same amount of dissolved salts; NaCl, $CaCl_2$ in a monitoring block 1,15,3. The figure indicates the sensitivity to the varying solubility of CO_2 in different types of brines and salinities.

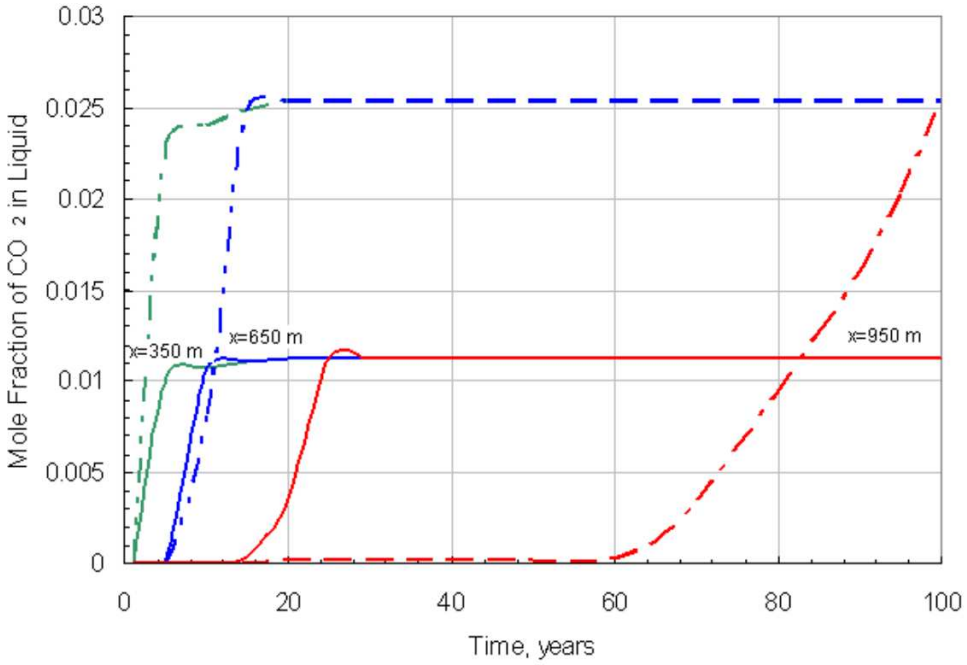

Figure 6.11: Solubility of CO_2 in fresh water (dashed line) and in 200,000 ppm NaCl brine (solid line) at different distances from the injector

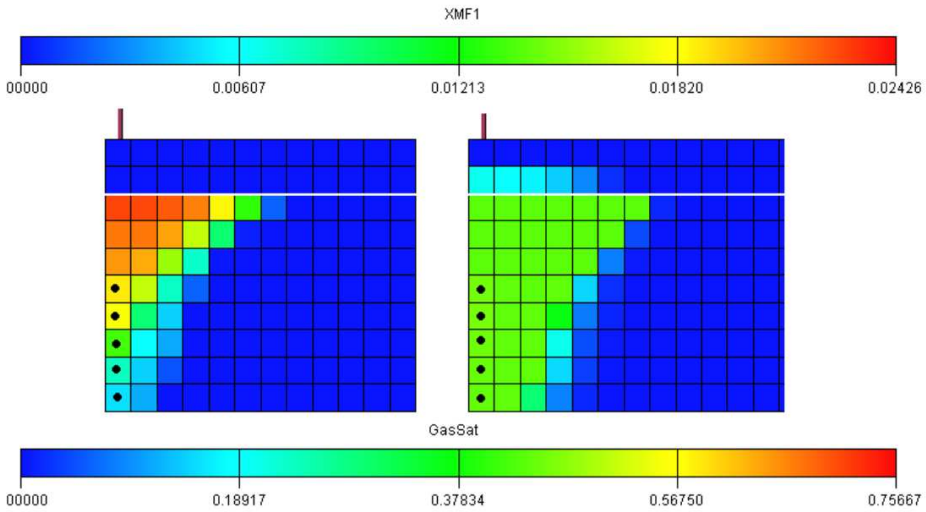

Figure 6.12: Gas saturation and mole fraction of CO_2 in an aqueous phase after 10 years injection into the aquifer containing 200,000 ppm $CaCl_2$ left=saturation profile, right= mole fraction (gas saturation scale is in the bottom, and mole fraction scale is in the top)

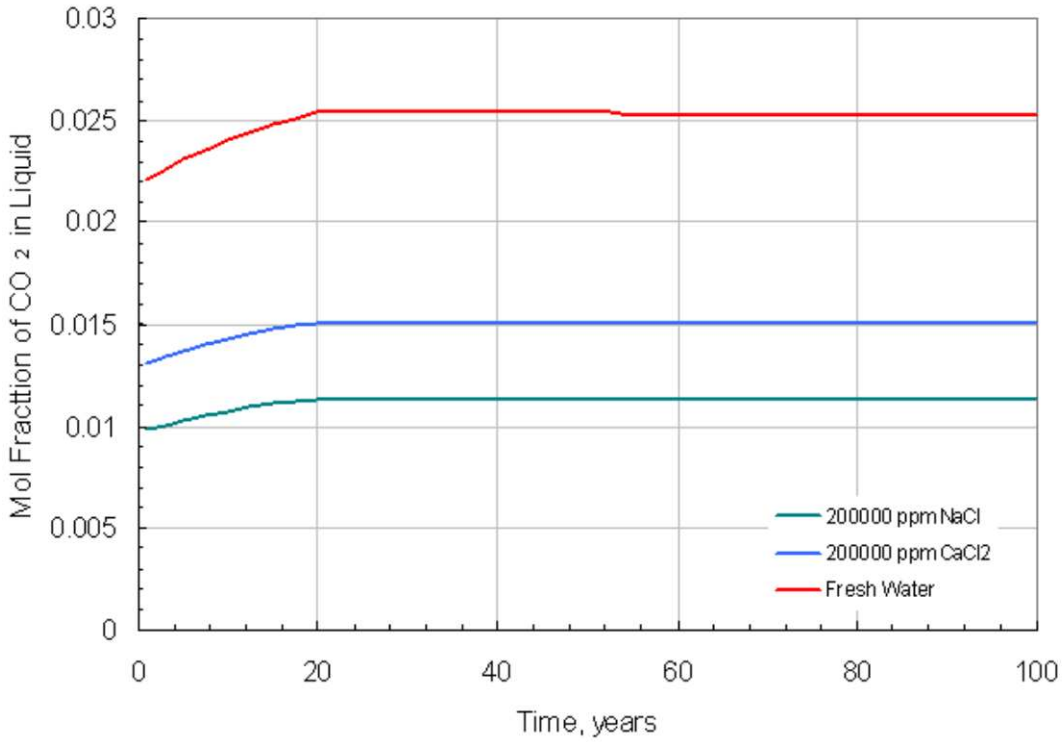

Figure 6.13: Solubility performance of CO_2 with time in aqueous solutions of NaCl, $CaCl_2$ and fresh water with time

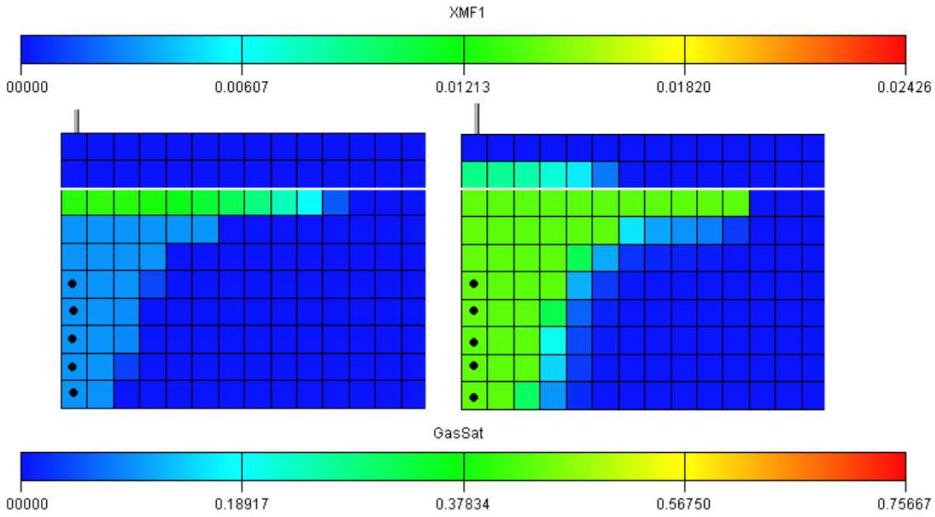

Figure 6.14: Gas saturation and mole fraction of CO_2 in an aqueous phase 240 years after termination of injection into the aquifer containing 200,000 ppm $CaCl_2$ left=saturation profile, right= mole fraction (gas saturation scale is in the bottom, and mole fraction scale is in the top)

After a relatively long elapsed time, following the injection phase of CO_2 almost all gas would be stored in the top structure, underlying the cap rock. However, when CO_2 has contact with under-saturated formation water, it dissolves in it. As CO_2 dissolves the density of formation water increases (Figure 6.15, 6.16 and 6.17). The more dense CO_2 saturated formation brine relative to the surrounding formation water will segregate downward in the aquifer and will be replaced by water with less CO_2 content. Density-driven flow enhances dissolution by convective mixing process.

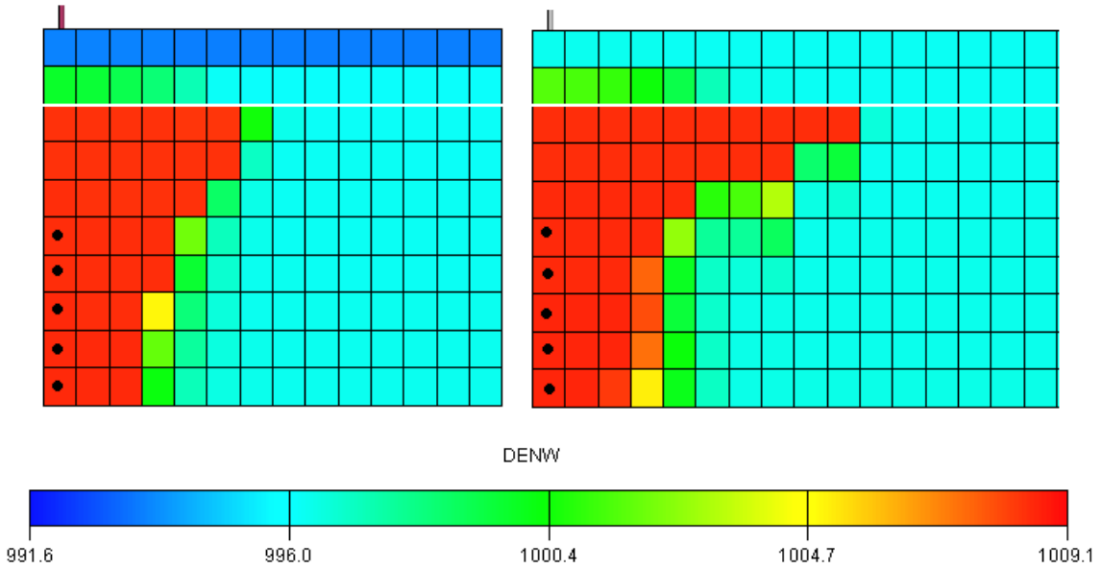

Figure 6.15: Density of aqueous phase left= after 10 years CO_2 injection, right= 240 years after termination of injection into fresh water

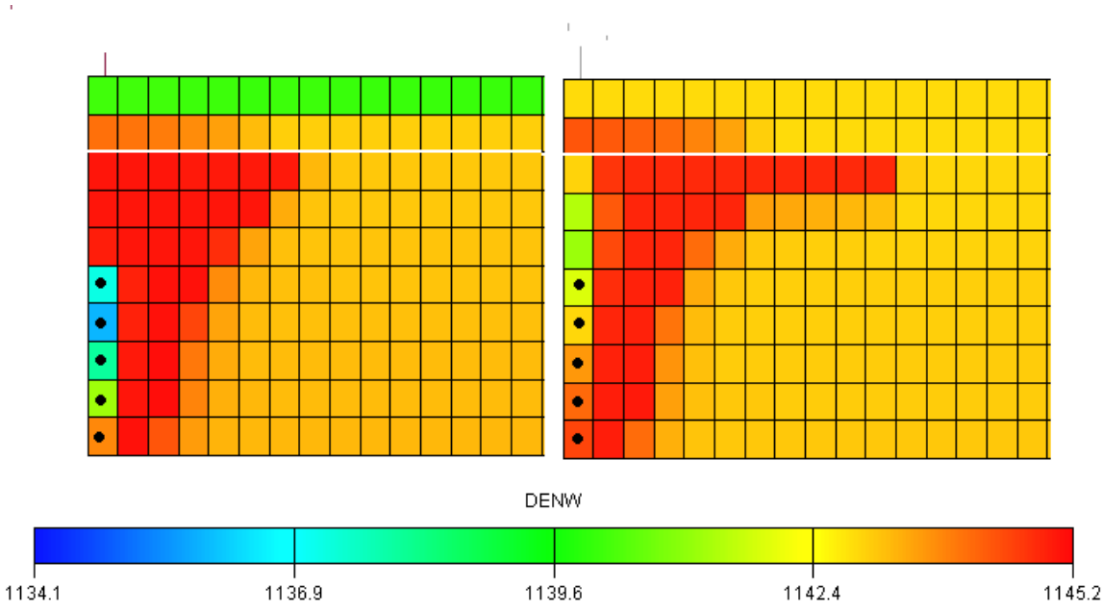

Figure 6.16: Density of aqueous phase left=after 10 years CO_2 injection, right=240 years after termination of injection into aquifer containing 200,000 ppm NaCl

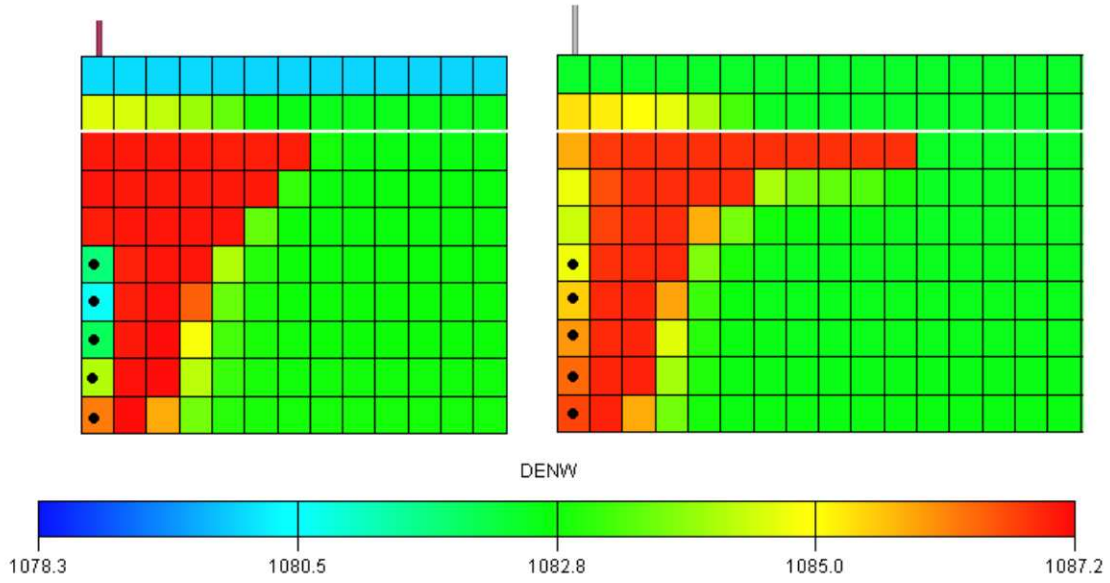

Figure 6.17: Density of aqueous phase left=after 10 years CO_2 injection, right=240 years after termination of injection into aquifer containing 200,000 ppm $CaCl_2$

As shown in the previous figures, the gas migrated 1200 m underneath the cap rock after 250 years. It can be concluded that there is a considerable contact area and time between the injected gas and cap rock. This enhances the risks CO_2 through cap rock in the long term.

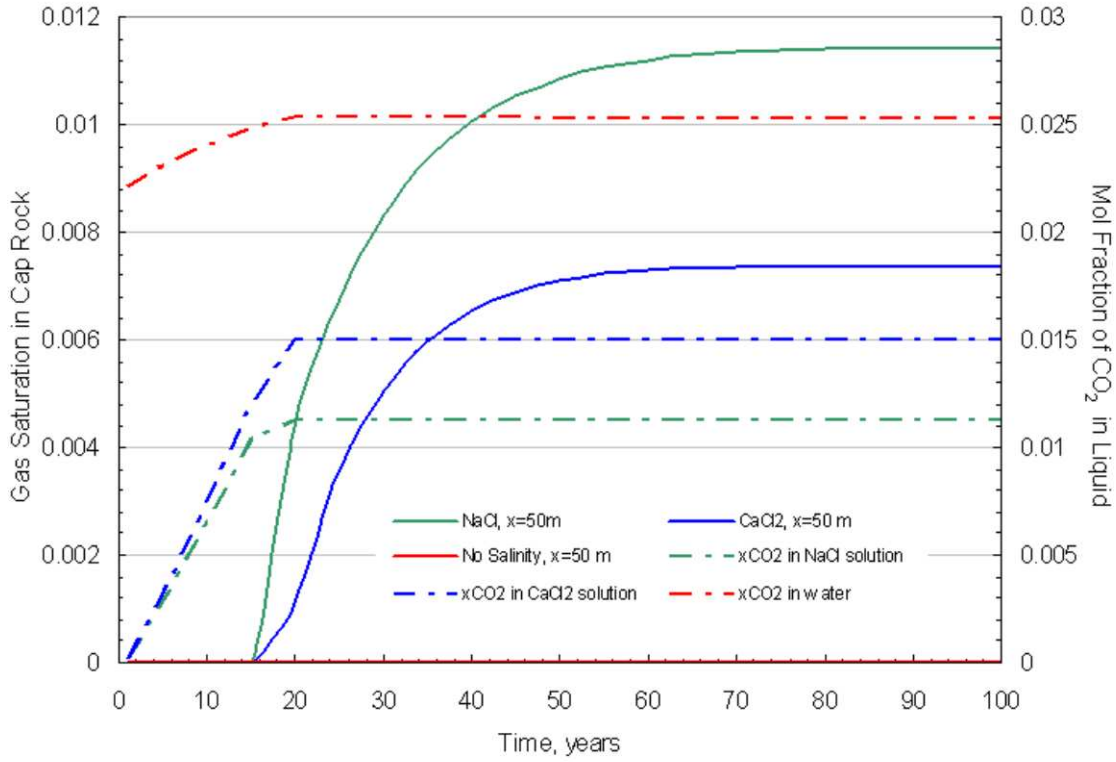

Figure 6.18: Gas saturation and solubility performance of CO_2 with time in cap rock formation, 2^{nd} layer with time

Figure 6.19 shows the gas saturation and solubility performance of CO_2 in the cap rock overtime. Gas appears in a dissolved form before it is evident as a gas phase. Figure 6.19 presents the gas saturation and solubility performance of CO_2 in fresh water and aqueous solutions in the cap rock at different distances from the injector. It can be concluded that even for the calculation of gas losses, brine composition must be accurately taken into account.

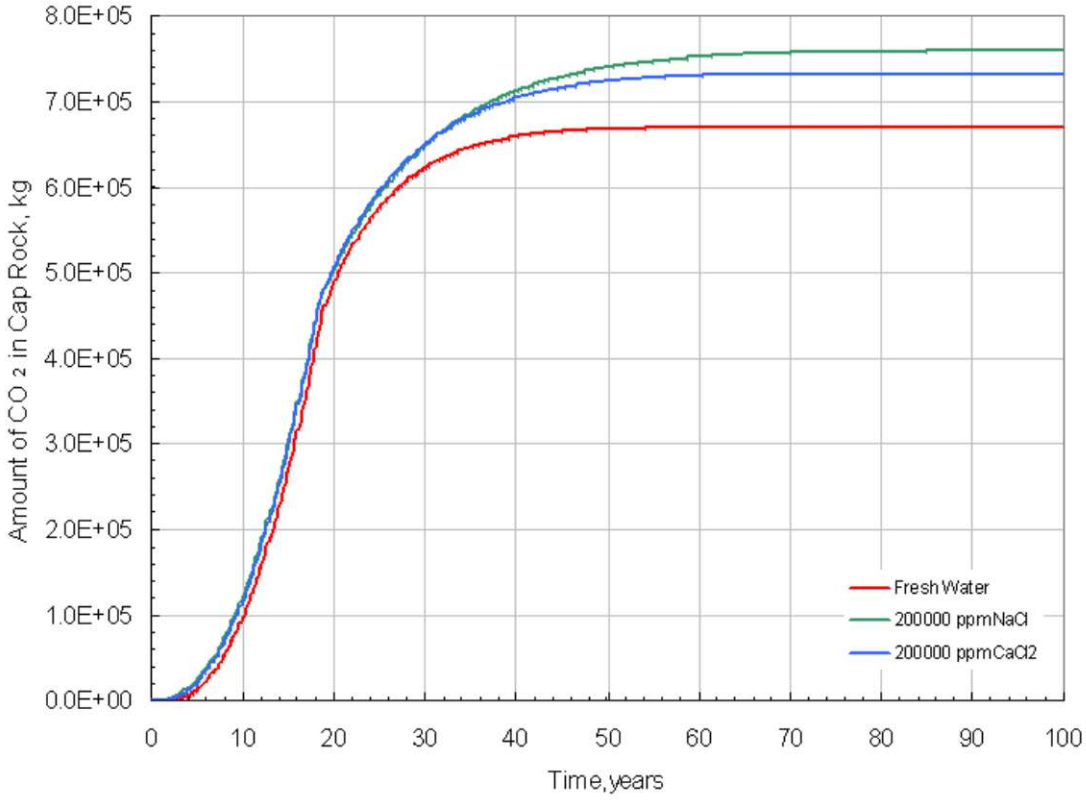

Figure 6.19: CO_2 (free gas and dissolved gas) influx from storage formation to cap rock in a 200,000 ppm NaCl (green line), 200,000 ppm $CaCl_2$ (blue line) and fresh water (red line) aquifers

It can be concluded that the risk of gas losses depend on salinity and brine composition. Therefore, the accurate modeling of pVT properties including salinity and composition effects is critical for the prediction of solubility trapping capacity of the aquifers.

6.2.2 Effect of k_v/k_h ratio

The migration of injected gas mainly depends on the permeability and the vertical to horizontal permeability ratio (k_v/k_h). The k_v/k_h ratio affects the distribution of CO_2 in the aquifer. Figure 6.20 shows that at low values of k_v/k_h, CO_2 tends to migrate laterally in the formation layers, whereas an increase in this ratio enhances the vertical migration

and CO_2 spreads out underneath the cap rock laterally (Figure 6.21). In order to visualize the effect of anisotropy, the gas distributions in the injection interval, between layers 6 and 10 are compared in the following gas saturation profiles (Figures 6.20- 6.23).

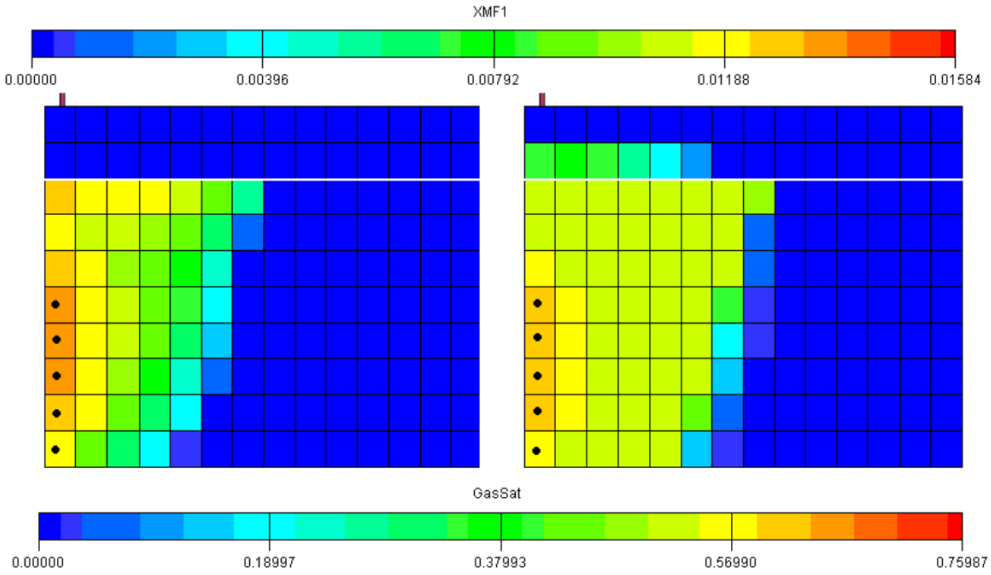

Figure 6.20: Gas saturation and mole fraction of CO_2 in saline aqueous phase, after 10 years injection into aquifer with ratio of k_v/k_h=0.01, left=saturation profile, right= mole fraction

The comparison of Figures 6.23 and 6.22 shows the situation at the end of injection (10 years) and 90 years later. The conversion of free gas into dissolved gas can be observed, as well as the migration of dissolved gas into the cap rock. The vertical migration is followed by lateral flow along the cap rock. The larger the k_v/k_h, the more extensive is the contact with the cap rock and tendency of leakage. In the case of lower k_v/k_h, the gas tends to move more uniformly in the lateral direction in the layer and thus reduces the risk of leakage but decreases the efficiency of solubility trapping.

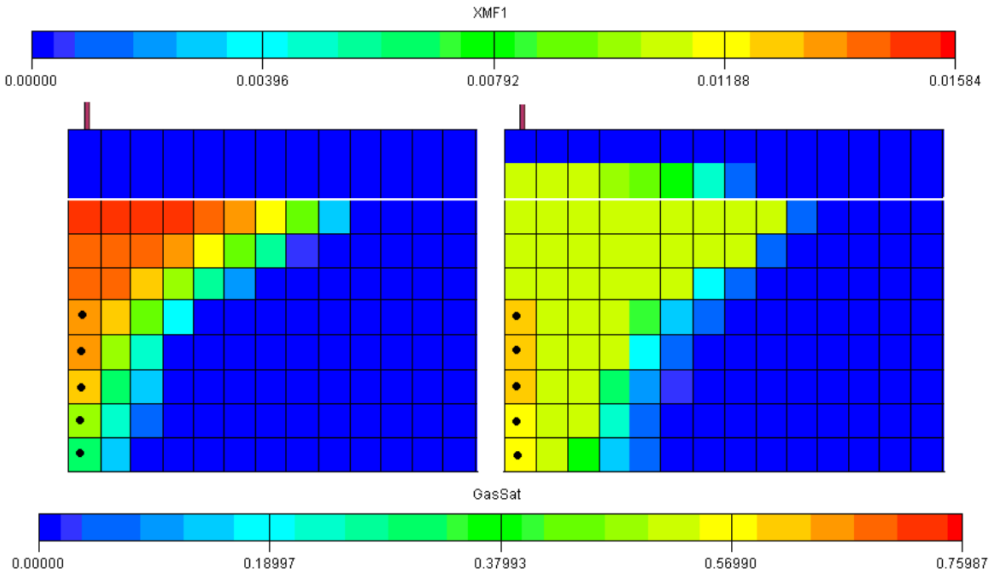

Figure 6.21: Gas saturation and mole fraction of CO_2 in saline aqueous phase, after 10 years injection into aquifer with ratio of k_v/k_h=0.1, left=saturation profile, right= mole fraction

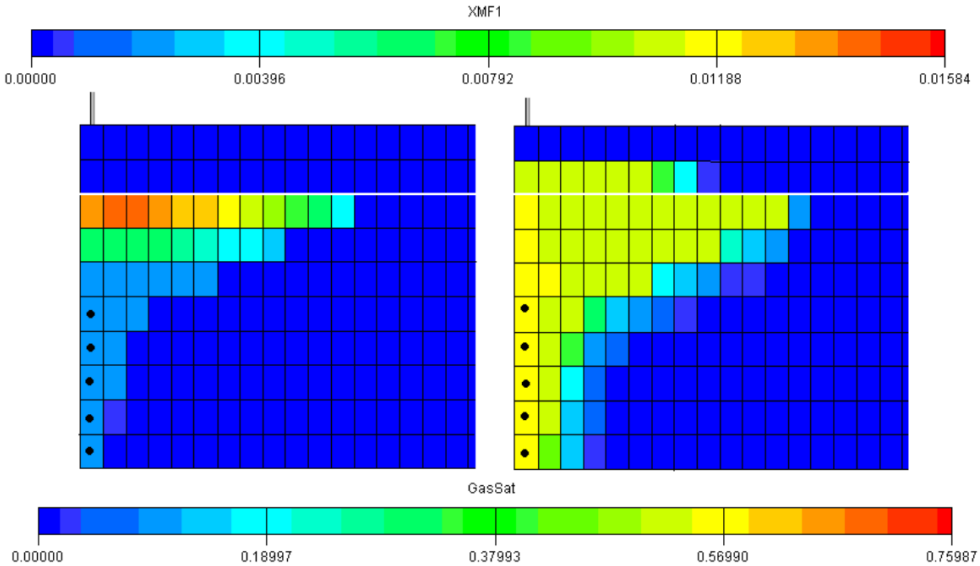

Figure 6.22: Gas saturation and mole fraction of CO_2 in saline aqueous phase, 90 years after termination of injection into aquifer with ratio of k_v/k_h=1, left=saturation profile, right= mole fraction

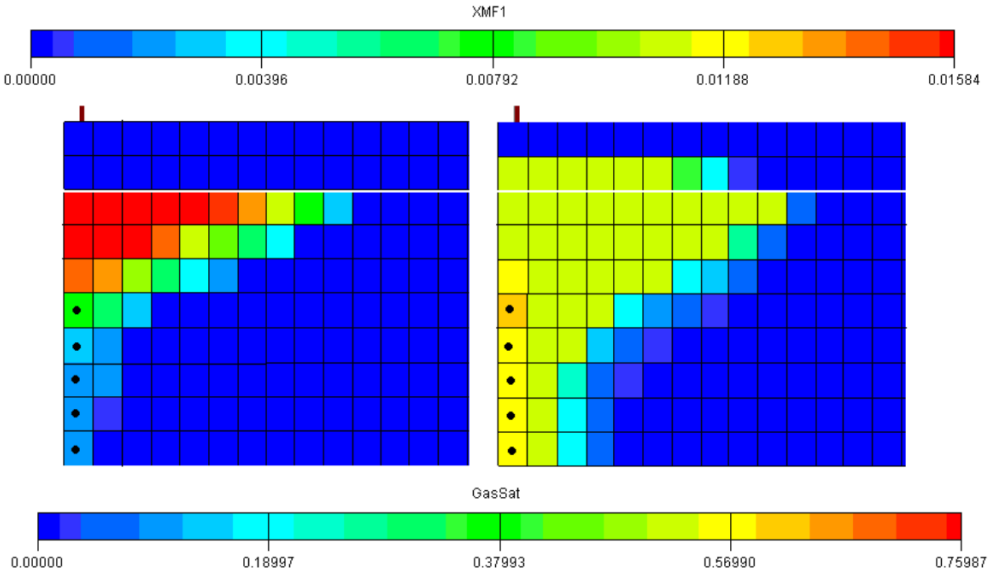

Figure 6.23: Gas saturation and mole fraction of CO_2 in saline aqueous phase, after 10 years injection into aquifer with ratio of k_v/k_h=1, left=saturation profile, right= mole fraction

6.2.3 Effect of Residual Phase Saturations

The reversible model which was derived from Corey relative permeability functions and Van Genuchten capillary pressure function was used in the simulation. Three cases are compared. The base case (Case 1) has a relatively large irreducible liquid saturation, and small critical gas saturation (S_{wi}=0.25, S_{gc}=0.1). In Case 2 only the critical gas saturation value was changed (S_{wi}=0.25, S_{gc}=0.3) and Case 3 has small residual water saturation and large critical gas saturation (S_{wi}=0.15, S_{gc}=0.3). The irreducible water and critical gas saturation parameters used in simulation is given in Table 6.3 and indicated in Figure 6.24.

Table 6.3: Residual phase saturations for the cases considered

	S_{wi}	S_{gc}
Case 1	0.25	0.1
Case 2	0.25	0.3
Case 3	0.15	0.3

Figure 6.25 shows the gas distribution in a 200,000 ppm NaCl aquifer in which the

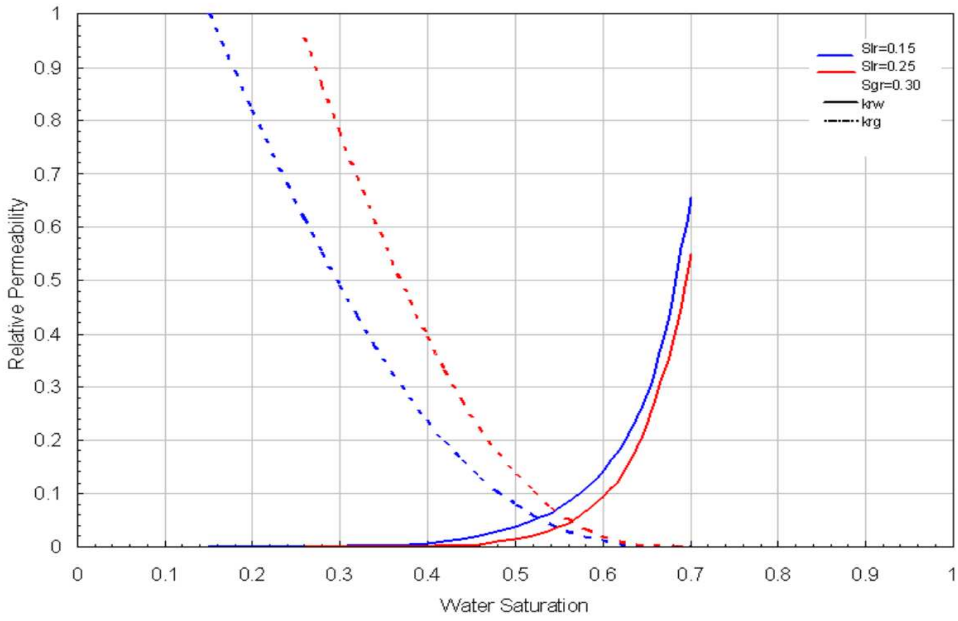

Figure 6.24: Relative permeability curves of assumed cases

irreducible water saturation is 0.25 and critical gas saturation is 0.3 (Case 2). This profile should be compared with Figure 6.4 of the base case (S_{wi}=0.25, S_{gc}=0.1). For small critical gas saturation during the injection period, CO_2 mostly migrates as a gas phase. This increases the contact between CO_2 and brine, and thus enhances the dissolution of CO_2. The effect of increasing the critical gas saturation is that the gas can be more effectively trapped as residual gas with reduced solubilization into the aquifer brine (Figure 6.26).

The effect of decreasing irreducible water saturation was also studied. Figure 6.28 shows the gas saturation and solubility of CO_2 after 100 years in the saline aquifer with S_{wi}=0.15, S_{gc}=0.3 (Case 3). Comparing Figure 6.25 and 6.28, it can be concluded that increasing the irreducible water saturation is beneficial in terms of ultimate storage capacity of the aquifer. As the gas is being injected it displaces the water through immiscible displacement in the top layer and occupies its place. However, a residual amount of water saturation remains. This water is in direct contact with gas and is in equilibrium with gas at that pressure

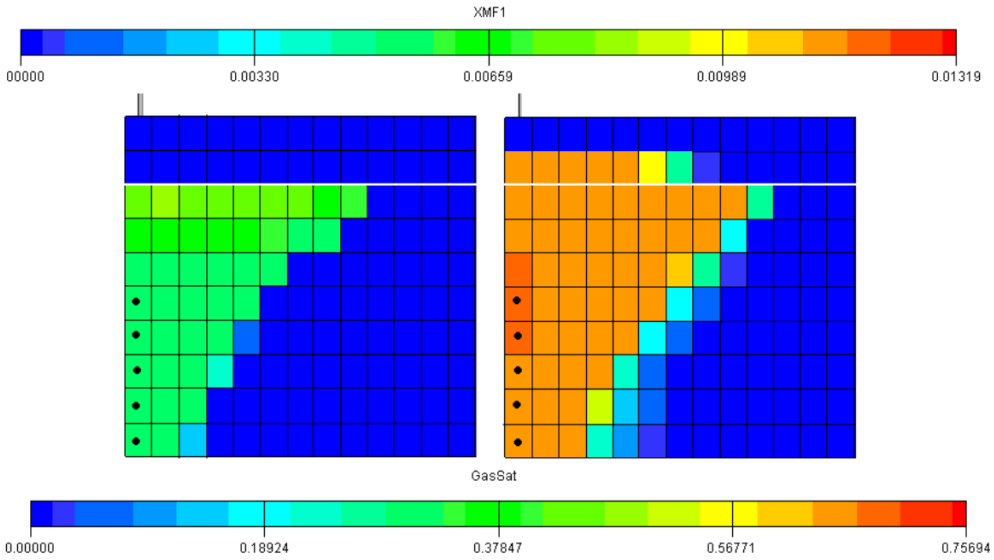

Figure 6.25: Gas saturation and mole fraction of CO_2 in saline aqueous phase 90 years after termination of injection ($S_{wi} = 0.25$, $S_{gc} = 0.3$) left=saturation profile, right= mole fraction

and temperature. The concentration of CO_2 in the residual water in this region is the maximum throughout the aquifer. Therefore, an increase in the residual water saturation is advantageous for dissolving larger quantities of gas within the gas plume (Figure 6.27). This two-phase region extends about 1 km beyond the gas bubble in the storage formation.

Solubility trapping is a major mechanism in geologic storage of CO_2. In this section, it has been demonstrated that solubility trapping is strongly dependent on the following issues.

- Brine salinity and composition
- Density differences between injected gas and formation water
- Permeability anisotropy
- Critical gas saturations/irreducible gas saturations

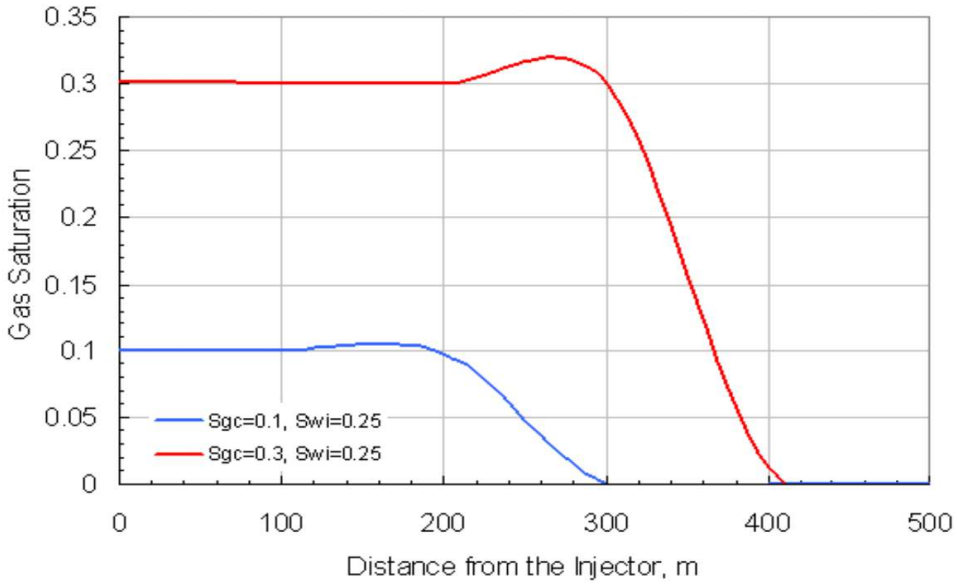

Figure 6.26: Gas saturation profile of CO_2 in the 6^{th} layer 90 years after termination of injection; comparison of different critical gas saturations ($S_{wi} = 0.25$, $S_{gc} = 0.1$ and 0.3)

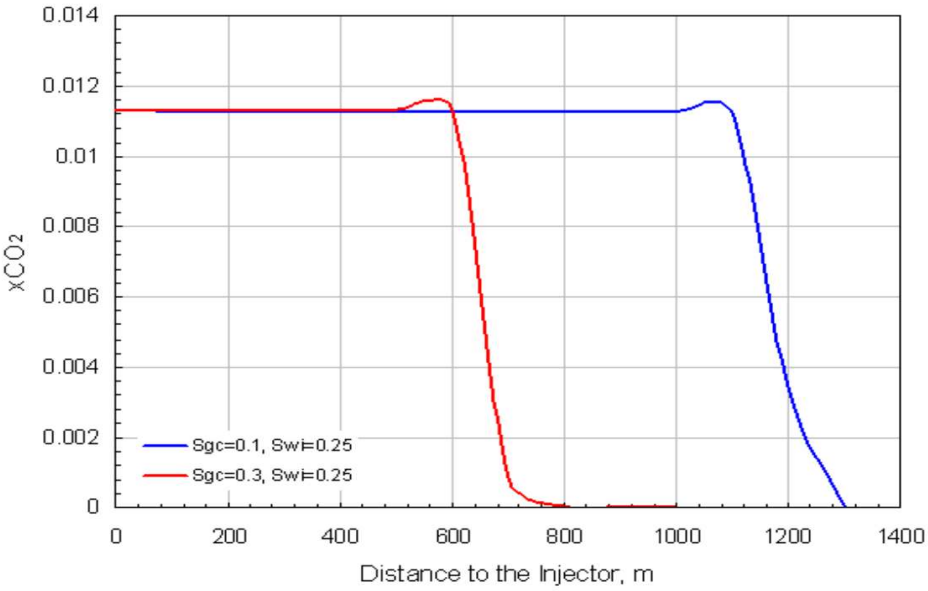

Figure 6.27: Solubility profile of CO_2 in the 3^{rd} layer of saline aquifer 90 years after termination of injection; comparison of different critical gas saturations (S_{wi}=0.25, S_{gc}=0.1 and 0.3)

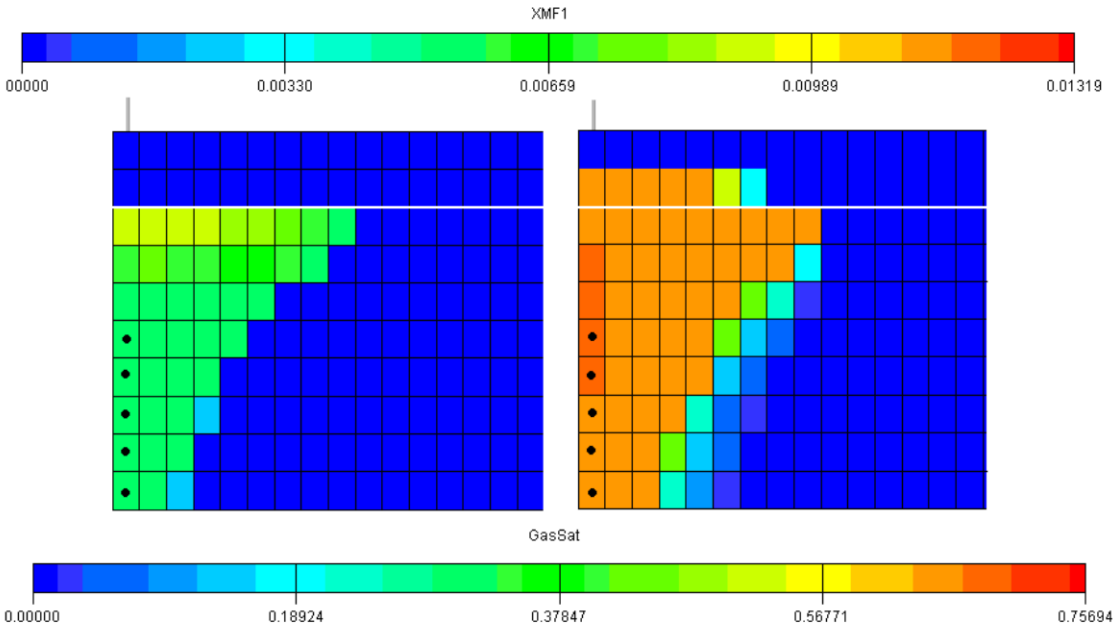

Figure 6.28: Gas saturation and mole fraction of CO_2 in saline aqueous phase 90 years after termination of injection (S_{wi}=0.15, S_{gc}=0.3) left=saturation profile, right= mole fraction

6.3 Capillary Trapping

The risk of CO_2 leakage into the atmosphere through faults, cap rock formations or wellbore must be evaluated for the long term safety of storage. For CO_2 sequestration in a saline aquifer capillary trapping of CO_2 is one of the essential mechanisms controlling the upward and lateral migration of CO_2 plumes after injection. Assessment of CO_2 immobilization requires accurate modeling of multi phase flow performance.

The relative permeabilities of brine and CO_2 are taken from Bennion and Bachu (2005) experimental data [6]. The drainage capillary pressure curve was calculated with van Genuchten correlation. These petrophysical properties are illustrated in Figure 6.29 and 6.30.

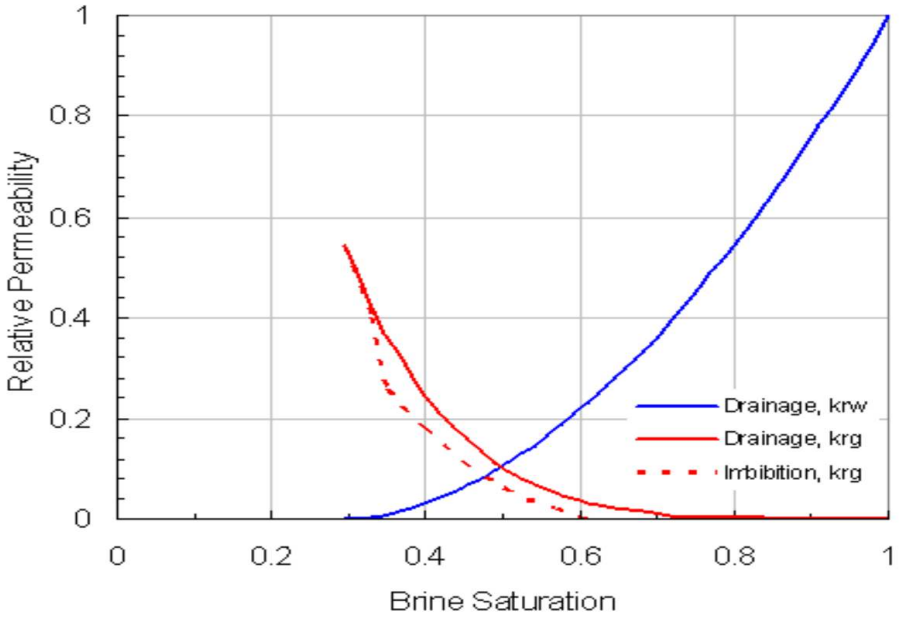

Figure 6.29: Relative permeability and capillary pressure curves used in simulations, taken from Bennion and Bachu (2005)[6], relative permeability to gas for the imbibition direction calculated from Land equation [33]

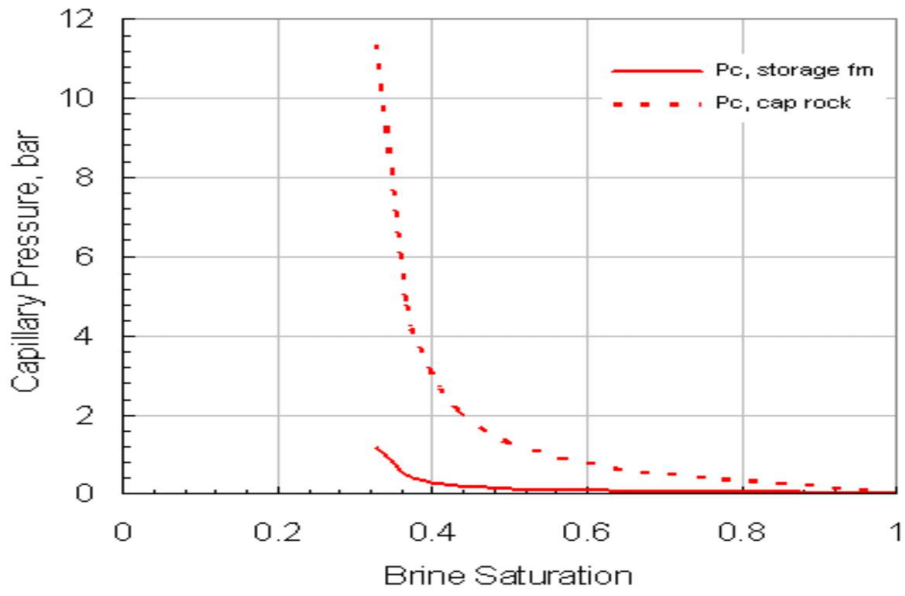

Figure 6.30: Capillary pressure calculated with Van Genuchten correlation, the saturation data taken from Bennion and Bachu (2005) [6]

6.3.1 Effect of Relative Permeability Hysteresis

The formation is initially filled with brine and CO_2 injection is controlled by rate and at 300 bar flowing pressure. CO_2 was injected into a 200,000 ppm NaCl containing saline aquifer for 10 years with a maximum rate of 100,000 sm^3/d, and the results were taken after 500 years. Figures 6.31 and 6.32 shows the gas saturation profile in a X-Z cross section through the injector after 10 years and 500 years respectively for an observation cross section (1, 15, 1-10).

It can be seen from Figure 6.31 that during the injection phase the hysteresis phenomena has no impact on the simulation of CO_2 injection. Also the solubility profiles for cases with and without hysteresis effect are the same.

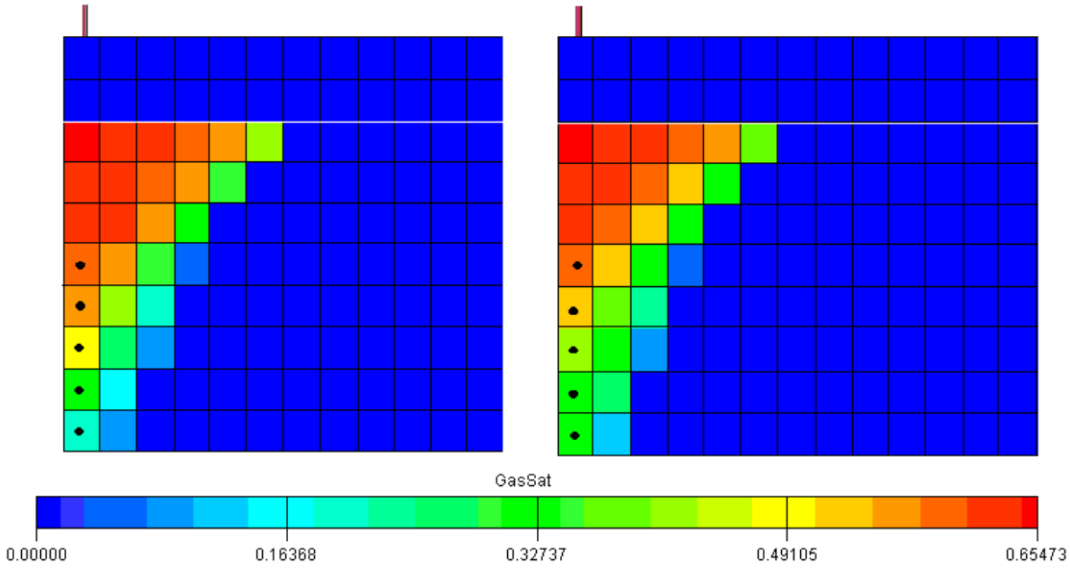

Figure 6.31: Gas saturation profile of CO_2 after 10 years of injection into saline aquifer left=saturation profile with neglecting hysteresis effect, right= saturation profile with considering hysteresis effects

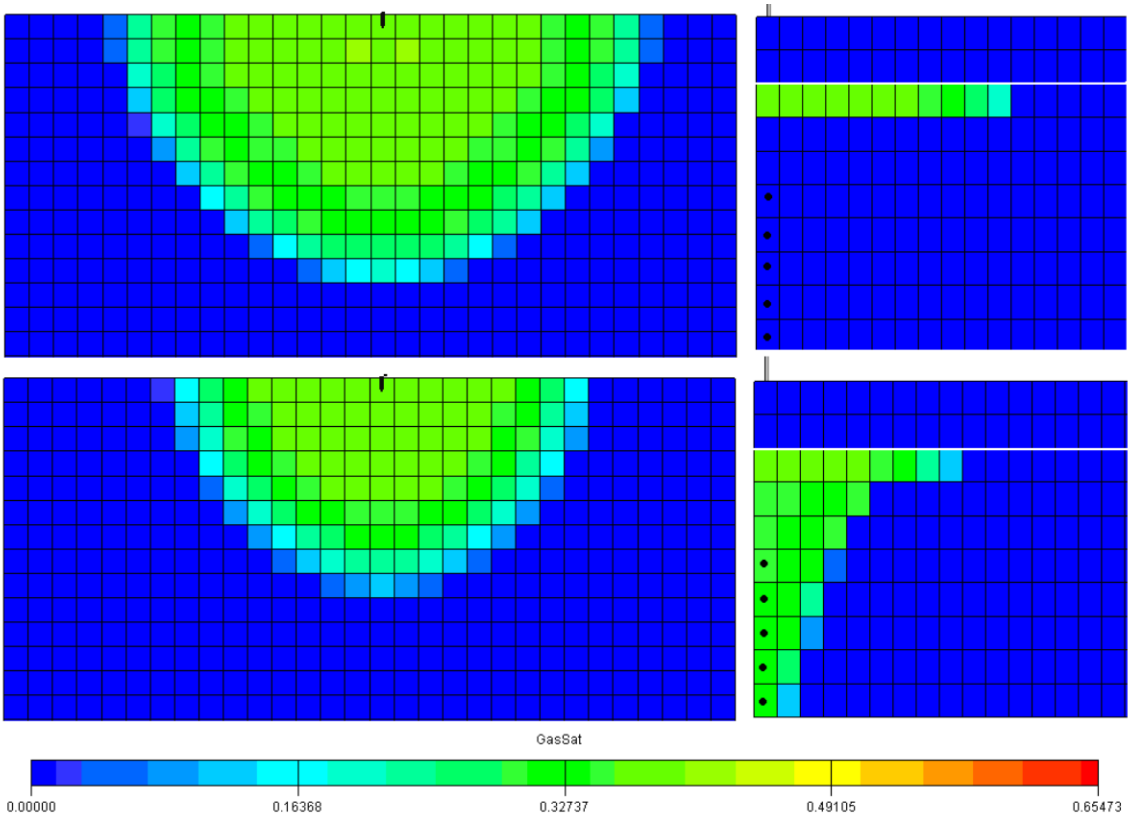

Figure 6.32: Gas saturation profile of CO_2 in 3^{rd} layer (top of the storage formation) and observation cross-section (1, 15) after 500 years; left=areal saturation profile with neglecting hysteresis (top) and with considering hysteresis effects (bottom), right= vertical saturation profile without and with hysteresis effects

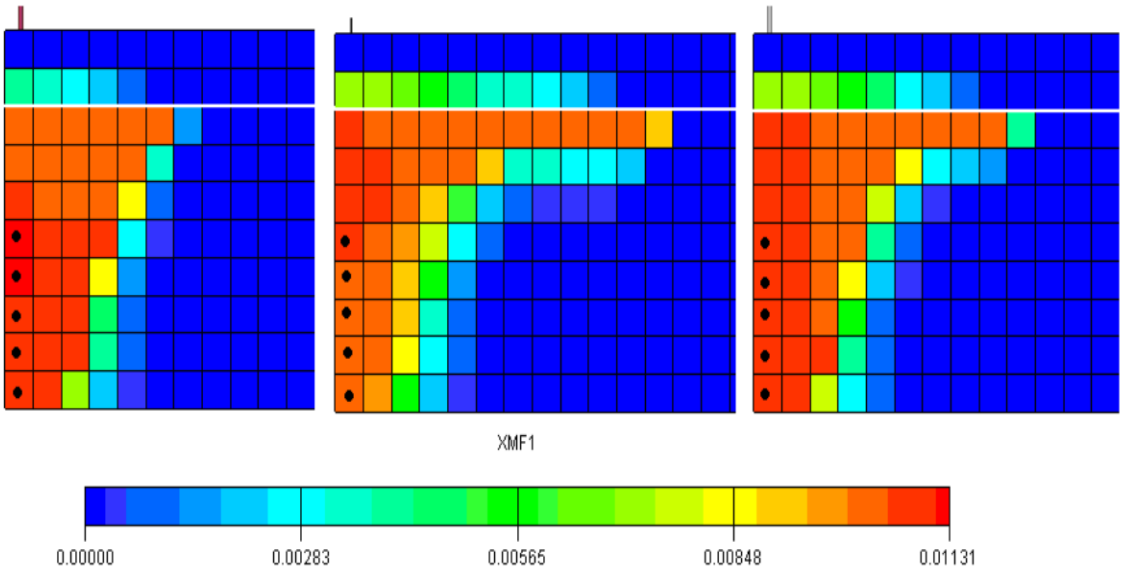

Figure 6.33: Solubility profiles of CO_2 in saline aquifer in observation cross-section (1, 15) after 10 years (left) and 500 years neglecting hysteresis effects (center) and 500 years with considering hysteresis effect (right)

Once the injection ceases, the CO_2 plume continue migrating upward due to buoyancy forces and laterally due to diffusion forces (Figure 6.33). However, in the case where trapping of gas occurs (Figure 6.32) the areal extension of the gas plume is reduced and gives less contact with overburden. Figure 6.34 indicates the gas saturation performance with time in the observation grid block (2, 15, 1), which is just below the caprock and 100 meter away from the injector. When the effect of capillary pressure and hysteresis are neglected, the saturation reaches a constant value of 0.7 corresponding to the irreducible water saturation (1-S_{wir}). When the effect of capillary pressure is taken into account but the effect of hysteresis is neglected, first the saturation of CO_2 increases, then decreases while the CO_2 migrates through neighboring blocks without leaving any residual gas (Figure 6.32, top). Considering hysteresis effects means that, during the injection the gas plume is draining. After termination of injection, the upper part of the gas plume is draining the water, but the lower part is displaced by water (imbibition). This can be seen in the saturation profile in Figure 6.32 and by the red curve in Figure 6.34. When the gas spreads out, the saturation decreases. At late times, in Figure 6.34 (red curve), the saturation becomes constant due to the trapping of gas.

Figure 6.35 indicates the gas saturation performance in the 6^{th} layer, which corresponds to the top of perforation into which CO_2 is injected. It can be observed that neglecting hysteresis effects, the plume migrates to the top of the storage formation and a very small amount of gas is trapped near the well. However, when hysteresis effects are accounted for the injected gas becomes partly trapped in the vicinity of the well and gas saturation remains constant. The entrapment of gas near the well may be problematic since CO_2 could leak through a potentially damaged injection well.

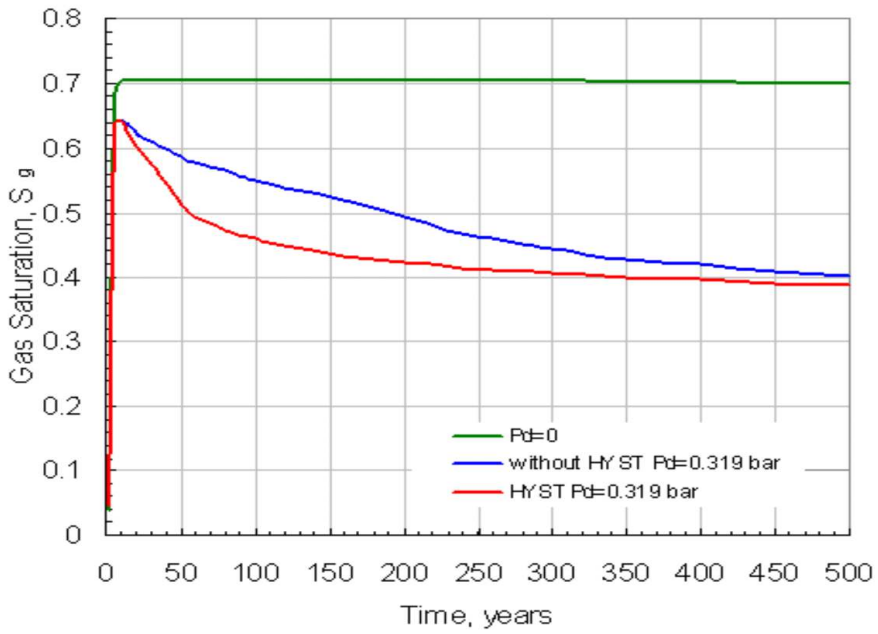

Figure 6.34: Gas saturation performance in the observation grid block (2 15, 1) without capillary and hysteresis effects (green), with capillary effects and neglecting hysteresis (blue) and including capillary and hysteresis effects (red)

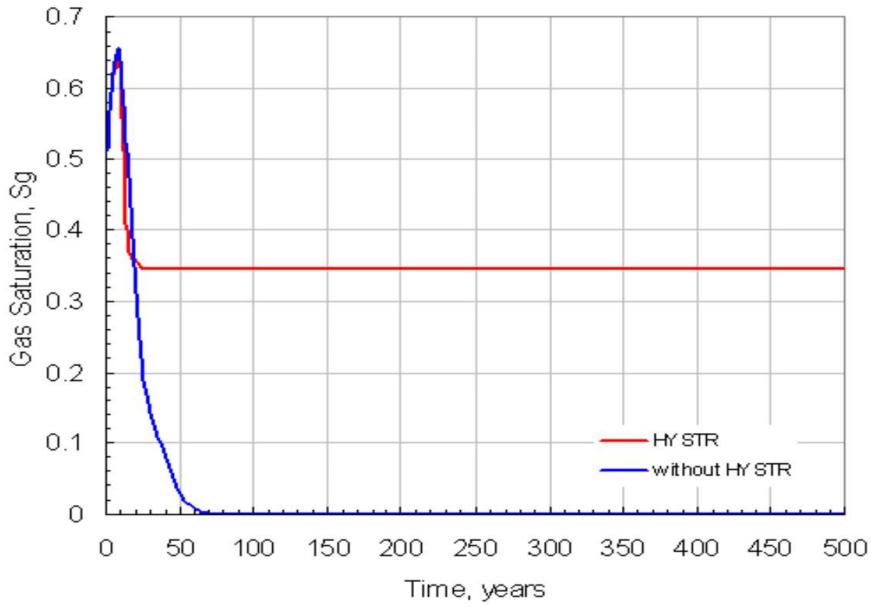

Figure 6.35: Gas saturation performance in the grid block (2 15, 6) for cases neglecting hysteresis effect (blue line) and considering hysteresis effect (red line)

Figure 6.36 shows a comparison of free and dissolved gas volume in the storage formation for cases without hysteresis and those with hysteresis effects. It can be seen that in Figure 6.36 when the hysteresis effects are taken into account more gas can be trapped as free gas (solid lines). The dashed line shows the volume of dissolved gas compared to the injected CO_2 volume.

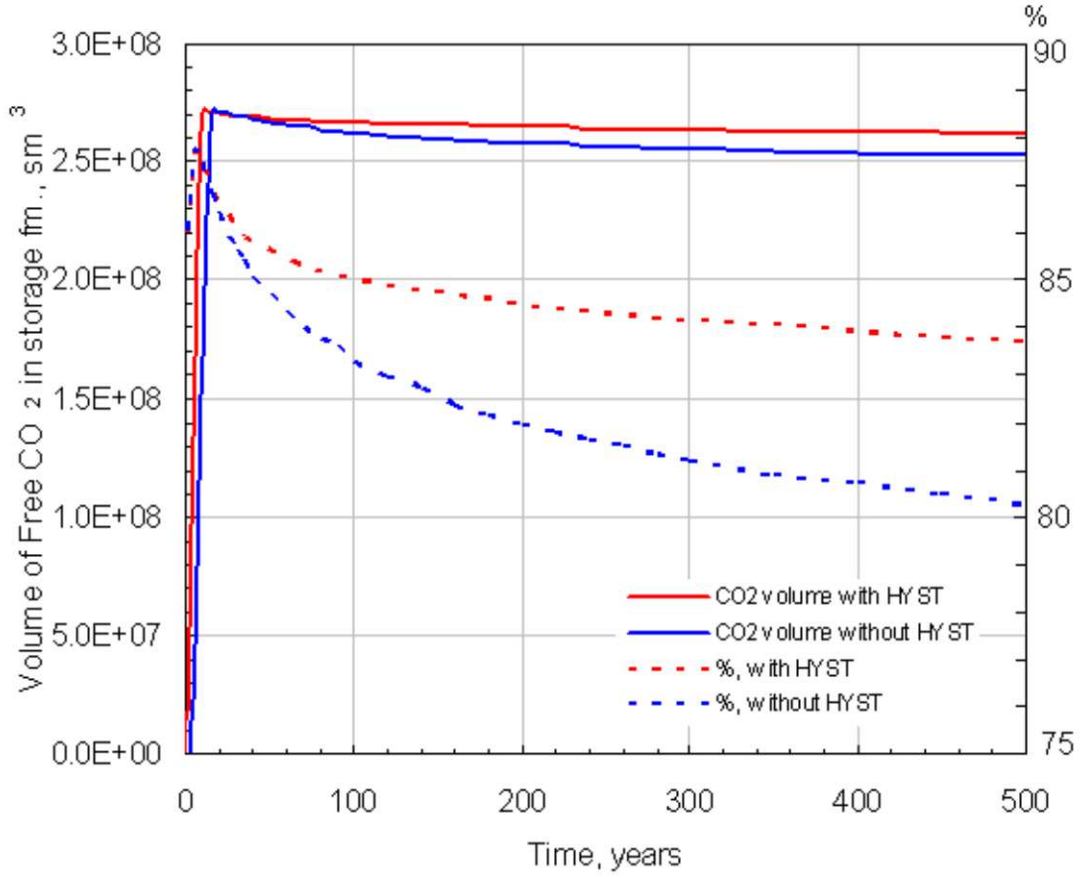

Figure 6.36: Free gas volume, and free gas volume compared to total injected CO_2 volume neglecting hysteresis effect (blue line) and considering hysteresis effect (red line) in the storage formation

However, the dissolution rates of CO_2 in models neglecting hysteresis effect are obviously larger than that of hysteresis models. The reason is related to the contact areas because

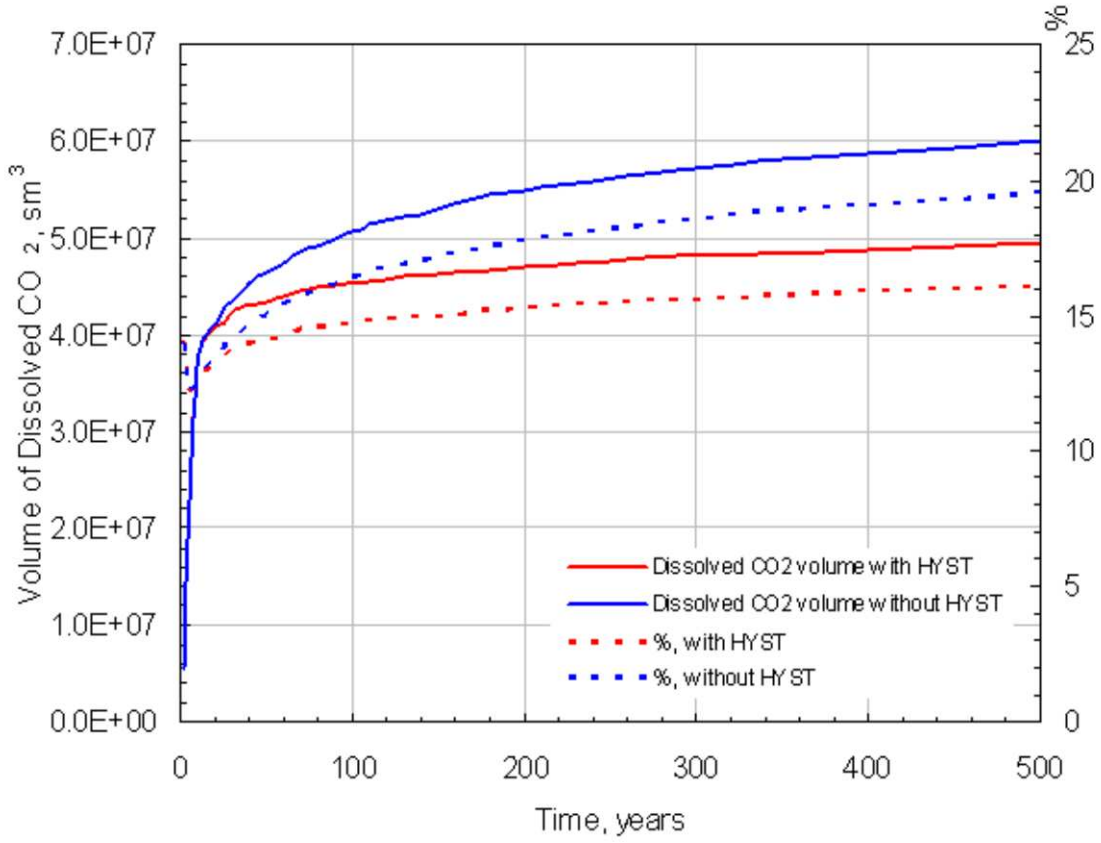

Figure 6.37: Dissolved gas volume and the dissolved gas volume compared to total injected CO_2 volume neglecting hysteresis effect (blue line) and considering hysteresis effect (red line) in the storage formation

the more free gas spreads out into the aquifer the contact areas for dissolution is increased. However, when CO_2 dissolves in brine, the density of brine increases and sinks to the bottom of the aquifer (Figure 6.15, 6.16, 6.17). The trapped gas in the vicinity of injection interval that comes in contact with already saturated brine and trapped CO_2 can not dissolve further in brine. In the non-hysteresis models, gas stays on the top of the formation, and has more contact with under-saturated brine. Hence more gas is dissolved as it shown in Figure 6.33 (center) and 6.37.

As a concluding remark on the importance of capillary trapping, sequestration of CO_2

in saline aquifer, capillary trapping remains one of the essential mechanisms controlling the upward and lateral migration of CO_2 plumes after injection. Trapping of CO_2 as residual gas may be advantageous in CO_2 sequestration projects, more gas is trapped thus becoming immobile. Entrapment of CO_2 occurs during the imbibition process as CO_2 is displaced upward. Residual gas is left behind and the free gas spreads out in the vicinity of the injection interval into the aquifer. This extents the lateral migration thereby enlarging the contact area with the aquifer brine which then improves local solubility. It can be concluded that the accurate modeling of multi phase flow behavior including capillary pressure and hysteresis effects is a requirement for the precise prediction of trapping capacity of aquifers as options for storage.

6.4 Aquifer Parameters

Many of the available data are site specific, and have to be adjusted to the geological model to simulate the CO_2 storage performance and assess the quantity of CO_2 that can be stored at the selected site. Sensitivity to the aquifer parameters, were performed by changing the aquifer properties, such as the aquifer thickness, permeability and shale layers within the storage formation. From the paper of Ulker and Pusch (2007) it is known that hysteresis is important for mechanical trapping as well as for solution trapping but for the sake of simplicity it was not used in this section.

6.4.1 Aquifer Volume

Thickness of the aquifer is of course, a certain value in the geological model. However, in order to determine the impact of the thickness on the storage capacity prediction, different assigned thickness in the range of 20 m to 120 m were studied.

Comparison of Figures 6.1 and 6.43 shows that a thicker aquifer is highly desirable, since more gas can be injected without extending the bottom hole pressure for a long time during

the injection (6.43). For the aquifer with 120 m thickness gas was injected with a maximum rate of 100,000 sm^3/d and 500,000 sm^3/d and injection was controlled with a bottom hole pressure of 300 bar. Consequently when the BHP exceeds 300 bar, the injection rate was reduced automatically. Figure 6.38 indicates the injection rate (bold line) and bottom hole pressure regarding to injection pressure(dashed line). Figure 6.43 depicts the cumulative injected CO_2 after 10 years into a 120 m 200,000 ppm saline aquifer. It can also be seen in Figure 6.4 at reduced thickness results in the fast migration of gas to the top of the storage, even when the CO_2 was injected into the lower part of the aquifer.

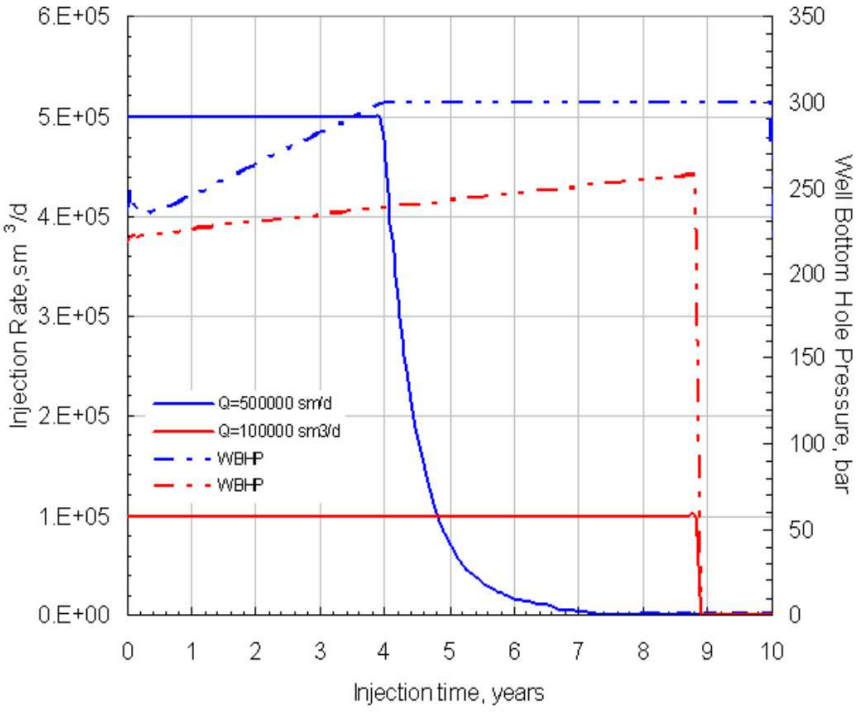

Figure 6.38: Gas injection rate and WBH pressure response

The thickness of the aquifer determines the rate of injection and thus the distribution of the gas in aquifer, the thickness of gas plume, as well as the rate of leakage through the cap rock (Figures 6.39 - 6.42).

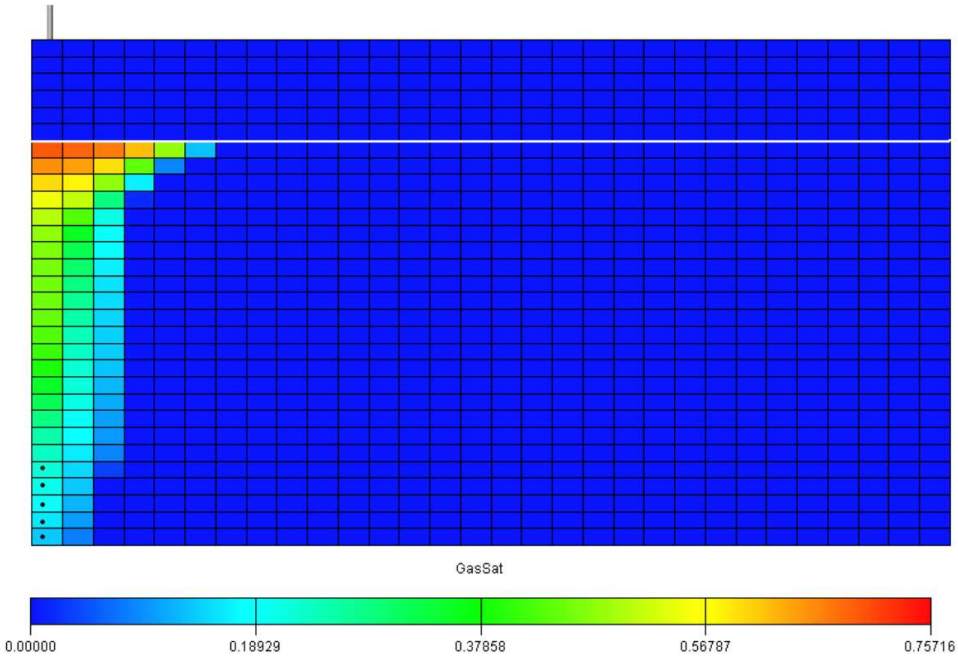

Figure 6.39: Gas saturation profile in 120 m thick aquifer after 10 years of injection with a rate of 100,000 sm^3/d

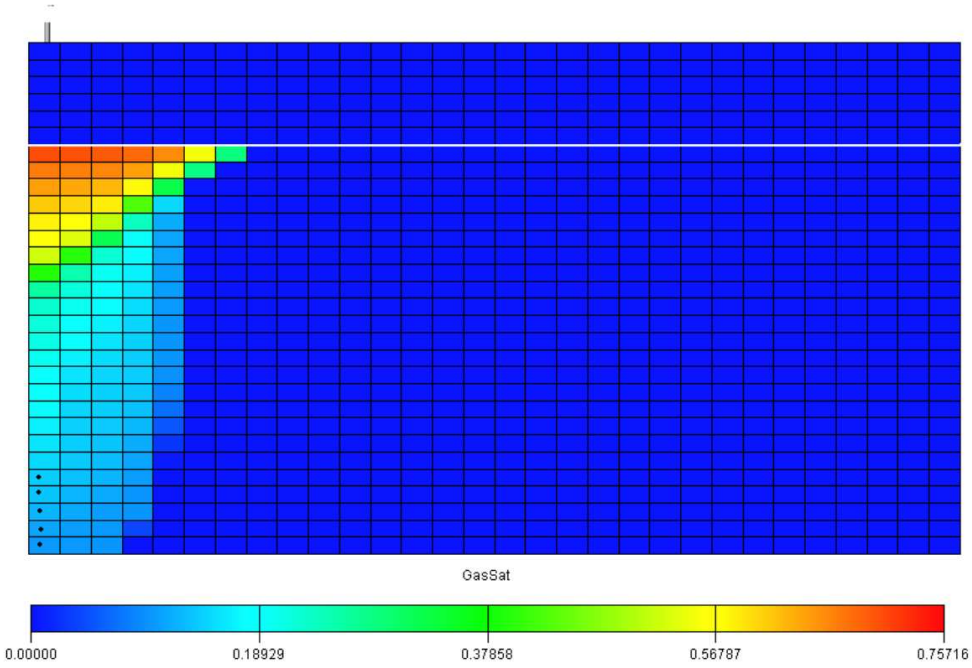

Figure 6.40: Gas saturation profile in 120 m thick aquifer after 10 years of injection with a rate of 500,000 sm^3/d

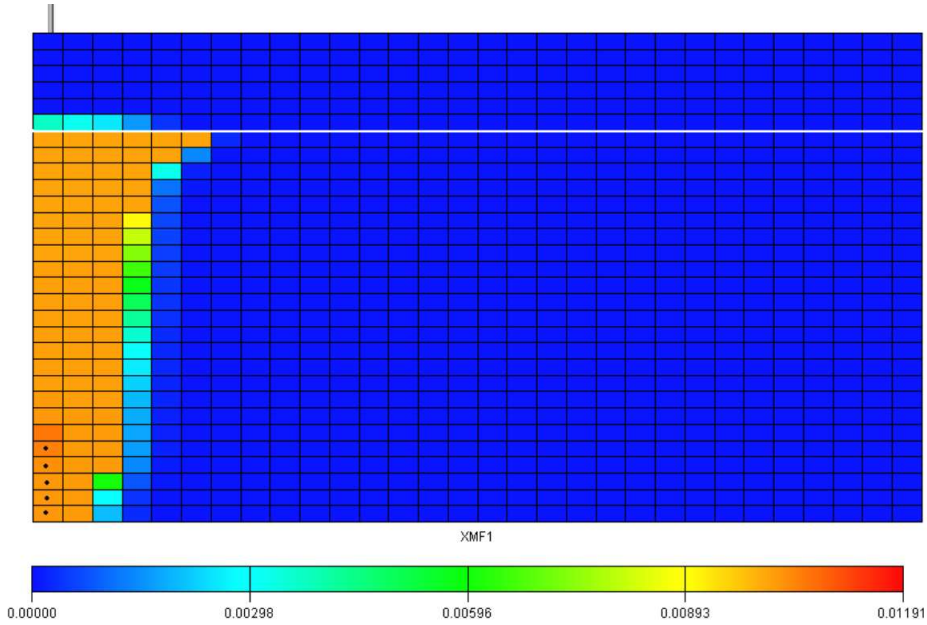

Figure 6.41: Gas mole fraction in 120 m thick aquifer after 10 years of injection with a rate of 100,000 sm^3/d

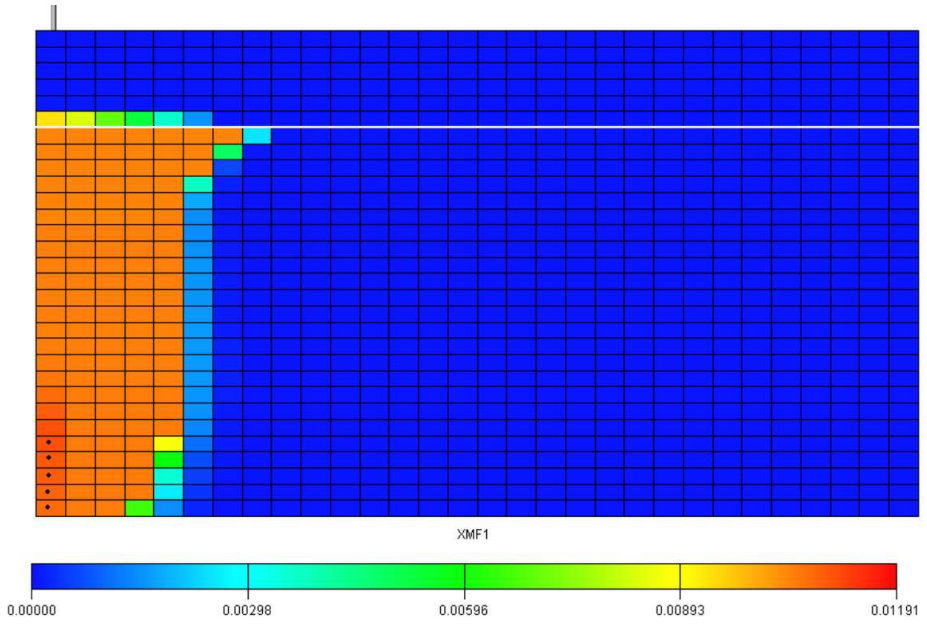

Figure 6.42: Gas mole fraction in 120 m thick aquifer after 10 years of injection with a rate of 500,000 sm^3/d

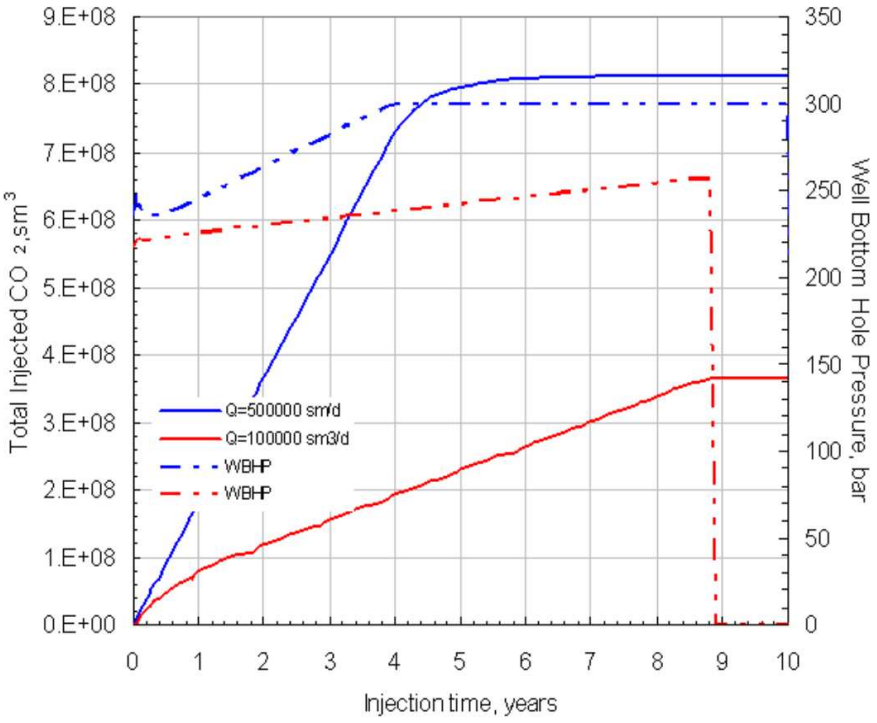

Figure 6.43: Gas injection history and WBH pressure response

6.4.2 Mean Permeability and Ratio of Vertical to Horizontal Permeability

Simulations were performed with different mean permeability values ranging 100 mD to 1000 mD which are the acceptable values for the sandstone formations. Figures 6.44 - 6.53 depicts the gas saturation and mole fraction at different times for different mean permeability.

It is expected that low permeability reduces gas injection. Gas injection rate remains a critical parameter for the economic feasibility of geologic sequestration projects. It can be seen from the following figures 6.44 - 6.50, that the mean permeability has a significant effect on the migration of the gas plume. In a higher permeability case, injected gas migrates rapidly to the top of the storage formation leading to an increase the contact between CO_2 and formation brine resulting in an increase in the dissolution of CO_2 (Figure 6.53).

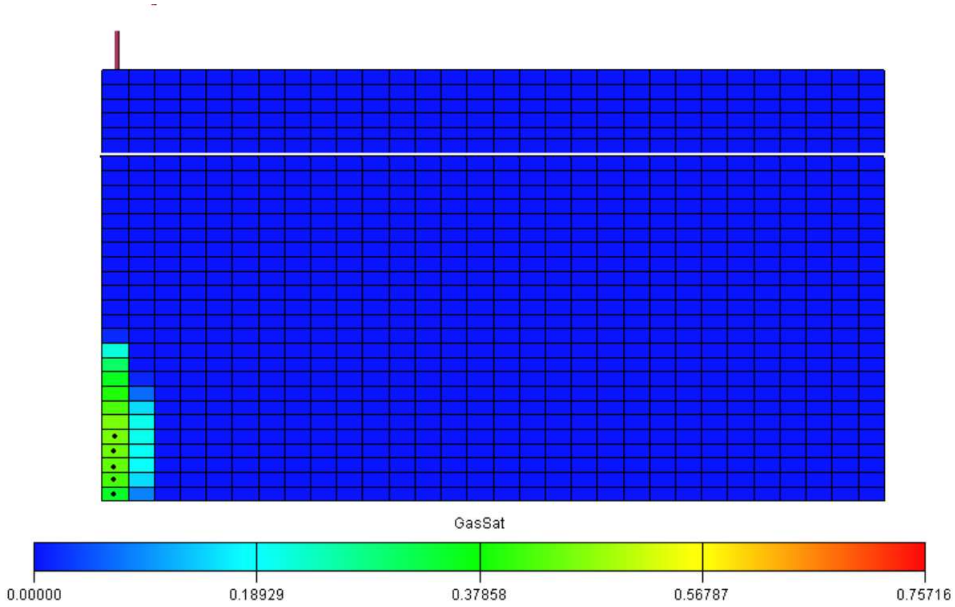

Figure 6.44: Gas saturation profile after 1 year injection of CO_2 into the storage formation with a mean permeability of 100 mD

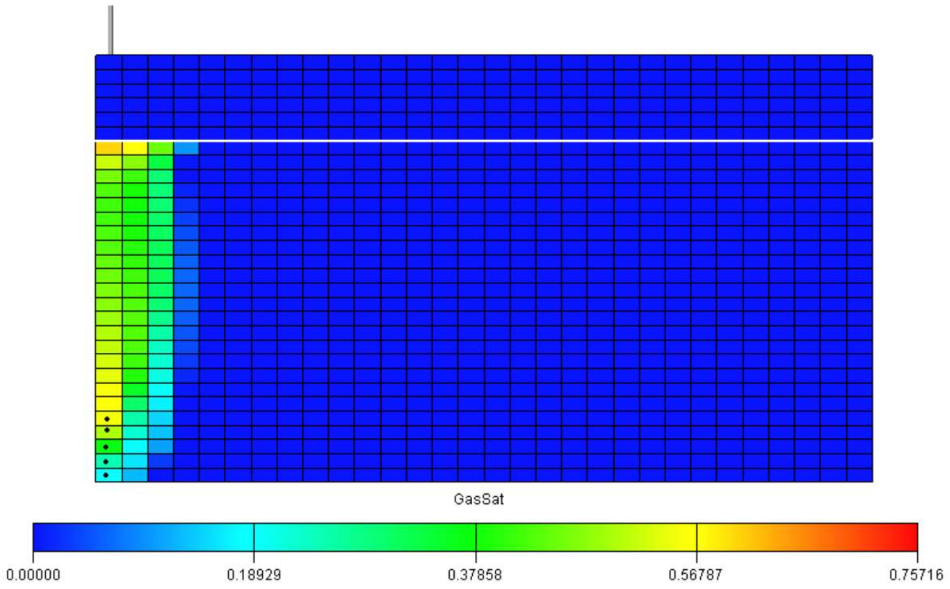

Figure 6.45: Gas saturation profile after 10 years injection of CO_2 into the storage formation with a mean permeability of 100 mD

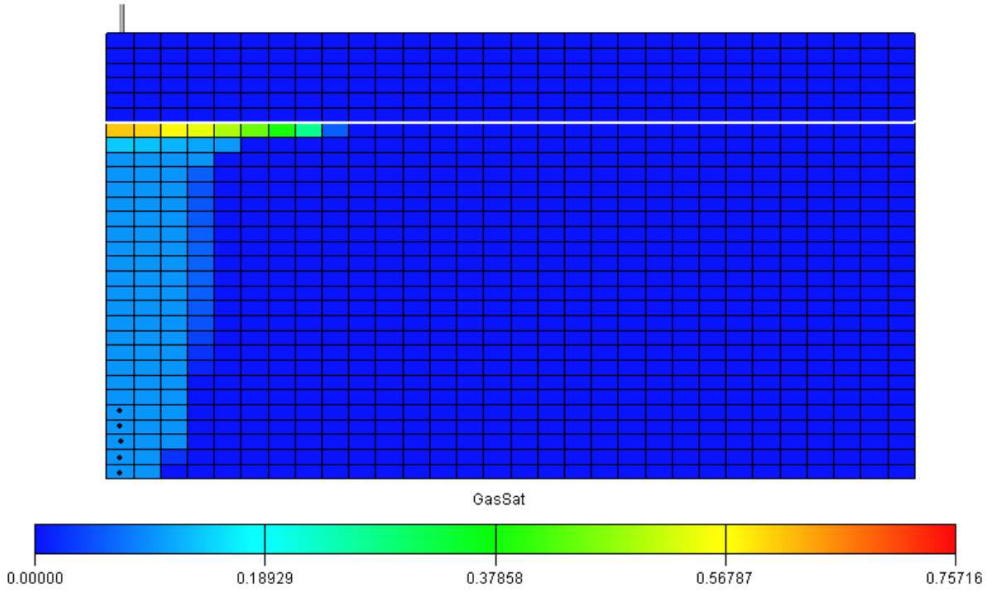

Figure 6.46: Gas saturation profile 90 years after termination of injection of CO_2 into the storage formation with a mean permeability of 100 mD

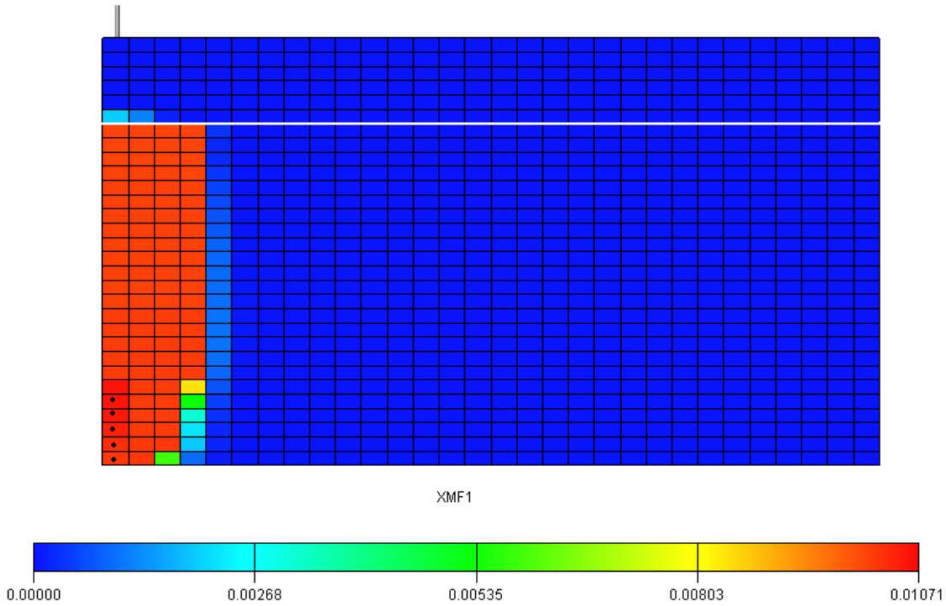

Figure 6.47: Mole fraction of CO_2 in the aqueous phase after 10 years injection of CO_2 into the storage formation with a mean permeability of 100 mD

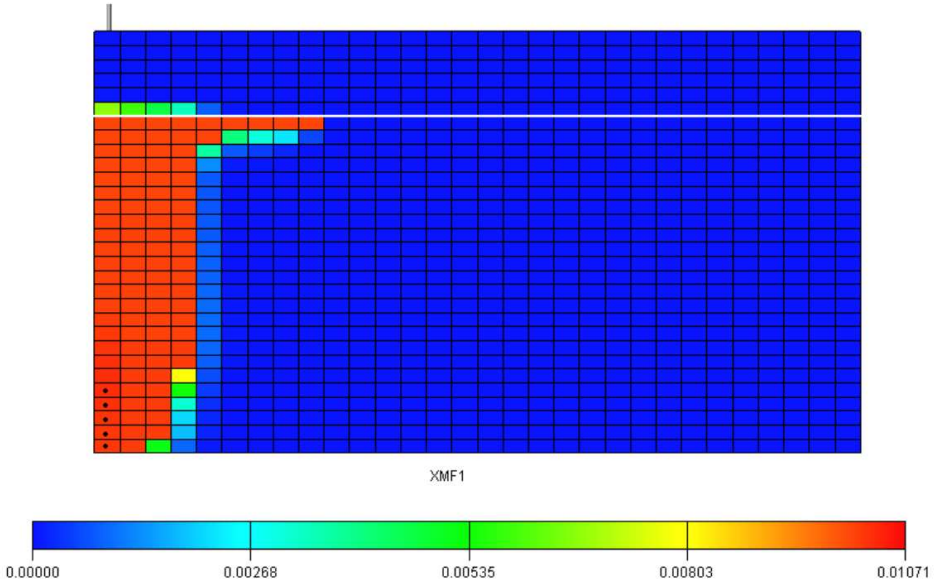

Figure 6.48: Mole fraction of CO_2 in the aqueous phase 90 years after termination of injection of CO_2 into the storage formation with a mean permeability of 100 mD

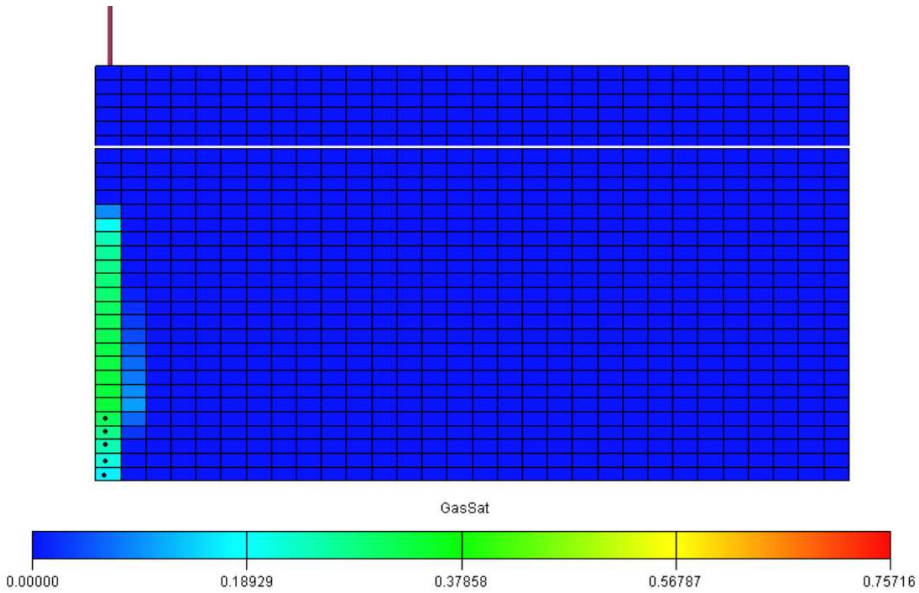

Figure 6.49: Gas saturation profile after 1 year injection of CO_2 into the storage formation with a mean permeability of 1000 mD

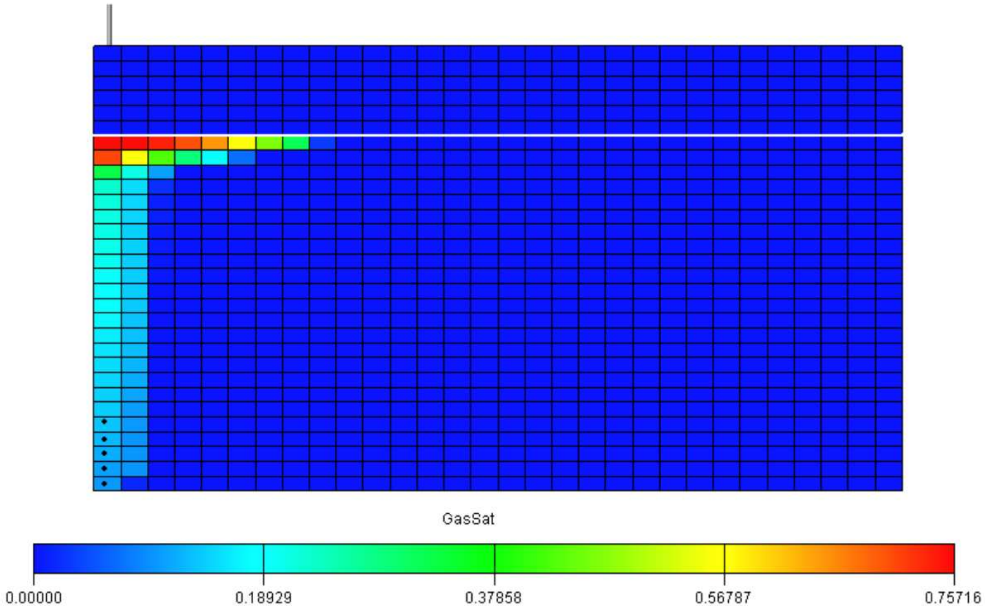

Figure 6.50: Gas saturation profile after 10 years injection of CO_2 into the storage formation with a mean permeability of 1000 mD

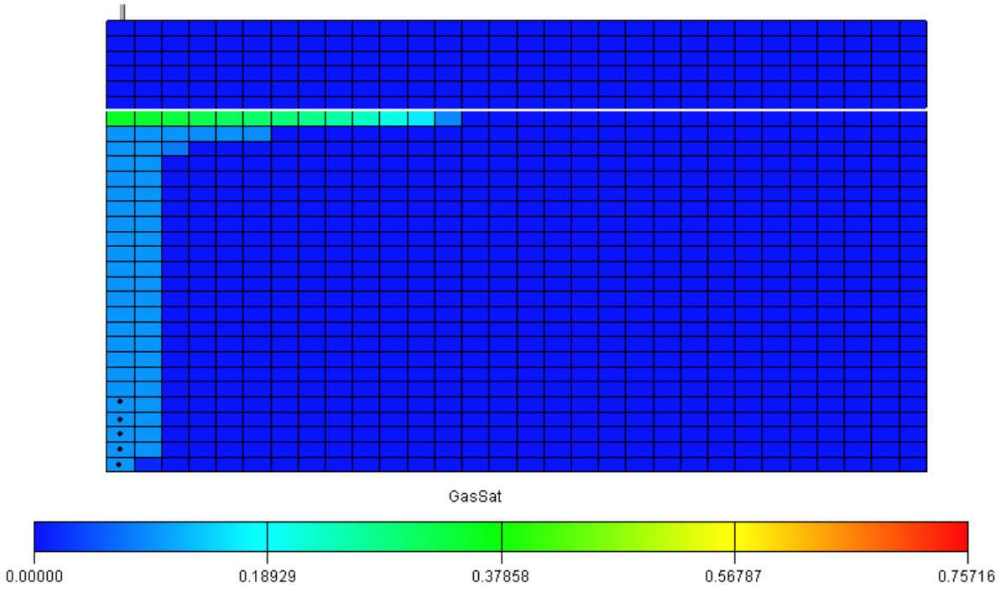

Figure 6.51: Gas saturation profile 90 years after termination of injection of CO_2 into the storage formation with a mean permeability of 1000 mD

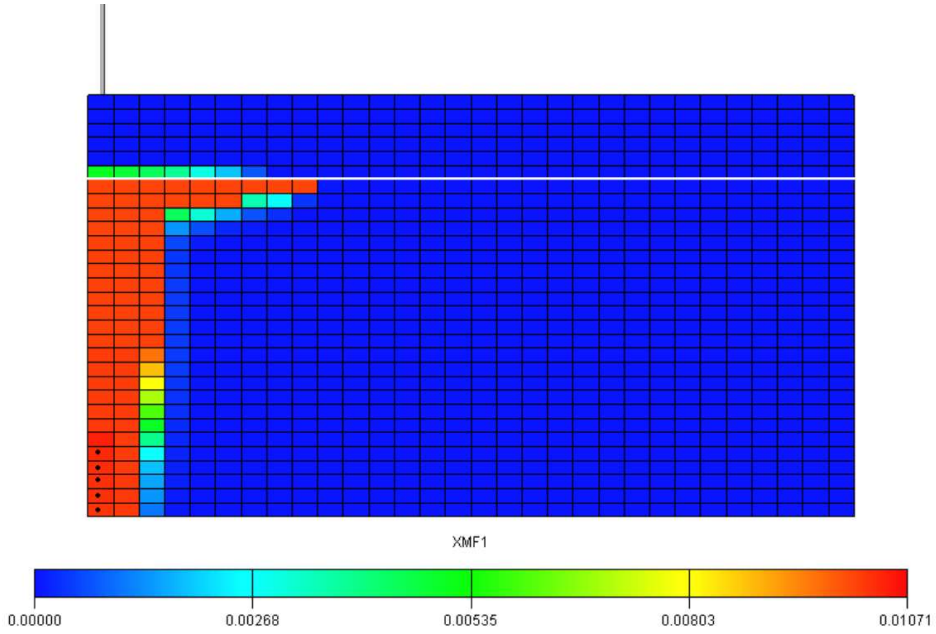

Figure 6.52: Mole fraction of CO_2 in the aqueous phase after 10 years injection of CO_2 into the storage formation with a mean permeability of 1000 mD

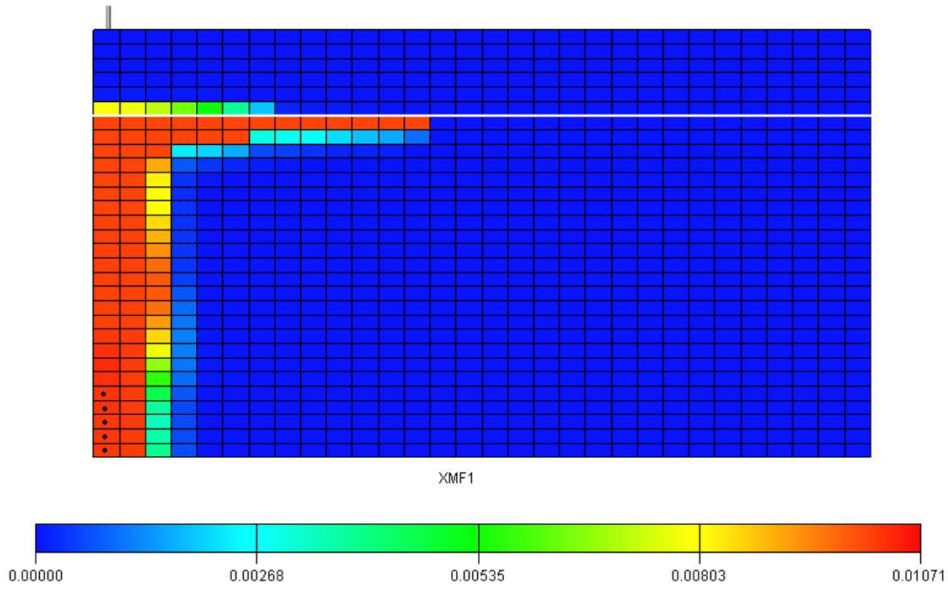

Figure 6.53: Mole fraction of CO_2 in the aqueous phase 90 years after termination of injection of CO_2 into the storage formation with a mean permeability of 1000 mD

k_v/k_h strongly affects the migration of the gas plume and volume flux. Simulations were performed for a k_v/k_h range 0.1 to 1. The standard value of 0.1 is used in this study as a base case. However, a wide range of values are possible for sensitivity investigations for the precise prediction of CO_2 storage capacity and selection of the best aquifer candidates for future storage projects.

In all cases either for smaller or higher k_v/k_h values, the injected gas tends to migrate up to the top of the storage formation due to the buoyancy forces. However, the k_v/k_h ratio controls the degree, how fast the injected gas flows laterally into the storage formation, and how far the gas plume extends underneath the cap rock. As expected, in higher vertical to horizontal permeability ratio the gas migrates rapidly to the top of the storage formation in comparison to cases with smaller ratio, leading to an increase in the contact between CO_2 and under-saturated formation brine thus increasing the dissolution of CO_2 in the aqueous phase. Lateral flow along the cap rock increases, the contact area with cap rock with a corresponding increase in the risk of leakage (Figure 6.54).

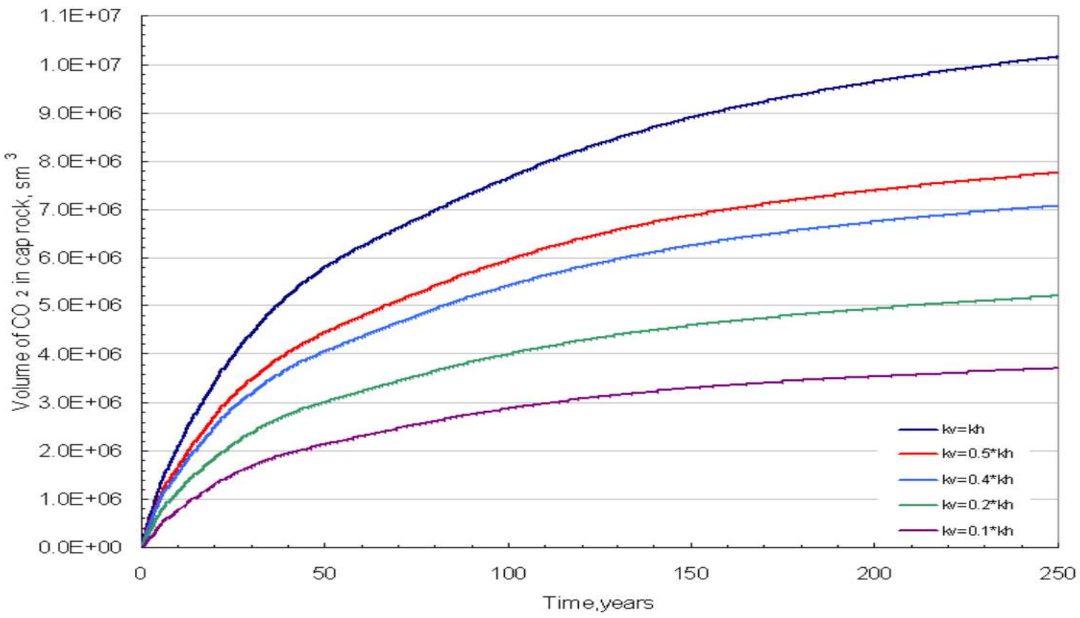

Figure 6.54: Gas volume in cap rock with different k_v/k_h

The findings of this work justifies the conclusions made by Ennis-King and Peterson [21], that a high k_v/k_h ratio is more beneficial for the long term storage of CO_2. This is because it encourages convective mixing.

6.4.3 Shale Layers within the Storage Formation

Reservoirs frequently contain shale layers within the sandstone formation. Shaly-siltstone fractions are also observed in Butsandstein aquifers which calls for the need to account for shaliness in the storage formation. The aquifer thickness is 100 m and for the five siltstone layers within the storage formation the permeability was reduced from 200 mD to 0.1 mD to investigate the impact of vertical barriers to upward migration of the gas plume. The injection well was perforated in the intervals between these shale layers.

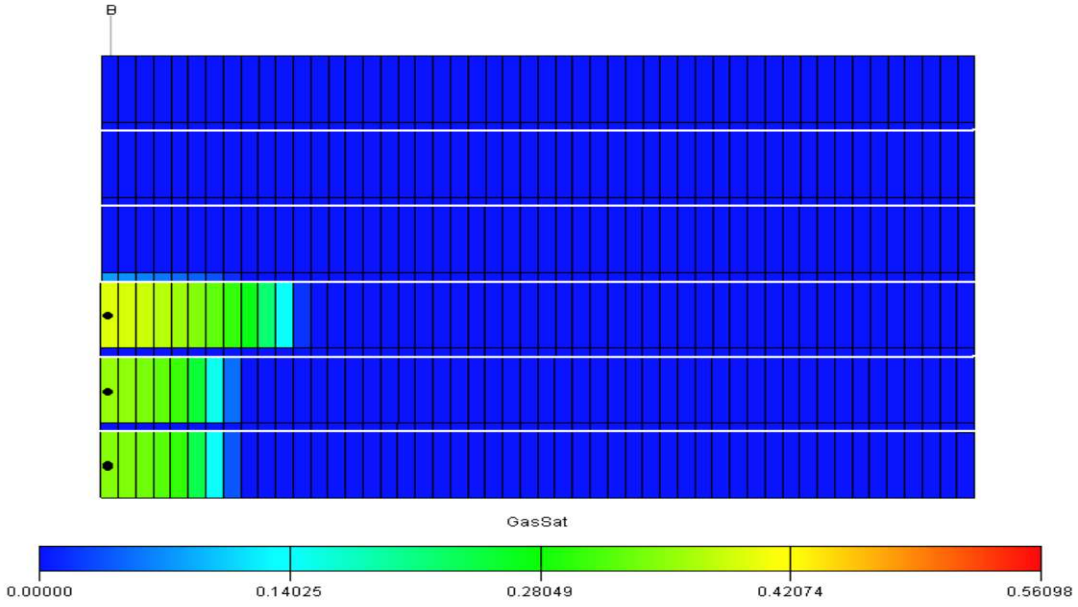

Figure 6.55: Gas saturation profile after 10 years injection of CO_2 into the storage formation beneath the shale layers

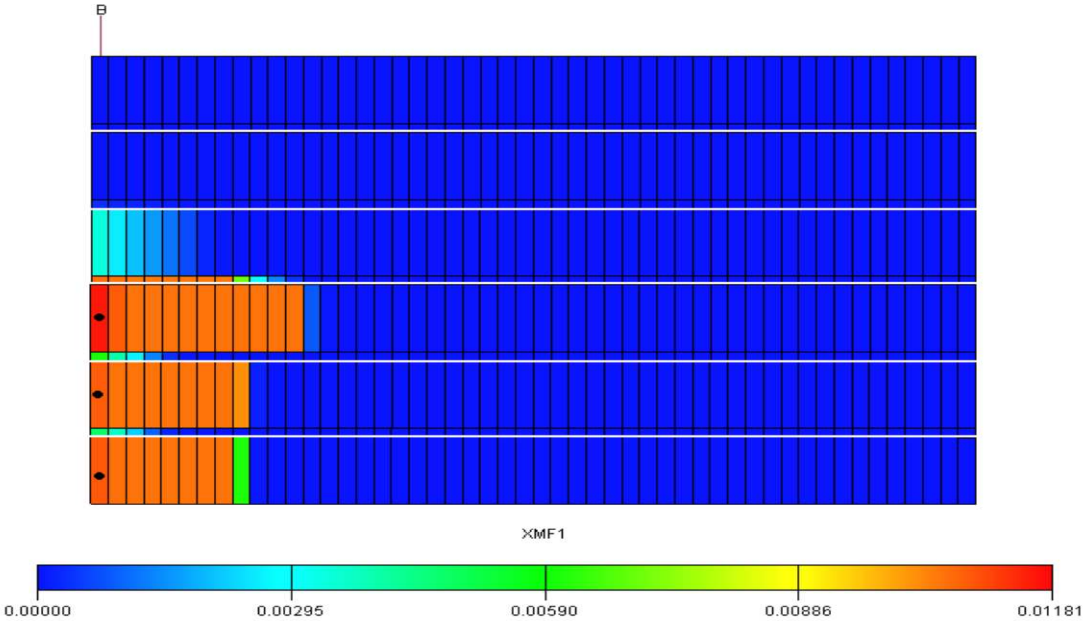

Figure 6.56: Mole fraction of CO_2 in the aqueous phase containing 200,000 ppm NaCl after 10 years of injection

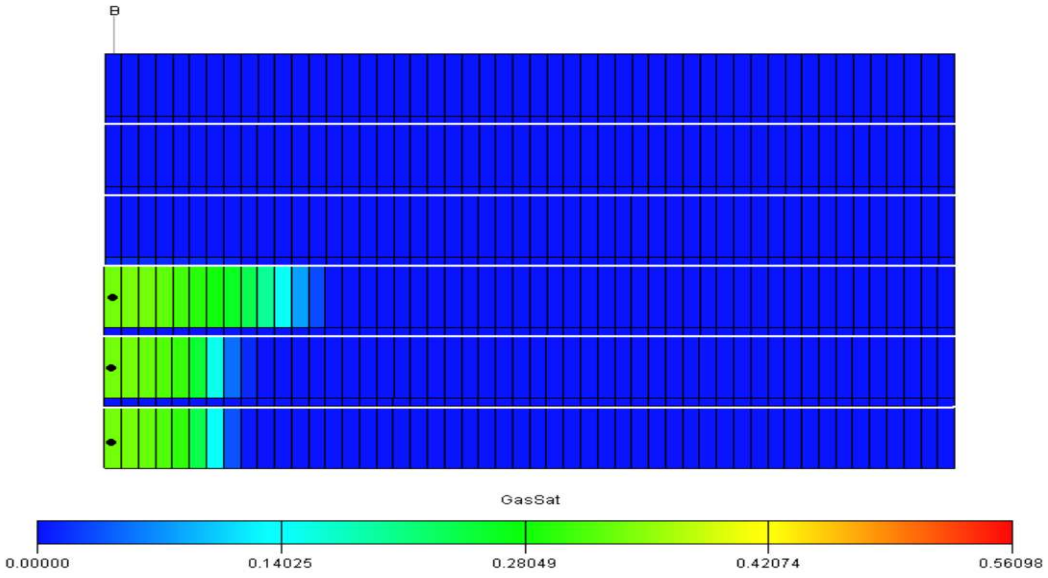

Figure 6.57: Gas saturation profile 490 years after termination of injection into the storage formation beneath the shale layers

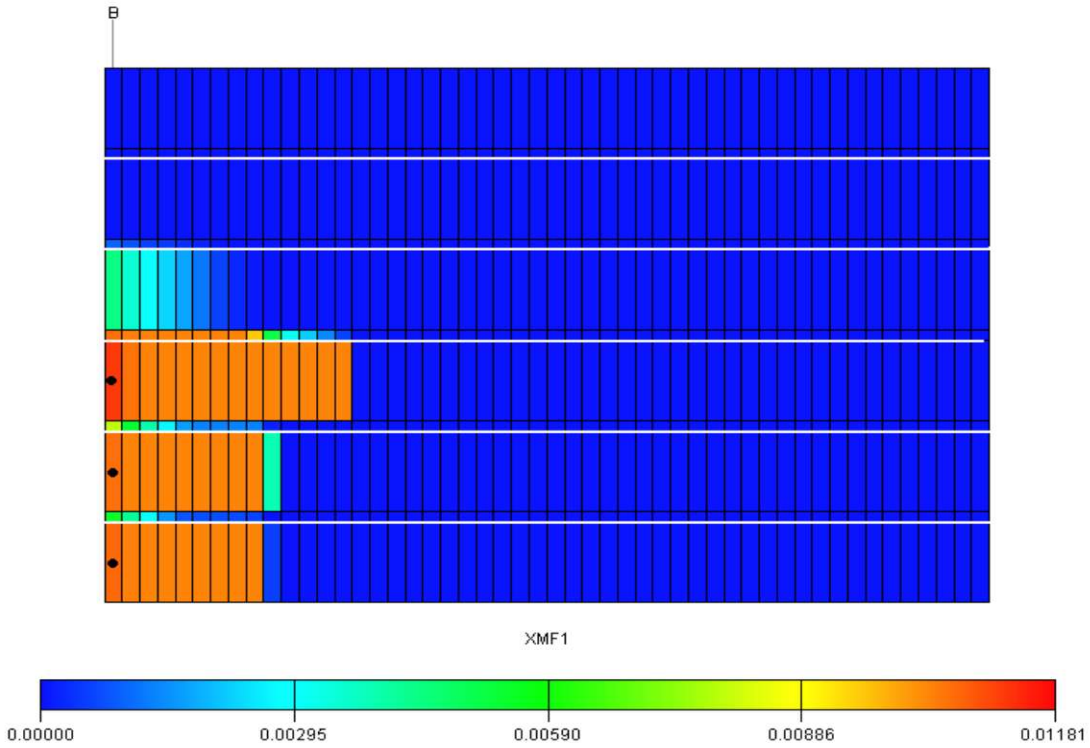

Figure 6.58: Mole fraction of CO_2 490 years after termination of injection into the aqueous phase containing 200,000 ppm NaCl

It can be concluded from the figures (Figure 6.55- 6.58) that when the gas is injected into the lower part of the aquifer, some leakage through the shale layers above would be acceptable, since the volume of the aquifer in this region is sufficiently large to act as an intermediate storage. Shale layers within the storage formation is beneficial in that they act as multiple barrier system which enhanced the storage of larger quantity of CO_2 without reaching to the top of the storage formation and the cap rock for that matter.

6.5 Possible CO_2 Leakage Pathways

Developing the framework for managing geological storage requires an understanding of the processes and risks, including the likely timescales and flux rates involved. The key subsurface processes are the migration of CO_2 after injection into the primary storage

trap, potential further movement out of the trap, physical trapping, dissolution, residual gas trapping, mineralization and adsorption. The storage capacity for underground CO_2 storage projects must be related not only to the quantity of CO_2 that can be stored, but also to the residence time for the injected CO_2. In order to describe the basic concept of risk analysis for the CO_2 leakage from a geological sequestration operation, necessary elements of a leakage scenario are summarized for the evaluation of risks. Mechanisms, paths, and sequestration structures are considered. Causes of leakage could be categorized in as follows:

- physical path and mechanisms
- distribution of the leakage probability and volume in time and space
- effect of leakage

Leakage from underground CO_2 storage sites can occur through three main pathways:

1. through the cap rock (seal)
2. through the faults
3. through well bores (existing wells or in injection wells; possibly due to deterioration of the well completion materials (steel or cement) caused by corrosion by acidic brine (dissolved CO_2))
4. through the aquifer trap (spill point underriding)

6.5.1 CO_2 Leakage through the Cap Rock

Since the injected CO_2 tends to move upward in the storage formation due to buoyancy and laterally flows beneath the cap rock, storage safety is thus controlled by the confining ability of cap rock. Reservoir simulations and investigations of gas leakage through cap rock

concluded that leakage through the top seal can basically occur by three processes or by a combination of any of these three:

- Diffusion through the pore system
- Capillary transport through the pore system of the seal
- Multi-phase migration

The prerequisite for the occurrence of volume flow is a pressure difference across the cap rock. In gas storage and sequestration projects, generally, the initial reservoir pressure is taken as the base value. However, the confining ability of the cap rock to stop the flux of CO_2 through is indicated by the partial solubility of CO_2 in the formation water. The capillary pressure is given by;

$$P_c = \frac{2\sigma \cos\theta}{r} \tag{6.1}$$

where σ is the interfacial tension between the non-wetting phase (gas) and the wetting phase (brine), θ is the contact angle and r is the radius of pore throat. The minimum entry pressure is the capillary pressure at which the non-wetting phase starts to displace the wetting phase. From equation 6.1, it can be inferred that the capillary entry pressure can be significant for very small pore throats in other words, for low permeability. The ability of the injected CO_2 to be retained in the storage formation over long time is mainly attributed to the high sealing pressure of the cap rock. This part of the study aims to emphasize the importance of the gas threshold pressure in order to estimate the gas leakage accurately through the cap rock. In aquifer injection projects, the cap rock and the storage formation characteristics are investigated during the development. But in depleted reservoirs, there is always a proven cap rock to retain oil/gas in the reservoir. When this media are replaced by the injected CO_2, the lower interfacial tension of CO_2/brine system relative to that of

hydrocarbon/brine system results in a lower capillary sealing pressure of the rock. Another criterion for the selection of CO_2 storage injection pressure is the fracture pressure of the reservoir rock or the cap rock. The criterion assumes that the injection is safe provided that the critical fracture pressure is not exceeded. This is risky in practice when the sealing pressure of the cap rock is lower than the fracture pressure. In such a case, the injected CO_2 will breakthrough the cap rocks and leak into the upper formations before the fracture pressure is reached [42]. Experimental results for different pelitic cap rocks by Hildenbrand et al. [26] are given in Table 6.4.

Table 6.4: Interfacial tension for different fluid systems

Systems	Conditions(p, T)	IFT (mN/m)
CH_4/water	100-300 bar, 40-80°C	48.6-61.7
N_2/water	100-300 bar, 40-80°C	53.7-61.2
Medium oil/water	> 69 bar, 54.4-81.1°C	30-35
CO_2/water	100-300 bar, 40-80°C	16-30

The storage formation relative permeabilities of brine and CO_2 are taken from Bennion and Bachu (2005) experimental data [6]. Due to the importance of hysteresis effects investigated as shown in Section 6.3, the relative permeability hysteresis effects were taken into account (Figure 6.59 and 6.60).

Figure 6.61 and 6.62 depict the mole fraction of CO_2 in cap rock layer, just above the storage formation. Once the injection ceases, the gas still continues to spread out laterally underneath the cap rock. Dissolved gas migrates into the cap rock by diffusion whereas the free gas remains below critical saturation.

Figure 6.63 emphasizes the necessity of accurate gas threshold pressure determination (GTP) and thus sealing capacity in CO_2 storage and performance is estimated by showing the volumetric gas losses into the cap rock over time. The volumes included free gas plus dissolved gas.

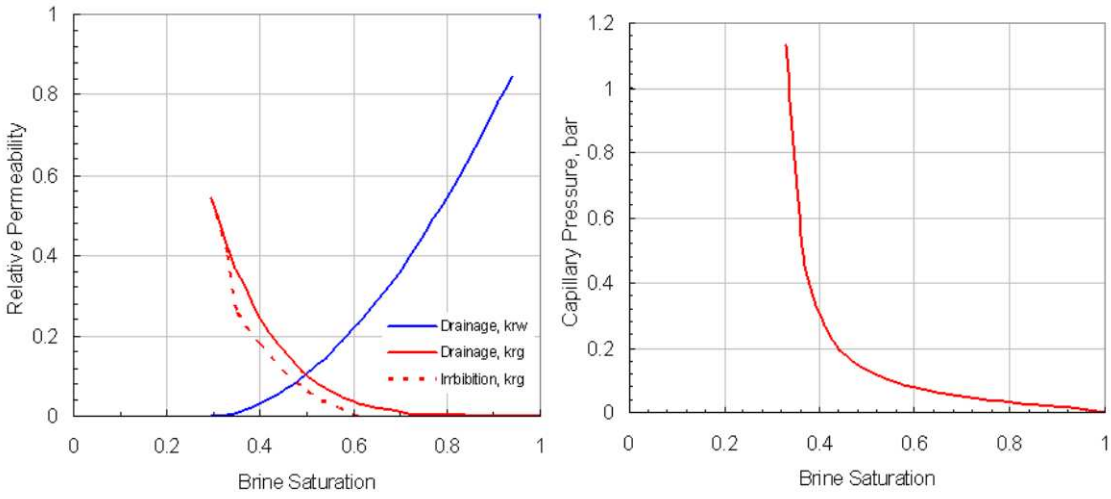

Figure 6.59: Relative permeability and capillary pressure curve for CO_2-water-storage formation rock system

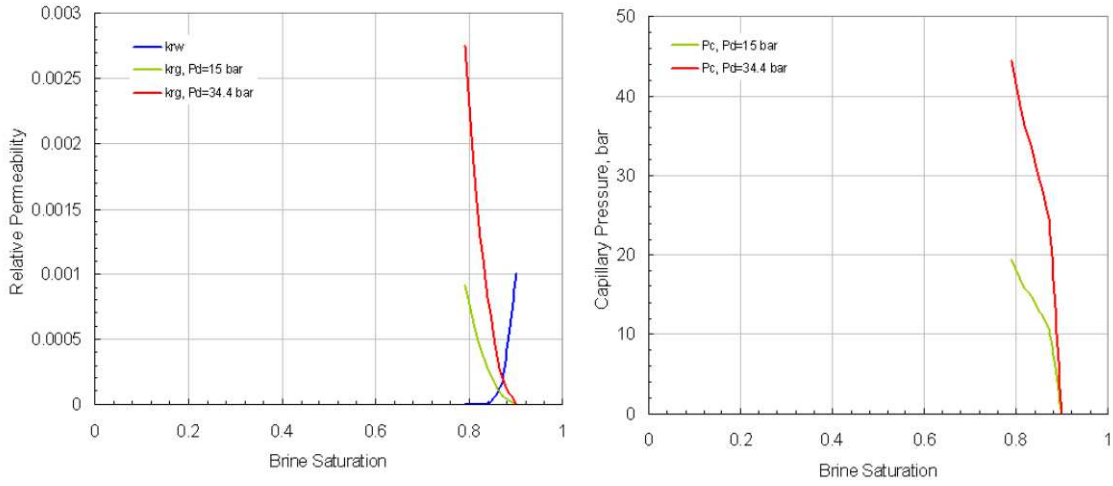

Figure 6.60: Relative permeability and capillary pressure curve for CO_2-water-cap rock formation rock system for different gas threshold pressures

Figure 6.63 it can be determined under which conditions the volume flow after exceeding the GTP becomes critical and dangerous for a CO_2 storage project. Since the prerequisite for the occurrence of volume flow is that the pressure difference across the cap rock must exceed the breakthrough pressure, the storage pressure must be controlled. To avoid volume

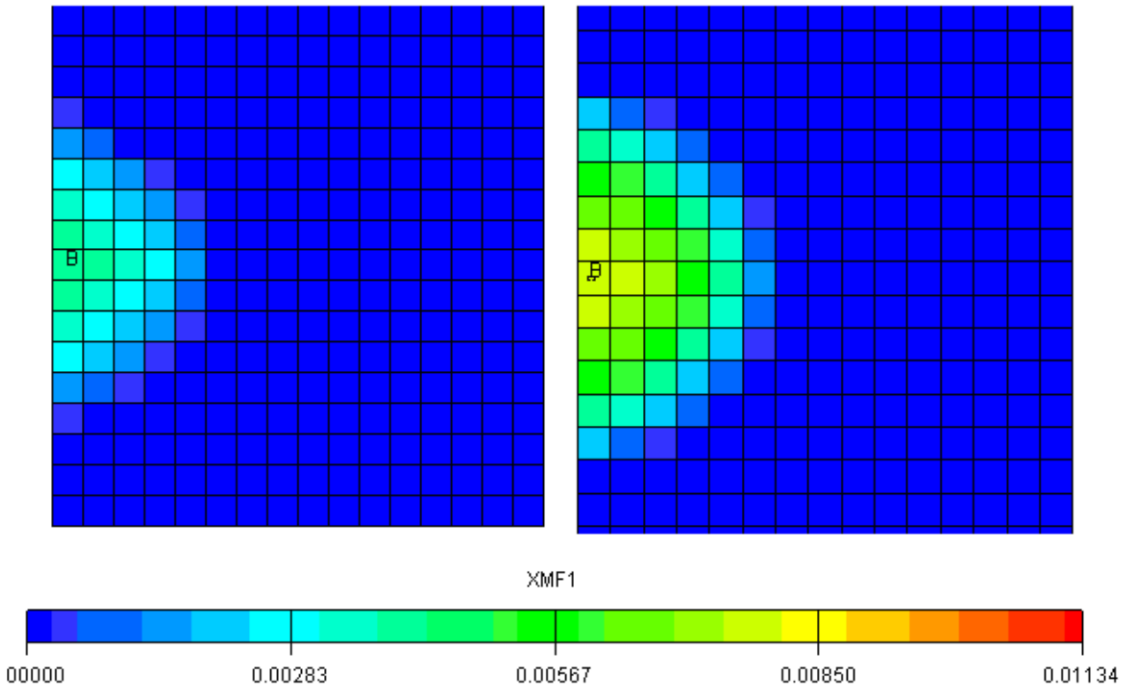

Figure 6.61: Areal view of the mole fraction of CO_2 in 2^{nd} layer (cap rock) in saline aqueous phase after 10 years injection into a saline aquifer left=GTP=34.4 bar, right= GTP=15 bar

flow, the cap rock sealing pressure should be determined and must not be exceeded during CO_2 injection. In depleted reservoirs, the difference between the interfacial tension of hydrocarbon/brine and CO_2/brine system should be taken into account to re-evaluate the sealing capacity of the same cap rock (Table 6.4). The accurate modeling of multi phase flow performance and sealing capacity is therefore more critical for the prediction of trapping capacity of the aquifers. To minimize the gas migration through the cap rock, the gas breakthrough should be determined before the start of any gas storage or CO_2 sequestration project in aquifers.

In order to compare the effect of the gas threshold pressure on CO_2 with natural gas storage, CH_4 injection was simulated and the percentage of leakage calculated by normalizing the total injection amount. The same leakage mechanisms are valid for the natural gas

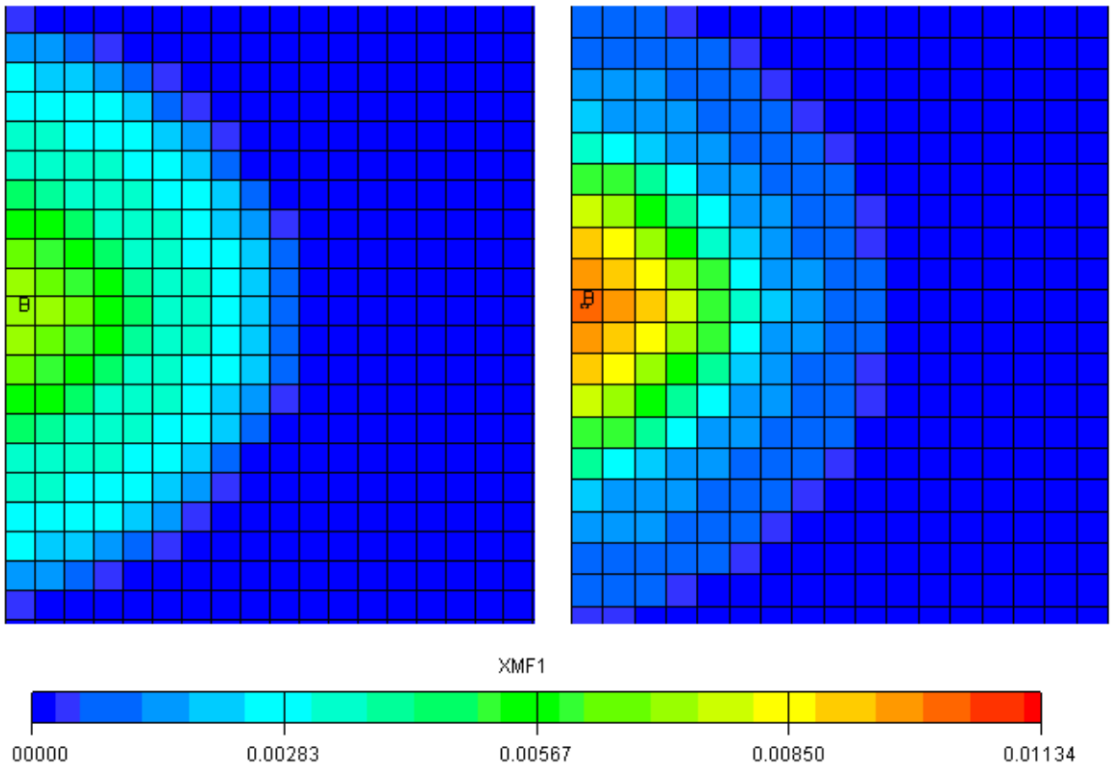

Figure 6.62: Areal view of the mole fraction of CO_2 in a saline aqueous phase in 2^{nd} layer (cap rock) in saline aqueous phase after 10 years injection into a saline aquifer left=GTP=34.4 bar, right= GTP=15 bar

storage. However, aquifer storage reservoir requires gas injection at higher than the initial pressure value to displace the water. Therefore, this over-pressuring increases the risk of gas migration into the cap rock. Other than for CO_2 storage, natural gas leakage poses, in addition to safety, also an economic problem.

It can be concluded from Figure 6.64, the estimated CH_4 leakage rate is more than that of the CO_2. Buoyancy forces the upward migration of CO_2 and CH_4 and the magnitude of buoyant force depends on the density difference of formation water and injected gas. The viscosity plays a significant role in the mobility of gas. For conditions of storage, the viscosity of CH_4 is approximately three times lower than viscosity of CO_2. Therefore; CH4 migrates faster than CO2 and comes into contact with cap rock which increases the

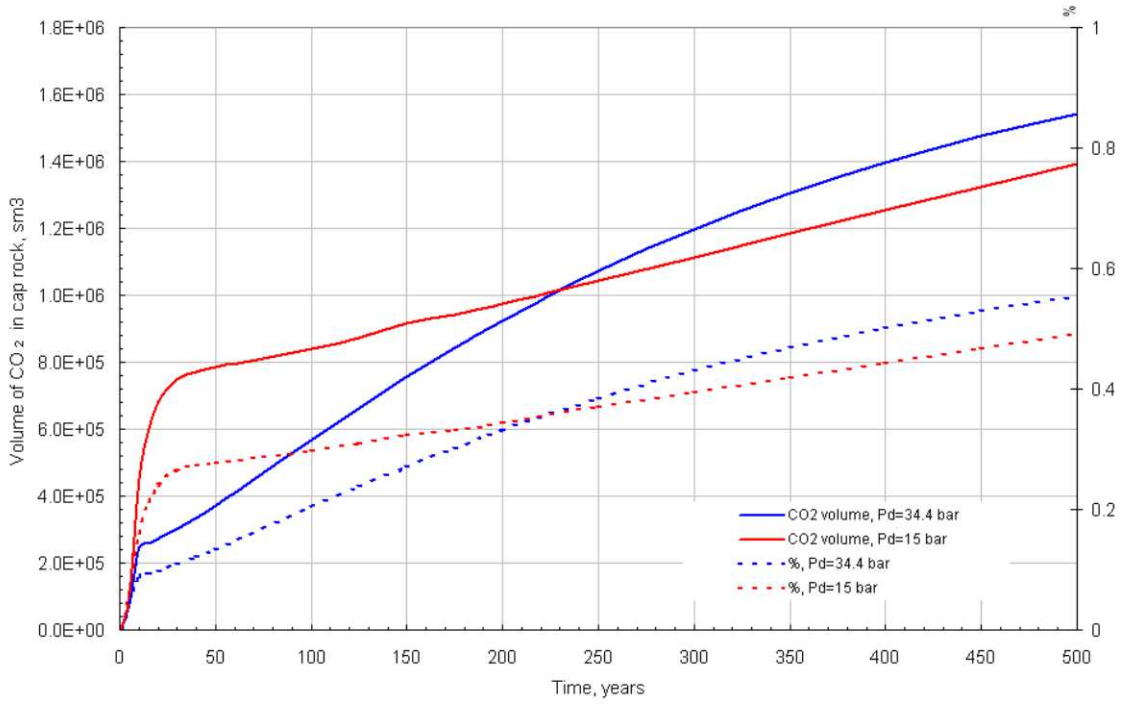

Figure 6.63: CO_2 (free and dissolved gas) flow volume from storage formation to cap rock as a percentage of total injected CO_2 for different GTP

risk of leakage. The leakage rate discrepancy may also be due to the solubility differences. CH_4 is relatively insoluble in formation water. However, CO_2 is soluble in water and as it dissolves, the formation water density increases. The denser CO_2-saturated brine relative to the original brine segregates downwards the aquifer and impedes the upward migration of CO_2 and thus decreases the risk of leakage through the cap rock. These leakage estimates can be useful in EOR CO_2 flood projects which offer an extended life of oil reservoirs while providing means of CO_2 disposal.

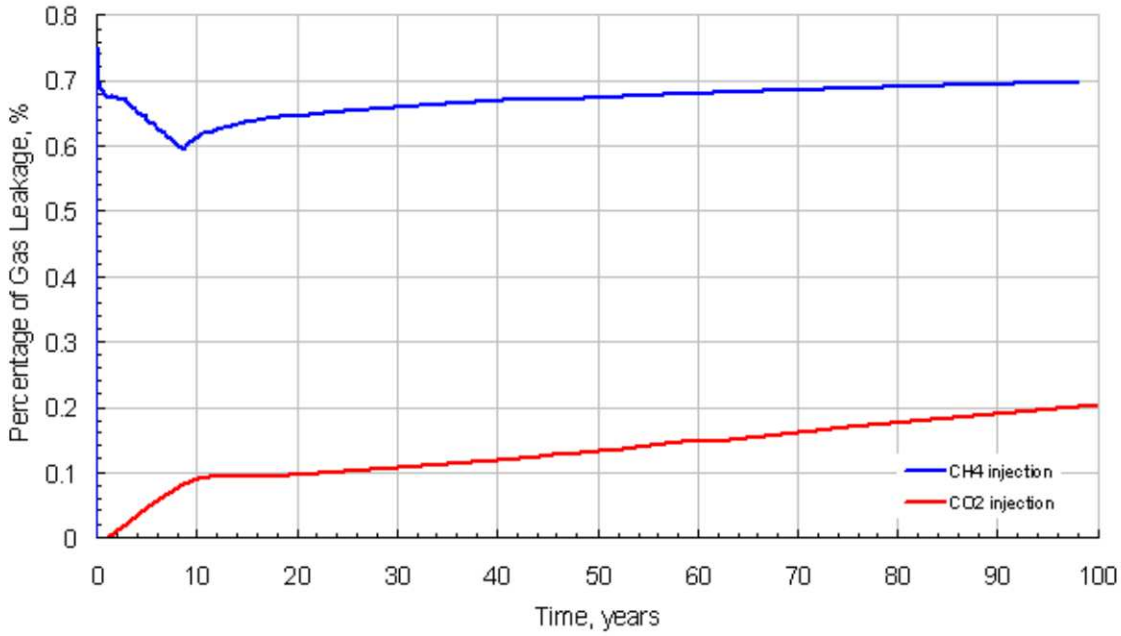

Figure 6.64: Leakage percentage normalized by total injection amount of gas as a function of time, GTP= 34.4 bar

Simulation runs and investigations of this study did not focus on the cap rock property changes due to the physico-chemical reactions between the cap rock formation and diffused CO_2 in the long-term containment. But for the future work, the physico-chemical reactions in cap rock should be taken into account in order to investigate changes in cap rock properties, such as permeability.

6.5.2 CO_2 Leakage through the Existing Wells

Another potential leakage path is the migration along the wellbore due to poor cementation. Both gas injection and abandoned wells are potential paths because they are the direct connections between the surface and the reservoir; and they are man-made constructions. An improper design or construction results in the casing or cementation failures which cause the leakage through or along the wells. The diffusion of CO_2 through the cement or casing

caused by corrosion is another concern of risk, however it is a slow process in compared to the leakage through the failed injection wells [13]. Also, it is still uncertain how injected CO_2 and brine affects the cement in the long term storage timescale. Saline aquifers are not economically beneficial such as hydrocarbon-reservoirs. Therefore the existence of old wells is rare and consequently the risk for CO_2 leakage through the wells is low.

The wells may suffer from a variety of factors that limit their integrity, including improper cementation, improper plugging, overpressure, corrosion, and other failure conditions. Therefore, first it is aimed to simulate the leakage through the injection well. The leaky injection well is represented with a very fine grid with a grid cell of 0.25 m in x any y directions. The effective permeability of this vertical length was taken as 10 Darcy. The gas was injected into the storage formation and the leakage was monitored in the upper permeable aquifer. Figure 6.65 indicates the gas distribution in the storage formation and upper permeable aquifer.

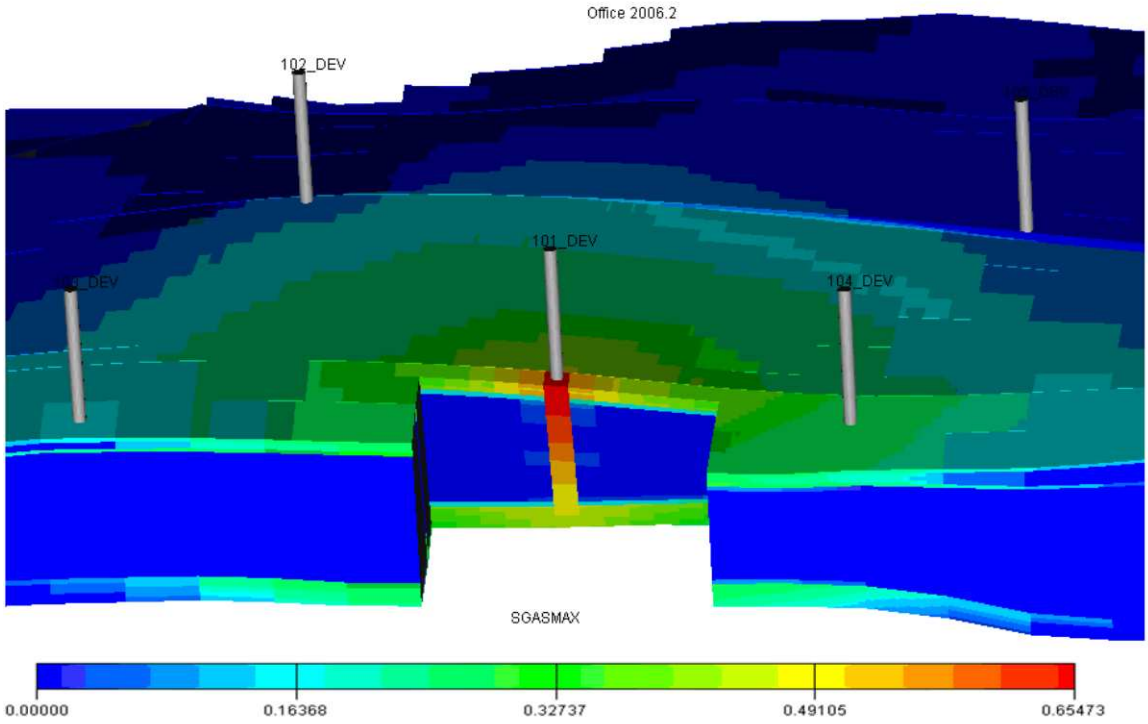

Figure 6.65: Gas saturation profile in 3D, in the cross section of leaky injection well 101

Figure 6.66 shows leakage from the injection well. The leakage rate is around 30% of injection rate which obviously is not acceptable in CO_2 sequestration projects. This significant leakage is due to the very high permeability of the annulus of the injection well. The leaky injection well annulus has 10 Darcy permeability whereas the storage formation has permeability around 200 mD. Therefore, the preferred path of the gas flow is through the high permeable vertical column.

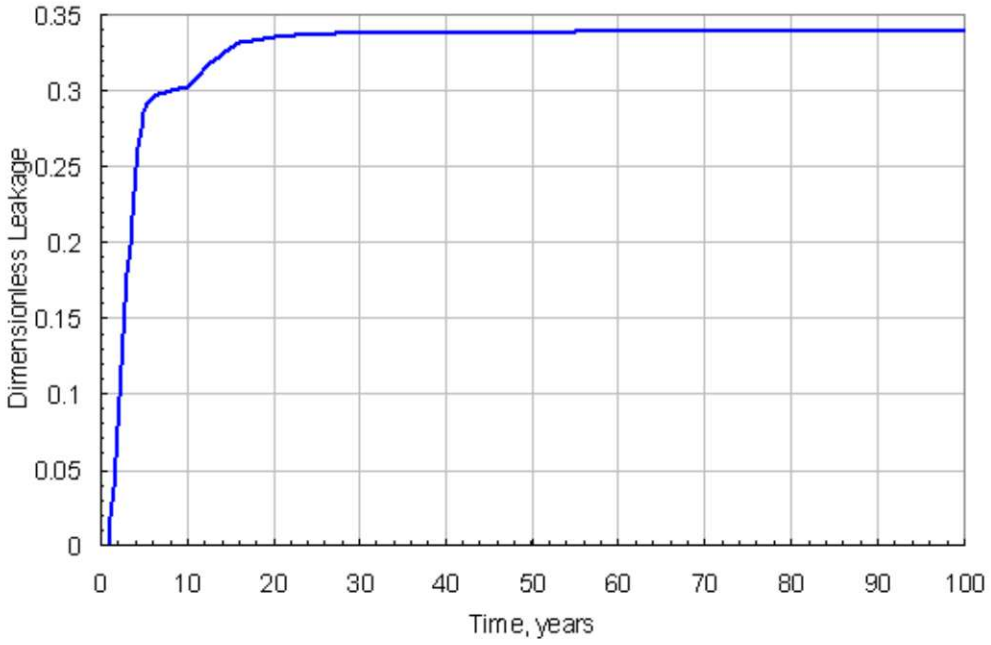

Figure 6.66: Dimensionless leakage from the leaky injection

Second case is aimed to investigate the leakage of CO_2 to the upper permeable aquifer through an abandoned well located at 300 m away from the injection well. Again, the leaky well has a permeability of 10 Darcy. The reservoir was assumed to be infinite acting means the outer boundary is allowed to continue to expand indefinitely. The gas was injected into the storage formation for 10 years and Figure 6.67 shows the gas saturation profile 90 years after termination of injection.

At the beginning of CO_2 injection, injected gas has not arrived immediately to the abandoned well. However, the pressure pulse has arrived. This pressure increase pushes the formation water, and it may begin to leak. Figure 6.68 represents the simulation results considering the leaky well annulus permeability 10 Darcy. This solution identifies the maximum leakage rate is around 2.5 % of injection rate. Although the leaky well has a high permeability, the amount of leakage from a single well is relatively small.

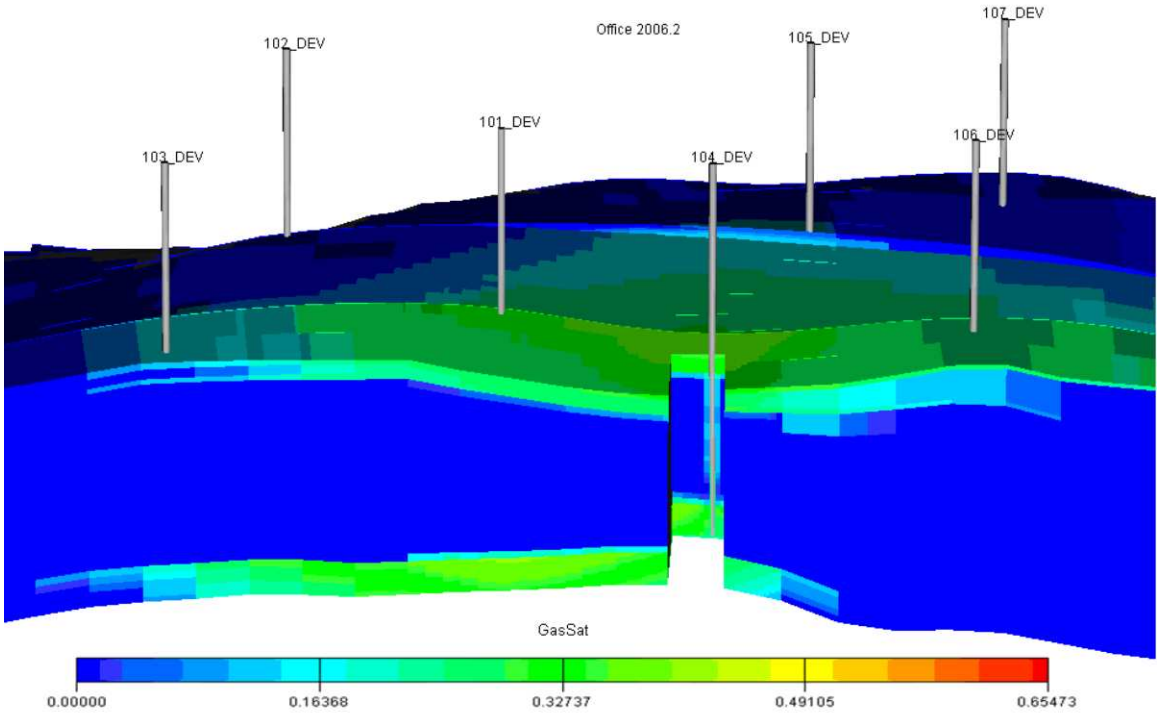

Figure 6.67: Gas saturation profile in 3D, in the cross section of leaky well 104

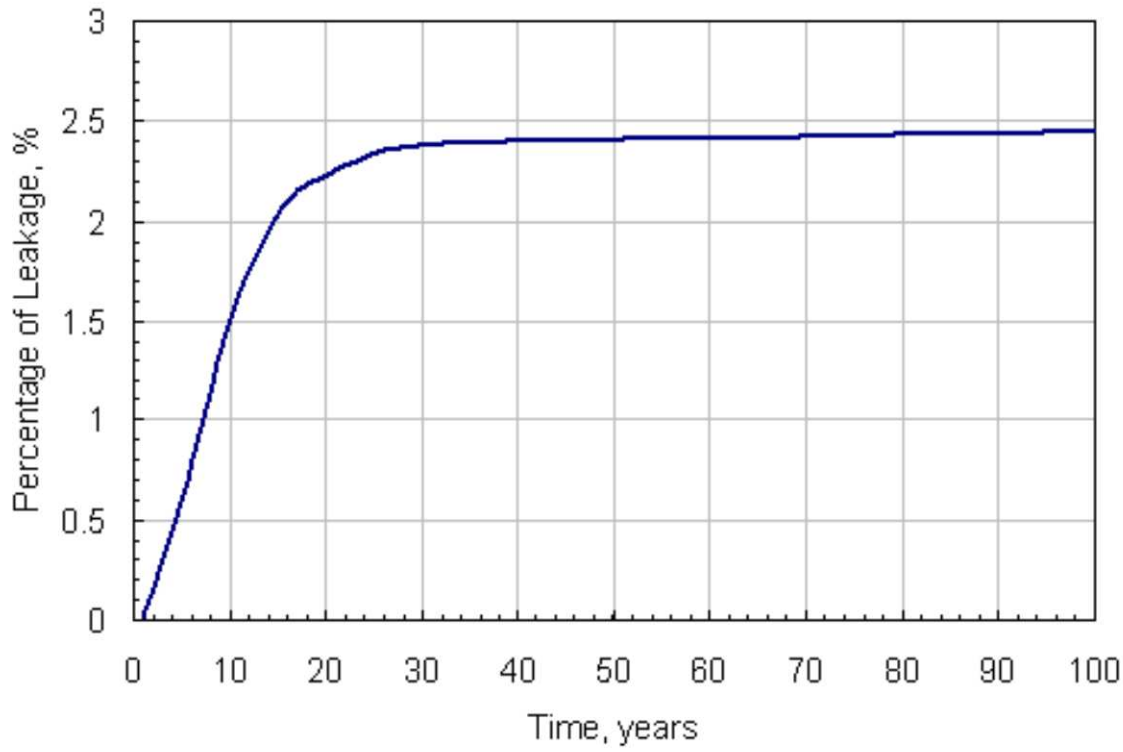

Figure 6.68: Dimensionless leakage from the leaky abandoned well

6.6 Injection Strategies

Gas injection strategy is very critical for proper gas storage operations. Leakage risk of injected CO_2 in vertical and horizontal well modes was compared to identify the most effective injection geometry for a controlling the tendency of leakage. Also injection rate, the number of injection wells which are expected to have a significant effect on the gas placement. Therefore, in this section, the effect of injection well placement and strategies with respect to gas plume migration was studied.

6.6.1 Placement of Gas Injection Intervals (Perforations)

Two cases are illustrated, where gas was injected through a vertical well perforated across the entire interval of storage formation and through a horizontal well. The amount of CO_2 injected into the aquifer through the vertical well was at a maximum rate of 100,000 sm^3/day for 20 years whereas in the case of the horizontal well the maximum rate was 500,000 sm^3/day for a period of 4 years. Both injection strategies were controlled by 300 bar BHP. In both cases the injected gas migrates upwards in the storage formation and followed by lateral extension along the cap rock. Figures 6.69 and 6.70 present the gas saturation profiles of CO_2 after 2 and 500 years respectively.

In the case of horizontal well, when gas is injected into the lower part of the storage formation, it has more contact area with the under-saturated brine and dissolves better. As CO_2 dissolves, the formation brine density increases. The denser CO_2-saturated brine relative to the original brine segregates downwards in the aquifer and impedes the upward migration of gaseous CO_2. As a consequence the contact area between gas plume and cap rock is reduced (Figure 6.70) which tend to restrict the risk of leakage.

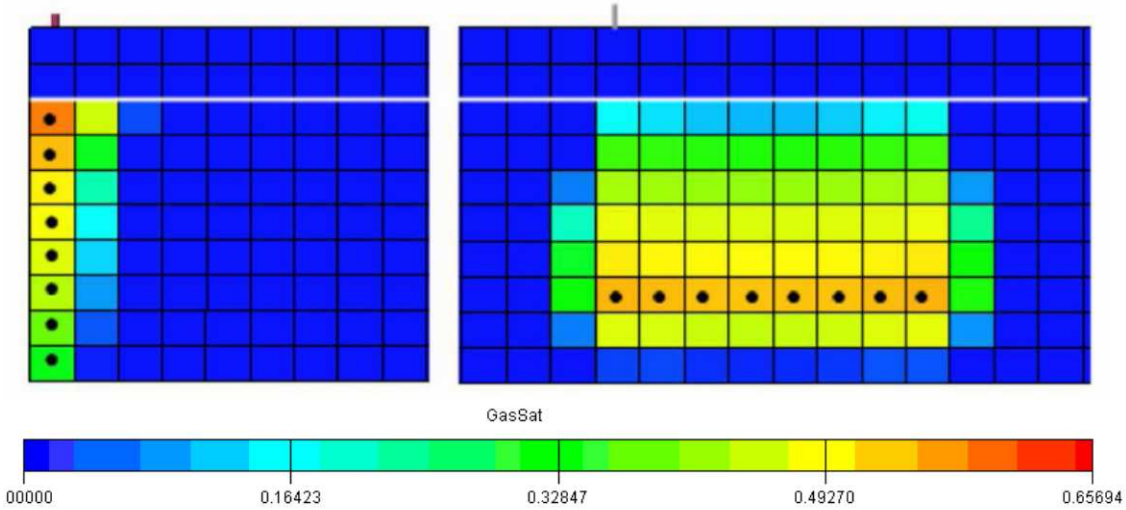

Figure 6.69: Gas saturation profile after 2 years, left= saturation profile of vertical well injection across the entire storage formation, right= saturation profile of horizontal well injection

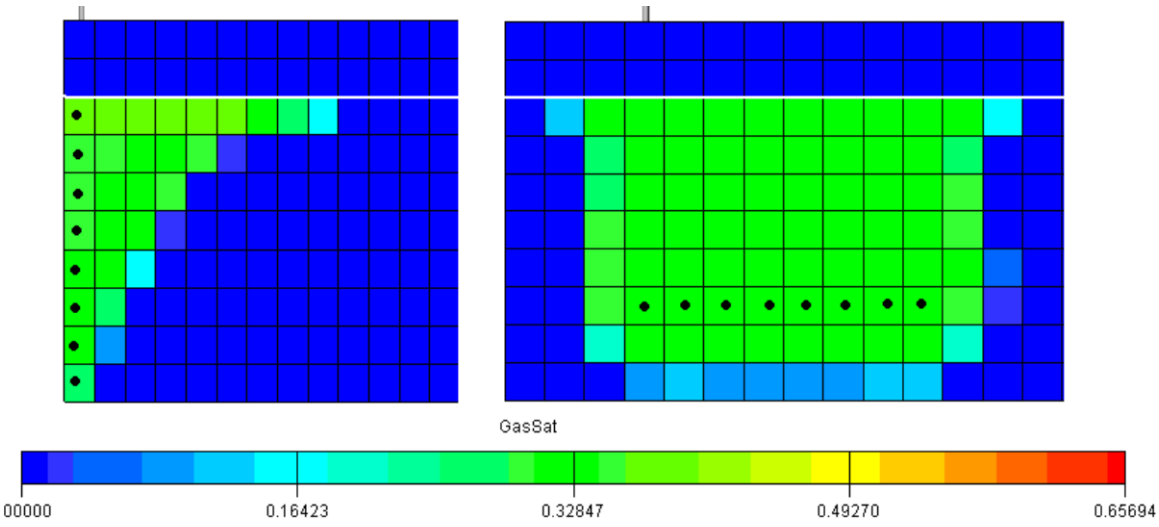

Figure 6.70: Gas saturation profile after 500 years, left= saturation profile of vertical well injection across the entire storage formation, right= saturation profile of horizontal well injection

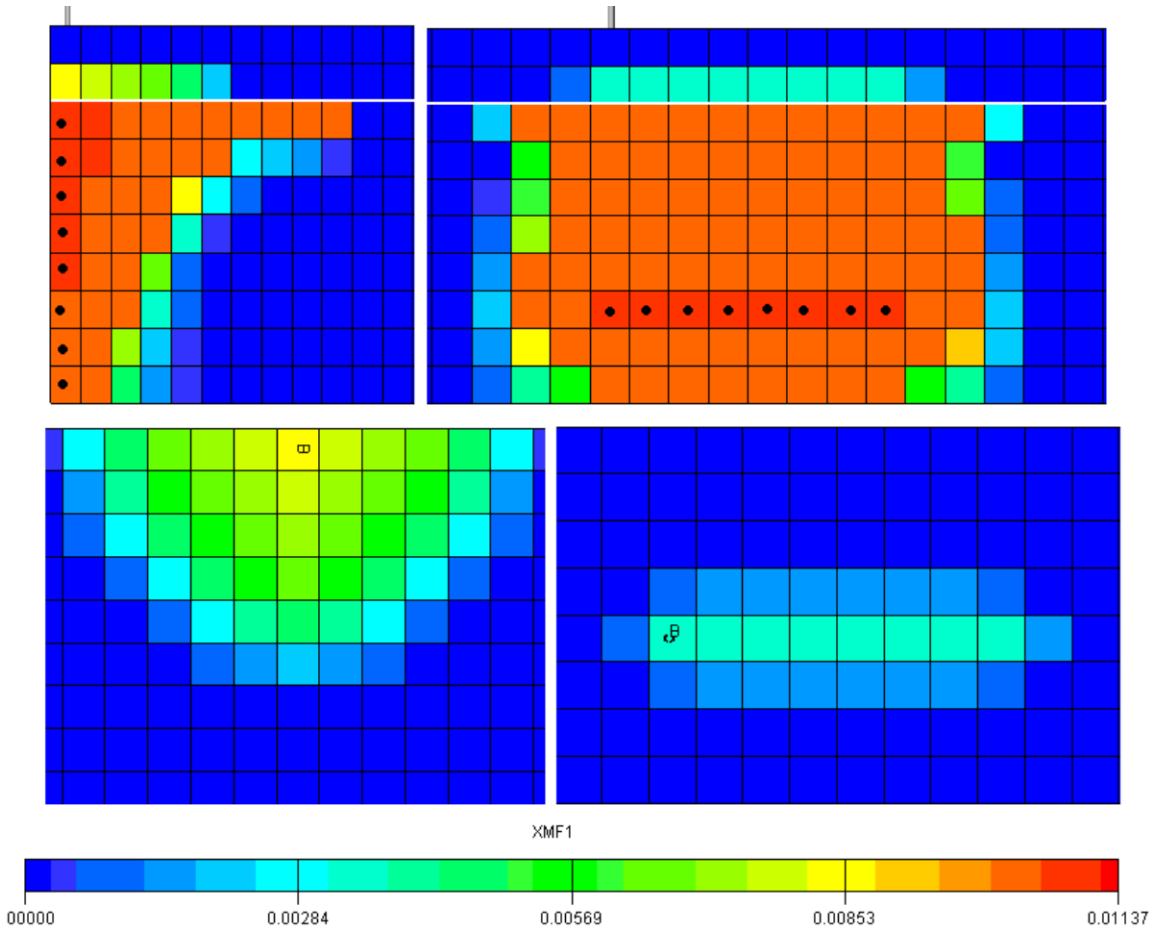

Figure 6.71: Vertical gas solubility profiles of CO_2 after 500 years in cross section (1, 15) on top and areal mole fraction in 2^{nd} layer (cap rock) at bottom: left= vertical well, right= horizontal well

Figure 6.71 represents the vertical and areal gas solubility profiles for the vertical well and a horizontal well injection scenarios.

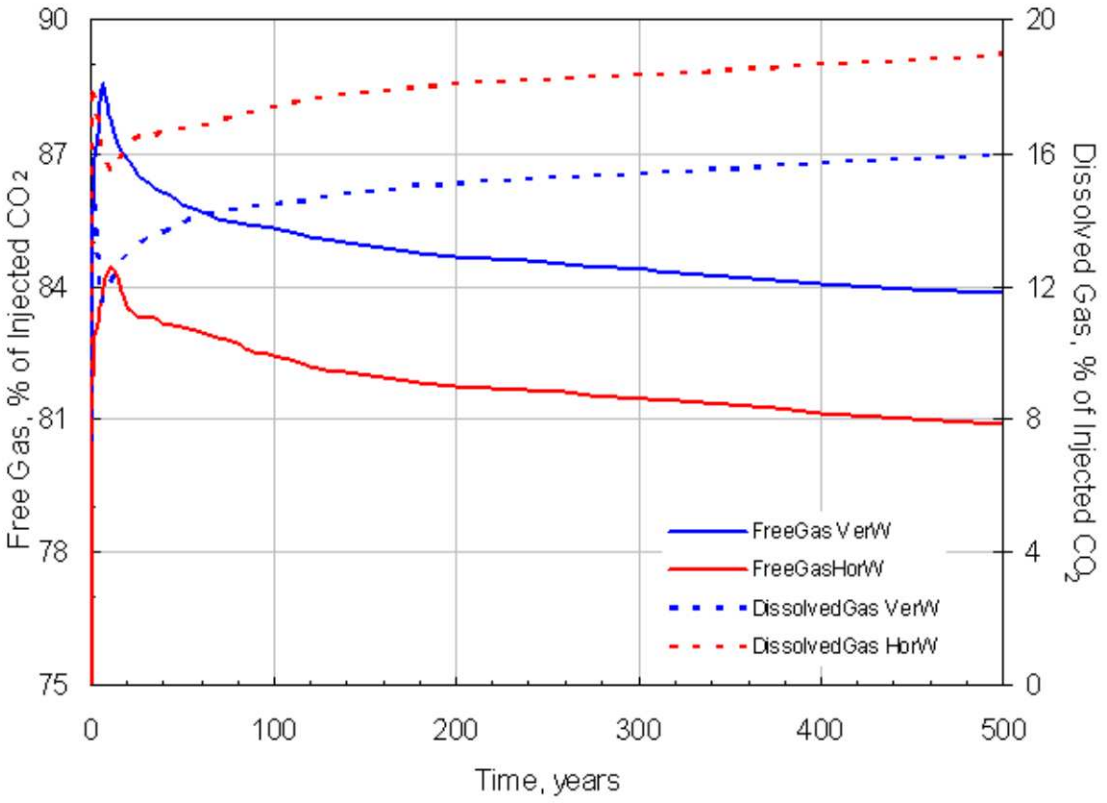

Figure 6.72: Percentage of gas stored (free and dissolved gas) in the cases of vertical and horizontal well injection

It can be observed in Figure 6.73 that injecting through a vertical well across the entire storage interval leads to an extensive contact with the cap rock and more gas could leak through the cap rock compared to the horizontal injection geometries. Horizontal wells located in the lower part of the formation increase the gas solubilization capacities and eliminate contact with cap rock immediately. Due to the segregation of CO_2-containing brine downwards, the risk of leakage decreases. A conclusion can therefore be drawn that CO_2 injection through the horizontal well has advantages over vertical well for effective

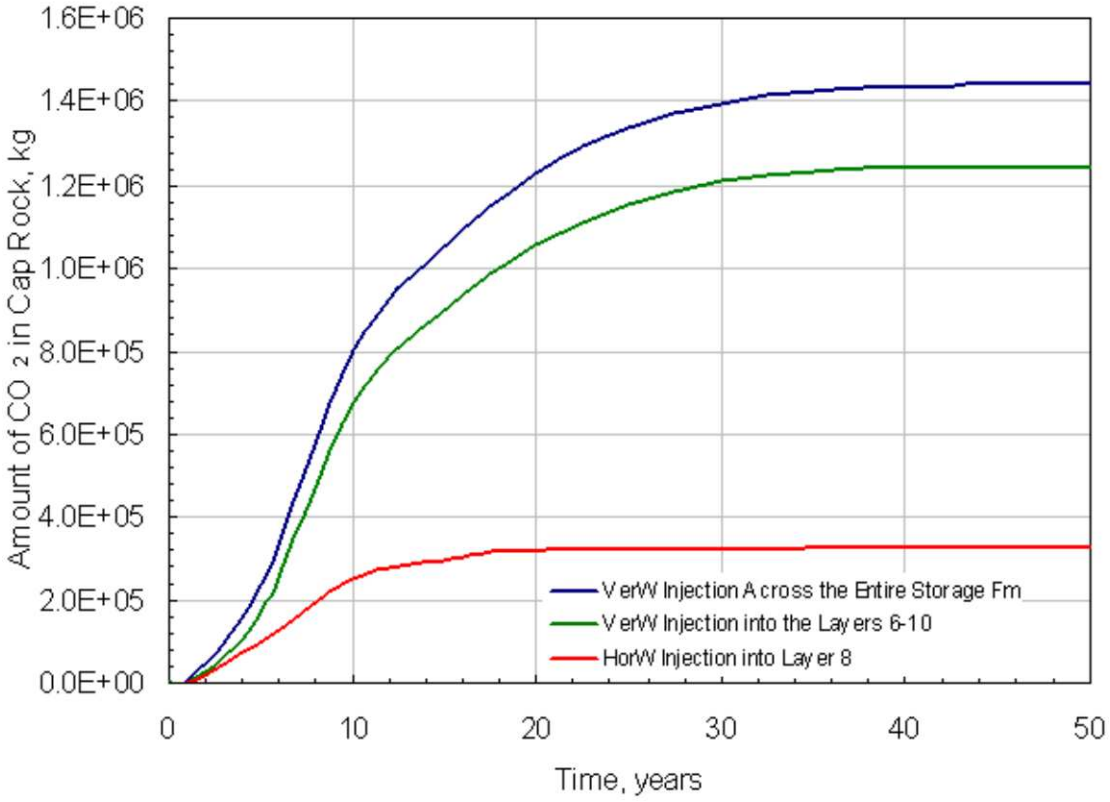

Figure 6.73: Comparison of gas losses into the cap rock through the different injection placement; vertical well perforated at bottom layer, vertical well perforated across the entire reservoir and horizontal well

geologic storage which effectively eliminated the risk of leakage through the cap rock.

6.6.2 Injection Rate

The ratio of viscous/capillary forces is strongly dependent on the injection rate. Near the injection well flow velocity is high and viscous forces are dominating. Further away from the injection well the velocity in radial flow mode is reduced and capillary forces become more dominant. Differences in gas saturation distribution are therefore observed between near well bore region and areas further away as shown by the saturation profiles in this study. Figure 6.74 shows the gas saturation performance during a period of 1 year, 10 years and 50 years for the same amount of CO_2 injection.

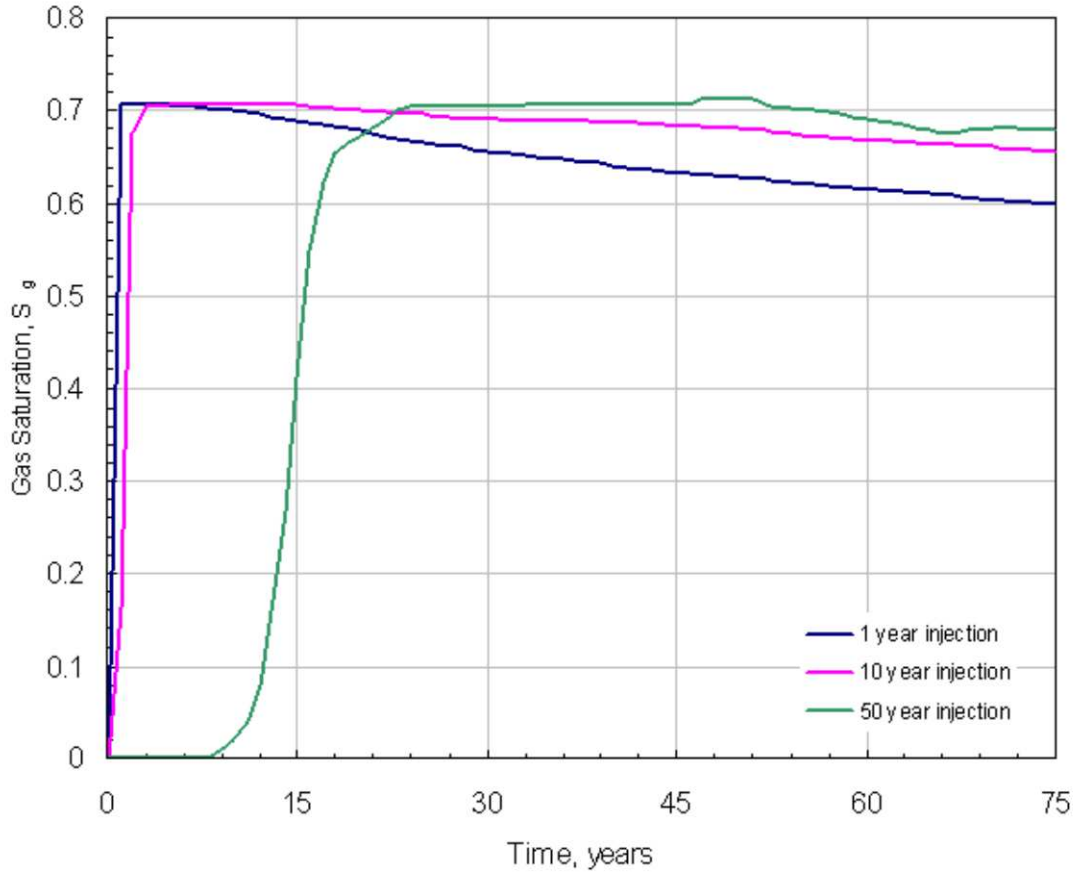

Figure 6.74: Gas saturation performance with same volume CO_2 injected over different time

If we look at the saturation-time performances, the smaller injection rate (50 years) has an adverse affect on the overall trapping. This can be explained by three main reasons. First, injection stops earlier, the displacement path changes earlier from a drainage to an imbibition process. During the longer drainage process, the gas has time to move to the top and trapping mechanisms do not significantly affect the system until injection ceases. As the connected gas phase travels to the top, it establishes fast moving flow paths that become more occupied with gas as injection continues. Secondly, when gas is injected at a high rate, it migrates up in the storage formation near the well. The gas spreads arially first before gravity forces become dominant. When the gas spreads arially, trapping becomes more efficient as water invades a larger domain of gas saturated rock in which trapping can occur. Finally, with higher injection rates, the initial gas saturation in the rock is higher as it is less able to move out of the way for more incoming gas.

6.7 CO_2 Injection into Buntsandstein Prototype Aquifer

Series of generic reservoir simulations were performed to determine the sensitivity parameters, solubility and capillary trapping effects on the migration of the injected CO_2 gas plume. The aim simulating a generic model is to avoid the geological complexity and the reservoir heterogeneity to reduce the simulation run time. The permeability distribution of the real reservoir is shown in Figure 2.20. The reservoir model pore volume is approximately $72x10^6$ rm^3 in which the cap rock formation has a volume of $23x10^6$ rm^3 and the storage formation is $48x10^6$ rm^3 with an initial pressure of 200 bar at the top of the formation. In the model there are nine wells, seven of them are vertical wells and open to the bottom layers of the reservoir and two of them are horizontal well. Due to the lack of information on the horizontal well data such as the length of perforations, the total length of the horizontal well, the gas was only injected through the vertical wells.

The pVT properties of gas were calculated with implemented EOS (modified Redlich-Kwong equations) in CO2SEQ option of ECLIPSE 300. The relative permeability curves are taken from Bennion and Bachu [6] experimental data and the curves are plotted in Figure 6.29. Hysteresis affects the gas phase only as seen in the large disparity between drainage and imbibition gas relative permeability curves (Figure 6.29). Scanning curves of relative permeabilities were constructed using Killough's [30] hysteresis model for different initial gas saturations S_{gi} with a Land trapping parameter C of 1.278. Experimental initial-residual capillary curves needed to calculate the trapping coefficient were not available so the parameter had to be estimated.

The Buntsandstein prototype reservoir was assumed to be at isothermal conditions of 87°C. Pure CO_2 was injected at a maximum rate of 500,000 sm^3/day through each vertical well for 20 years, with the injection controlled by a maximum bottom hole pressure (BHP) of 300 bar. The reservoir and process parameters of the Buntsandstein prototype reservoir can be seen in Table 6.1. The following figures represent the result of simulation runs with fresh water and saline aquifer containing 200,000 ppm NaCl and $CaCl_2$ scenarios.

Sensitivity analysis of the Buntsandstein prototype reservoir model has been performed with the cases tabulated in Table 6.5.

Table 6.5: Sensitivity case parameters of Buntsandstein prototype reservoir simulation model

	Case 1	*Case 2*	*Case 3*
Aquifer size	3500 mx1400 m	3500 mx1400 m	3500 mx1400 m
Storage formation thickness	15 m to 20 m	15 m to 20 m	15 m to 20 m
Vertical to horizontal permeability	0.1	0.1	0.1
Salinity	No Salinity	200 g/l NaCl	200 g/l $CaCl_2$
Initial water saturation	100 %	100 %	100 %
Irreducible water saturation	25 %	25 %	25 %
Critical gas saturation	10 %	10 %	10 %
Maximum injection rate	500,000 sm^3/day per well	500,000 sm^3/day per well	500,000 sm^3/day per well
Maximum injection pressure	300 bar	300 bar	300 bar
Number of well	7 vertical wells	7 vertical wells	7 vertical wells

Figure 6.75 and 6.77 indicate the gas saturation profile at the top of the storage formation after 10 and 250 years respectively. It has been proved that the injected gas tends to move to the top of the storage formation due to buoyancy forces. From following figures, it can be also concluded that some of the faults are not perfectly sealing, therefore, the gas to pass through.

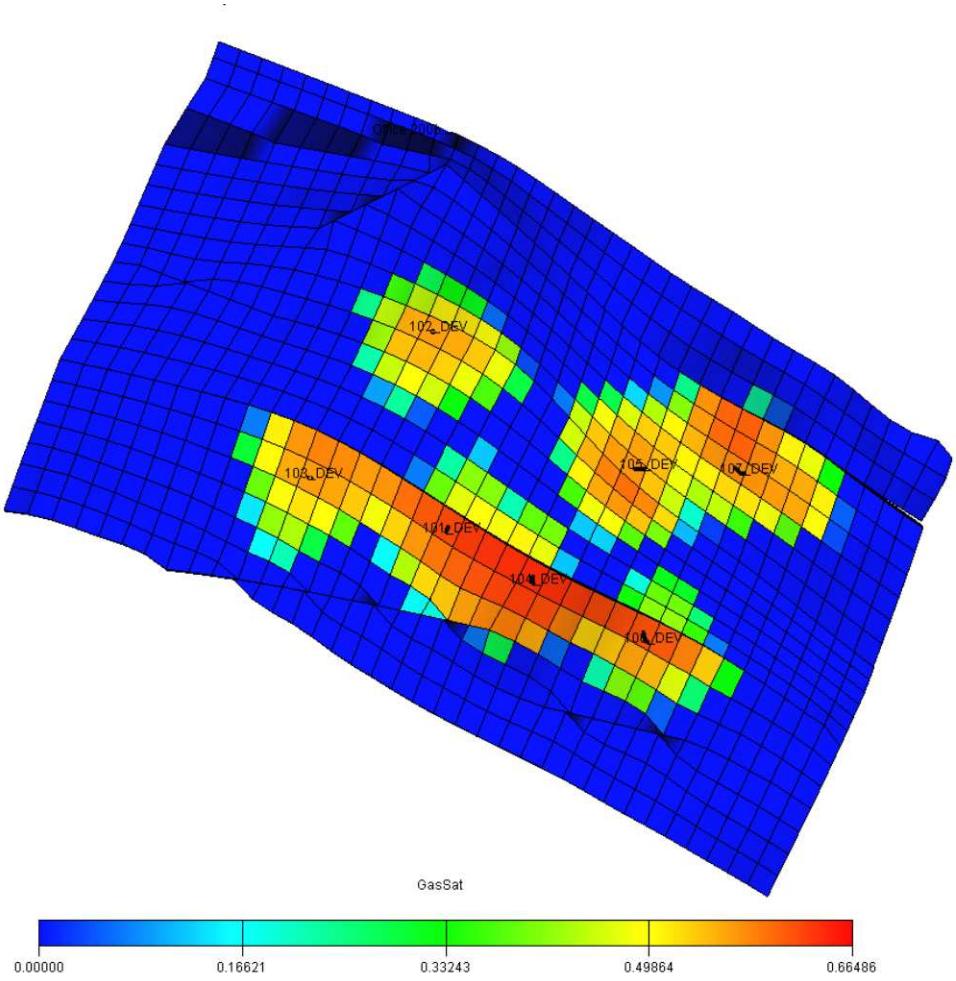

Figure 6.75: Gas saturation profile in Buntsandstein prototype reservoir model in the top layer of the storage formation after 10 years of injection into fresh water

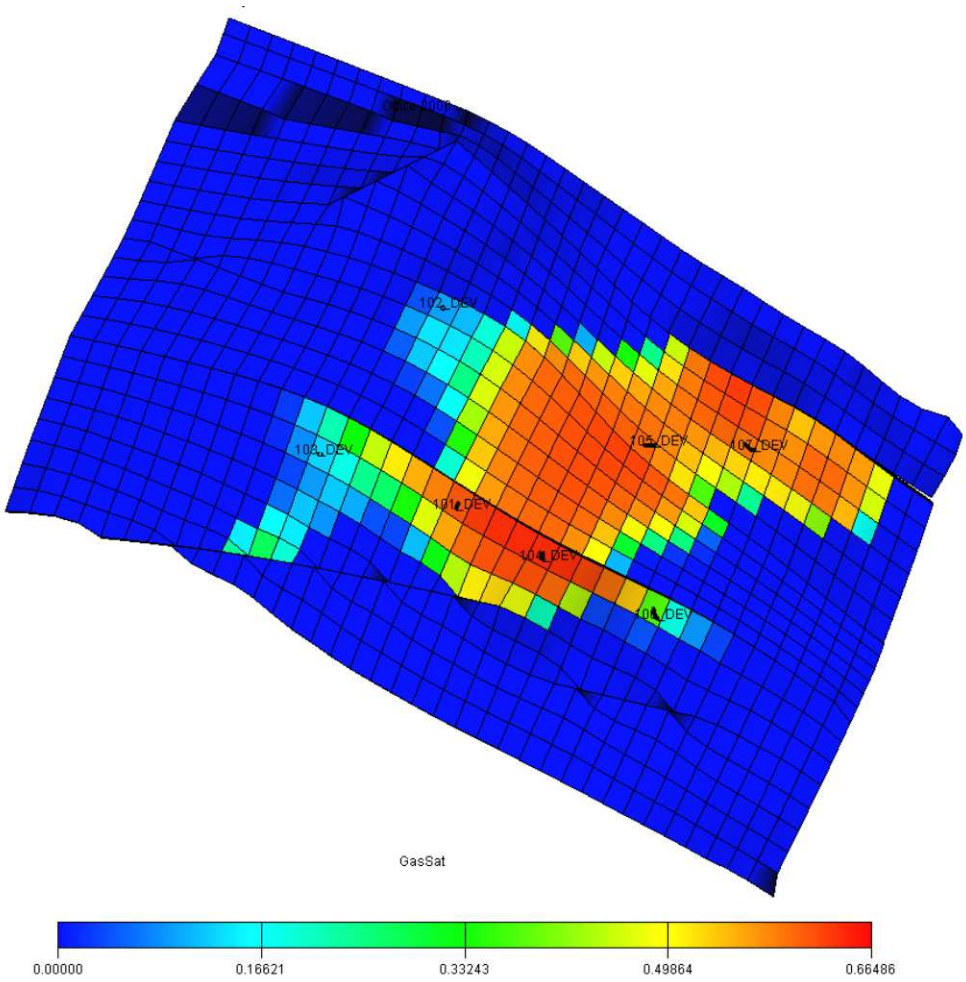

Figure 6.76: Gas saturation profile in Buntsandstein prototype reservoir model in the top layer of the storage formation 250 years after termination of injection into fresh water

Figure 6.77 and 6.78 represents the gas solubility profile in the top of the storage formation and the overlaying cap rock layer. The CO_2 migrates into the caprock due to the molecular diffusion and the higher the density difference between the gas and formation volume, the more the risk of leakage (Figure 6.78 and 6.80). This conclusion can also be seen in Figure 6.19. These figures emphasize the importance of salinity and brine composition of the aquifer in the estimation of CO_2 leakage.

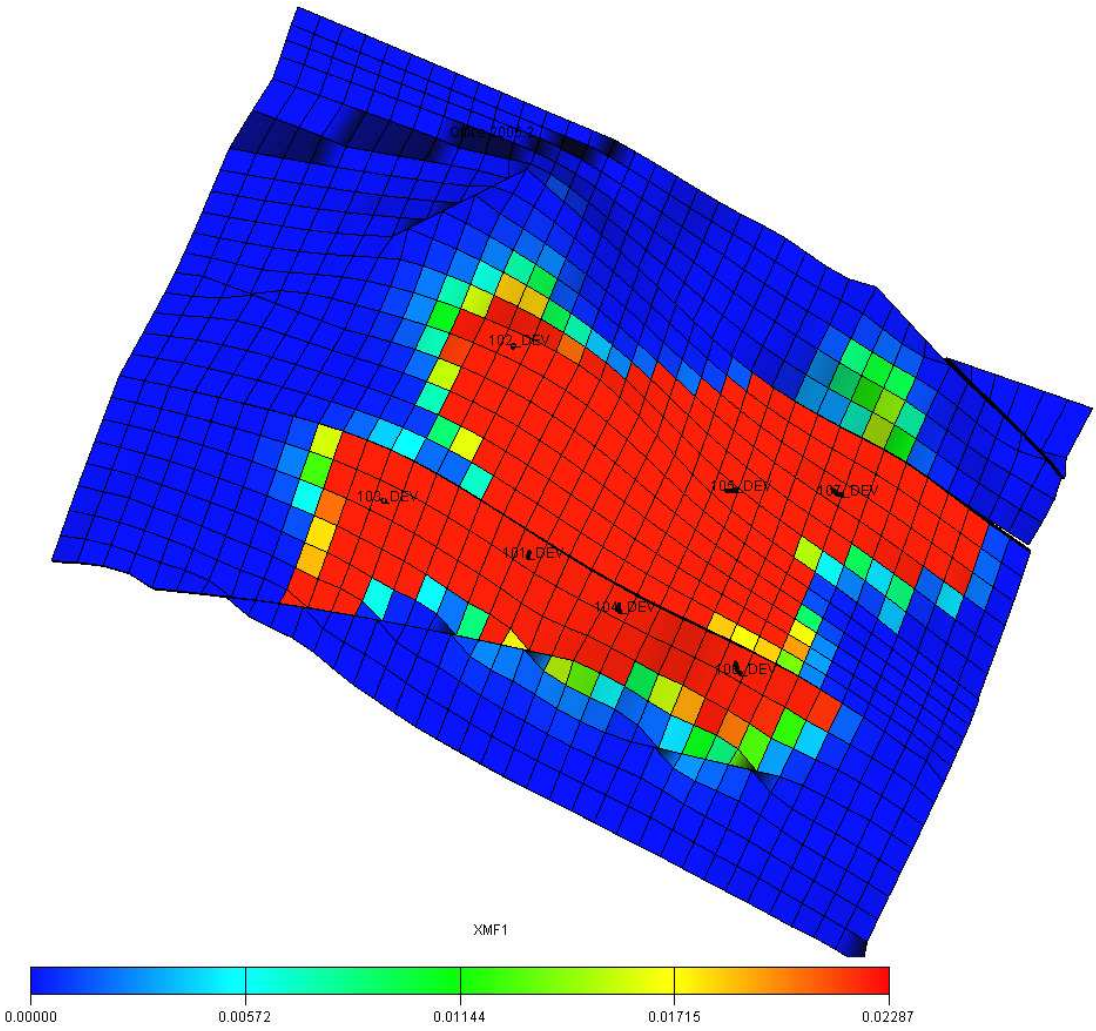

Figure 6.77: Gas concentration profile in the Buntsandstein prototype reservoir model in the top layer of the storage formation 250 years after termination of injection into fresh water

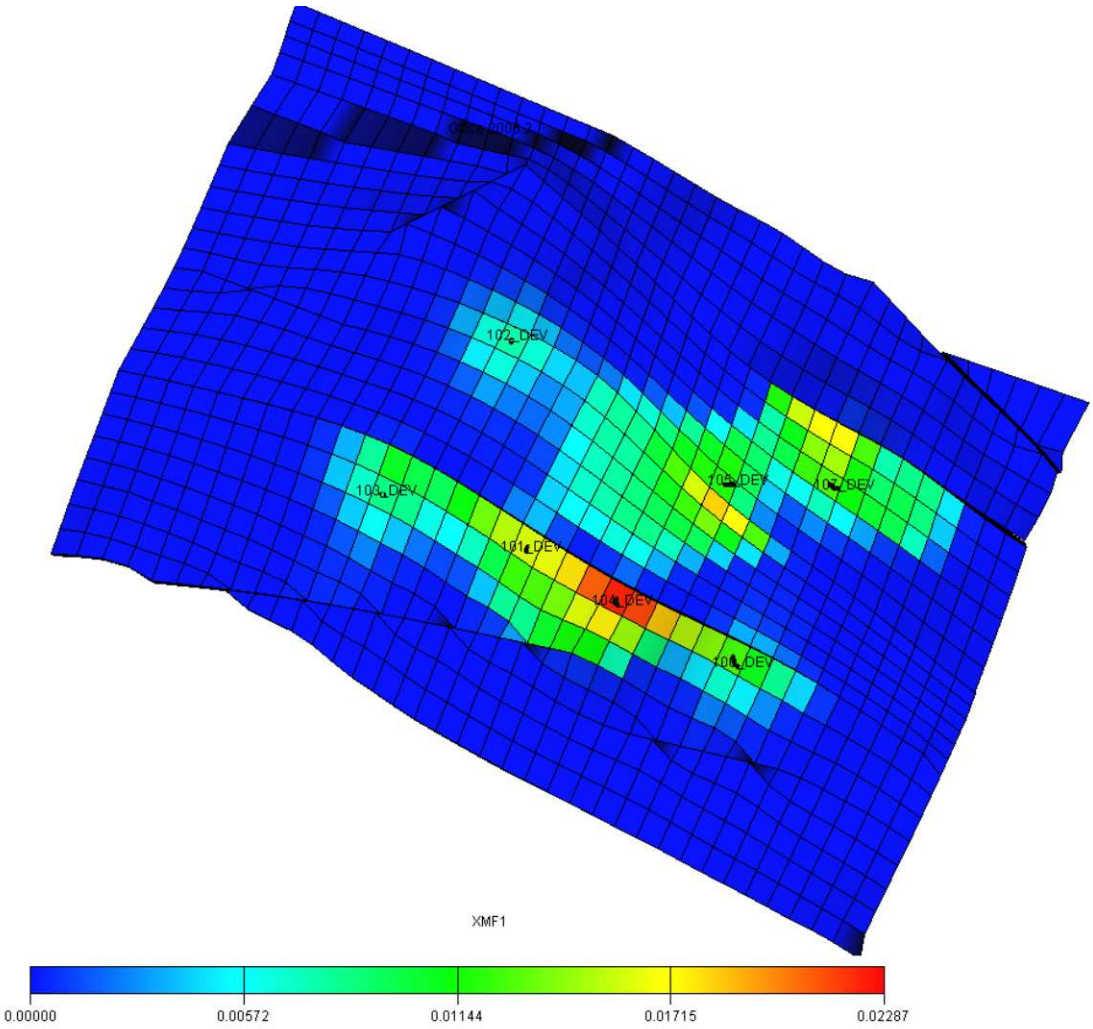

Figure 6.78: Gas concentration profile in the Buntsandstein prototype reservoir model in the cap rock just above the storage formation 250 years after termination of injection into fresh water

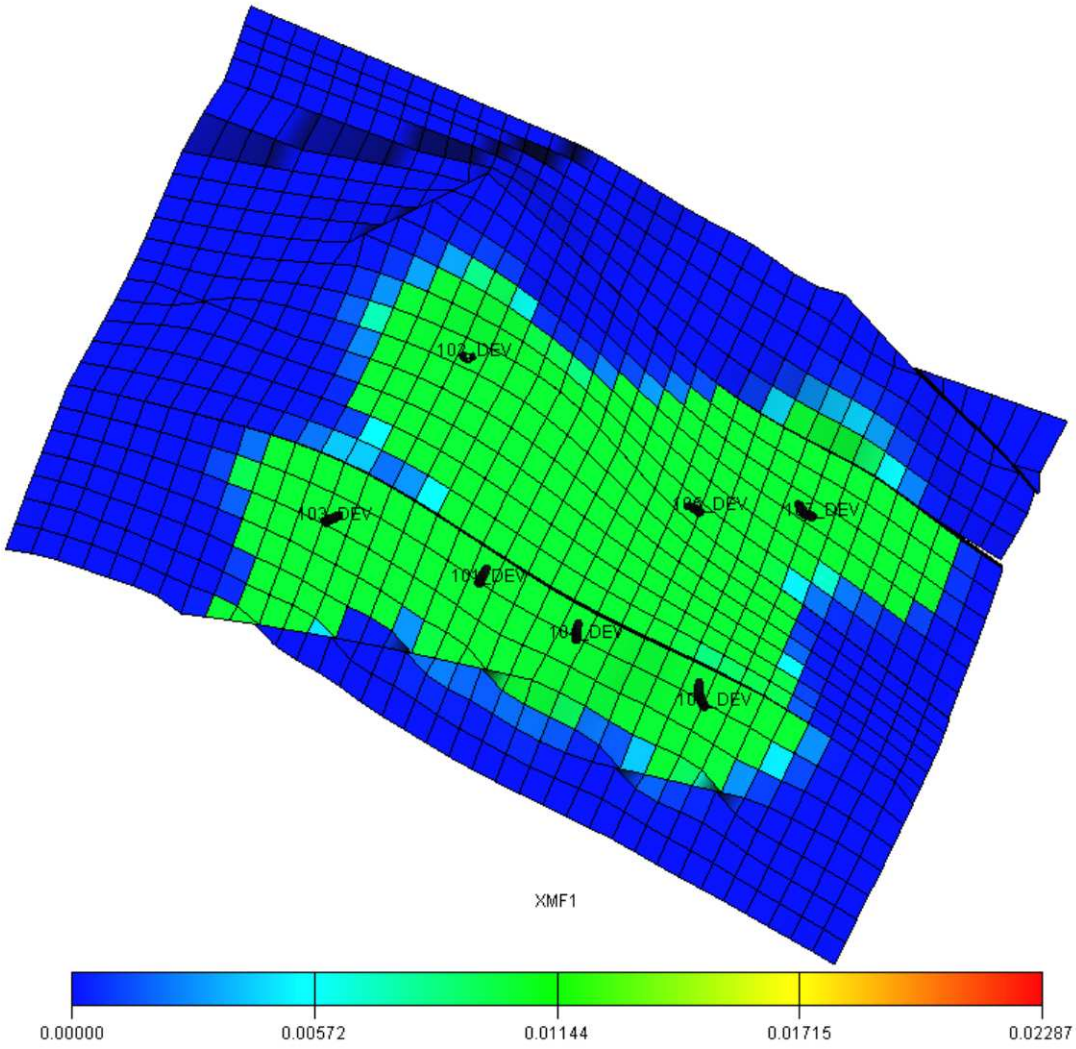

Figure 6.79: Gas concentration profile in the Buntsandstein prototype reservoir model in the top layer of the storage formation 250 years after termination of injection into aqueous phase containing 200,000 ppm NaCl

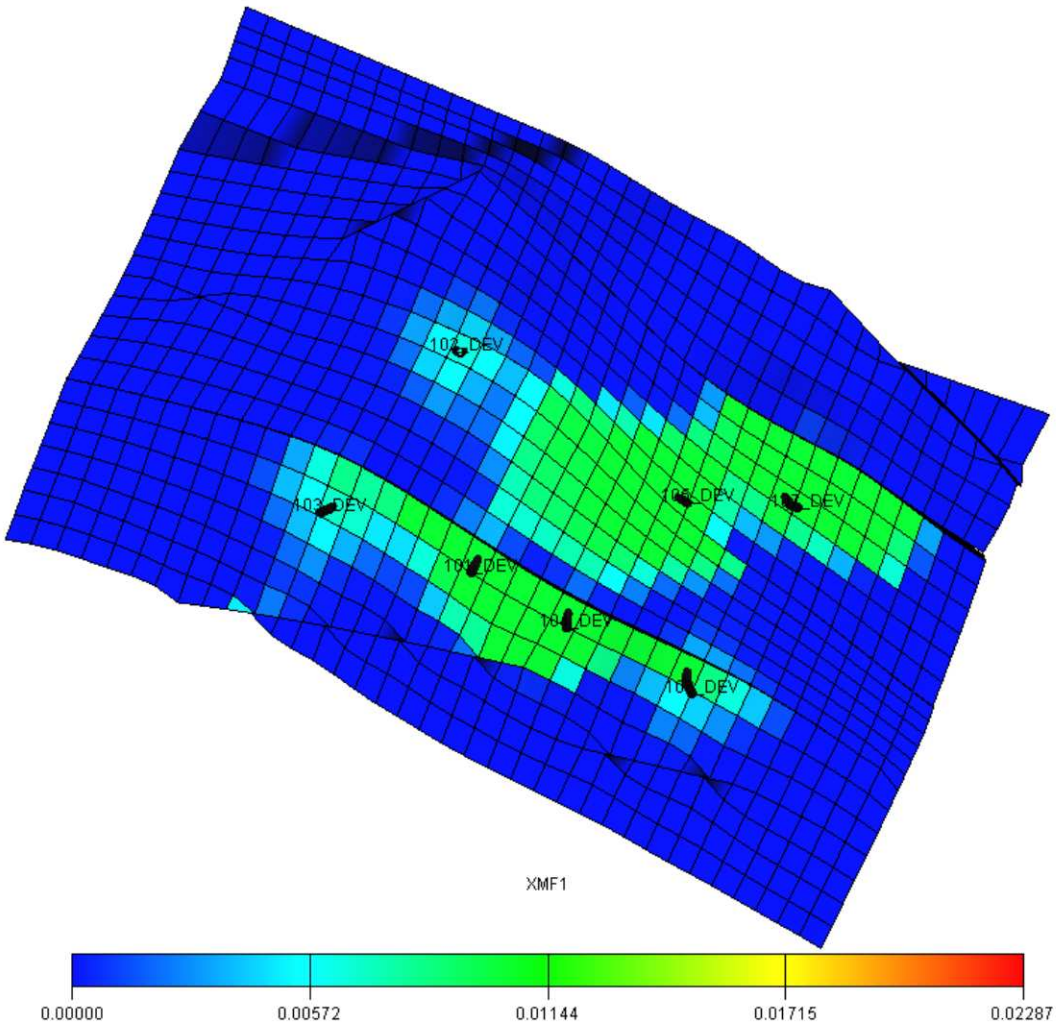

Figure 6.80: Gas concentration profile in the Buntsandstein prototype reservoir model in the cap rock just above the storage formation 250 years after termination of injection into aqueous phase containing 200,000 ppm NaCl

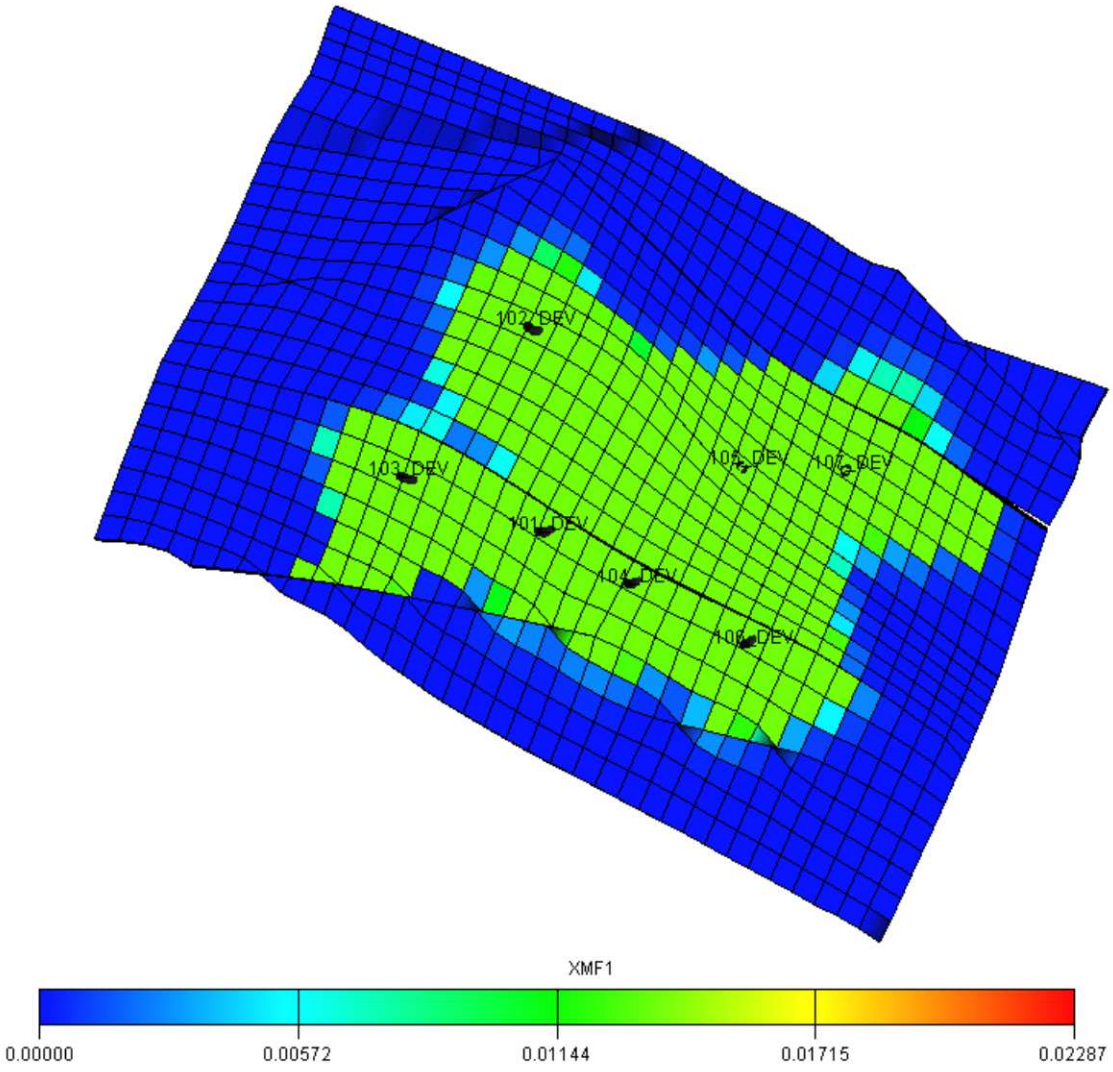

Figure 6.81: Gas concentration profile in the Buntsandstein prototype reservoir model in the top layer of the storage formation 250 years after termination of injection into aqueous phase containing 200,000 ppm $CaCl_2$

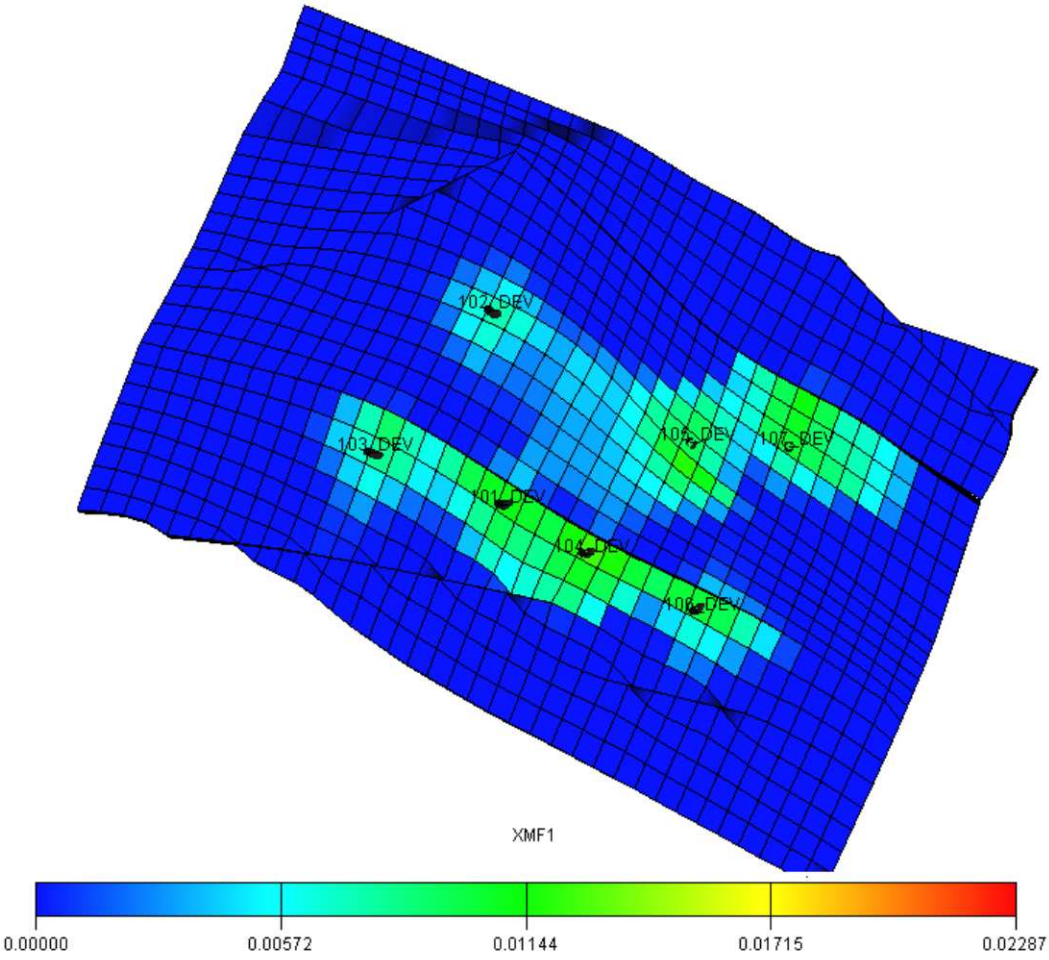

Figure 6.82: Gas concentration profile in the Buntsandstein prototype reservoir model in the cap rock just above the storage formation 250 years after termination of injection into aqueous phase containing 200,000 ppm $CaCl_2$

From the geological model of the Buntsandstein prototype reservoir, layer 16 is clay-intercalated sandstone. This zone can be beneficial for the CO_2 storage strategies. Since the clay-intercalated sandstone has less permeability and porosity relative to the sandstone, this layer can slow down the vertical migration of CO_2 if the gas is injected into the layer 17. Figure 6.83 and 6.84 represent the gas saturation profiles in the observation cross section after 10 and 250 years respectively.

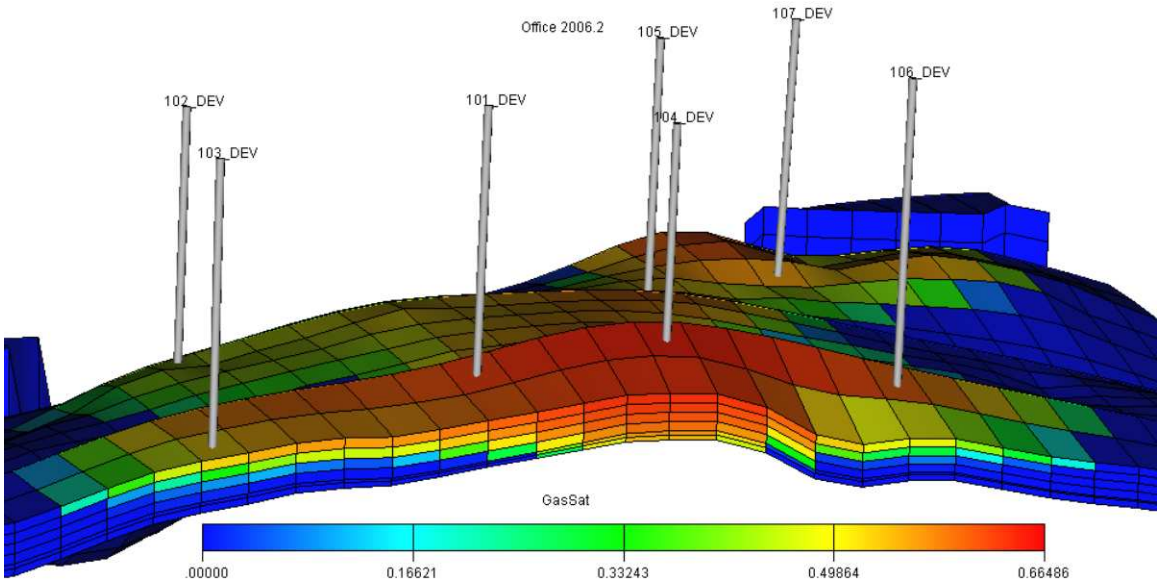

Figure 6.83: Gas saturation profile in Buntsandstein prototype reservoir model in the observation cross section (I,21,12-17) after 10 years of injection into fresh water

The main concern of CO_2 storage is the storage capacity of the aquifer which remains a common source of misleading estimates due to simplifications usually made the calculation of the aquifer capacity for CO_2 storage. Initially calculations, for example, have assumed that an aquifer can be represented by a uniform sheet, of constant thickness, and constant porosity across an entire sedimentary basin. A simple calculation can be made of the amount

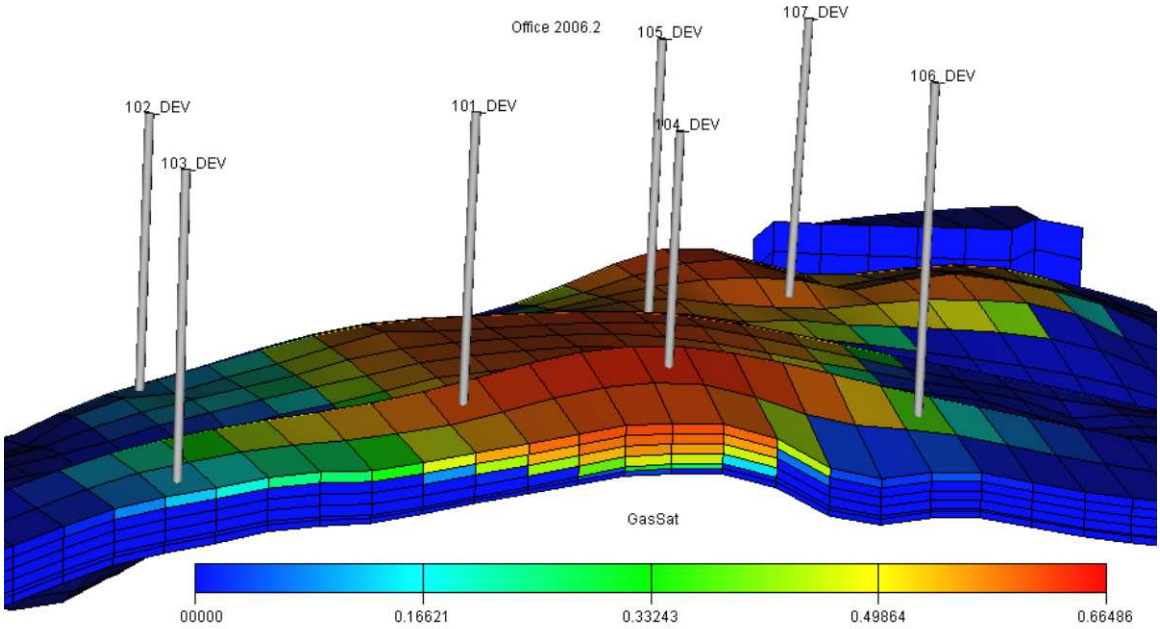

Figure 6.84: Gas saturation profile in Buntsandstein prototype reservoir model in the observation cross section (I,21,12-17) 250 years after termination of injection into fresh water

of water present, multiplied by the solubility of CO_2 to generate a theoretical storage figure.

Numerical simulations are performed in order to estimate the storage capacity of aquifer more accurately considering solubility of CO_2 in the formation water and aquifer heterogeneity.

The simulation results are tabulated for three cases in the Table 6.6, 6.7 and 6.8 respectively.

Table 6.6 summarizes the simulation process parameters and the resulting aquifer storage capacity for fresh water. CO_2 can be injected into only 15% of pore volume (PV) of the storage formation. The simulation runs were also performed for different irreducible water saturations in order to determine the sensitivity of storage capacity to this parameter. Increasing the irreducible water saturation resulted in significant decrease in aquifer storage capacities. For an irreducible water saturation of 50 %, the storage capacity decreases to

Table 6.6: The storage capacity of the aquifer for Case 1, fresh water

	Case 1, No Salinity
Maximum injection rate	50,000 sm^3/day per well
Total injection amount	1.96x10^8 sm^3
Injection Time	20 years controlled by maximum BHP, 300 bar
Initial water saturation	100 %
Critical gas saturation	10 %
Irreducible water saturation	25 %
Number of wells	7 vertical wells
Results: Storage Capacity	**0.15xPV**
Results: Average Field Pressure	**247 bar**

11% of pore volume. For Case 1, the average field pressure is 247 bar the pressure increases near the injection area at the early times, but due to the effect of buoyancy forces, the gas migrates upwards in the storage formation and the pressure build-up at the top of the storage of formation becomes stronger than around the injection well. The pressure increase at the top of the formation is about 80 bars above hydrostatic. This increase should be taken into account in order to get the more realistic view of the processes including the potential leakage into the cap rock.

Table 6.7: The storage capacity of the aquifer for Case 2, saline aquifer containing 200,000 ppm NaCl

	Case 2, 200 g/l NaCl containing aquifer
Maximum injection rate	50,000 sm^3/day per well
Total injection amount	1.76x10^8 sm^3
Injection Time	20 years controlled by maximum BHP, 300 bar
Initial water saturation	100 %
Critical gas saturation	10 %
Irreducible water saturation	25 %
Number of well	7 vertical wells
Results: Storage Capacity	**0.07xPV**
Results: Average Field Pressure	**246 bar**

Table 6.7 summarizes the simulation process parameters and the resulting aquifer storage capacity for NaCl brine. CO_2 can be injected into only 7% of pore volume (PV) of the storage formation. With the injection of CO_2 the average field pressure increases to about

40 bars above hydrostatic.

Table 6.8: The storage capacity of the aquifer for Case 3, saline aquifer containing 200,000 ppm $CaCl_2$

	Case 2, 200 g/l $CaCl_2$ containing aquifer
Maximum injection rate	50,000 sm^3/day per well
Total injection amount	1.80x10^8 sm^3
Injection Time	20 years controlled by maximum BHP, 300 bar
Initial water saturation	100 %
Critical gas saturation	10 %
Irreducible water saturation	25 %
Number of well	7 vertical wells
Results: Storage Capacity	**0.09xPV**
Results: Average Field Pressure	**253 bar**

Table 6.8 summarizes the simulation process parameters and the resulting aquifer storage capacity for $CaCl_2$ brine. CO_2 can be injected into only 9% of pore volume (PV) of the storage formation. The average field pressure reaches 253 bar.

The results of simulations emphasizes the fact that the simplistic storage capacity estimation approaches are not accurate. The true storage capability is observed to be much less, and needs to be reduced appropriately to account for factors such as aquifer heterogeneity, excluded locations near active faults, and especially the realization that CO_2 takes hundreds of years to dissolve in formation water. Thinking in human time scales of decades, the storage capacity mainly depends on the CO_2-volume, that establishes a free phase in the underground formation, usually in a state of a supercritical fluid. The CO_2-volume dissolved into the aquifer water is comparatively small in this period. The storage process relies on the creation of underground space based on the compressibility of the existing pore water and the rock matrix.

6.8 Summary of Simulation Results

Prediction of safety of injected CO_2 is necessary for large-scale implementation of CO_2 storage in saline aquifers. Finding simple scaling relationships that characterize the long term behavior of the sequestration process are useful for better understanding the final disposition of CO_2 in saline aquifers. In this study, we have used direct numerical simulations to determine appropriate scaling relationships for injection amount, rate of dissolution of CO_2, trapped gas amount and the risk of leakage. The results of the numerical simulations of CO_2 sequestration in Buntsandstein aquifers conducted are as follows:

1. Injection rate, times and volumes of CO_2 strongly depend on the aquifer volume. As expected, the greater the aquifer, the more volume of CO_2 can be injected without exceeding the BHP and the critical position of GWC at the spill point. The gas can be injected through the existing wells in the aquifer like in the case of Buntsandstein prototype reservoir. Injection through many wells increases the injectivity and dissolution of CO_2 into formation water since injected gas comes into contact with water at different locations and tends to dissolve more rapidly.

2. Numerical simulations with the generic model assume a homogeneous and isotropic porous media. However assuming a single permeability value in a storage formation may not be representative. From the results with the prototype model it can be conclude that permeability heterogeneity might have a great influence on density-driven instabilities.

3. Once the injection ceases the ratio of vertical to horizontal permeability (k_v/k_h) has a significant effect on the flow path. An increase of k_v/k_h ratio enhances the vertical gas migration, which brings the gas into contact with a larger volume of brine and thus leads to convective mixing, and more CO_2 dissolution trapping. Therefore, k_v/k_h ratio should be accurately provided for simulation.

4. The simulations of based on the generic model show that shale layers within the storage formation impedes the vertical migration of injected CO_2. Therefore, injection into the lowest layer of the Buntsandstein prototype reservoir model will be beneficial. The overlaying layer (layer 16) is siltstone with lower permeability relative to the other layers, slowing down the vertical migration and promoting the lateral movement of injected gas under low permeability layers. The risk of leakage through the cap rock (into the layer 11) decreases tremendously .

5. Brine composition has a significant effect on the estimation of the leakage rate results indicate that ignoring $CaCl_2$ contents and simplifying it as NaCl in the numerical modeling results in more leakage.

6. The storage capacity of the aquifer strongly depends on the salinity which affects the dissolution of the CO_2, aquifer parameters, and irreducible water saturation. Numerical simulations show that the CO_2 storage capacity of a 200,000 ppm NaCl containing aquifer is 7% of its pore volume whereas the capacity in fresh water aquifer is 15%. Also, increasing the irreducible water saturation resulted in a significant decrease in fresh water aquifer storage capacity. In case of assuming an irreducible water saturation 50%, the storage capacity decreases to 11% of pore volume.

7. The simulation results emphasizes the importance of the multi phase flow modeling in case of CO_2 sequestration in a saline aquifer. After the injection phase the upward and lateral migration of CO_2 is controlled by capillary trapping. During the injection phase, the drainage process dominates. However, the entrapment of CO_2 occurs during the imbibition process, as CO_2 is displaced upward, residual gas is left behind and the free gas spreads out in the vicinity of the injection interval into the aquifer. This tends to extent the lateral migration, enlarges the contact area with the aquifer brine and improves local solubility.

8. The simulations of the generic model show that the injection interval has an impact on the safety of CO_2 storage. The study emphasizes injection into the bottom layers of the storage formation. In fact, a horizontal well has an advantage over the vertical well in CO_2 injection. Horizontal wells located in the lower part of the formation increase the capacity of gas solubilization and eliminate contact with cap rock immediately.

Chapter 7

Conclusions

This project contributes to the characterization of Buntsandstein prototype aquifer for CO_2 sequestration and the determination of the sensitivity parameters that affect the prediction of CO_2 storage capacity by;

- Characterization of the Buntsandstein prototype aquifer, construction of the geologic model to define the spatial distributions of reservoir rock properties
- Compilation and interpretation of relevant phase behavior and phase property data CO_2/ brine
- Determination of the sensitivity of injected CO_2 behavior to the rock and sediment heterogeneity
- Modeling the time dependent changes in the distribution and dissolution of injected CO_2 into the heterogeneous aquifer
- Assessing the validity of hysteretic relative permeability models and examination of the impact of relative permeability and capillary forces on capillary trapping simulations
- Determination of the extent of CO_2 migration

- Assessing the optimal CO_2 injection amount and injection geometry
- Evaluating the leakage risk of CO_2 to the surface through the faults and cap rock formation

In Chapter 2, the geological model of a Buntsandstein prototype aquifer was defined based on an industry geo-model. It was determined from the core data, well logs, well test interpretation that the porosity of Buntsandstein aquifer is between 15% to 25% in the storage formation. The permeability was derived from the porosity - permeability correlations and confirmed by the well test analyses. The permeability distribution strongly resembles the primary porosity distribution and values between 129 mD to 178 mD. Accurate estimation of permeability would be valuable for future work in order to determine the migration path of CO_2 and predict the storage capacity of the aquifer precisely.

Chapter 3, describes the thermophysical properties of the individual fluids as well as fluid mixtures, evaluating the impact of the various corrections in ECLIPSE for aqueous and gaseous phases. The accurate modeling of phase behavior of gaseous/super critical CO_2 mixtures with formation brine is a prerequisite for solubility trapping of CO_2 in aqueous phase since it controls the dissolution of CO_2 when the gas comes into contact with undersaturated brine. The formation conditions under which CO_2 is likely to be injected, make numerical investigations more complex. Therefore, it is necessary to take into account the non-ideal behavior of both the mixed electrolytes dissolved in brine and the CO_2 gaseous phase.

In Chapter 4, the well-known "two-phase" hysteretic models accounting for trapping of the non-wetting phase were analyzed. However these models fail to reproduce the irreversibility of relative permeability scanning curves. There has been little experimental work to characterize the reduction in secondary drainage permeability analytically. Additionally, it is not well known how the simulation can accurately predict the secondary

and subsequent drainage paths. Future work should constitute development of predictive pore-network models valid for these displacement paths. The irreversibility of scanning curves is likely to be dependent on intrinsic rock properties easily explored using pore-network simulators. Experimental data is also beneficial to our understanding of this type of behavior.

The ECLIPSE simulator version was discussed in Chapter 5 including additional enhancements (CO2SEQ) in the phase equilibria model and thermophysical properties of fluid mixtures. Injection of CO_2 into saline aquifers will give rise to a variety of coupled physical and chemical processes, including pressurization of reservoir fluids, immiscible displacement of an aqueous phase by the CO_2 phase, partial dissolution of CO_2 into the aqueous phase. Therefore, the numerical simulator should have capabilities of modeling the physical and chemical processes involved to evaluate the technical feasibility of CO_2 storage into aquifers.

The work in Chapter 6 mainly focused on solubility trapping including different salinities and brine compositions, capillary entrapment including relative permeability hysteresis and leakage through the cap rock. It should be mentioned that the injected gas can leak also through the damaged wellbore and faults. However, the well test analysis and geological modeling of Buntsandstein prototype reservoir show that the faults act like no-flow boundaries, and therefore leakage through the faults as well as the effects of regional groundwater flow throughout the reservoir was not studied.

As CO_2 dissolves, the formation brine density increases. This density difference causes instability and induces convective-diffusive mixing in the aquifer which also enhances the dissolution rate of CO_2. Solubility trapping is mainly affected by brine salinity and brine composition, density differences between formation water and gas, permeability anisotropy, and critical gas saturations.

Capillary trapping is a major mechanism controlling the upward and lateral migration of CO_2 plumes after the injection phase in the geological storage of CO_2. When the relative

permeability hysteresis is taken into account, the dissolution of CO_2 in formation water decreases, on the other side the gas is stored as trapped gas in the vicinity of the injector. The capillary trapping is mainly affected by varying the CO_2 injection rate, hysteresis between drainage and imbibition processes and residual phase saturations.

The main concern of CO_2 injection into aquifer structures is that there is no proven gas tight cap rock a priori existing. This has to be confirmed by in-situ and laboratory investigations. In the case of having the proven cap rock overlying the storage formation, the gas leakage is less than 1 % of injected gas volume and it can be reduced by choosing the proper aquifer and injection strategies. Since the leakage rate depends mainly on the aquifer thickness, aquifer petrophysical properties, mean permeability, vertical to horizontal permeability ratio, residual phase saturations, injection rate, salinity of the aquifer, and the placement of the injection.

It can be also concluded from this study that, due to buoyancy forces, the injected gas always tends to migrate upward in the storage formation. Well completions and injection intervals play an important role after the injection ceases. When the supercritical CO_2 enters the storage formation near the top seal, it flows laterally underneath the cap rock and thus increases the contact area with cap rock and may eventually find an escape path. On the other hand, when the gas was injected in the lower part of the aquifer, gravity-driven flow reduces the amount of mobile gas either by dissolving or trapping in the vicinity of the wellbore before it migrates to the top of the formation. However, the time scale for the reduction of free gas strongly depends on petrophysical parameters and the thickness of the aquifer.

Chapter 8

Recommendations for the Future Work

This project contributes the characterization of Buntsandstein prototype aquifer and investigation of sensitivity parameters that affect the prediction of CO_2 storage capacity of the aquifer. Several issues considered in this study deserve further study and should be subject of future research as follows:

1. The simulations show that the accurate modeling of multi phase flow behavior including capillary pressure and hysteresis effects is required for the precise prediction of trapping capacity of the aquifers. Therefore, more experimental data for CO_2-brine system is required. A trapping and relative permeability model can be developed for Buntsandstein aquifer which can be applicable for the whole range of rock wettability

2. In order to minimize the gas leakage through the cap rock the gas breakthrough depending on the gas threshold pressure should be determined before the start of carbon dioxide sequestration project in aquifers. Therefore, the interfacial tension, breakthrough pressure, and gas threshold pressure should be investigated.

3. Geochemical modeling, chemical reactions between the aquifer solids and injected gas would also beneficial in terms of investigating the possible permeability changes in

the aquifer, if the transport models become available.

4. Geomechanics should be taken into account in order to define the acceptable injection rates and capacity limits with request to the pressure build-up phase beyond the hydro-static pressure. Since the injectivity of CO_2 is strongly affected by the mean permeability.

5. Gas mixtures with various compositions will become target of future disposal and should be investigated with request the solubility trapping capacity

6. The local grid refinement option with its higher resolution can be useful for definite answers to the viscous fingering.

A complete evaluation of the feasibility of geologic carbon disposal in aquifers will require the study of several other issues that are beyond the scope of this work including geomechanics and chemical reactions. In addition, it is not yet possible to predict with confidence storage volumes and integrity over long time periods of the target formations, and many additional issues must be addressed to reduce costs, gain public acceptance and ensure safety.

Bibliography

[1] *Eclipse manual 2006.2.*

[2] Roman A., *Sequenzstratigraphie und fazies des unteren und mittleren buntsandsteins im östlichen teil des germanischen beckens (Deutschland, Polen)*, Ph.D. thesis, Halle-Wittenberg, 2004.

[3] S. Bachu and J.J. Adams, *Sequestration of CO_2 in geological media in response to climate change: Capacity of deep saline aquifers to sequester CO_2 in solution*, Energy Conversion and Management **44** (2003), no. 20, 3151–3175.

[4] S. Bachu, W.D Gunter, and E.H. Perkins, *Aquifer disposal of CO_2: Hydrodynamic and mineral trapping*, Energy Conversion Management **35** (1994), 296–279.

[5] M. Batzle and Z Wang, *Seismic properties of pore fluids.*, Geophysics **57** (1992), no. 11, 1396–1408.

[6] B. Bennion and S. Bachu, *Relative permeability characteristics for supercritical CO_2 displacing water in a variety of potential sequestration zones in the western canada sedimentary basin*, (2005), presented at SPE Annual Technical Conference and Exhibition, Dallas, Texas SPE 95547.

[7] R.G. Bruant, A.J. Guswa, M.A. Celia, , and C.A. Peters, *Safe storage of CO_2 in deep saline aquifers*, Environmental Science and Technology **36** (2002), no. 11, 240–245.

[8] Philibert; C. and J. Pershing, *Beyond Kyoto – energy dynamics and climate stabilization*, Tech. report, IEA-International Energy Agency/ OECD, Paris, 2002.

[9] F.M. Carlson, *Simulation of relative permeability hysteresis to the nonwetting phase*, (1981), presented at SPE Annual Technical Conference and Exhibition, San Antonio, TX, October 5-7 SPE 10157.

[10] J.J. Carroll, J.D. Slupsky, and A.E. Mather, *The solubility of carbon dioxide in water at low pressure*, Journal of Physical and Chemical Reference Data **20** (1991), no. 6, 1201–1209.

[11] Y.B. Chang and B.K. Coats, *A compositional model for CO_2 floods including CO_2 solubility in water*, SPE Reservoir Evaluation & Engineering (1998), 155–160, presented at SPE Permian Basin Oil & Gas Recovery Conference, Midland, Texas, SPE 35164.

[12] A.T Corey, *The interrelation between gas and oil relative permeabilities*, Producers Monthly (1954), 28–31.

[13] Faaij A. Turkenburg W. Damen, K., *Healthy, safety and environmental risks of underground co_2 sequestration*, Tech. report, Copernicus Institute of Sustainable Development and Innovation, The Netherlands, 2003.

[14] C. Doughty, *Modeling geologic storage of carbon dioxide: Comparison of non-hysteretic and hysteretic characteristic curves*, (2006), Proceedings, TOUGH Symposium, Berkeley, California.

[15] C. Doughty and K. Pruess, *Modelling supercritical CO_2 injection in heteregenous porous media*, (2003), presented at the 2003 TOUGH Symposium, Berkeley, California.

[16] Z. Duan, N. Möller, and J.H. Weare, *An equation of state for the CH_4–CO_2–H_2O system: I. pure systems for 0 to 1000 °C and 0 to 8000 bar.*, Geochimica et Cosmochimica Acta **56** (1992b), 2605–2617.

[17] Z. Duan, N. Moller, J. Greenberg, and J. Weare, *The prediction of methane solubility in natural waters to high ionic strength from 0 to 250°C and from 0 to 1600 bar*, Geochimica er Cosmochimica Acta **56** (1992), 1451–1460.

[18] Z. Duan and R. Sun, *An improved model calculating CO_2 solubility in pure water and aqueous NaCl solutions from 273 to 533 K and from 0 to 2000 bar*, Chemical Geology **193** (2003), 257–271.

[19] R.M. Enick and S.M. Klara, *CO_2 solubility in water and brine under reservoir conditions*, Chemical Engineering Communications **90** (1990), 23.

[20] J. Ennis-King and L. Paterson, *Engineering aspects of geological sequestration of carbon dioxide*, (2002), presented at the Asia Pacific Oil and Gas Conference and Exhibition, Melbourne, Australia, 8-10 October, SPE 77809.

[21] Paterson L. Ennis-King, J., *Role of convective mixing in the long-term storage of carbon dioxide in deep saline formations*, (2003), presented at SPE Annual Technical Conference and Exhibition, Denver, Colorado, SPE 84344.

[22] A. Fenghour, W. A. Wakeman, , and V. (1998) Vesovic, *The viscosity of carbon dioxide*, Journal of Physical and Chemical Reference Data **27** (1998), no. 1, 31–44.

[23] J.E. Garcia, *Density of aqueous solutions of CO_2*, Technical Report LBNL 49023, Lawrence Berkeley National Laboratory, Berkeley, CA, 2001.

[24] J.E Garcia, *Fluid dynamics of carbon dioxide disposal into saline aquifers*, Ph.D. thesis, University of California, Berkeley, 2003.

[25] A. Hildenbrand, B.M. Schlömer, S. Krooss, and R. Littke, *Gas breakthrough experiments on pelitic rocks:Comparative study with N_2, CO_2 and CH_4*, Geofluids **4** (2004), 61–80.

[26] A. Hildenbrand, S. Schlömer, and B.M. Krooss, *Gas breakthrough experiments on fine-grained sedimentary rocks*, Geofluids **2** (2002), 3–23.

[27] J.T. Houghton, Y. Ding, D.J. Griggs, P.J. Noguer, M.and van der Linden, X. Dai, K. Maskell, and C.A. Johnson, *Climate change 2001: The scientific basis. Contribution of working group I to the third assessment report of the intergovernmental panel on climate change*, IPCC, 2001 ed., Cambridge University Press, 2001.

[28] G. R. Jerauld and S. J. Salter, *Effect of pore-structure on hysteresis in relative permeability and capillary pressure: pore-level modeling*, Transport in Porous Media **5** (1990), 103–130.

[29] R. Juanes, E.J. Spiteri, Orr Jr.F.M. , and M.J. Blunt, *Impact of relative permeability hysteresis on geological CO_2 storage*, Water Resources Research **12** (2006), W12418.

[30] J.E. Killough, *Reservoir simulation with history dependent saturation functions*, (1974), no. Carlson, F.M., presented at SPE-AIME 49^th Annual Fall Meeting, October 6-9 in Houston, SPE 5106.

[31] A. Kumar, *A simulation study of carbon sequestration in deep saline aquifers*, Master's thesis, The University of Texas Austin, August 2004.

[32] A. Kumar, R. Ozah, M. Noh, G.A. Pope, S. Bryant, and Wl.W. Sepehrnoori, K. amd Lake, *Reservoir simulation of CO_2 storage in deep saline aquifers*, (2005), presented at 2004 SPE/DOE Symposium on Improved Oil Recovery, Tulsa, SPE 89343.

[33] C.S. Land, *Calculation of imbibition relative permeability for two and three phase flow from rock properties*, (1968), SPE 1942.

[34] ———, *Comparison of calculated with experimental imbibition relative permeability*, (1971), presented at SPE Rocky Mountain Regional Meeting, June 2-4, in Billings SPE 3360.

[35] L. D. Landau and E. M. Lifshitz, *Statistical physics; course of theoretical physics*, 3rd ed., vol. 5, Butterworth-Heinemann, 1996.

[36] R. J. Lenhard and J. C. Parker, *A model for hysteretic constitutive relations governing multiphase flow, 2. permeability-saturation relations*, Water Resources Research **23** (1987), 2197–2206.

[37] Y. Li and L.X. Ngheim, *Phase equilibria of oil, gas and water/brine mixtures from a cubic equation of state and Henry's law*, Canadian Journal of Chemical Engineering **64** (1986), 486–496.

[38] Z. Li, M. Dong, S. Li, and S. Huang, *CO_2 sequestration in depleted oil and gas reservoirs—caprock characterization and storage capacity*, Energy Conversion and Management **47** (2006), 1372–1382.

[39] D. A. Neild and A. Bejan, *Convection in porous media*, 2nd ed., Springer Verlag, New York, 1999.

[40] K. Pruess and J. E. Garcia, *Multiphase flow dynamics during CO_2 disposal into saline aquifers*, Environmental Geology **42** (2002), 282–295.

[41] C.F. Prutton and R.L Savage, *The solubility of carbon dioxide in calcium-chloride-water solutions at 75, 100, 120° C and high pressure*, Journal of the American Chemical Society **67** (1945), 1550–1554.

[42] Ren Q.Y., Chen G.J., Yan W., and Guo T.M, *Interfacial tension of CO_2 + CH_4+ water from 298 K to 373 K and pressures up to 30 MPa*, Journal of Chemical Engineering Data **45** (2000), 610–612.

[43] B. Rumpf, H. Nicolaisen, C. Öcal, , and G. Maurer, *Solubility of carbon dioxide in aqueous solutions of sodium chloride: Experimental results and correlations*, Journal of Solution Chemistry **23** (1994), 432–448.

[44] R. Span and W. Wagner, *A new equation of state for carbon dioxide covering the fluid region from the triple-point temperature to 1100 K at pressures up to 800 MPa*, Journal of Physical and Chemical Reference Data **25** (1996), no. 6, 1509–1596.

[45] N. F. Spycher, K. Pruess, and J. Ennis-King, *CO_2-H_2O mixtures in the geological sequestration of CO_2. I. assessment and calculation of mutual solubilities from 12 to 100 °C and up to 600 bar*, Geochimica et Cosmochimica Acta **67** (2003), no. 16, 3015–3031.

[46] B. Ulker, H. Alkan, and G. Pusch, *Implications of the phase-solubility behaviour on the performance predictions of the CO_2 trapping in depleted gas reservoirs and aquifers*, prepared for presentation at the SPE Europec/EAGE Annual Conference and Exhibition held in London, United Kingdom, 11–14 June 2007, SPE 107189-MS.

[47] M.T. van Genuchten, *A closed-form equation for predicting the hydraulic conductivity of unsaturated soils*, Soil Science Society of America Journal **44** (1980), 892–898.

[48] N. B. Vargaftik, Y. K. Vinogradov, and V. S. Yargin, *Handbook of physical properties of liquids and gases*, 3. ed., Begell House, New York, 1996.

[49] V. Vesovic, W. A. Wakeham, G. A. Olchowy, J. V. Sengers, , and J. T. R. Watson, *The transport properties of carbon dioxide*, Jornal of Chemical Engineering Data **19** (1990), no. 3, 763–808.

[50] R. Wiebe and V. L. Gaddy, *The solubility of carbon dioxide in water at various temperatures from 12 to 40° C and at pressures to 500 atmospheres: critical phenomena*, Journal of American Chemical Society **62** (1940), 815–817.

[51] ———, *Vapor phase composition of carbon dioxide water mixtures at various temperatures and at pressures to 700 atmospheres*, Journal of American Chemical Society **63** (1941), 475–477.

[52] I.D. Zaytsev and G.G. Aseyev, *Properties of aqueous solutions of electrolytes*, CRC Press, 1993.